

**REGULATION OF TENSILE STRESS IN RESPONSE TO EXTERNAL  
FORCES COORDINATES EPITHELIAL CELL SHAPE TRANSITIONS  
WITH ORGAN GROWTH AND ELONGATION**

---



**Ramya Balaji**

Ludwig-Maximilians-Universität München

---

**München 2018**



**REGULATION OF TENSILE STRESS IN RESPONSE TO EXTERNAL  
FORCES COORDINATES EPITHELIAL CELL SHAPE TRANSITIONS  
WITH ORGAN GROWTH AND ELONGATION**

---

**Dissertation**

an der Fakultät für Biologie  
der Ludwig-Maximilians-Universität München

**vorgelegt von**

Ramya Balaji

München, den 24. Mai 2018

Erstgutachter: Dr. Anne-Kathrin Classen  
Zweitgutachter: Prof.Dr. Nicolas Gompel  
Tag der Abgabe: 24. Mai 2018  
Tag der mündlichen Prüfung: 23. Oct 2018

## Declaration

### *Eidesstattliche Versicherung*

Hiermit erkläre ich an Eides statt, dass ich die vorliegende Arbeit selbständig und ohne unerlaubte Hilfe von Dritten angefertigt habe.

München, den 24. Mai 2018

.....

Ramya Balaji

### *Erklärung*

Hiermit erkläre ich, dass die Dissertation weder als Ganzes, noch in Teilen an einem anderen Ort einer Prüfungskommission vorgelegt wurde. Ich habe weder an einem anderen Ort eine Promotion angestrebt, noch angemeldet oder versucht eine Doktorprüfung abzulegen.

München, den 24. Mai 2018

.....

Ramya Balaji

## DECLARATION

### *Contributions*

Contributions from people who assisted in generating specific data sets are credited in the figure legends and are also mentioned in the Aim of this study.

### *Manuscript under revision/preparation*

Parts of this work have been used for a manuscript that is currently under revision.

## Acknowledgements

As this journey sees its sunset, I can think of countless moments where I am grateful to have met, interacted and worked with some amazing people who I shall cherish in my memory for years to come.

First, I would like to thank Anne. Thank you for this huge opportunity to challenge myself in innumerable ways. I thank you for your indefinite patience and open-mindedness towards what ranged from naïve to bizarre ideas I might have had and countless discussions thereupon. I also thank your constant flux of inspiring ideas, your numerous hi-fi moments and your ability to find several silver linings at moments of my despair. You are a huge role model and hero for me. I admire your scientific spirit, constant enthusiasm, persistence and your practical sensibilities for doing research. Thank you for your unwavering support in finding my path in life.

Second, I would like to thank my TAC advisors including Frank Schnorrer, Carsten Grashoff, Heinrich Leonhardt, Giorgios Pyrowolakis, Soeren Lienkamp for giving their valuable time and inputs on my projects. I thank my thesis reviewers for taking the time to read through it and their comments. I thank our collaborators Hartmann Harz and Guillaume Salbreaux for their vital thoughts and discussions on my projects. I thank members of Stephan Grill's group for hosting and training me for crucial laser ablation experiments. I also thank the numerous practical students (Jack, Sebastian, Manuela) and Master theses students (Caroline, Simone and Martino) who joined me in my experimental endeavors.

Third, my wonderful lab mates without whom the pleasure of coming to work would always be incomplete. Thank you -Addie, Christina, Marco and Andrea, for helping me settle into my life in Munich. The Friday beers, potluck lunches, ensuing discussions and bunch-of-laugh are memories I treasure. Thank you, Marco, for your patience with my nagging statistics queries in my "statistics voice". You are a wonderful teacher! My Freiburg lab family, including Vanessa, Janhvi, Andrea, Isabelle and the newbies- Deepti, Abhay and Carlo. Thank you for enduring my apparent bossiness (I still protest the wildly exaggerated terror stories, but alas, they have become unchangeable history!), clumsiness, impatience for lunch and lack of diplomacy in a lot of things. I have enjoyed laughing at my idiosyncrasies. Thank you for

## ACKNOWLEDGEMENTS

helping me identify my “Cow sound” and appointing me as the “Finisher of our goodies”! Thanks for your time both inside and outside the lab, the never-ending supply of cakes, chocolates, chips and occasional healthy stuff, cooking sessions, hikes, sunny day radlers, grey day radlers and millions of discussions beyond science. I count myself very lucky to have been in such a supportive and reflective environment. I could not have asked for more fun teams to be part of, in Munich and Freiburg. I am definitely going to miss you all when it’s over. Lots of love and hugs (on print!) you guys!

I thank my friends, Sushi and Luidmila for being my support system outside the lab.

And my family- I thank my Mom and Dad for their limitless, selfless support and love. I am where I am, because of decades of painstaking efforts and sacrifices on their part to get me to this milestone in my life. I thank them for being so open-minded about my dreams and aspirations, their belief in me and their strength in being so supportive despite being miles away from me. I thank my brother, Sudarshan for being my rock. You are always there for me despite all the distances and time zones. I am forever grateful to them.

Finally, a life lesson that I take with me from pursuing research keeping mankind’s quest for knowledge in perspective is summarized in this quote–

*“Try again. Fail again. Fail better.”*

*-Samuel Beckett*

# Contents

<b>DECLARATION</b>	<b>3</b>
<b>ACKNOWLEDGEMENTS</b>	<b>5</b>
<b>CONTENTS</b>	<b>7</b>
<b>LIST OF FIGURES</b>	<b>13</b>
<b>LIST OF TABLES</b>	<b>17</b>
<b>ABBREVIATIONS</b>	<b>19</b>
General abbreviations	19
Gene and protein abbreviations	20
<b>SUMMARY</b>	<b>21</b>
<b>ZUSAMMENFASSUNG</b>	<b>22</b>
<b>1 INTRODUCTION</b>	<b>23</b>
1.1 Epithelial cell shape: function and relevance	23
1.2 Features of epithelia – packing, polarity, adhesion and contractility	25
1.2.1 Epithelial packing	25
1.2.2 Epithelial cell polarity	25
1.2.3 Epithelial cell junctions	26
1.2.4 Focal adhesions	27
1.2.5 Adherens junctions	27

## CONTENTS

1.3	Epithelial mechanics	29
1.3.1	Actomyosin contractility	29
1.3.2	Actomyosin contractility generates tensile force on AJs by anchoring on $\alpha$ -catenin	30
1.3.3	Mechanosensing through Crumbs and spectrin network	33
1.3.4	Material properties of epithelial cells	33
1.3.5	Probing physical properties and forces on epithelial cells	34
1.4	Epithelial morphogenesis	35
1.4.1	Morphogenesis driven by cell-autonomous mechanisms	35
1.4.2	Morphogenesis driven by mechanisms external to epithelia	37
1.5	Egg chamber - model system to study epithelial cell shape transitions	40
1.5.1	Epithelial tissue models in <i>D. melanogaster</i>	40
1.5.2	Egg chamber – model for epithelial cell shape transitions	40
<b>2</b>	<b><u>AIM OF STUDY</u></b>	<b>44</b>
<b>3</b>	<b><u>RESULTS</u></b>	<b>46</b>
3.1	Onset of columnar cell shape is suppressed by nurse cell contact and initiates prior to cell flattening	46
3.2	Cell polarity, adhesion and cytoskeletal proteins that correlate with cell shape transitions and germline contact	50
3.3	Reorganization of adherens junctions and contractility is driven by cell-autonomous mechanisms of follicle cells	56
3.3.1	Reorganization of the actomyosin cortex on the apical surface of follicle cells	56
3.3.2	Uniform onset of corrugations in adherens junctions correlate with germline growth	58
3.4	Tensile stress on junctions decreases to accommodate the expansion of the germline	61
3.4.1	Existing FRET based E-Cad tension sensors do not reveal any differences in junctional tension between NCCs and OCCs	61
3.4.2	Laser ablation experiments reveal differences in tensile forces on adherens junctions during stages 6 to 10	64

3.5	Reduction of Myosin and AJs sensitizes the NCCs to greater shape deformation than OCCs	67
3.5.1	Reduction of Myo II and its upstream activator deforms NCCs more than OCCs	67
3.5.2	Increasing corrugations in AJs promotes NCC shape deformation	72
3.6	Organ level consequences of NCC shape deformation	75
3.6.1	NCC-OCC transitions are delayed upon aberrant NCC flattening	75
3.6.2	Anterior expansion of the oocyte is delayed at tears in NCC	76
3.6.3	Summary of consequences of NCC deviation from cuboidal shape	82
3.7	Nurse cell cluster elongation is aided by NCCs	83
3.8	Different properties of nurse cells surfaces compared to the oocyte surface promote sensitivity of mutant NCCs to flattening	87
<b>4</b>	<b><u>DISCUSSION</u></b>	<b>91</b>
4.1	Decrease in tensile stress on the AJs accommodates germline growth	92
4.1.1	How is decrease in tensile stress on AJs achieved?	92
4.1.2	Junction excluded Myo II exerts forces on junctions	95
4.1.3	Dumping stage of egg chambers show complete loss of tensile stress in AJs	96
4.1.4	Limitations of recoil velocity measurements in understanding biomechanical properties of epithelia	96
4.2	Epithelial cell shapes in a relaxed epithelium	97
4.2.1	Cuboidal cell shape is a result of local resistance to nurse cell derived forces mediated by actomyosin contractility	97
4.2.2	Columnar cell shape is not generated by apical contractility	99
4.2.3	Is there a developmental signal that controls columnar-fate?	104
4.2.4	Squamous cell shape	104
4.3	Sources of external forces during germline growth	104
4.3.1	Nurse cell and oocyte cortices are different	104
4.3.2	Mechanosensing forces from nurse cells to generate resistance in NCCs	105
4.4	Organ shape is modulated by local contractility in the epithelium	106

## CONTENTS

4.4.1	Local apical contractility from NCCs constrains the nurse cell compartment into elongation	106
4.4.2	Completion of cuboidal to columnar shape transitions relies on balance of localized increase in tensile stress and AJ length in NCCs	107
<b>5</b>	<b>CONCLUSION</b>	<b>110</b>
<b>6</b>	<b>MATERIALS AND METHODS</b>	<b>111</b>
6.1	Fly husbandry and genetic manipulation systems	111
6.2	Dissection and immunohistochemistry of egg chambers	112
6.3	Electron microscopy	112
6.4	Live imaging culture conditions	112
6.4.1	FLIM imaging	113
6.4.2	Laser ablation	113
6.4.3	Collagenase treatment of egg chambers	113
6.5	Image Analysis and Quantification using Fiji	113
6.5.1	Quantification of cell areas, heights and corrugations	113
6.5.2	Fluorescence intensity quantification	114
6.5.3	mTFP fluorescence life-time analysis	114
6.5.4	Analysis of vertex displacement, cortical area changes and initial recoil velocities after laser ablation	116
6.5.5	Germline aspect ratio measurements	118
6.5.6	Germline area and nurse cell-oocyte area ratio measurements	118
6.6	Fly stocks	118
6.7	Antibodies	119
6.7.1	Primary antibodies	119
6.7.2	Secondary antibodies and Phalloidin	120
6.8	Consumables	120
6.9	Equipment	121

6.9.1	Microscopes	121
6.9.2	Other technical equipment	122
6.9.3	Software	122
<b>REFERENCES</b>		<b>123</b>
<hr/>		
<b>7</b>	<b>APPENDIX</b>	<b>134</b>
<hr/>		
7.1	Genotypes	134
7.2	Quantifications	136
7.2.1	Epithelial cell junctional area and height measurements at stage 7 and stage 9	136
7.2.2	Junction corrugation and roughness measurements	140
7.2.3	Laser ablation data analysis	142
7.2.4	FLIM analysis	144
7.2.5	Nurse cell aspect ratio and area measurements	145
7.3	Statistics and analysis for recoil curves	147
<b>CURRICULUM VITAE</b>		<b>148</b>
<hr/>		



## List of Figures

Figure 1 Simple epithelial cell shapes	24
Figure 2 Features of epithelial tissue – packing, polarity and adhesion	29
Figure 3 Contractile force generation and actomyosin recruitment on AJs under tension	32
Figure 4 Myo II contractility mediated apical constriction	37
Figure 5 Cell adhesion and contractility on different surfaces can generate different epithelial cell shapes	39
Figure 6 Egg chamber development	42
Figure 7 Epithelial cell shape correlates with apposition to oocyte or nurse cell compartments	47
Figure 8 Developmental fate can be used for tracking squamous-fated cells but no specific known developmental fate tracks with all columnar-fated cells	48
Figure 9 Summary of cuboidal-columnar cell shape transitions between stage 6 to 10A	49
Figure 10 Columnar cell shape of FCE correlates even with mis-positioned oocytes	50
Figure 11 A screen for polarity, junctional and cytoskeletal proteins for FCE cell shape and germline contact-dependent correlations	52
Figure 12 E-cad/ $\beta$ -cat levels are modulated by cell non-autonomous, germline contact-dependent mechanisms	53
Figure 13 MyoII levels are modulated by cell non-autonomous, germline contact-dependent mechanisms	54
Figure 14 Change in AJ and Myo II levels in OCCs is regulated by differently	56
Figure 15 MyoII and $\beta_H$ -spectrin reorganization in apical domain of FCE during stages of germline surface area expansion	57
Figure 16 Actin reorganization in NCC apical domain during stages of germline surface area expansion	58
Figure 17 Emergence of junctional corrugations in FCE during stages of germline surface expansion	60
Figure 18 Summary of follicle cell-autonomous and non-autonomous processes that remodel the entire apical domain of FCE during stages of germline surface area expansion and epithelial cell shape transitions	61

## LIST OF FIGURES

Figure 19 Fluorescence life-time analysis using a DE-Cad FRET based tension sensor does not reveal differences in tension in the junctions of NCCs and OCCs	63
Figure 20 Laser ablation analysis of junctions and medial cortices in FCE	66
Figure 21 RNAi efficiency tested with antibodies	68
Figure 22 Regulators of actomyosin contractility are required to prevent NCC flattening	69
Figure 23 NCCs are more sensitive to deformations when contractility or AJs are perturbed between stage 6 to 10	70
Figure 24 Junctional catenins and apical polarity factors are required to prevent NCC flattening	71
Figure 25 Canoe overexpression does not relocate excluded Myo II onto the junctions.	72
Figure 26 Increasing junctional corrugations specifically promotes NCC flattening	74
Figure 27 Organ-level consequences of NCC flattening on disruption of contractility and AJ regulators	76
Figure 28 Crb localisation on the oocyte membrane	78
Figure 29 Localization of Crb and its binding partners on oocyte membrane	79
Figure 30 Crb hypomorph and cytoskeleton-binding domain deficient germline mutants have normal oocyte anterior membrane extension	80
Figure 31 FCE integrity and number of columnar-fated cells are important for final oocyte size.	81
Figure 32 Summary of consequences of NCC deviation from cuboidal shape	<b>Error</b>
<b>! Bookmark not defined.</b>	
Figure 33 NCC are required to withstand nurse cell derived-forces and to promote egg chamber elongation	85
Figure 34 Bulging of nurse cells is constrained in the DV axis by NCC cell shape	86
Figure 35 E-cad adhesion does not mediate NC-NCC interactions and apical protrusions are features of NCC apical domain	<b>Error</b>
<b>! Bookmark not defined.</b>	
Figure 36 Interactions between the nurse cells and NCCs are stronger than between the oocyte and the OCCs	90
Figure 37 Epithelium tension relaxation during stages of germline surface area expansion by junctional lengthening and Myo II exclusion	93
Figure 38 Complete loss of junctional tension during nurse cell dumping	98
Figure 39 Small germline has columnar cells over the nurse cells	99

Figure 40 Reorganisation of trafficking components potentially by germline contact-dependent cues could promote OCC columnarisation	100
Figure 41 Volume of follicle cells decreases in $\beta$ -PS deficient cells	101
Figure 42 What sets the limit of apical area in columnar-fated cells?	103
Figure 43 Round egg chambers show cuboidal-columnar cell shape gradient dependent on germline contact	107
Figure 44 Balance of local contractility and junction length over the nurse cells controls cell shape transitions and egg chamber shape	109
Figure 45 FLIM data analysis	115
Figure 46 Laser ablation data analysis	117



## List of Tables

Table 1 Fly stocks: All fly stocks used in this study are listed with their source.	118
Table 2 Primary antibodies: Antigen, Source, Catalog number, Dilution and Manufacturer	119
Table 3 Secondary antibodies: Antigen, Conjugate, Source, Dilution and Manufacturer	120
Table 4 Buffers and reagents	120
Table 5 Microscopes with key equipment	121
Table 6 Technical equipment	122
Table 7 Softwares	122
Table 8 Detailed genotypes of individual images presented in this work	134
Table 9 FCE cell junctional area measurements at stage 7 and stage 9 in wildtype egg chambers	136
Table 10 FCE cell height measurements at stage 7 and stage 9 in wildtype egg chambers	137
Table 11 FCE height measurements in egg chambers with misplaced oocytes upon germline specific expression of <i>shg</i> RNAi	138
Table 12 Cell junctional area measurements in FCE specific knockdown and overexpression of different genes at stage 9	138
Table 13 Cell height measurements in FCE specific knockdown and overexpression of different genes at stage 9	139
Table 14 Junction corrugation measures at stage 6 and stage 9	140
Table 15 Junction corrugations in NCCs and OCCs at stage 9	141
Table 16 Vertex displacement analysis	142
Table 17 Medial cortical area change analysis	143
Table 18 Calculated junctional recoil velocities upon laser ablation	144
Table 19 Calculated medial cortical area recoil velocities upon laser ablation	144
Table 20 Fluorescence life times of junctions in NCCs and OCCs at stage 9 in DE-Cad TS egg chamber	144
Table 21 Fluorescence life times of the front and rear of a migrating border cell cluster in DE-Cad TS egg chambers	145
Table 22 Fluorescence life times of the front and rear of a migrating border cell cluster in DE-Cad TS control egg chambers	145

## LIST OF TABLES

Table 23 Total germline area measurements for different genotypes	145
Table 24 NC to OO area ratio measurements for different genotypes	146
Table 25 Nurse cell compartment, oocyte and total germline AP length for wildtype and FCE expression of <i>crb</i> RNAi	146
Table 26 Nurse cell compartment bulging measurements for different genotypes at stage 9	146
Table 27 Nurse cell compartment aspect ratio measurements upon Collagenase treatment	147
Table 28 Fitting parameters for recoil curves in Figure 20	147
Table 29 t- and P-values for the fitting parameters in Table 28	147

## Abbreviations

### General abbreviations

<b>Abbreviations</b>	<b>Full Form</b>
ECM	Extracellular matrix
EC	Egg chamber
NCC	Nurse cell Contacting Cell
OCC	Oocyte Contacting Cell
FCE	Follicle cell epithelium
GL	Germline
CCC	Cadherin-Catenin Complex
GFP/RFP	Green/red fluorescent protein
ROI	Region of interest
DAPI	4',6-diamidino-2-phenylindole
FRET	Fluorescence Resonance Energy Transfer
AFM	Atomic Force Microscopy
AJs	Adherens Junctions
SJs	Septate Junctions
GJs	Gap Junctions
TS	Tension Sensor
AP	Antero-Posterior
DV	Dorso-ventral
OE	Overexpression

**Gene and protein abbreviations**

<i>gene</i>	<i>full form</i>	<b>Protein</b>	<b>Full form</b>
<i>shg</i>	<i>shotgun</i>	DE-Cad	Drosophila E-Cadherin
<i>sqh</i>	<i>spaghetti-squash</i>	MRLC	Myosin II Regulatory Light Chain
<i>zip</i>	<i>zipper</i>	MHC	Myosin II Heavy Chain
<i>rok</i>	<i>rock</i>	ROCK	Rho kinase
<i>Rac1</i>	<i>Rac1</i>	Rac1	Ras-related C3 botulinum toxin substrate 1
<i>cno</i>	<i>canoe</i>	Cno	Canoe
<i>crb</i>	<i>crumbs</i>	Crb	Crumbs
<i>arm</i>	<i>armadillo</i>	$\beta$ -cat	$\beta$ -catenin
<i>aPKC</i>	<i>atypical Protein Kinase C</i>	aPKC	atypical Protein Kinase C
<i>vkg</i>	<i>viking</i>	Coll IV	Collagen IV
<i>kst</i>	<i>karst</i>	$\beta$ <sub>H</sub> -spec	$\beta$ <sub>H</sub> -spectrin
<i>cher</i>	<i>cheerio</i>		
<i>N-Cad</i>	<i>N-Cadherin</i>	N-Cad	N-Cadherin
<i>ed</i>	<i>echinoid</i>	Ed	echinoid
<i>dlg</i>	<i>discs large</i>	Dlg	Discs large
<i>baz</i>	<i>bazooka</i>	Baz	Bazooka
<i>cad99c</i>	<i>cadherin99c</i>	Cad99c	Cadherin99c
<i><math>\alpha</math>-cat</i>	<i><math>\alpha</math>-catenin</i>	$\alpha$ -cat	$\alpha$ -catenin
<i>tj</i>	<i>traffic jam</i>		
<i>mirr</i>	<i>mirror</i>		
<i>pnt</i>	<i>pointed</i>		
<i>utABD</i>	<i>Utrophin Actin Binding Domain</i>		
		Rab11	Ras in the brain 11
		RabX1	Ras in the brain X1
		Sec6	Secretory 6
		Sec10	Secretory 10
		CD8	Cluster of Differentiation 8
		PH	Pleckstrin Homology
		Fas II	Fasciculin II
		Cdc42	Cell division control protein 42
		Myo II	Non-muscle Myosin II

## Summary

While cell-autonomous roles for actomyosin contractility and adherens junction regulation in epithelial morphogenesis have been studied extensively, little is understood about how contractility and adhesion in epithelial tissue respond to external forces, for example arising from growth of neighboring tissues. Epithelial cells must adjust their mechanical properties and accommodate external forces to maintain tissue integrity and their desired 3D cell shape. We use the *Drosophila* egg chamber to address how growth of a neighboring tissue is accommodated by an epithelial sheet while also undergoing 3D cell shape transitions. The developing egg chamber is composed of a growing germline which serves as the source of external forces acting on the enveloping follicle epithelium. We demonstrate that adherens junction lengthening and junctional exclusion of Myosin II (Myo II) correlate with a decrease in tension at adherens junctions (AJs) of the follicle epithelium while the germline grows. As the tension in the junctional network decreases, the epithelium undergoes a cuboidal to columnar cell shape transition which correlates with contact to specific germline cells. Strikingly, despite the decrease in tension in the junctions, the epithelium locally reinforces its Myo II and AJ levels dependent on contact with specific germline cells to stabilize cuboidal cell shape against external forces arising from germline growth and shape. We furthermore implicate Myo II and AJ reinforcement in sculpting the overall shape of the egg chamber by imposing local circumferential constraints on germline. This work provides insight into how 3D epithelial cell shapes arise in the context of external forces, how relaxation and resistance to forces coordinates expansion of two neighbouring tissues and how isotropic growth can be redirected into polarized organ morphogenesis.

## Zusammenfassung

Trotz der intensiven Untersuchungen der Morphogenese von Epithelien, welche Actomyosin-Kontraktilität und Adhäsion als wichtige Faktoren hervorgebracht haben, ist bisher nur wenig darüber bekannt, wie Epithelien in Bezug auf ihre Kontraktilität und Adhäsion auf externe Kräfte reagieren, welchen sie von wachsenden und sich veränderten benachbarten Geweben ausgesetzt sind. Epithelzellen müssen ihre mechanischen Eigenschaften den externen Kräften anpassen, um die Integrität des Gewebes zu gewährleisten.

Wir machen Gebrauch von der *Drosophila melanogaster* Eikammer, um zu untersuchen, wie ein Epithel, das ein Gewebe umgibt, auf das Wachstum desselben reagiert und wie das Epithel dabei unterschiedliche 3D-Zellformen aufrecht erhält. Die Eikammer setzt sich aus der Keimbahn und dem Einzelschichtepithel, welches die Keimbahn umgibt, zusammen. Die Keimbahn übt externe Kräfte auf die Epithelzellen aus, da sie im Laufe ihrer Entwicklung drastisch ihr Volumen vergrößert. Wir zeigen, dass während die Keimbahn wächst, die Verlängerung von Adhäsionsverbindungen und der Ausschluss von Myosin II aus diesen Verbindungen, mit einer Relaxierung der Adhäsionsverbindungen des Epithels korreliert. Während das Epithel relaxiert, ändern die Epithelzellen ihre Form von kuboidal zu kolumnar, was mit den jeweiligen Keimbahnzelltypen, welche sie kontaktieren, korreliert. Trotz der Abnahme der Zugkraft im Epithel, erhöht das Epithel bemerkenswerterweise lokal, abhängig von dem Keimbahnzelltyp, welchen es kontaktiert, seine Myo II und Adhäsionsverbindungslevels und sichert damit die kuboidale Zellform vor Verformungen durch externe Kräfte, welche durch das Keimbahnwachstum und die Keimbahnform generiert werden. Zusätzlich beschreiben wir eine Rolle für Myo II und Adhäsionsverbindungen im Formen der Eikammer, in dem lokal und zirkumferenziell der Widerstand gegen das Wachstum der Keimbahn erhöht wird.

Diese Arbeit liefert Einblicke in das Entstehen von 3D-Zellformen im Kontext von externen Kräften, wie das Nachgeben und der Widerstand gegen externe Kräfte die Ausdehnung zweier benachbarter Gewebe koordiniert und wie isotropisches Wachstum zu anisotroper Organmorphogenese umgewandelt werden kann.

# 1 Introduction

## 1.1 Epithelial cell shape: function and relevance

Epithelial tissue is evolutionarily the most ancient tissue of metazoans. There is evidence of epithelial tissue throughout the animal kingdom from early multicellular organisms like sponges to humans (Leys, Nichols et al. 2009) and epithelial-like architecture is seen even in pre-metazoans like *Dictyostelium* (Dickinson, Nelson et al. 2011). Epithelia function primarily as physical barriers to the external world or as a lining of internal cavities and organs. In addition, they perform functions of selective permeability, absorption, secretion and protection. These different functions are associated with morphological diversity in their cell shape and tissue organization.

There are three primary cell shapes in simple epithelial tissues; namely, columnar, cuboidal and squamous (Figure 1). In humans, columnar cell shapes are seen in the inner lining of trachea and fallopian tubes. This epithelium has specialized structures called microvilli that are protrusions on its open surface to clean and filter the air we breathe or rhythmically beat to move the oocyte. Cuboidal cells like those found in gland ducts, intestines or lining of kidney tubules have characteristic functions in secretion of hormones, enzymes and absorption of nutrients. Squamous or flat cells on the other hand, are extensively seen in capillaries and lung alveoli to facilitate rapid diffusion and exchange of gases. There are several examples of epithelia where all these cell shapes are found in multilayered organization called stratification. For example, the stratified columnar epithelium as seen in the male urethra and ducts of some glands, stratified cuboidal epithelium as seen in sweat, salivary and mammary glands and stratified squamous epithelium as seen in the epidermis, esophagus and vagina. Stratified epithelia can be composed of all the three cell shapes, with the outer layer being squamous and the deeper layers being cuboidal and columnar as seen in the epidermis of humans. Yet another kind of stratified epithelium is called transitional epithelium, which is uniquely found in urinary system like the urinary bladder and ureters. The stratified outer layers of this epithelium can transiently change shape between cuboidal and squamous depending on the extent of distension of the organ as it fills up. When under greater stretch to accommodate greater volumes of urine, the outer cells appear squamous and when relaxed, they tend to appear cuboidal.

## INTRODUCTION

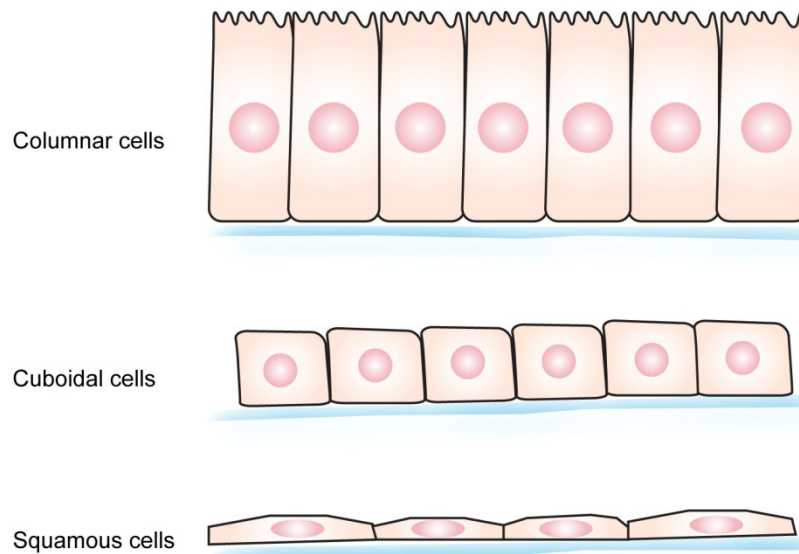


**Figure 1 Simple epithelial cell shapes**

Scheme depicts the three simple epithelial cell shapes- columnar, cuboidal and squamous classified by their vertical height.

Thus, there exists a beautiful and vast diversity in epithelial morphology and organization in metazoans. Disruption or improper development of cellular shapes and hence functions can lead to multiple disorders that can be debilitating for the human body. Further, approximately 85% cancers are epithelial in origin called carcinomas (Cancer Research Institute 2017). Carcinomas can originate in specific subtypes of cells like adenocarcinoma and basal cell carcinoma which develops in an organ or gland typically constituted of cuboidal and columnar cells respectively, and squamous cell carcinoma, which originates in the squamous epithelium. Thus, it is vital to understand the cell biological and mechanical principles of how this morphological diversity is established, maintained and restored for proper function of epithelia during development and disease.

## 1.2 Features of epithelia – packing, polarity, adhesion and contractility

### 1.2.1 Epithelial packing

A characteristic feature of epithelial tissue under a light microscope is its geometric regular organization. This organization is called polygonal packing because of appearance of cells in microscopic surface sections as polygons with edges and vertices (Figure 2A) (Gibson and Gibson 2009). However, cells are 3-dimensional structures which can be envisioned simplistically as two planar polygonal-packed surfaces connected by parallel lines from vertices on one plane to the other (Figure 2B). Several studies have demonstrated that packing is predominantly hexagonal as it promotes energy minimal states for epithelial tissues (Classen, Anderson et al. 2005, Farhadifar, Roper et al. 2007, Sugimura and Ishihara 2013). Epithelial polygonal packing is possible because of three other properties of the epithelium: - polarity, adhesion and contractility.

### 1.2.2 Epithelial cell polarity

An iconic feature of epithelial cells is their cell polarity. Decades of work have identified key polarity regulators and pathways that orchestrate the process of generating and maintaining polarity in these cells. Work in several model organisms has revealed conserved proteins in vertebrates and invertebrates that enable the cells to be polarized. This polarization differentiates the surfaces of the epithelial cells into so called apical, lateral and basal surfaces (Figure 2C). The apical polarity regulators include the Par and Crumbs complexes while the Scribble complex primarily functions as the basolateral polarity factor (Figure 2D). In addition to these protein complexes, lipid molecules, their effectors and the RHO GTPases - Cdc42, Rho1 and Rac1 are implicated in generating and maintaining the polarity in epithelial cells (Martin-Belmonte and Perez-Moreno 2011, Rodriguez-Boulan and Macara 2014). These complexes interact with each other, although the manner in which they confer polarity in the epithelium is dependent on organisms and developmental contexts.

In *Drosophila melanogaster*, the interactions between the apical polarity complexes Cdc42/aPKC/Par6/Baz, Crb/Sdt/PatJ and the basolateral complexes Lgl/Dlg/Scrib and Par1 have been extensively studied (Tepass 2012). The primary mechanism to maintain the identity of these domains is through mutual inhibitory phosphorylation activities of the kinases aPKC and Par1 (Figure 2D). For example, the phosphorylation of Lgl and Par1 by aPKC inhibits their presence in the apical surface. Conversely, Par1 phosphorylates Baz to prevent basolateral localization of the aPKC/Par6/Baz complex (Tanentzapf and Tepass 2003, Tepass 2012). While the Scrib complex inhibits aPKC in gastrulating embryos, another group of basolateral

## INTRODUCTION

regulators, called the Cora group (Figure 2D) have been specifically identified to inhibit Crb in *D. melanogaster* during mid-embryogenesis (Laprise, Lau et al. 2009).

The organization of the apical domain is a complex and highly orchestrated process involving the recruitment and regulation of aPKC. The Crb/Sdt complex is essential for enhancing the apical localization of the aPKC/Par6 complex through dynamic interactions. aPKC/Par6 in turn interacts with activated Cdc42 to maintain its apical positioning and then forms a complex with Baz, which is apically recruited through Crb/Sdt. Baz is phosphorylated by aPKC and subsequently dissociates from aPKC/Par6 to relocate to the adherens junctions (see section 1.2.3 for definition) (Nam and Choi 2003, Harris and Peifer 2005, Suzuki and Ohno 2006, Goldstein and Macara 2007, Krahn, Buckers et al. 2010, Krahn, Klopfenstein et al. 2010, Morais-de-Sa, Mirouse et al. 2010, Walther and Pichaud 2010). Little is known about which polarity factors define the basal side exclusively, although integrins have been extensively implicated in this process (Yu, Datta et al. 2005, St Johnston and Sanson 2011). The importance of apical-basolateral polarity in the maintenance of epithelial integrity, in organization of different adhesion and cytoskeleton modules, as well as in directing vesicle trafficking has been highlighted in several studies (St Johnston and Sanson 2011, Tepass 2012).

### 1.2.3 Epithelial cell junctions

Another iconic feature of epithelia is their ability to behave as a collective unit due to force-bearing, mechanosensitive adhesion of individual cells to their neighbors and physiological connectivity. Mechanical and physiological connectivity are maintained by several specialized ultra-structures, which appear as plaques of high density on the plasma membrane in electron micrographs, called cell-cell junctions. The broad classes of cell-cell junctions based on the emergent function they render are – tight junctions, gap junctions and anchoring junctions (Figure 2C-E).

Tight junctions (TJs) in vertebrates are located at the rim of the apical surface just above the adherens junctions. These junctions serve as barricades within the paracellular space and selectively restrict the passage of molecules from the apical to the basolateral side in the extracellular space between cells. In invertebrates, functionally similar junctions are located below the adherens junctions and are called septate junctions (SJs). In *D. melanogaster*, there are two types of septate junctions which are ultrastructurally different. Typical markers of septate junctions include Neuroglian, Contactin, Neurexin-IV, Coracle and Dlg. Disruption of these genes leads to defects in transepithelial sealing (Banerjee, Sousa et al. 2006, Izumi and Furuse 2014).

The gap junctions (GJs) are seen both in vertebrate and invertebrate epithelia with differences only in the composition of these junctions. These junctions couple neighbouring cells electrically, allowing passage of ions  $\text{Ca}^{2+}$  and small metabolites up to 1kDa in size. In *D. melanogaster*, the gap junctions are composed of a family proteins called Innexins (Bauer, Loer et al. 2005). Thus, both TJs and GJs are junctions serving physiological functions of epithelia like permeability, electrical and metabolite coupling across epithelia. These junctions, however, do not mechanically couple epithelial cells.

Mechanical coupling between neighboring cells and between cells and the ECM is possible because of anchoring junctions. Importantly, the morphological diversity in epithelial tissue shapes ranging from sheets, to tubes, acini and sacs need anchoring junctions. Anchoring junctions can be further classified into cell-cell junctions and cell-ECM junctions. Cell-cell junctions are represented by adherens junctions (AJs) and desmosomes, whereas cell-ECM junctions by focal adhesions (FAs) and hemidesmosomes. AJs and FAs are structurally conserved across vertebrates and invertebrates to mechanically couple their neighbors and environment respectively.

#### 1.2.4 Focal adhesions

FAs are constituted by the Integrin family of transmembrane proteins that bind to the dense Extracellular Matrix (ECM) on the basal side of epithelial cells. The ECM in *D. melanogaster*, is constituted by a network of proteins like Collagen IV, Perlecan, Laminins and Nidogen. Integrins form heterodimeric structures composed of  $\alpha$ - and  $\beta$ -subunits, whose extracellular domains interact with the ECM molecules to form anchoring FAs. Intracellularly, integrins bind to a complex of proteins like Talin and Vinculin. Vinculin in turn binds the Actin cytoskeleton (Schwartz 2010, Yurchenco 2011, Hynes 2012). Thus, focal adhesions serve as force-bearing structures for epithelial cells while interacting with the environment (ECM).

#### 1.2.5 Adherens junctions

The most prolifically studied adhesive coupling and force-bearing structures between epithelial cells are AJs. To study the mechanics of epithelial cell shapes, it is important to highlight the molecular composition of AJs and their regulation. The adhesion function of AJs is primarily mediated by the Cadherin family of proteins. Cadherins are transmembrane proteins that undergo homophilic interactions with cadherins on neighboring cells through their extracellular domains in a  $\text{Ca}^{2+}$ -dependent manner (Gumbiner 2005). The Cadherin highly expressed in epithelial cells is called E-Cadherin (DE-Cadherin, *shotgun*, *shg*, in *D. melanogaster*). On the intracellular side, cadherins bind to another family of proteins called catenins. In epithelial cells, the cadherin-catenin complex (CCC) typically appears to localize as a uniform adherent belt around the apical surface forming the AJ belt. In *D. melanogaster*, AJ localization and extent is

## INTRODUCTION

determined by Baz (St Johnston and Sanson 2011). The formation of AJs is driven by the mutually inhibitory differentiation of the apical and basolateral membranes which together regulate Baz exclusion (see section 1.2.2). Baz exclusion from the apical surfaces limits the apical expansion of AJs. Thus, AJs forms a demarcation of the apical surface from the basolateral surface in addition to providing adhesive linkage between cells (Tepass 2012).

Adhesive coupling through *trans* homophilic interactions of the extracellular domains of Cadherin has been structurally elucidated *in vitro* to be in several types of conformations including simple strand dimer conformation (slip bond) and X-dimer conformation (catch bond) depending on the amount of force loaded on AJs (Leckband and de Rooij 2014)( see section 1.3.1). This mechanical loading of AJs requires the presence of catenins. Of the catenin family of proteins,  $\beta$ -cat and p-120 cat bind directly to E-Cad on its intracellular domain but at different sites (Kowalczyk and Nanes 2012).  $\alpha$ -cat binds to  $\beta$ -cat and hence is indirectly anchored onto E-Cad.  $\beta$ -cat and  $\alpha$ -cat have structural roles in AJ formation.  $\alpha$ -cat is known to bind F-Actin directly or indirectly by recruiting Vinculin (Gumbiner 2005). Thus, the catenin complex links E-Cad to the Actin cytoskeleton and allows internal mechanical forces (see section 1.3.1) to be anchored on AJs (Figure 3B, C).

AJs are highly dynamic structures even as they serve as mechanical contacts between epithelial cells. Studies have shown both *in vitro* and *in vivo* that E-cadherin is constantly internalized by clathrin-mediated endocytosis and recycled back to AJs from the basolateral domains of epithelial cells and via Rab 11 recycling vesicles. Dynamin has been implicated in the removal of E-Cad whereas exocyst complex protein Sec10 interacts with  $\beta$ -cat which trafficks together with E-Cad to recycle molecules back to the AJs (Baum and Georgiou 2011, Woichansky, Beretta et al. 2016). Furthermore, the function of p-120 cat largely lies in balancing stability of AJs to E-cad turnover (Nanes, Chiasson-MacKenzie et al. 2012, Bulgakova and Brown 2016). Other regulators including Rac1 and Afadin have been implicated in regulating E-Cad endocytosis via interactions with p-120 cat (Akhtar and Hotchin 2001, Hoshino, Sakisaka et al. 2005). Recently, more *in vitro* studies have deciphered how faster rates of endocytosis correlates directly with the higher tension on AJs (de Beco, Perney et al. 2015), see section 1.3). However, very little is understood about the feedback of mechanical coupling and forces on the regulation of E-Cad turnover *in vivo*.

To summarize, the CCC and the anchored Actin cytoskeleton are vital for epithelial cells to sense their neighbors, adhere and exert forces on them and to ensure the tissue's mechanical homeostasis.

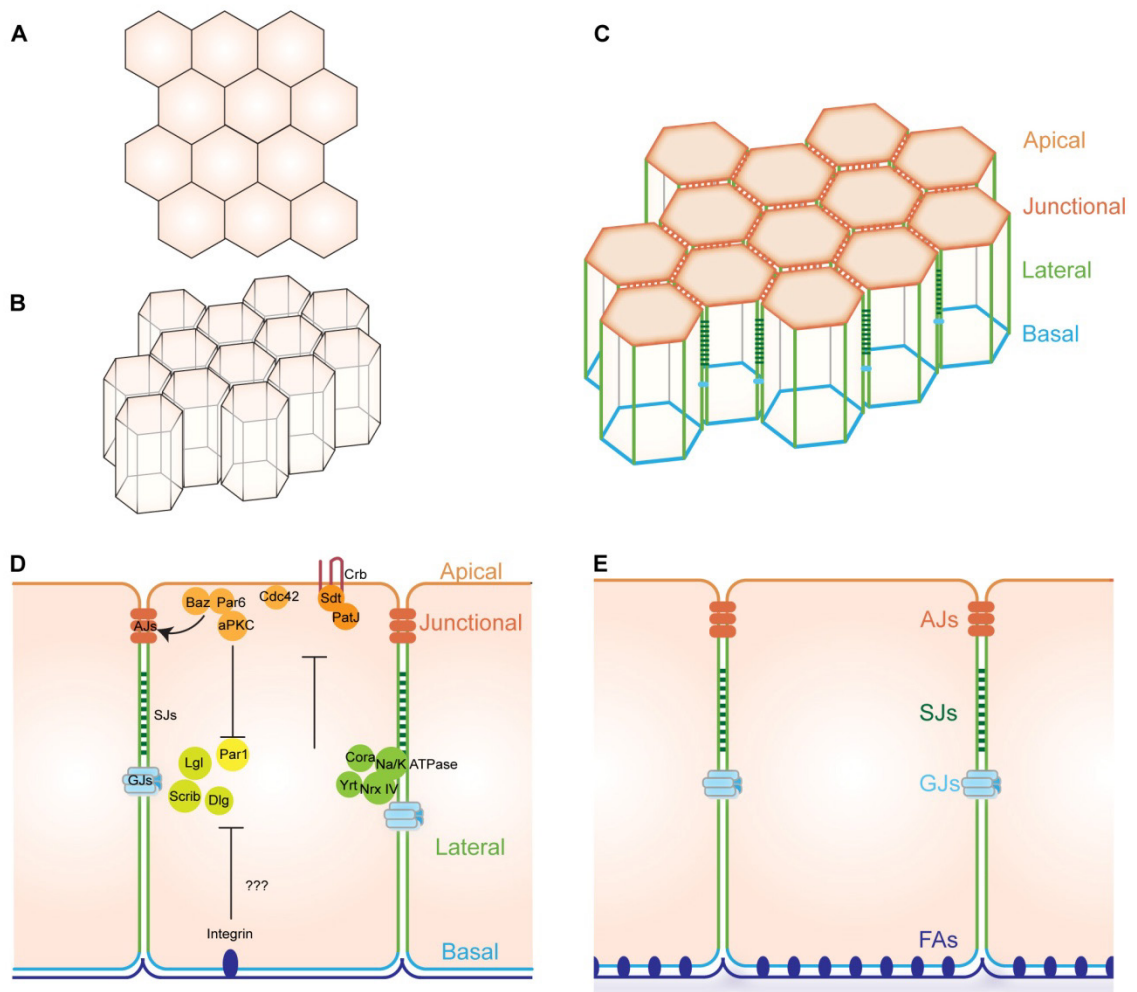


**Figure 2 Features of epithelial tissue – packing, polarity and adhesion**

(A-B) Scheme shows hexagonally packed surface view of a sheet of epithelium (A) and a 3-dimensional organization of epithelial cells as two hexagonally packed surfaces connected by vertical lines. (C-D) Scheme of an epithelial sheet with the different polarized surfaces (C) and a scheme of these cells when sliced along the apico-basal axis showing different polarity complexes in a typical epithelial cell. (E) Different types of junctions along the apico-basal axis of epithelial cells – AJs-adherens junctions, SJ-septate junctions, GJs-gap junctions, FAs-focal adhesions.

## 1.3 Epithelial mechanics

### 1.3.1 Actomyosin contractility

The primary force generating mechanism in cells is actomyosin contractility. The theory of muscle myosin II minifilaments walking on anti-parallel Actin bundles to generate contraction of the Actin network was first developed to explain skeletal muscle contraction (Huxley 1969). It has since been extended and applied to different Myo families, including non-muscle Myo II (henceforth, abbreviated to Myo II), present ubiquitously. Briefly, a Myo II unit

## INTRODUCTION

is a hexamer formed by 2 Myosin Heavy Chains (MHC, *zipper*, *zip*), 2 Myosin Essential Light Chains and 2 Myosin Regulatory Light chains (MRLC, *spaghetti-squash*, *sqh*). Phosphorylation of the MRLC allows the hexamer to undergo a conformational switch from a folded form to expose rod-like domains and globular head domains of its heavy chains. Phosphorylation of MRLC is mediated by kinases in various regulatory pathways including Rho kinase (ROCK), citron kinase (both activated by RhoA) and Myosin Light Chain Kinase (MLCK, activated by  $\text{Ca}^{2+}$ /Calmodulin). Following Myo II phosphorylation, individual hexamers cluster using their heavy chain rod-like domains with other activated Myo II hexamers to form Myo II minifilaments. In this arrangement of minifilaments, the heavy chain globular head domains are exposed to bind F-Actin filaments (Lecuit, Lenne et al. 2011). The globular heads have binding sites for ATP, which gets hydrolyzed upon binding. This activates the head domains to bind F-Actin forming cross-bridges. When ADP is released, the activated head domains pivot toward the plus end of the attached F-Actin filament and slide it. Thus, in each cross-bridge cycle, the energy released from hydrolysis of ATP upon binding Myo II globular heads is converted to the power stroke - the physical movement of Myo II which slides the attached F-Actin filament. This movement of Myo II motors on anti-parallel F-actin network can generate either contraction or extension of the actin cytoskeletal network depending on the organization of the filaments relative to Myo II minifilament (Figure 3A). However, contractile movement of the actomyosin network gets favoured as opposed to extensile ones, because of actin regulators and resulting self-organisation of the actomyosin (Murrell, Oakes et al. 2015).

### **1.3.2 Actomyosin contractility generates tensile force on AJs by anchoring on $\alpha$ -catenin**

For the mechanical movement of the F-Actin network to translate into force used and felt by cells, the actomyosin network must be anchored to the plasma membrane. The entire actomyosin network in cells is typically anchored to the plasma membrane by several membrane-bound Actin regulators and scaffolds to form the actomyosin cortex (henceforth cortex). Thus, any contractile movement of F-Actin filaments is translated into an inward directed force within the cortex called cortical tension. It is important to note that, the cortex is not static but highly dynamic where contractility is coupled to dynamic turnover of F-Actin filaments and Myo II activation cycles (Lecuit and Lenne 2007, Lecuit, Lenne et al. 2011) (Murrell, Oakes et al. 2015).

In epithelial cells, in addition to the general cell cortex, actomyosin is anchored to AJs and FAs (Figure 3A-B). In AJs,  $\alpha$ -cat anchors F-Actin filaments and hence the entire contractile machinery at the junctions. Therefore, on every junction edge, adhesion and contractility generate forces in opposite directions leading to a net junctional tension. As every AJ edge is

mechanically-coupled to neighboring edges, the net junctional tensions are coupled and transmittable between edges. Therefore, epithelial tissues can be visualized as a sheet under tension generated by inward contractile force acting on AJs and outward adhesion force of cadherin mediated cell-cell linkage (Figure 3D-D').

Importantly, in addition to transmitting and transducing forces, individual AJs components act as molecular mechanosensors. It has recently been demonstrated that the CCC is a mechanical transducer that senses external forces through molecular unfolding of  $\alpha$ -cat. Under tension,  $\alpha$ -cat opens to reveal binding sites for F-Actin and Vinculin, which in turn can load more F-Actin on the junctions (Figure 3C). In addition to Vinculin, a plethora of F-Actin regulators localize at the CCC via  $\alpha$ -cat opening under tension which initiates F-Actin polymerization on a longer time scale (Heisenberg and Bellaiche 2013, Leckband and de Rooij 2014, Hoffman and Yap 2015).

In contrast to the current state of knowledge about force transmission, sensing and transduction across AJs, relatively little is understood about how the basal contacts with ECM perform the same in epithelial cells (Puech, Taubenberger et al. 2005, Dray, Lawton et al. 2013, Julich, Cobb et al. 2015). A lot of our understanding of integrin-based FAs and forces acting upon them are from 2-dimensional cell cultures of migrating cells (Gardel, Schneider et al. 2010, Schwarz and Gardel 2012, Murrell, Oakes et al. 2015). Only recently, focal adhesion-like structures have been identified during embryogenesis of *D. melanogaster* that were shown to dampen force transmission across the AJs between cells (Goodwin, Ellis et al. 2016). However, the mechanistic functions of FAs *in vivo* are largely unexplored. Still lesser evidence exists for the presence of contractility and force anchoring mechanisms on the lateral surface in epithelial cells (Sherrard, Robin et al. 2010).

## INTRODUCTION

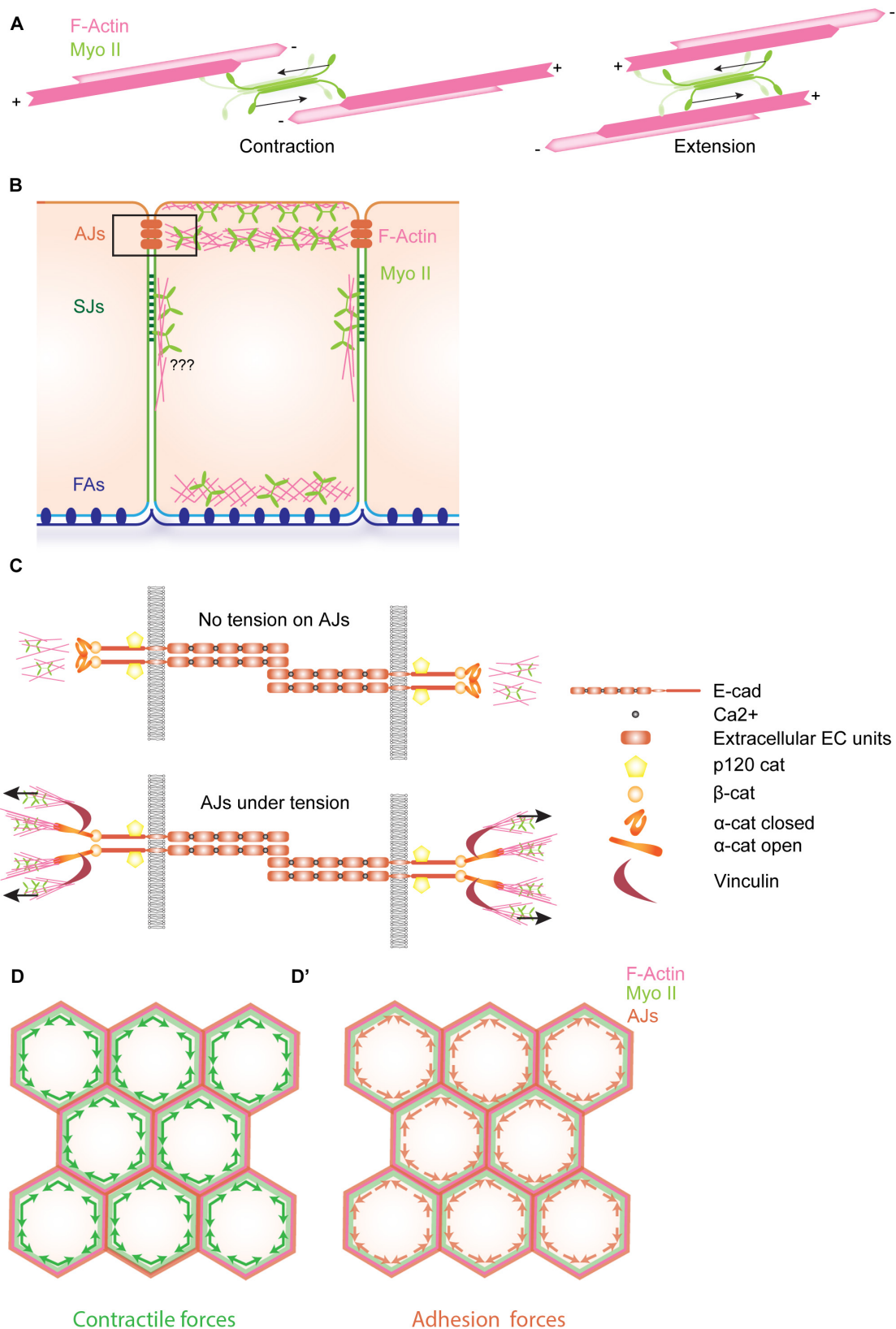


**Figure 3 Contractile force generation and actomyosin recruitment on AJs under tension**

(A) Scheme showing antiparallel actin filaments with Myo II minifilament sitting across them in two arrangements with actin filaments. The arrows show the direction of motion of activated Myo II motor heads i.e. towards the + end of the Actin filaments in every ATP cycle, thus moving the actin filaments. Depending on the position of Actin filaments relative to each other,

the sliding filaments generate contraction or extension in the cytoskeleton network. Thus, the actomyosin network can theoretically generate contractile or extensile forces in the cortex. **(B)** Scheme shows the actomyosin cortices along the different polarized surfaces and anchoring junctions –AJs, SJs, FAs of the epithelial cell. The complexes that couple the lateral actomyosin to SJs or other lateral membrane anchors are not known. AJs and FAs are relatively better studied. Black box at the AJs is magnified in **(C)**. **(C)** Scheme shows the CCC complex when not under tension and when under tension. The  $\alpha$ -catenin conformational opening under tensile forces are key to recruiting actomyosin to the junctions directly and indirectly through Vinculin and a plethora of other actin remodeling proteins (not shown here) (Heisenberg and Bellaiche 2013, Leckband and de Rooij 2014, Hoffman and Yap 2015). **(D)** Scheme shows a surface view of AJs with contractile forces (green arrows) acting on each junction. **(D')** Adhesive coupling of the junctions opposes the contractile force on each junction. The balance of these two forces generates net tension along each edge. Mechanical coupling of the junctions couples the net tension along every edge to that of neighboring edges.

### 1.3.3 Mechanosensing through Crumbs and spectrin network

Crb, the only transmembrane protein in the apical polarity complexes has traditionally been studied in the context of maintaining epithelial polarity. It has several intracellular binding partners like Sdt, Par6 and aPKC that are necessary for its function in polarity (Bulgakova and Knust 2009). However, recent studies have indicated that the extracellular domain is important for both *cis*- and *trans*- homophilic interactions (Roper 2012, Thompson, Pichaud et al. 2013). In addition, its intracellular domain binds Moesin, Yurt and  $\beta_H$ -spectrin, allowing stretch mechano-sensing at the apical surfaces via the apical  $\alpha$ - $\beta_H$  spectrin cytoskeleton. This mechano-sensing has been implicated in controlling tissue growth and size (Medina, Williams et al. 2002, Fletcher, Elbediwy et al. 2015). Thus, in addition to AJs and FAs, the spectrin cytoskeleton network anchored by Crb is a potential hub for mechano-sensing and transduction.

### 1.3.4 Material properties of epithelial cells

To understand the complete effects of force generation and the resulting stresses on epithelial tissues, one needs also consider the structural and material properties of cells. Cells are primarily viscoelastic materials. Viscoelastic materials behave as solid-like or elastic materials on short time scales but can show more fluid-like or viscous properties on longer time scales. At a molecular level, viscoelasticity is due to the presence of stress relaxation, usually through non-covalent bond dissociations. At time scales shorter than the bond dissociation time, stresses cannot be relaxed and the materials act like elastic solids, whereas on longer timescales, the bonds dissociate and the material flows like fluids. Thus, the application of forces can have short and long-time scale effects in cells. A central component modulating viscoelastic behavior of cells is the cytoskeleton. This means that on a shorter time scale, the cytoskeleton can resist deformation because of its elastic properties while on a longer-time scale it can dissipate the effects of the deforming force by remodeling i.e. making, breaking and reorganizing cytoskeletal elements in a controlled manner (Gardel, Kasza et al. 2008, Fletcher and Mullins 2010, Hoffman, Grashoff et al. 2011, Katta, Krieg et al. 2015).

## INTRODUCTION

A common property of solid elastic materials is its elastic or Young's modulus which is defined as the ratio of the stress (force per unit area along a dimensional axis) to the strain (ratio of change in dimension of the object to the initial dimension along that axis). Thus, it defines the ability of an object to restore its initial form after the stress is released. This material property is independent of the shape of the object. Stiffness is directly proportional to the elastic modulus and additionally depends on the shape of the object i.e. it is a structural property (Katta, Krieg et al. 2015). It defines the ability of an object to resist deformation. Several studies have shown the importance of modulation of actomyosin contractility for tissue stiffness during development (Zhou, Kim et al. 2009, Gutzman and Sive 2010, Zhou, Pal et al. 2015, West, Zulueta-Coarasa et al. 2017). For example, during embryogenesis in *Xenopus*, the stiffness of the embryo increases by up to 50-fold, relying primarily on actomyosin remodeling. This stiffness has been implicated as being important in generation of less deformable structures of a maturing embryo like the vertebrate body plan and neural tube from a highly deformable early embryo (Zhou, Kim et al. 2009).

### 1.3.5 Probing physical properties and forces on epithelial cells

Over the last two decades several methods have been optimized to measure the forces and stresses acting in epithelial tissues during cell and tissue morphogenesis (Sugimura, Lenne et al. 2016). A common method to measure relative tension or tensile stress (force per unit length of the junctions) in epithelial junctions is by laser ablation of AJs (Farhadifar, Roper et al. 2007, Landsberg, Farhadifar et al. 2009). A high-power UV laser is used to focus on a junction to cut across it, much like a scalpel making an incision. The vertices where the junctions meet neighboring cell-cell contacts recoil just like a snapped rubber band due to the tension felt by the junction. The initial recoil velocity of an ablated junction is directly proportional to the tension on the AJs. Tension in turn depends on net force exerted on the junctions and its's stiffness. Actomyosin contractility is a significant contributor to the tension on AJs as it controls the amount of force on the junctions and the stiffness of the junctions. Importantly, decreasing contractility has been shown to decrease tension on AJs (Landsberg, Farhadifar et al. 2009, Mayer, Depken et al. 2010).

Another method developed more recently to measure forces on junctions relies on molecular tension sensors. A peptide sequence that behaves like a molecular spring is inserted between a FRET pair module to build a FRET tension sensor. This sensor is then integrated into force-bearing molecules in cell-cell junctions like DE-Cad (see section 3.4) or in cell-ECM junctions like Vinculin. The FRET efficiency of the module inversely depends on the extent of tension on the junctions or cell-ECM structures (Cost, Ringer et al. 2015). In addition, Atomic

Force Microscopy (AFM) and traction force microscopy have been employed to obtain stiffness and elastic modulus of cells directly. Other methods including microplate, pipette aspirations, optical and magnetic tweezer which generate pushing or pulling forces or compressive or tensile stresses on cells or tissues, have further helped to analyze properties like stiffness and surface tension (Sugimura, Lenne et al. 2016).

## **1.4 Epithelial morphogenesis**

### **1.4.1 Morphogenesis driven by cell-autonomous mechanisms**

Equipped with mechanisms to sense, transmit and transduce forces, epithelia can undergo cellular and hence tissue-level shape transformations, sculpting into a plethora of organ forms and shapes. Over the last couple of decades, the study of epithelia undergoing shape transformations during development has exploded into the field of epithelial morphogenesis.

Two kinds of dominating physical forces are being generated within every epithelial cell and are postulated to affect its shape. Firstly, contractile forces on all cortices – apical, junctional, lateral and basal that tend to constrict surfaces and reduce their area. Secondly, adhesion forces between cells and between cells and ECM, as well as the internal pressure of the cells oppose contractile forces working to reduce cortical surface areas. Thus, any shape of the cell is an equilibrium state achieved by the balancing point of these intrinsic forces (Lecuit and Lenne 2007, Mao and Baum 2015).

As actomyosin has been observed to enrich as a circumferential belt at AJs, a purse-string like mechanism was thought to constrict the apical-junctional surface (Figure 4A-B). Examples of purse-string actomyosin arrangement leading to apical constriction have been seen at the level of individual cells like in vertebrate neural tube and supracellularly (purse-string spanning several cells behaving in unison) in salivary gland development and dorsal closure (Heisenberg and Bellaiche 2013, Mao and Baum 2015). However, a second population of actomyosin in the apical surface has been identified to be important for apical constriction. This pool is known to be pulsatile i.e. appearing and disappearing in the medial region of the apical cortex (henceforth apico-medial cortex). Cortical oscillations are accompanied by the junctions shrinking in a coordinated manner (Figure 4B'-B'') (Martin, Kaschube et al. 2009). Recent studies suggest that junctions are coupled to pulsatile apico-medial Myo II through a radial F-actin filament network emanating from the junctions into the apico-medial cortex (Vasquez and Martin 2016, Coravos, Mason et al. 2017). Depending on the extent of coordination of actomyosin contractility in the plane of an epithelial sheet, various tissue shapes are known to be generated. For example, constriction of a row of cells can generate furrows, while constricting a more circular patch of cells would lead to tubule formation or a sac (Chanet,

## INTRODUCTION

Miller et al. 2017). Therefore, changes in the apical-junctional or basal surfaces could alter the shape of cells from columnar to wedge-like and could drive events like tissue folding and buckling (Figure 4A-A', Figure 5A).

These events have largely been studied in epithelia in 2-D, along the apical or basal surface of the cells, thereby ignoring the third dimension ie the height of the cells. 2-D epithelial morphogenetic studies have largely been possible because volume of cells in these tissue models is conserved and thus alterations to the height of the cells are assumed to be 'passive' reaction to active actomyosin driven changes in the apical or basal plane of cells. Nevertheless, the cellular mechanisms that allow the 'passive' height changes to take place have not been studied. Furthermore, very little is known about how epithelial cells acquire shape in 3-D along the squamous-cuboidal-columnar spectrum of cell shapes during morphogenesis of epithelia. To bring about 3-D changes between squamous, cuboidal and columnar epithelial cell shapes, the height of the cells needs to be altered in concert with changes in the apical and basal areas. Limited examples of lateral contractility as a force generator to shorten the lateral surface of epithelial cells have been identified to date (Sherrard, Robin et al. 2010). However, other mechanisms of lateral height modifications have been discovered. For example, lateral adhesion based on Fas II may inhibit height shortening (Szafranski and Goode 2004) whereas endocytosis of Fas II promotes it (Gomez, Wang et al. 2012). Conversely, mechanisms to increase the cell height in *Drosophila* wings discs have been proposed to rely on concomitant apical and basal contractility (Widmann and Dahmann 2009) (Figure 5). Microtubule filaments along the lateral surface tilt into the apical surface and extend along the apico-junctional surface to expand embryonic amnioserosa cell areas and simultaneously decrease their heights in *Drosophila* (Pope and Harris 2008, Picone, Ren et al. 2010, Wang, Khan et al. 2012). However, no study has been able to simultaneously tackle understanding cellular mechanisms that control all the three dimensions of epithelial cell shape. In summary, the epithelial cell shape change in 3-D is thought to be executed in a cell intrinsic, autonomous manner by concerted and coordinated modulation of contractility and adhesion forces acting on different surfaces in the cell (Figure 5).

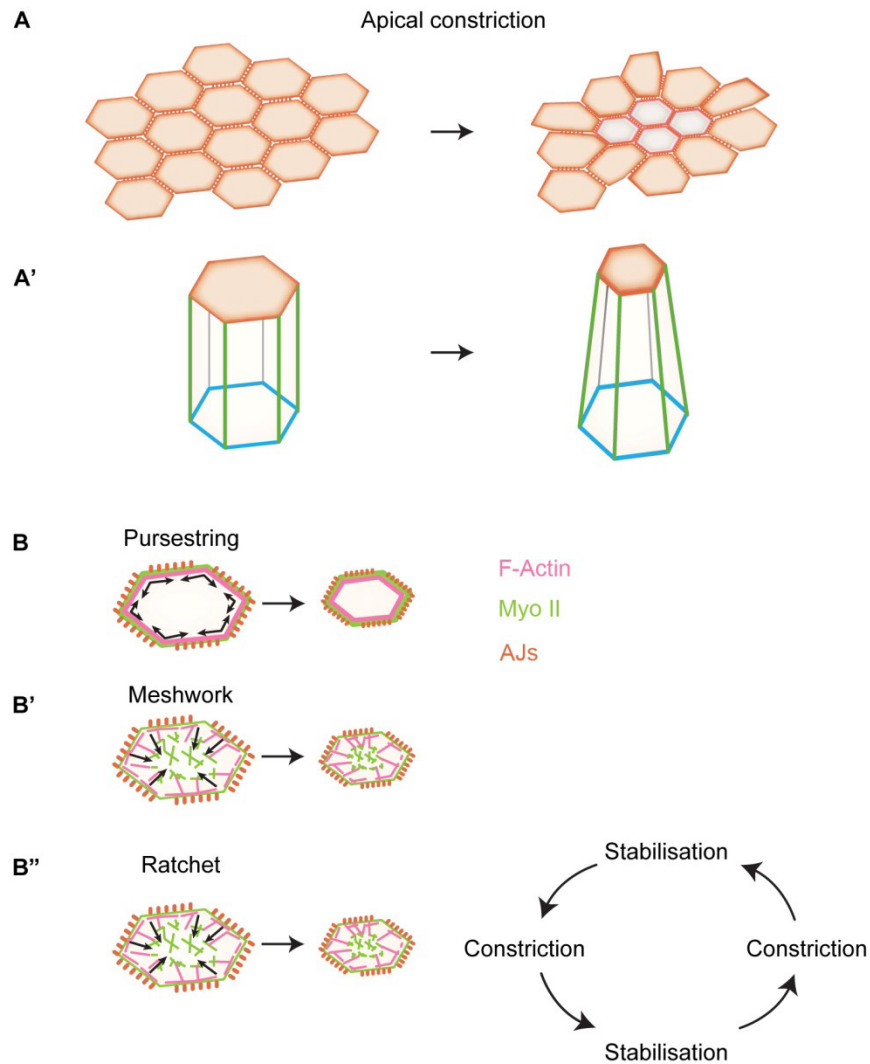


**Figure 4 Myo II contractility mediated apical constriction**

**(A-A')** Scheme showing constriction of the apical surface of epithelial cells (central cells with lighter shading) leading to formation of wedge-shaped cells (**A'**). **(B-B'')** Ways in which actomyosin contractility can mediate apical constriction are through a purse string-like constriction of actomyosin on the junctions (**B**), a meshwork of actomyosin in the apical–medial cortex (**B'**) and by ratcheting which is a sequential constriction and stabilization of the apical membrane (**B''**) (adapted from (Martin 2010)).

### 1.4.2 Morphogenesis driven by mechanisms external to epithelia

Since epithelial tissues are a mechanically coupled network of contractile cell surfaces, forces actively produced in one cell or a group of cells of the tissue can be felt by neighboring cells. The forces perceived by these neighboring cells can thus be termed extrinsic and non-autonomous. They could, for example, arise from distant-site tissue contractions or neighboring cell and tissue growth. Non-autonomous forces can thus contribute to 3D epithelial cell shape and overall tissue sculpture. One example in humans of external force dependent shape

## INTRODUCTION

transitions is seen in the epithelium which lines the organs of the urinary system like the urinary bladder and ureters. These epithelia can distend on increasing volume of urine. They are multilayered with more columnar shapes in the deeper layers and cuboidal and squamous cells in the outer layers depending on the degree of distension they see when the volume of the organ increases. In another example from *Drosophila* embryos, the mesoderm invaginates and exerts forces on the neighboring ectoderm which contributes to the elongation of the germband. Thus, active constriction of a group of cells could drive the neighboring non-constricting cells to passively respond and alter their shape to aid in shaping the cells and tissue (Mao and Baum 2015). Thus, in the context of external forces, epithelial cells can either relax to or resist external forces and coordinately acquire different 3D cell shapes on the squamous-cuboidal-columnar spectrum. But little is known about the cellular mechanisms that maintain epithelial cell shapes when external forces act.

The actomyosin cytoskeleton responds to external non-autonomous forces and tunes itself through mechanical feedback. Cells in culture if placed under external stretch are known to remodel their cytoskeleton and recruit actomyosin to dissipate the stretch. One example is the generation of Actin stress fibers attached to integrin-based FAs when external mechanical load is applied on fibroblasts (Orr, Helmke et al. 2006, Schwartz 2010, Humphrey, Dufresne et al. 2014). Actomyosin contractility reinforcement to resist external forces has been reported *in vivo*. In *D. melanogaster* wing disc epithelia, studies have shown how peripheral parts of the tissue can be in a stretched state because of high rates of cell growth and divisions in the interior. The stretched state of these peripheral cells is also associated with increased junctional Myo II to withstand the expansion forces from interior tissue growth. Loss of Myo II in these peripheral cells, causes them to stretch and widen their apical areas, suggesting Myo II localization is consequence of the increased stretch of the peripheral tissue (Legoff, Rouault et al. 2013, Mao, Tournier et al. 2013). Studies in *D. melanogaster* pupal wing demonstrate that Myo II localization on the junctions can be reduced when external stretch is lowered (Sugimura and Ishihara 2013). Myo II is preferentially recruited to stiff cell boundaries during embryogenesis suggesting a force-sensitive feedback recruitment of Myo II (Chanet, Miller et al. 2017). In contrast to mounting a Myo II mediated resistance or heightened stiffness to withstand external forces, some studies have shown how epithelial tissues can relax during organogenesis like elongation of primordial tissue during brain morphogenesis and dorsal closure in embryos. Epithelial relaxation mechanisms have been shown to impinge on Myo II phosphatases and Arf GEFs to reduce or shut down actomyosin contractility (Gutzman and Sive 2010, West, Zulueta-Coarasa et al. 2017). Although some molecular modulators of actomyosin activity have been identified, our understanding of the cellular organization of the contractile machinery for epithelial relaxation in response to external forces is still largely incomplete.

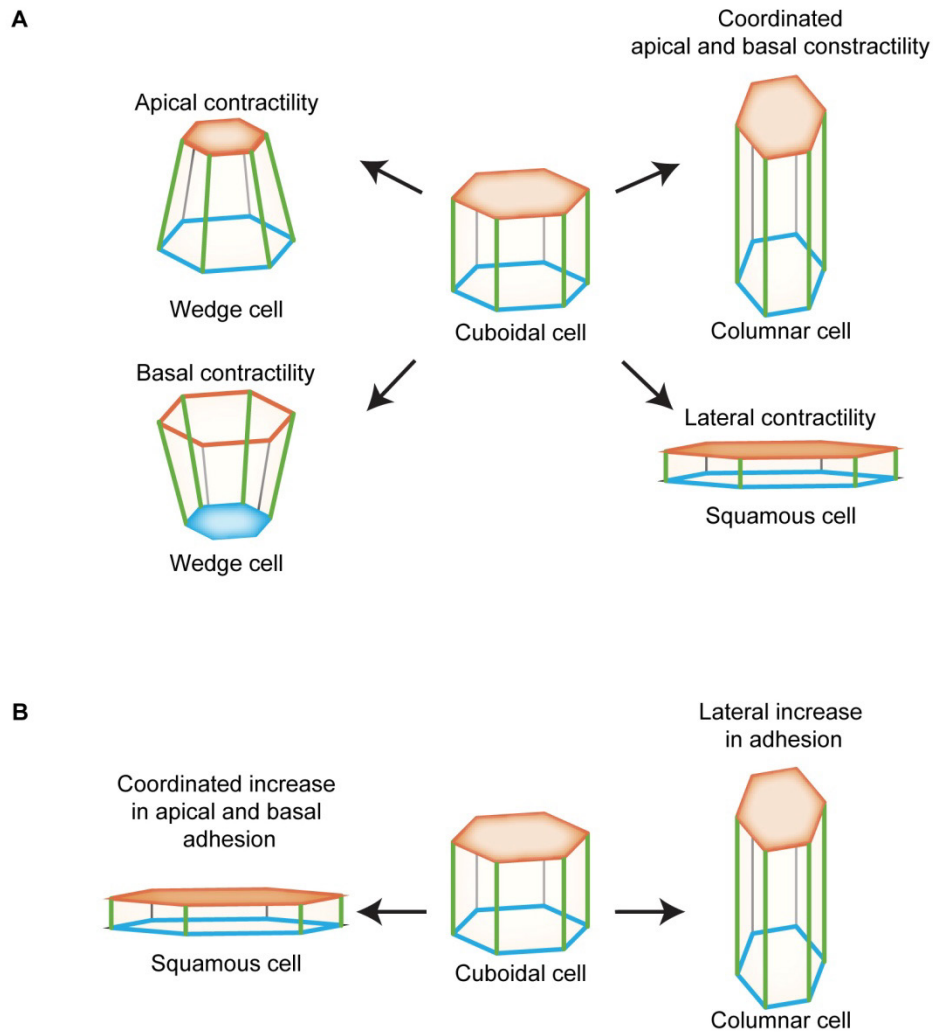


**Figure 5 Cell adhesion and contractility on different surfaces can generate different epithelial cell shapes**

(A) When apical contractility or basal contractility alone is the dominant force generator, wedge-shaped cells can be generated. Whereas, when apical and basal contractility is coordinated columnar cell shapes can form. Activation of lateral contractility may generate squamous cell shapes. (B) When adhesion between lateral surfaces is dominant, columnar cell shapes can be generated, whereas, coordinated adhesion-mediated expansion of the apical and basal surfaces can generate squamous cell shapes. Note that implicit in this simplified scheme is the assumption that the initial cell shape is cuboidal cell and that cell volume is conserved (adapted from (Mao and Baum 2015)). More complex variations of these two central mechanisms are possible.

In summary, the final shape of an epithelial cell arises from the collective effect of viscoelastic properties of the cell, intrinsic cell-autonomously generated forces, direct application of external non-autonomous forces and feedback mechanism resisting or relaxing in response to these external forces. How epithelial cells undergo mechanical feedback to remodel their cytoskeleton to resist or relax to external forces and coordinately acquire or maintain different overall 3D cells shape is an open field of research.

### **1.5 Egg chamber - model system to study epithelial cell shape transitions**

#### **1.5.1 Epithelial tissue models in *D. melanogaster***

In *D. melanogaster*, several epithelial tissues have been rigorously studied over the last few decades and advanced the field of epithelial polarity, morphogenesis and cancer. A subset of commonly used tissues is mentioned briefly here. The fly embryo forms a monolayer epithelium which undergoes extensively studied morphogenetic events like gastrulation and dorsal closure. In the larval stages, primordial epithelial tissues called imaginal discs form vital organs for the future adult fly, such as legs, wings and eyes (Bate 1993). In adult females, the ovaries contain developing egg chambers, which are enveloped by a monolayer follicle cell epithelium (FCE), which I used to investigate how epithelial cell shapes arise in the context of external forces.

#### **1.5.2 Egg chamber – model for epithelial cell shape transitions**

Each ovary in the female fly is organized as a cluster of string-like structures called ovarioles. Each ovariole is an assembly line of individual egg chambers at different developmental stages. For oogenesis, development of egg chambers starts in the so-called germarium containing germline and somatic stem cells and progresses through developmental stages 2-14, which takes 7.3 days to complete (Spradling 1993).

During egg chamber development, a monolayer epithelium called the follicle cell epithelium (FCE) envelops the germline (GL). The germline is composed of a posteriorly positioned oocyte and 15 nurse cells. The germline is a syncytial unit where nurse cells and the oocyte are connected to each other by ring canals (Roth and Lynch 2009). When the egg chamber is released later from the germarium at stage 2, the follicle cell epithelium envelops the germline thereby assembling the egg chamber. Between stage 2 and stage 6 which lasts 4 days, the follicle cells undergo rapid cell divisions, whereas the germline increases in volume driven by endoreplication (Bastock and St Johnston 2008, Duhart, Parsons et al. 2017). It has been suggested that follicle cell divisions compensate for the growing internal volume of the germline allowing the FCE to maintain a cuboidal shape during these stages (Wang and Riechmann 2007).

After stage 6, there are about 900 cells in the epithelium and the FCE switches from mitotic divisions to endoreplication (Duhart, Parsons et al. 2017). Therefore, after stage 6 all cells of the egg chamber undergo endoreplication till stage 10. The germline grows in volume up to 10-fold in these stages (Kolahi, White et al. 2009) (Figure 6) which takes 24 hours. In volume expansion, the overall shape of the egg chamber gets sculpted into an ellipsoid with a

pointy anterior tip and a blunt posterior pole from an initially spherical shape (Fig 6). This process takes 24 hours. During stage 11, the nurse cells ‘dump’ all their contents into the oocyte, in a relatively fast developmental process that lasts only about 30 minutes. Following nurse-cell dumping, the FCE undergoes patterned morphogenetic events to generate the dorsal appendages (structures for breathing) and the micropyle (structure for sperm entry) before being released from the oviduct as a mature oocyte at stage 14 (Dobens and Raftery 2000, Duhart, Parsons et al. 2017). Thus, during the growth of the germline and the shifting landscape of overall egg chamber shape both pre- and post-dumping, integrity of the FCE must be maintained.

Cells in a sac-like epithelium subject to an internal expanding volume are expected to flatten uniformly. Instead the FCE undergoes 3 rounds of endoreplication during the slow growth (stage 6-10) of the germline and concomitant cell shape changes accommodate the increasing germline volume. The result of these transitions is that about 800 cells acquire a columnar shape when positioned over the oocyte and the remaining 100 cells stretch flat over the nurse cells. From stage 6, future cell shapes established by stage 10A can be tracked by expression of *dpp* to identify squamous-fated cells; *mirr* and *pnt* to identify columnar-fated cells (Dobens and Raftery 2000, Xi, McGregor et al. 2003, Horne-Badovinac and Bilder 2005). Thus the “accommodation” of germline growth is mediated by follicle cells which become squamous, while the remainder of the epithelium appears to acquire a columnar state “resistive” to flattening to accommodate the change in internal volume. The mechanical state of cuboidal cells in the intermediate stages is thus far unclear. Cuboidal to columnar shape transitions were thought to be driven by apical constriction (Horne-Badovinac and Bilder 2005, Wu, Tanwar et al. 2008). However, an increase in lateral height driven by cellular growth could account for columnarisation (Kolahi, White et al. 2009). This paper also described a mathematical model for the cell shape gradient seen in the egg chamber using a stiffness gradient from the posterior to the anterior, which could allow lateral growth and columnarisation of the follicle cells. Several genetic studies further implicate Actin, non-muscle Myosin II (MyoII), Spectrins and Integrins as essential to maintain cuboidal shape and establish columnar cell shapes in the posterior (Zarnescu and Thomas 1999, Baum and Perrimon 2001, Conder, Yu et al. 2007, Wang and Riechmann 2007, Conder, Yu et al. 2016, Ng, Selvaraj et al. 2016). Conversely, the lower stiffness of anterior cells in this model allows them to become compliant to the germline growth and flatten out. At a cellular level, squamous cell formation correlates with decreasing the length of the lateral membrane by endocytosis of Fas II from the lateral membrane (Gomez, Wang et al. 2012). In addition, breakage of AJs has been reported during squamous cell changes (Grammont 2007, Brigaud, Duteyrat et al. 2015, Chlasta, Milani et al. 2017). However, none of these studies have revealed cellular mechanisms through which the cytoskeleton and cell

## INTRODUCTION

adhesion act to ensure cell shape transitions between stage 6 and 10A, nor have they provided insight into how these components mediate adaptation to the dramatic surface expansion during germline growth. Furthermore, the cellular mechanisms and molecular players that can initiate resistance and relaxation in the FCE are unknown.

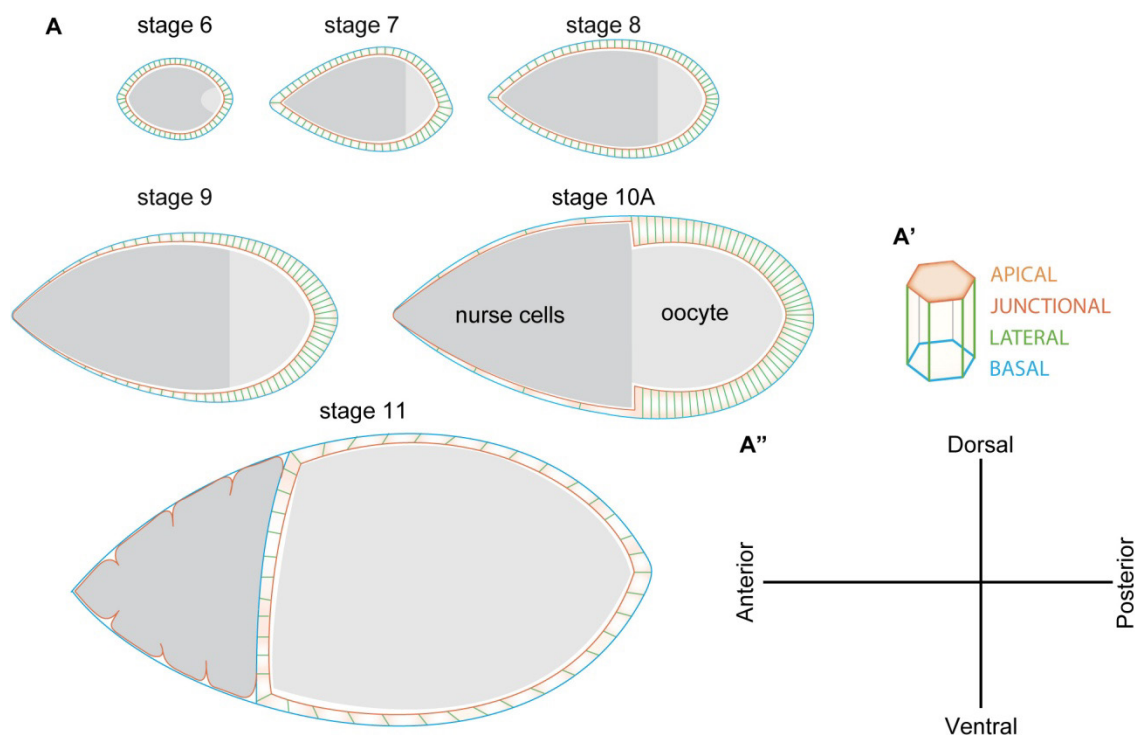


**Figure 6 Egg chamber development**

(A-A'') Scheme of egg chambers in different stages of interest for this study. Each egg chamber is composed of an internal germline made of 15 nurse cells (dark grey) and a posteriorly located oocyte (light grey). Enveloping the germline is a monolayer epithelium with a fixed number of cells after stage 6 with the apical surface (A') facing the germline. (A'') Antero-posterior (AP) and dorso-ventral (DV) axes are depicted.

Throughout egg chamber development, the apical surface of the epithelium faces the interior germline (Figure 6). Thus, any changes in germline volume must be matched by a change in apical epithelial area. While apical MyoII has been proposed to withstand forces from germline growth prior to stage 6 and to promote cell divisions to compensate for germline surface growth during early stages (Wang and Riechmann, 2007), nothing is known about how contractility is integrated with expansion of the apical surface of the epithelium between stages 6 to 10 after ceasing follicle cell divisions. Furthermore, how the “resistive” state of the columnar cells is switched off to allow uniform flattening of these cells during nurse cell dumping at stage 11 is not known.

Several studies have reported the roles for actomyosin contractility and the basement membrane in sculpting the overall shape of the egg chamber. A gradient of apical actomyosin contractility in early stages 2-5 from the poles controlled by JAK-Stat has been implicated in egg chamber elongation (Alegot, Pouchin et al. 2018). Polarized ECM filaments laid out by a rotating egg chamber between stages 6 and 8 have been implicated to form a molecular corset for the egg chamber in the DV axis, thus promoting elongation along AP axis (Haigo and Bilder 2011). Another study showed that planar polarization mediated by Fat2, an atypical Cadherin is sufficient to elongate the egg chambers in the absence of rotations (Aurich and Dahmann 2016). Basal Myo II oscillations have been suggested to be important for egg chamber shape at late stage 9 and stage 10 (He, Wang et al. 2010). An ECM stiffness gradient from the anterior to posterior has been implicated to be important in elongating egg chamber shape and a softening of this stiffness is important for cuboidal to squamous transitions (Chlasta, Milani et al. 2017, Crest, Diz-Munoz et al. 2017). However, very little is known about the role of the apical surface of FCE in affecting the overall organ shape through interactions with the germline.

## 2 Aim of study

Cell-autonomously generated actomyosin contractility at adherens junctions (AJs) and in the apical cortex of epithelial cells has been extensively studied and mediates morphogenetic movements, like apical constriction during gastrulation and epithelial cell intercalation for tissue elongation. To date little is understood about how contractility and adhesion in epithelial tissue responds to external forces arising from growth and shape of closely apposed neighboring tissues. Epithelial cells must resist or relax to external forces and maintain or adapt 3D shape in the tissue. We thus sought to understand if resistance and relaxation in response to external forces is modulated by contractility and adhesion during 3D epithelial cell shape transitions. Furthermore, we sought to elucidate how epithelial cell shape transitions are coordinated with a neighboring growing tissue to establish overall organ shape.

In this study, the *Drosophila* egg chamber is used to achieve these aims. The egg chamber is composed of a monolayer epithelium enveloping a growing germline. The epithelium undergoes multiple transitions along the squamous-cuboidal-columnar cell shape spectrum during egg chamber development. Germline growth serves as a source of external force acting on the epithelium during shape transitions. Since very little is known about the molecular mechanisms that control the mechanics of epithelial cell shape transitions while the germline grows, I wanted to first establish a correlation between localization of adhesion or actomyosin components and epithelial cell shape transitions. Second, I wanted to conduct a rigorous genetic analysis of molecular players that alter the mechanical state of cells to dissect their specific roles in maintaining epithelial cell shapes in the context of germline-derived forces. Third, using laser ablation perturbations of the epithelium, I sought to quantify the relative changes in tensile stress experienced by AJs in epithelial cells during germline expansion. Finally, I wanted to analyze how coordinating epithelial cell shape transitions with germline growth contributes to shaping the egg chamber at the level of the entire organ.

This study aimed to provide insight into how an epithelium and a closely apposed tissue coordinate their growth and morphogenesis to sculpt a final organ of the right size and

shape, a process of utmost importance to development of metazoans or in disease states like in cancer.

Work presented in this thesis was tremendously aided by the contributions of Vanessa Weichselberger (VW), Anne-Kathrin Classen (AKC), Marta Rodriguez (MR) and Guillaume Salbreux in the forms of ideas, experiments and discussions. Their experimental contributions to this thesis are indicated in figure legends when they appear.

## 3 Results

### 3.1 Onset of columnar cell shape is suppressed by nurse cell contact and initiates prior to cell flattening

We first thoroughly characterized the temporal onset of squamous-cuboidal-columnar cell shape differentiation, before characterizing the molecular players that are important for FCE cell shape in the egg chamber.

We could count between 30-32 epithelial cells in a medial cross-section of the elongating egg chamber at all stages after the end of cell division at stage 6 (Figure 7A). This implies there is no cell intercalation occurring in this epithelium as suggested previously too (Bilder and Haigo 2012). In the absence of cell intercalation, the follicle cells in the epithelium maintain fixed positions relative to each other throughout development and there is no contribution of cell intercalation in the cell shape transitions and egg chamber elongation. Thus, theoretically, the position of a follicle cell can be tracked between stages relative to the position of anterior membrane of the oocyte. As the egg chamber progresses through development from stage 6 to 10, sequentially more and more follicle cells contact the anteriorly growing oocyte. The oocyte displaces the contact of nurse cells with the overlying FCE, until stage 10A, when approximately 800 follicle cells contact the oocyte (Figure 7A, Figure 9A).

The FCE that envelops the germline prior to stage 6 is uniformly cuboidal (Wang and Riechmann 2007) (Figure 7A). Between stages 6 to 10A, the follicle cells contacting the oocyte acquire an increasingly columnar appearance with smaller apical areas and taller heights if compared to the remaining cells contacting the nurse cells (Figure 7B, C). Between stages 8 to 10, about 4 rows or 50 cells of FCE in the anterior initiate flattening. Thus, a gradient of cell shapes is visible most prominently at stage 9, with columnar cells in contact with the oocyte, cuboidal cells spanning the bulk of nurse cells and squamous cells over the anterior tip of the nurse cells. By stage 10A, the anterior cells have flattened completely over the nurse cell compartment and all remaining cells positioned over the oocyte acquired a columnar shape (Figure 7A).

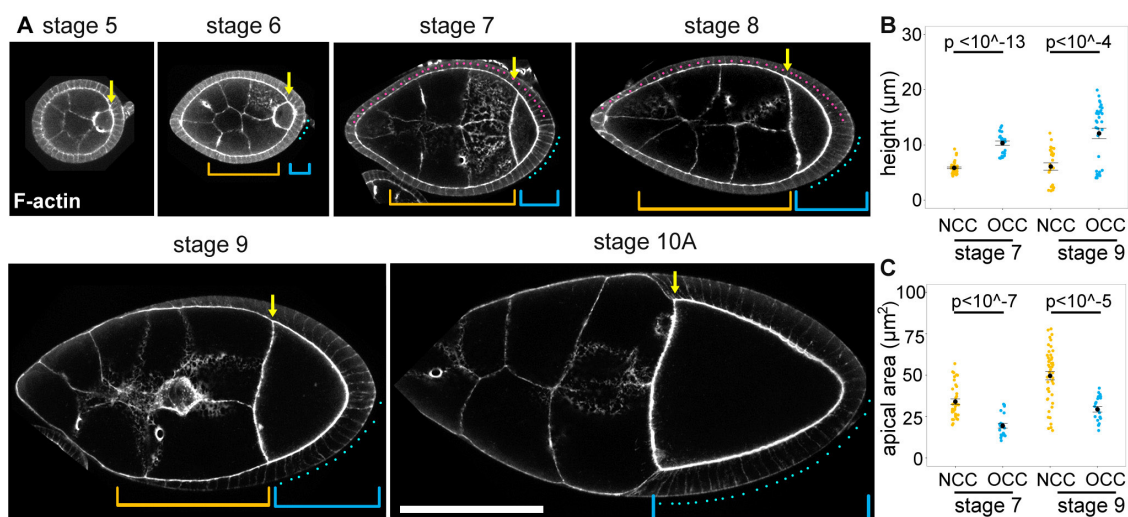


**Figure 7 Epithelial cell shape correlates with apposition to oocyte or nurse cell compartments**

(A) Medial section of stage 5 to 10A egg chambers stained for F-actin. Yellow arrows mark the position of the anterior oocyte boundary. Pink dots at stage 7 and 8 provide a count for all cells on one half of the cross-section (31 at stage 7 and 32 at stage 8). Blue brackets and cyan dots identify columnar cells in contact with the oocyte called oocyte-contacting cells (OCCs-, 4, 8, 10, 13 and 24 cells from stage 6 to 10A). Orange brackets identify cells in contact with the nurse cells called nurse-cell-contacting cells (NCCs). (B-C) Cell heights (B) and apical areas (C) of NCCs and OCCs at stages 7 and 9. Graphs display mean  $\pm$  S.E.M. WMW-tests were performed. For quantifications and sample sizes see Table 9 and Table 10. Scale bar = 100  $\mu$ m.

Anterior cell flattening can be tracked robustly with a developmental pre-patterned fate of these cells (Brigaud, Duteyrat et al. 2015) and are henceforth called the squamous-fated cells (Figure 8A). Conversely, all remaining cells can be termed columnar-fated cells as they acquire a columnar shape by stage 10. However, unlike the squamous cells, not one of developmental fates known to stably exist at these stages in columnar-fated cells, namely posterior-fate and main body-fate, track exclusively with either columnar or cuboidal cell shape respectively (Figure 8B-I') (Xi, McGregor et al. 2003, Horne-Badovinac and Bilder 2005). At stage 9, cuboidal main-body fated cells contact nurse cells, whereas columnar main-body fated cells contact the oocyte (Figure 8H-H'). However, all posterior-fated and main-body fated follicle cells ultimately become columnar by stage 10A (Figure 8E-E', I-I', Figure 9B). Together, this indicates that these known early developmental fate patterns are not sufficient to assign cuboidal or columnar cell shape.

## RESULTS

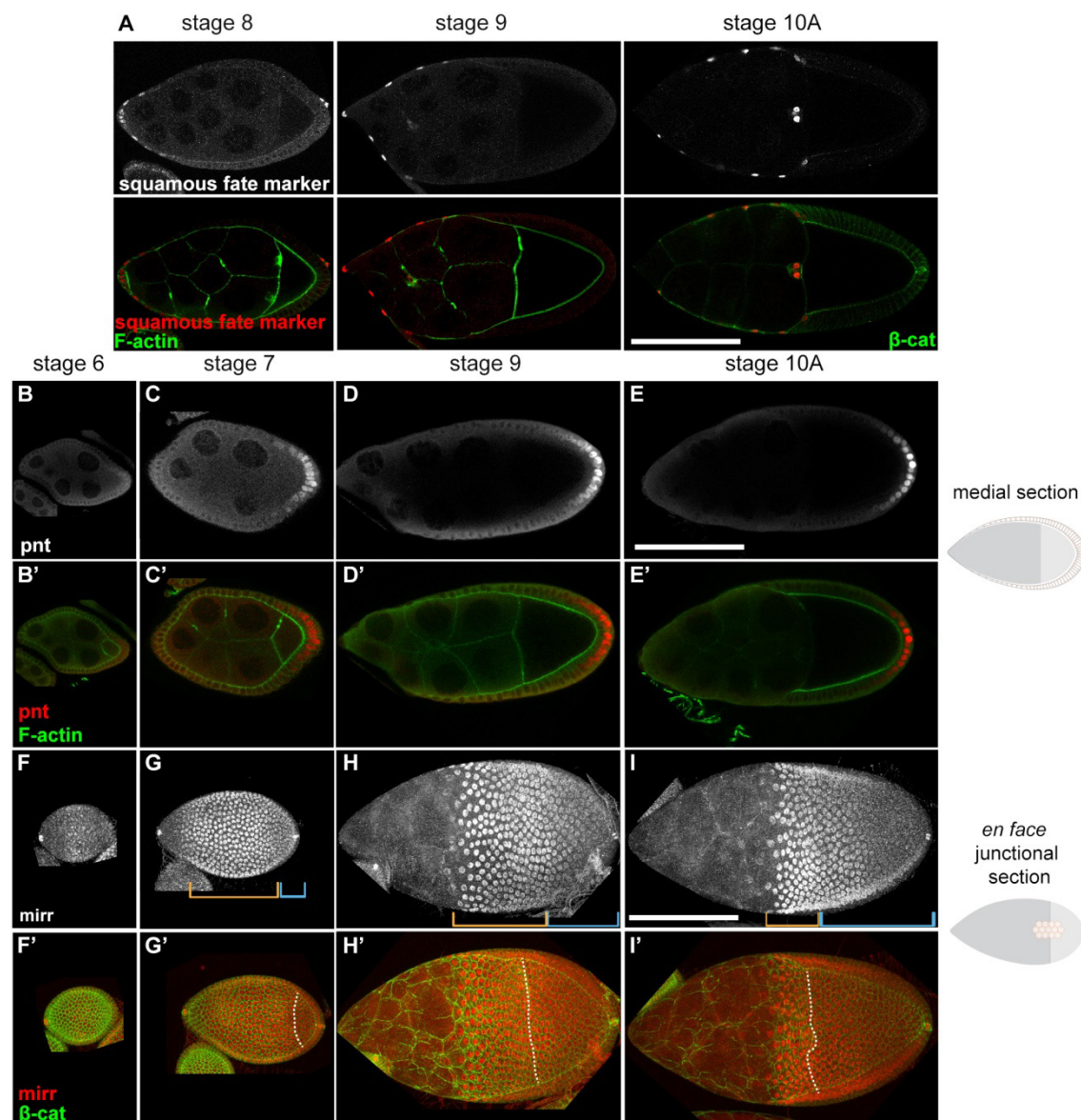


**Figure 8** Developmental fate can be used for tracking squamous-fated cells but no specific known developmental fate tracks with all columnar-fated cells

(A) Medial section of egg chambers expressing squamous-fate marker in stages 8 to 10A stained for squamous-fate marker (grey in top panel and red in bottom panel) and F-Actin (green in bottom panel). (B-E') Medial section of egg chambers expressing *pointed (pnt)-lacZ* in stages 6 to 10A stained for  $\beta$ -gal (grey in B, C, D, E, red in B', C', D', E') and F-Actin (green in B', C', D', E'). Scheme on left illustrates view of medial section. (F-I') Maximum projection of confocal sections to obtain *en face* view of AJs and nuclei over the curved surface of half of the egg chamber. Scheme on left illustrates *en face* section. Egg chambers expressing a GFP-tagged version of the main-body fate marker *mirr* in stages 6 to 10A (grey in F, G, H, I, red in F', G', H', I') and  $\beta$ -cat (green in F', G', H', I'). Note how *mirr*-expressing cells span both NCC (orange brackets) and OCC (blue bracket) populations at stage 9 (H). White dotted lines mark the anterior oocyte boundary. Scale bar = 100  $\mu$ m.

Instead, contact with oocyte appears to promote acquisition of columnar shapes and contact with nurse cells suppresses it and maintains cells in cuboidal shape. Due to this germline

contact-dependent shape correlation of the columnar-fated follicle cells up to stage 10, they are henceforth called Oocyte Contacting Cells (OCCs) and Nurse cell Contacting Cells (NCCs) (Figure 9C). It is important to note with this nomenclature, that the number of NCCs and OCCs is variable depending on the developmental stage of the egg chamber, but the total number of columnar-fated cells is fixed through developmental stages 6-10. In support of the notion that follicle cell shape correlates with nurse cell or oocyte contact, we found that in several genetic mutants with mis-positioned oocytes or two oocytes located anteriorly and posteriorly, the OCCs acquire a more columnar appearance if compared to NCCs (Figure 10). This demonstrates that posterior positioning of the oocyte and overall egg chamber elongation can be uncoupled from columnarisation of columnar-fated cells.

Taken together, FCE columnarisation starts prior to flattening during egg chamber development. The columnar shape correlation with oocyte contact suggests that columnarisation is specifically promoted by oocyte contact. Conversely, the nurse cell contact suppresses columnarisation and maintains follicle cells in their initial cuboidal shape.

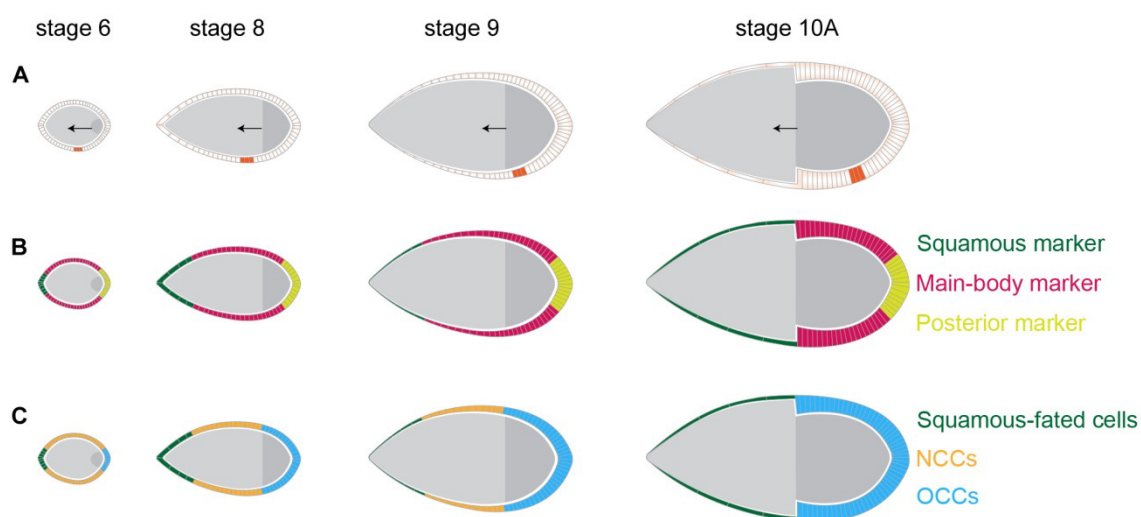


**Figure 9 Summary of cuboidal-columnar cell shape transitions between stage 6 to 10A**

(A-C) There are 31 follicle cells spanning each half of the egg chamber from the anterior to the posterior in the medial section of these schematic egg chambers. The egg chambers drawn in A-C can be superimposed according to stage. (A) Three brown cells which are initially over the bulk of the nurse cells (stage 6) are being tracked through all the stages as the oocyte grows anteriorly (black arrows). As the oocyte moves anteriorly, the three cells encounter the oocyte (stage 9). (B) If the columnar-fated cells are tracked with known developmental fate markers, we see that neither the main-body marker nor the posterior marker tracks exclusively with either cuboidal or columnar cell shapes. (C) The shape of the columnar-fated cells can be tracked with germline contact. They are cuboidal when over the nurse cells (NCCs), and columnar when the oocyte contacts them (OCCs). Note the brown cells in (A) are main-body marker labelled but change shape from cuboidal to columnar dependent only on contact with nurse cell or oocyte.

## RESULTS

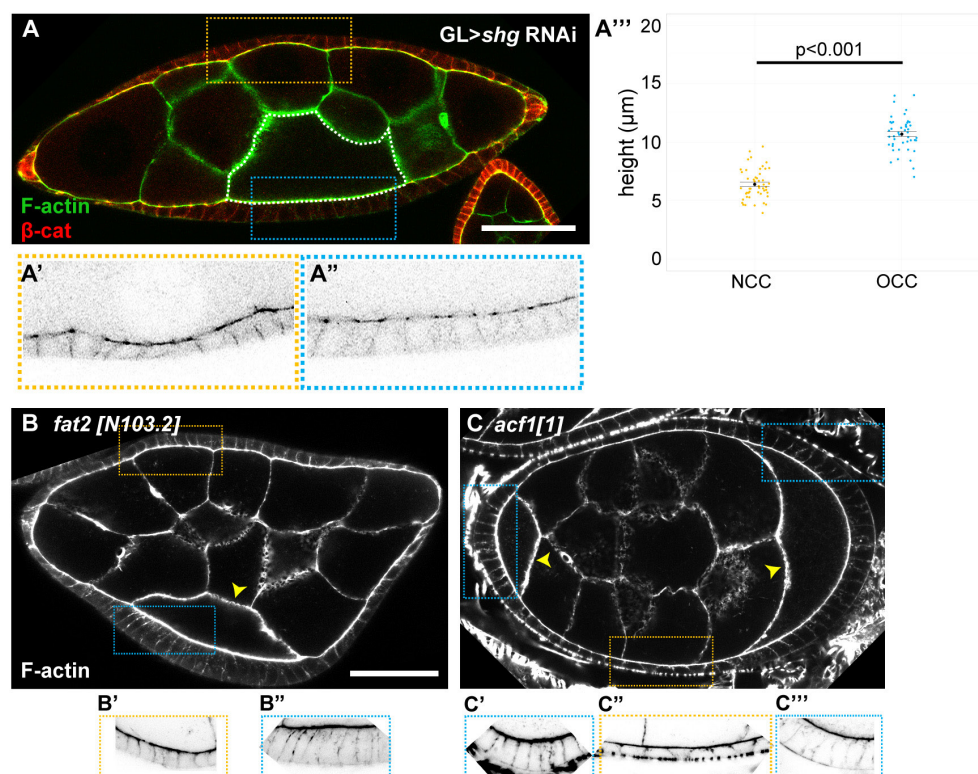


**Figure 10 Columnar cell shape of FCE correlates even with mis-positioned oocytes**

(A-A''') Medial sections (A, A', A'') to visualize stage 9 egg chambers. The germline expresses RNAi targeting E-cad (*shg*) resulting in a mispositioned oocyte (framed by white dotted lines, identified by denser actin cortex). (A''') Quantification of the height of NCCs and OCCs in egg chambers with misplaced oocyte. (n=49 NCCs and 46 OCCs from 6 egg chambers, see Table 11). WMW test was performed. (B-C) Other genetic mutants which mis-localize the oocyte (B, yellow arrowhead) or have defects in germline packing leading to two oocytes (C, yellow arrowheads). Orange (NCC) and blue (OCC) boxes in (A, B, C) are shown at higher magnification in (A', A'', B', B'', C', C'', C'''), respectively. Egg chambers were stained for F-actin (green in A, grey in B-C''') and  $\beta$ -cat (red in A, grey in A', A''). Compare the heights of NCCs and OCCs. Scale bar = 50  $\mu$ m

### 3.2 Cell polarity, adhesion and cytoskeletal proteins that correlate with cell shape transitions and germline contact

To determine which proteins are important for squamous-cuboidal-columnar shape transitions to occur, we performed a small screen of typical epithelial polarity, adhesion and cytoskeleton markers during stages 6-10, to test for their presence and correlations with cell shape (Figure 11).

We found that protein localizations typically fell into 3 categories:

- I. Uniform localization in follicle cells irrespective of their shapes: e.g.- aPKC, Dlg
- II. Levels correlated with squamous-fated cells: e.g.- Perlecan, Cher

III. Levels correlated with follicle cell contact with either nurse cell or oocyte: e.g.-  
DE-Cad

Category I includes apical and lateral polarity proteins like aPKC, Crb, Dlg and apical cytoskeleton regulators like Rok or Moesin (Figure 11A). Category II appears to be dependent on the induction of squamous cell fate at stage 7 (Xi, McGregor et al. 2003). Perlecan levels increase whereas Cher levels decrease in the squamous-fated cells prior to initiation of cell flattening at stage 7 (Figure 11B). It is important to note that, category I includes proteins that displayed comparable protein levels in all NCCs prior to squamous cell flattening but diluted in squamous-fated cells at stage 9 (eg: Crb,  $\beta_H$ -spectrin), suggesting spreading of the protein across increasing apical area if compared to NCCs. Conversely, this category also includes those proteins whose intensity increased in OCCs (e.g.: Rok, Moesin) likely due to decreasing apical area if compared to NCCs. Thus, effects of changing protein concentration due to apical area changes of the FCE are considered as uniform distribution in category I.

Category III was of interest since the levels of these proteins showed a correlation with germline contact which cannot be explained as concentration or dilution of proteins with apical surface area changes of the FCE. In specific, AJs proteins DE-Cad,  $\beta$ -cat and Baz showed a decrease in levels of proteins in the OCCs if compared to the NCCs (Figure 11C, Figure 12A-B'). Since,  $\beta$ -cat strongly co-localizes with DE-Cad during all stages of cellular trafficking (Bryant and Stow 2004, Baum and Georgiou 2011), henceforth,  $\beta$ -cat is used as a proxy for AJs. Surprisingly, other components of AJs like N-Cad and Echinoid (Ed) do not show decreased levels in the follicle cells positioned over the oocyte suggesting that only specific components of the AJs are regulated in a germline contact dependent manner (Figure 11A). When the oocyte is mis-positioned to the center of the egg chamber because of genetic manipulation, cells in contact with the oocyte still exhibit lower levels of  $\beta$ -cat, confirming the germline contact-dependent correlation (Figure 12C). Furthermore, *mirror* expressing cells representing main-body fate had either high (NCC) and low (OCC) levels of  $\beta$ -cat suggesting that there is no pre-patterned developmental fate determining cellular levels of these AJ proteins (Figure 12D-D').

## RESULTS

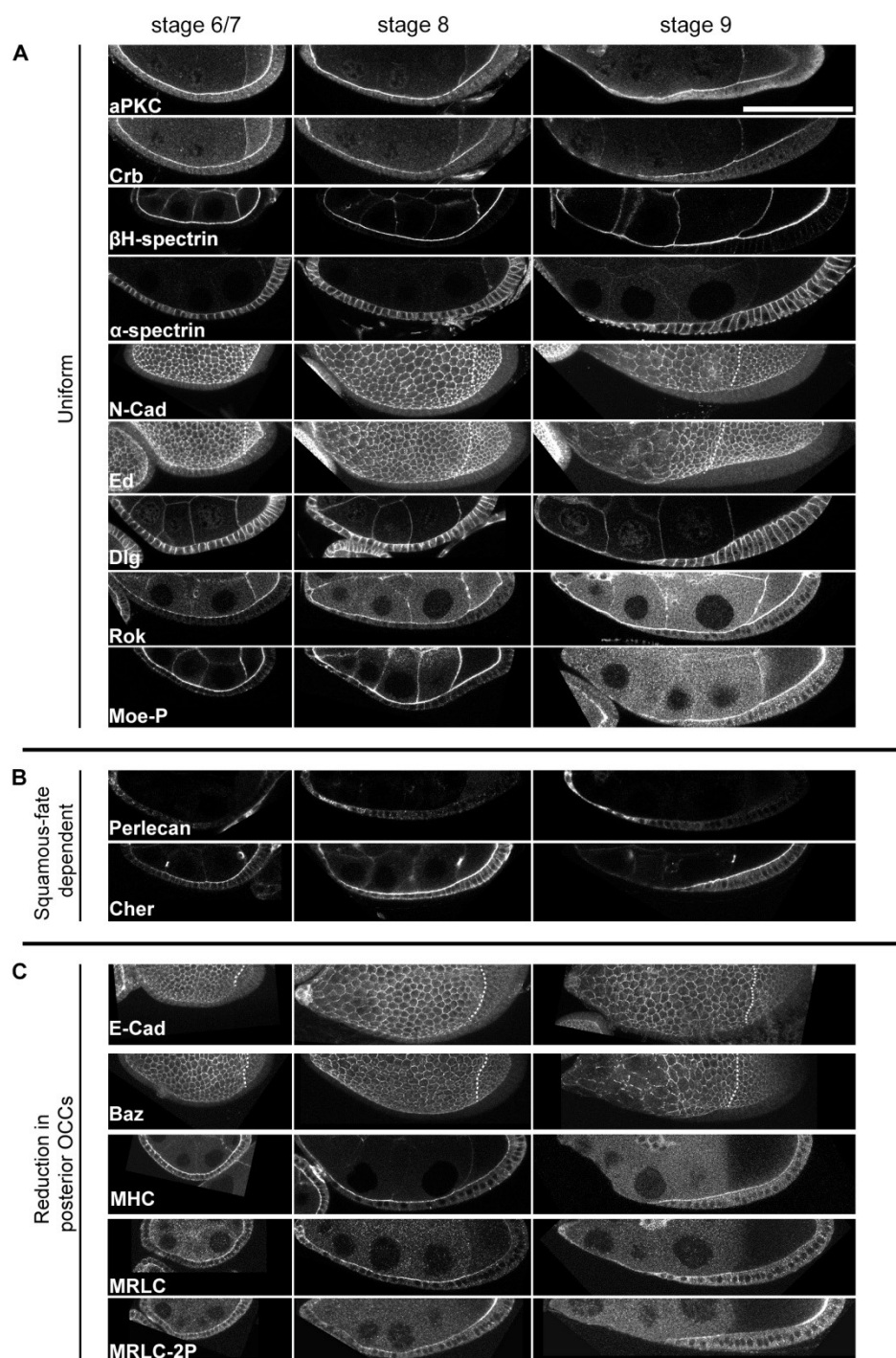


**Figure 11 A screen for polarity, junctional and cytoskeletal proteins for FCE cell shape and germline contact-dependent correlations**

(A-C) Medial sections (aPKC, Crb,  $\beta$ <sub>H</sub>-spectrin,  $\alpha$ -spectrin, Dlg, Rok, Phospho-Moesin, Perlecan, Cher, MHC, MRLC, MRLC-2P) and maximum projections of AJ sections (E-cad, Baz, N-cad, Ed) of egg chambers at stages 6/7, 8 and 9. Markers display uniform apical or lateral distribution in all epithelial cells (A), or are changing levels in a squamous-fated cell specific manner (B) or are reduced in OCCs and enriched in NCCs (C). White dotted lines mark the anterior oocyte boundary. Scale bar = 100  $\mu$ m. Ed images taken by VW. The bright signal in the posterior most region in MRLC-2P images at stages 8 and 9 comes from the oocyte and is not discussed in this work.

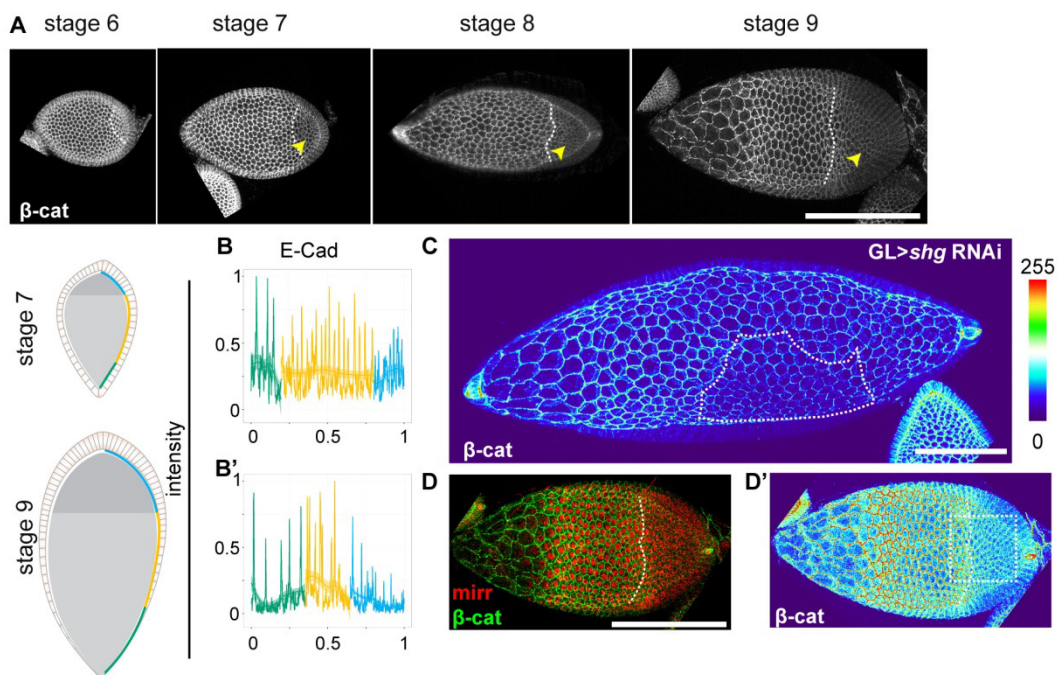


**Figure 12 E-cad/β-cat levels are modulated by cell non-autonomous, germline contact-dependent mechanisms**

(A) Maximum projection of confocal sections to obtain *en face* view of AJs in egg chambers stained for β-cat. Yellow arrowheads indicate low junctional β-cat in OCCs. (B-B') Representative line profiles of E-Cad fluorescence intensities at apical-junctional domains (see schemes on left) in medial sections of egg chambers at stages 7 and 9. Intensities normalized to the maximum measured value were plotted for squamous cells (green), NCCs (orange) and OCCs (blue) along the length of an egg chamber scaled from 0-1. Reproducible line profiles were obtained for  $n \geq 5$  egg chambers. Dotted lines mark the anterior oocyte boundary. (C) Maximum projection of confocal sections to visualize AJs (C) of stage 9 egg chambers. The germline expresses RNAi targeting E-cad (*shg*) resulting in a mispositioned oocyte (framed by white dotted line in C). The egg chamber was stained β-cat (C) shown in thermal scale. (D-D') Maximum projection of a confocal stack of an egg chamber expressing mirr-GFP (red in D) and stained for β-cat (green in D, thermal in D'). Note intensity differences across the oocyte-nurse cell boundary (white dotted line in D). Scale bars (A, D-D') = 100 μm, (C) = 50 μm. White box in D' is described in Figure 14.

## RESULTS

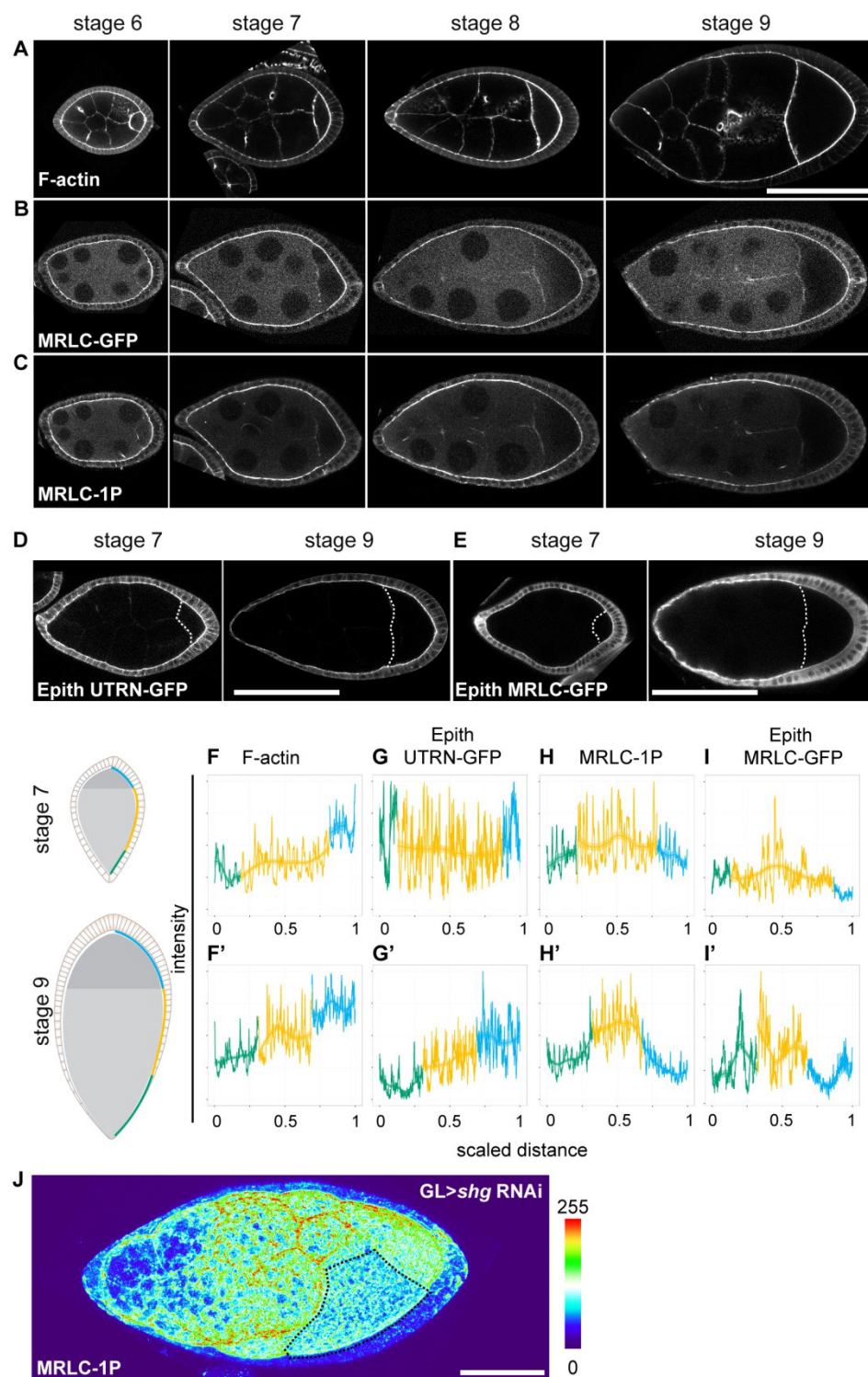


**Figure 13 MyoII levels are modulated by cell non-autonomous, germline contact-dependent mechanisms**

(A-C) Medial sections of egg chambers stained with F-actin (A), expressing MRLC-GFP (B) and simultaneously stained with MRLC-1P (C). (D-E) Medial sections of egg chambers expressing *utABD-GFP* (D) and MRLC-GFP (E) only in the epithelium at stages 7 and 9. Dotted lines mark the anterior oocyte boundary. (F-I') Representative line profiles of fluorescence intensities at apical-junctional domains (see schemes on left) in medial sections of egg chambers at stages 7 and 9. Intensities normalized to the maximum measured value were plotted for squamous cells (green), NCCs (orange) and OCCs (blue) along the length of an egg chamber scaled from 0-1.

Egg chambers were stained for F-actin (F, F'), epithelial expression of utABD-GFP (G, G'), MRLC-1P (H, H') and epithelial expression of MRLC-GFP (I, I'). For each marker, reproducible line profiles were obtained for  $n \geq 5$  egg chambers. (J) Maximum projection of confocal sections to visualize MRLC-1P in stage 9 egg chamber. The germline expresses RNAi targeting E-cad (*shg*) resulting in a mispositioned oocyte (framed by black dotted line). The egg chamber was stained with MRLC-1P shown in thermal scale. Scale bars A-E = 100  $\mu\text{m}$ , J = 50  $\mu\text{m}$ .

Since, AJs associate with cytoskeleton proteins, we next characterized the distribution of proteins like F-actin, Myo II,  $\beta_{\text{H}}$ - and  $\alpha$ -spectrin in these stages. The apical cortex of the follicle cells and germline cortex are not easily microscopically resolvable especially for the NCCs and nurse cell interface. Thus, I first report the combined distribution of fluorescence intensities of the two cortices and call it the apical interface. The levels of F-actin at the apical interface are higher in the OCC–oocyte interface if compared to the NCC–nurse cell interface. In contrast, apical interface levels of Myo II components (MRLC, MHC, activated MRLC- 1P and 2P forms) are lower at the OCC–oocyte interface if compared to the NCC–nurse cell interface (Figure 11C, Figure 13A-C, F-F', H-H'). Importantly, egg chambers with misplaced oocyte as a result of genetic manipulation, showed reduced MRLC-1P levels at the OCC–oocyte interface (Figure 13J). In contrast, levels of the apical spectrin complexes composed of  $\beta_{\text{H}}$ - and  $\alpha$ -spectrin were comparable between OCC and NCC interfaces (Figure 11A).

To dissect the contribution of the apical surface of FCE to total apical interface fluorescence intensities, we expressed a genetically encoded marker for Actin called Utrophin ABD-GFP (*utABD-GFP*) and fluorescence tagged MRLC for Myo II in a tissue specific manner in the FCE. Using this strategy, we observed higher apical levels of Actin in the OCCs if compared to NCCs. In contrast, the Myo II signals in the apical surface of OCCs were lower than in NCCs (Figure 13D, E, G-G', I-I'). Interestingly, the drop in the level of Myo II at the NCC-OCC boundary is very sharp (Figure 14A-B"). In comparison, the levels of  $\beta$ -cat drop typically 2-3 cell rows posterior to the oocyte boundary with the nurse cells (Figure 14C-C'). Thus, the levels of AJ complexes and apical Myo II are reduced in the OCCs but are reduced by potentially different mechanisms.

Taken together, these data indicate that AJ and Myo II mediated contractility in FCE are regulated by cell non-autonomous mechanisms dependent on germline contact. AJ and actomyosin levels thus correlate with the onset of columnarisation, which is germline contact-dependent too. Intriguingly, it appears that the change from cuboidal shape aspect ratios of NCCs to columnar aspect ratios of OCCs is not dependent on increasing actomyosin and adhesion levels, which are expected to decrease apical surface area. Thus, instead of a conventional apical contractile mechanism decreasing apical area, other cellular mechanisms must be at play that control columnarisation, that are promoted only on contact with the oocyte. Finally, the uniform distribution of other AJ, polarity and cytoskeletal proteins suggests the

## RESULTS

entire FCE utilizes cell autonomous mechanisms to regulate proteins localization independent of germline contact dependent ones.

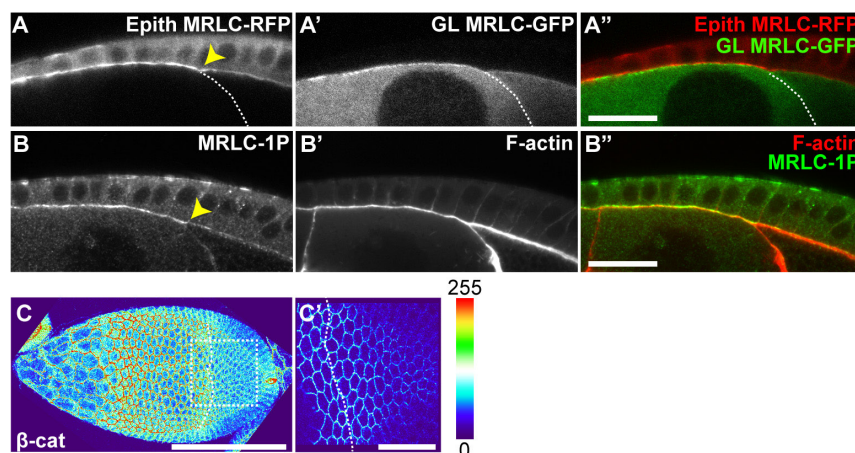


**Figure 14 Change in AJ and Myo II levels in OCCs is regulated by differently** (A-B'') Medial section of an egg chamber with epithelial expression of MRLC-RFP (A, red in A'') and germline (GL) expression of MRLC-GFP (A', green in A''), total MRLC-1P (B, green in B'') and F-actin (B', red in B''). Yellow arrowheads point to the sharp drop in MRLC-RFP and MRLC-1P levels at the oocyte boundary. (C-C') Thermal image of maximum projection of a confocal stack of an egg chamber stained for  $\beta$ -cat. Higher magnification (C') of box framing region in (C). Note the gradual drop in junctional  $\beta$ -cat intensities in OCCs. Scale bar (A-B'') = 20  $\mu$ m, (C) = 100  $\mu$ m, (C') = 25  $\mu$ m. Dotted lines mark the anterior oocyte boundary.

### 3.3 Reorganization of adherens junctions and contractility is driven by cell-autonomous mechanisms of follicle cells

#### 3.3.1 Reorganization of the actomyosin cortex on the apical surface of follicle cells

To test if contact-dependent mechanisms regulated remodeling of AJs and Myo II, we next analyzed the cellular distribution of these proteins. Markers of the Myo II minifilaments like activated MRLC and MHC and its upstream activator Rok localize at AJs and in the apico-medial cortex at stage 5-6. Strikingly, Myo II and Rok are lost from AJs and enrich in the apico-medial cortex by stage 9. Similarly,  $\beta_{\text{H}}$ -spectrin is excluded from AJs between stage 6 and 9 (Figure 15 A-G'). Myo II-free junctions could also be visualized in live imaging of stage 9 egg chambers, eliminating the possibility of any fixation artifacts (Figure 15H-H'). Interestingly, the extent of apico-medial coverage of Myo II is different from that of  $\beta_{\text{H}}$ -spectrin. While the latter spanned the apical surface extensively, Myo II appeared to localize in the form of a 'ring' with sparser localization in the center of the apico-medial cortex above the nucleus and denser localization at a closer proximity to the junctions (Figure 15, for example compare E' to G'). Importantly, this exclusion of Myo II and  $\beta_{\text{H}}$ -spectrin was seen uniformly in all follicle cells (Figure 15I-J).

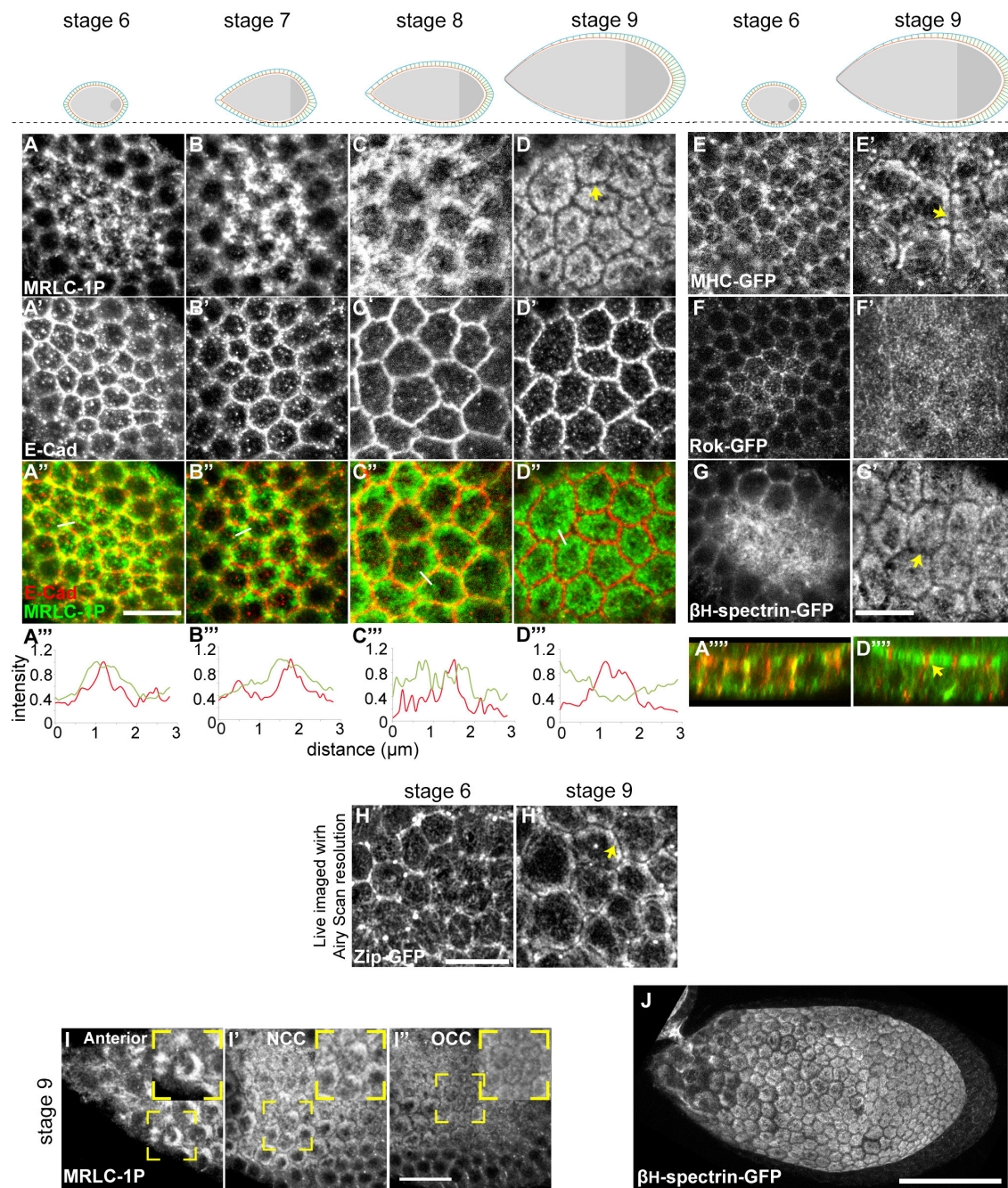


**Figure 15 MyoII and  $\beta_H$ -spectrin reorganization in apical domain of FCE during stages of germine surface area expansion**

(A-G') *En face* junctional sections of egg chambers at stages 6 to 9 (A-D'' and E-G'') stained for MRLC-1P (A-D, green in A''-D''), E-cad (A'-D', red in A''-D''), or expressing MHC-GFP (E, E'), Rok-GFP (F, F') or  $\beta_H$ -spectrin-GFP (G, G'). Black line across egg chamber schemes above indicates position at which sections were acquired. Line profile plots (A'''- D''') of MRLC-1P (green) and E-cad (red) fluorescence intensities along white lines (A''-D''). XZ-reslices of confocal stacks from stage 6 and 9 epithelia (A''', D''') shown in A and D. Yellow arrows point to clearance of markers from AJs. (H-H') *En face* junctional sections of a live MHC-GFP expressing egg chamber at stages 6 and 9. Yellow arrow points to clearance of MHC-GFP from AJs. (I-I'') *En face* junctional sections of squamous (I), NCC (I') and OCC (I'') cells stained for MRLC-1P. Insets show higher magnifications of yellow brackets. (J) *En face* junctional section overview of  $\beta_H$ -spectrin-GFP egg chamber at early stage 9 showing a uniform clearance of  $\beta_H$ -spectrin from junctions in squamous and columnar-fated cells. Scale bars (A-I'') = 10 $\mu\text{m}$ , (J) =

## RESULTS

50  $\mu\text{m}$ . (H-H') images taken by VW.

Next, we visualized Actin localization with fluorescently labeled F-Actin binder Phalloidin. F-Actin, unlike Myo II does not get excluded from the junctions but undergoes remodeling. At stage 6, there is junctional F-Actin and filaments in the apico-medial cortex. By stage 9, F-Actin filaments appear to reorganize into a dense filament meshwork spanning the apico-medial cortex with no specific orientation along the junctions (Figure 16A). Such a meshwork could potentially anchor the medial Myo II to the junctions as suggested previously and redirect the alignment of contractile forces from a junctional to a radial direction (Figure 16B) (Coravos and Martin 2016). Together, these data suggest pan-epithelial and cell autonomous reorganization of Myo II and  $\beta_{\text{H}}$ -spectrin by exclusion from junctions and F-Actin reorganization in the apico-medial network which is autonomous to the germline contact of these cells.

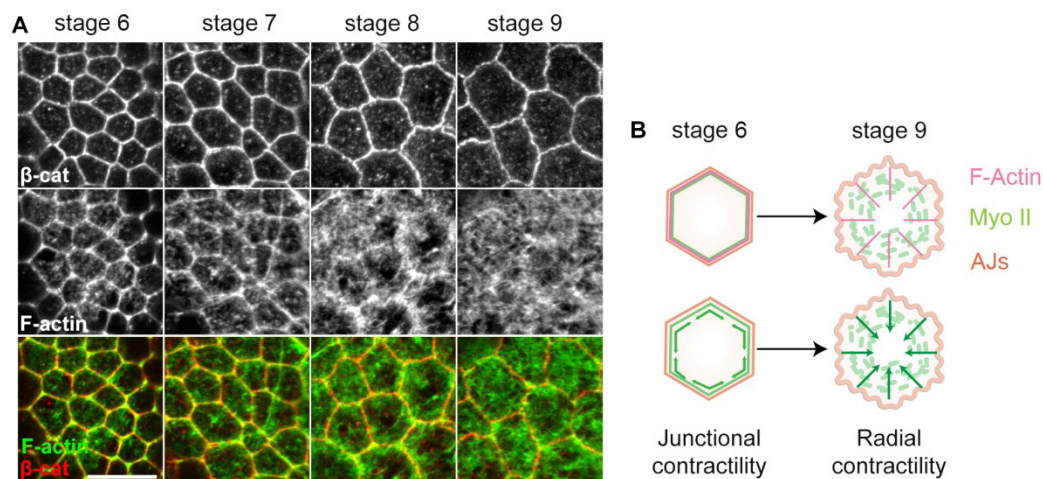


**Figure 16 Actin reorganization in NCC apical domain during stages of germline surface area expansion**

(A) *En face* junctional sections in egg chambers at stages 6 to 9 stained for  $\beta$ -cat (A) (grey in top row panels, red in bottom row panels), total F-actin (A) (grey in middle panels, green in bottom row panels). Scale bar= 10 $\mu\text{m}$  (B) Scheme depicting changes in the organization of junctions, Myo II and F-actin between stage 6 and stage 9 and how this could potentially change the dominant direction of contractile forces (green arrows) exerted on the AJs- from a junctionally directed network to a radially directed one.

### 3.3.2 Uniform onset of corrugations in adherens junctions correlate with germline growth

Accompanying the drastic remodeling of the actomyosin and spectrin cortex, AJs also undergo a change in their appearance. Junctions are straight at stage 6. Progressively, AJs acquire a more corrugated appearance by stage 9 with a tripling in junctional roughness (Figure 17A-A'', see Section 6.5.1 for definition used for quantification). This characteristic corrugation

is visible only at the level of AJs. In contrast, lateral membranes are straight (Figure 17B-C”). In addition, we observed that other components of AJs like Ed and N-cad also display corrugations (Figure 17D, E). Finally, the onset of AJ corrugations was independent of the position of follicle cells over the germline and their final 3D shape. However, the degree of junctional roughness was higher for NCCs if compared to OCCs. Another prominent feature of AJs during these stages are the occurrence of discontinuities in them (Figure 17F-H). By stage 10A-10B, the number of breaks coupled with corrugations, makes AJs almost indiscernible in columnar cells (Figure 17I-I’). Thus, a uniform developmental program is initiated in the FCE to switch AJs from a straight to corrugated appearance that coincides with the exclusion of Myo II from the junctions.

Taken together, these data suggest the existence of a uniform cell-autonomous FCE program employed to remodel apical actomyosin, spectrin and AJ architecture during stages of steady germline surface area expansion of the germline. The formation of corrugated junctions rescales ratio of the length of AJs to the vertex distance at the respective edge and by extension the ratio of the length of AJs to the surface area of cells. We speculate that this rescaling allows the FCE to respond better to the surface area expansion of the germline. Similarly, the exclusion of Myo II from junctions potentially alters the net intrinsic contractile forces exerted on the junctions and stiffness of junctions to balance against the net extrinsic forces from surface area expansion related to germline growth. These changes potentially aid matching in the surface area of the FCE to that of the germline.

Superimposed on this cell-autonomous FCE behavior is the germline contact-dependent regulation of actomyosin and AJ protein levels. Specifically, NCCs show higher levels of corrugations as well as AJs and Myo II levels in the apico-medial cortex. Thus, the cell-autonomous FCE program is modulated by nurse cell contact-dependent cues and promotes maintenance of cuboidal cell shape if compared to columnar cells in contact with the oocyte. Thus, cell-autonomous and non-autonomous processes contribute simultaneously to remodeling entire apical domain of epithelial cells during stages of germline surface area expansion and cell shape transitions (Figure 18).

## RESULTS

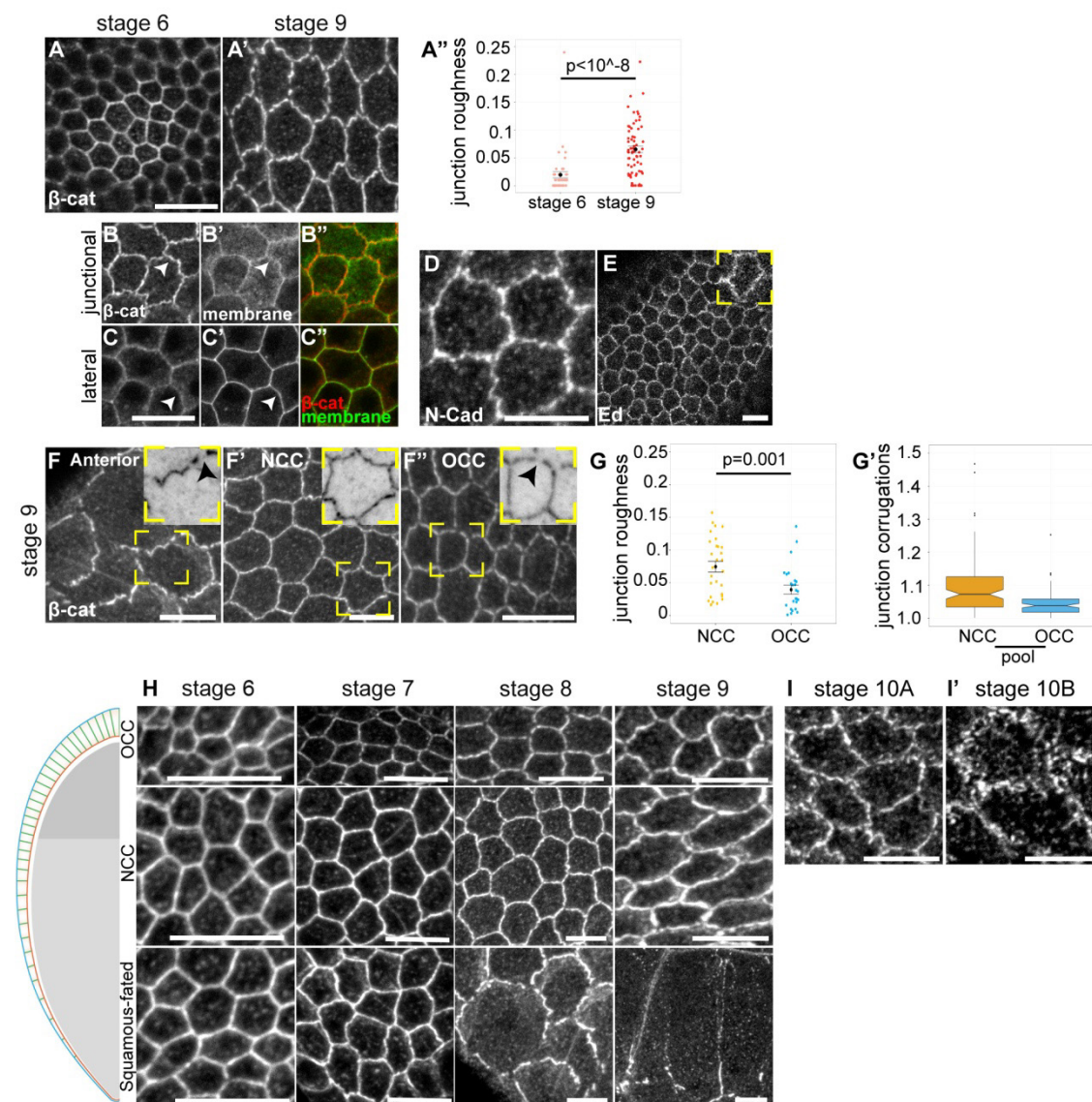


**Figure 17 Emergence of junctional corrugations in FCE during stages of germline surface expansion**

**(A-A'')** *En face* sections of NCC AJs at stage 6 (A) or 9 (A') stained for  $\beta$ -cat. Note the increase in junctional corrugations. Quantification of junctional roughness (A'', Table 14). Graphs display mean  $\pm$  SEM.  $n=46$  (stage 6) and  $n=65$  (stage 9) at NCC positions in 3 egg chambers at each stage. WMW-test was performed. **(B-C'')** *En face* sections of NCC AJs (B-B'') and lateral interface (C-C'') at stage 9 stained for  $\beta$ -cat (B, C, red in B'', C'') and the plasma membrane marker PH-GFP (B', C', green in B'', C''). Arrowheads point to corrugations (B, B') and their absence (C, C'). **(D-E)** *En face* junctional sections of stage 9 egg chambers stained with N-cad (D) and Ed (E, inset) showing corrugations. **(F-F'')** *En face* junctional sections at stage 9 in squamous cells (F), NCC (F') and OCC (F'') cells stained for  $\beta$ -cat. Insets show higher magnifications of yellow brackets to visualize discontinuities in AJs (black arrowheads). **(G)** Quantification of junctional roughness in NCCs and OCCs from one representative egg chamber ( $n=29$  NCCs,  $n=26$  OCCs, Table 15). Graphs display mean  $\pm$  SEM. Statistically significant differences were obtained for 3 additional egg chambers. WMW-tests were performed. **(G')** Combined box plot for the junctional corrugations data from all 4 egg chambers. Note the non-overlapping median values (105 NCCs and 95 OCCs). **(H)** *En face* junctional sections in squamous-fated cells, NCC and OCC positions between stages 6 and 9. Egg chambers were stained for  $\beta$ -cat to visualize onset of junctional corrugations. Scheme of a stage 9 egg chamber on the left illustrates the approximate positions imaged. **(I-I')** *En face*

junctional sections at stages 10A and 10B visualizes the extreme discontinuities and corrugations in the junctions at these stages. Scale bars = 10 $\mu$ m. Ed image taken by VW. (A'') measurements by AKC.

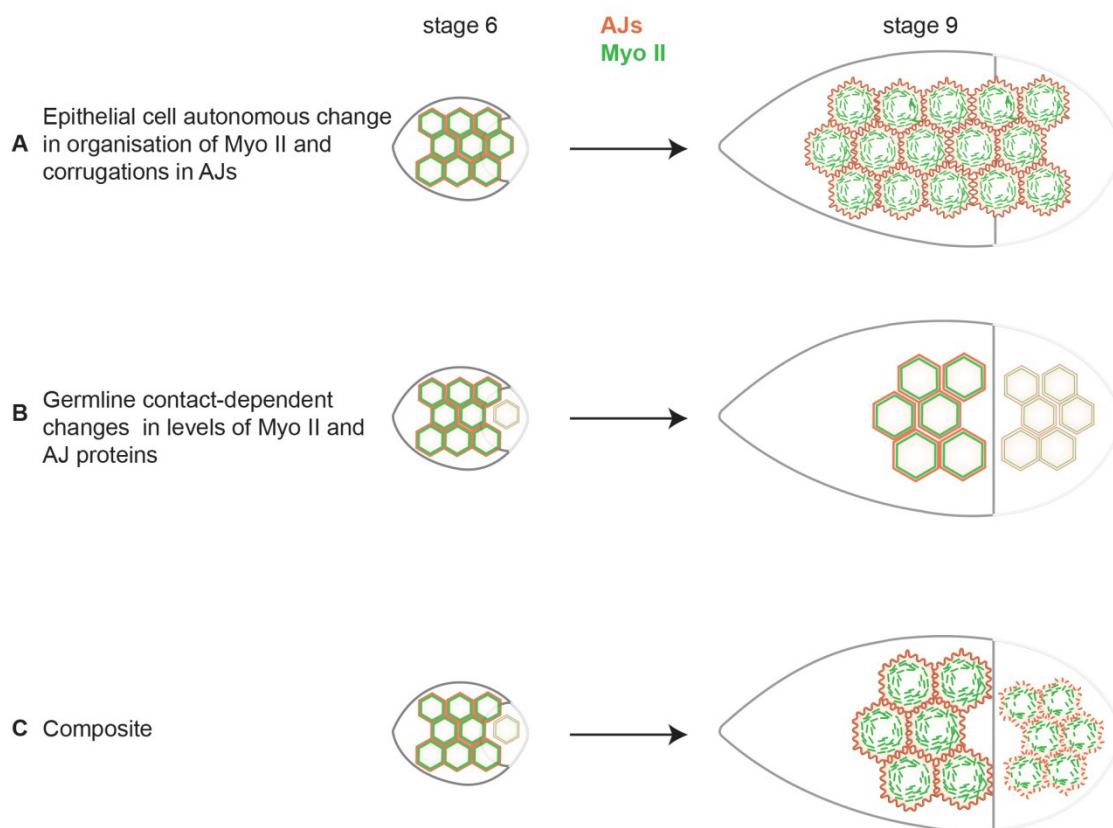


**Figure 18 Summary of follicle cell-autonomous and non-autonomous processes that remodel the entire apical domain of FCE during stages of germline surface area expansion and epithelial cell shape transitions**

Two events are occurring at the cellular level of the FCE. **(A)** All epithelial cells cell-autonomously exclude Myo II from the junctions and corrugate their AJs. **(B)** Simultaneously, the levels of these proteins are dependent on contact with nurse cells or the oocyte, with higher levels over the nurse cells. **(C)** A composite of these two events is the actual representation of the cellular organization of AJs and Myo II seen in the egg chambers during these stages which potentially enable the epithelium to match its surface areas to that of the expanding germline and coordinate cuboidal-columnar shape transitions.

### 3.4 Tensile stress on junctions decreases to accommodate the expansion of the germline

#### 3.4.1 Existing FRET based E-Cad tension sensors do not reveal any differences in junctional tension between NCCs and OCCs

To investigate if the described changes in Myo II and AJ organization in the context of germline surface area expansion, influence and reflect the tensile stress that is experienced at

## RESULTS

the AJs during stages 6 to 10, we wanted to measure tensile forces. We first attempted to do this using a FRET based tension sensor in DE-Cad previously employed to measure forces during border cell migration (Cai, Chen et al. 2014) (Figure 19A-A'). FRET efficiency (E) and lifetime of the FRET donor fluorophore are related inversely by  $E=1- \tau_{DA}/ \tau_D$ , where  $\tau_{DA}$  is the lifetime of the FRET donor when it is near a FRET acceptor and  $\tau_D$  is the lifetime of the donor in the absence of a FRET acceptor. It is more accurate to measure fluorescence life-times rather than FRET efficiencies from fluorescence intensities as used previously (Cai, Chen et al. 2014). However, upon performing a life-time analysis, we could not reproduce the differences in the FRET efficiencies for a tension-sensor and a negative control sensor unable to 'see' forces described previously for DE-Cad based structures in migrating border cells (Figure 19B-B'). Previously, the lifetime of the FRET donor mTFP used in the DE-Cad sensor was calculated to be 2.6 ns in the absence of a FRET acceptor (Day, Booker et al. 2008). The reported values in this study, for both the tension-sensor and the tension-less negative control sensor are lower and not statistically different from each other. Accordingly, we could measure no life time differences of tension-sensor when we compared FCE junctions at NCC and OCC positions (Figure 19C-C'). This could be due to the lack of sensitivity of the tension sensor to the tensile force range of the junctions or intermolecular FRET from crowded molecular organization of the junctions. Other recently published studies have identified the drawbacks in employing this method for tensile force measurements *in vivo* (Cost, Ringer et al. 2015, Eder, Basler et al. 2017). Amongst several controls and tests described in these references to optimize the use of a FRET based tension sensor, we need tension sensors in different force ranges to be certain about the lack of sensitivity of the existent ones. This was beyond the scope of this thesis and we had to employ other methods of measuring tensile forces acting on AJs during germline surface area expansion.

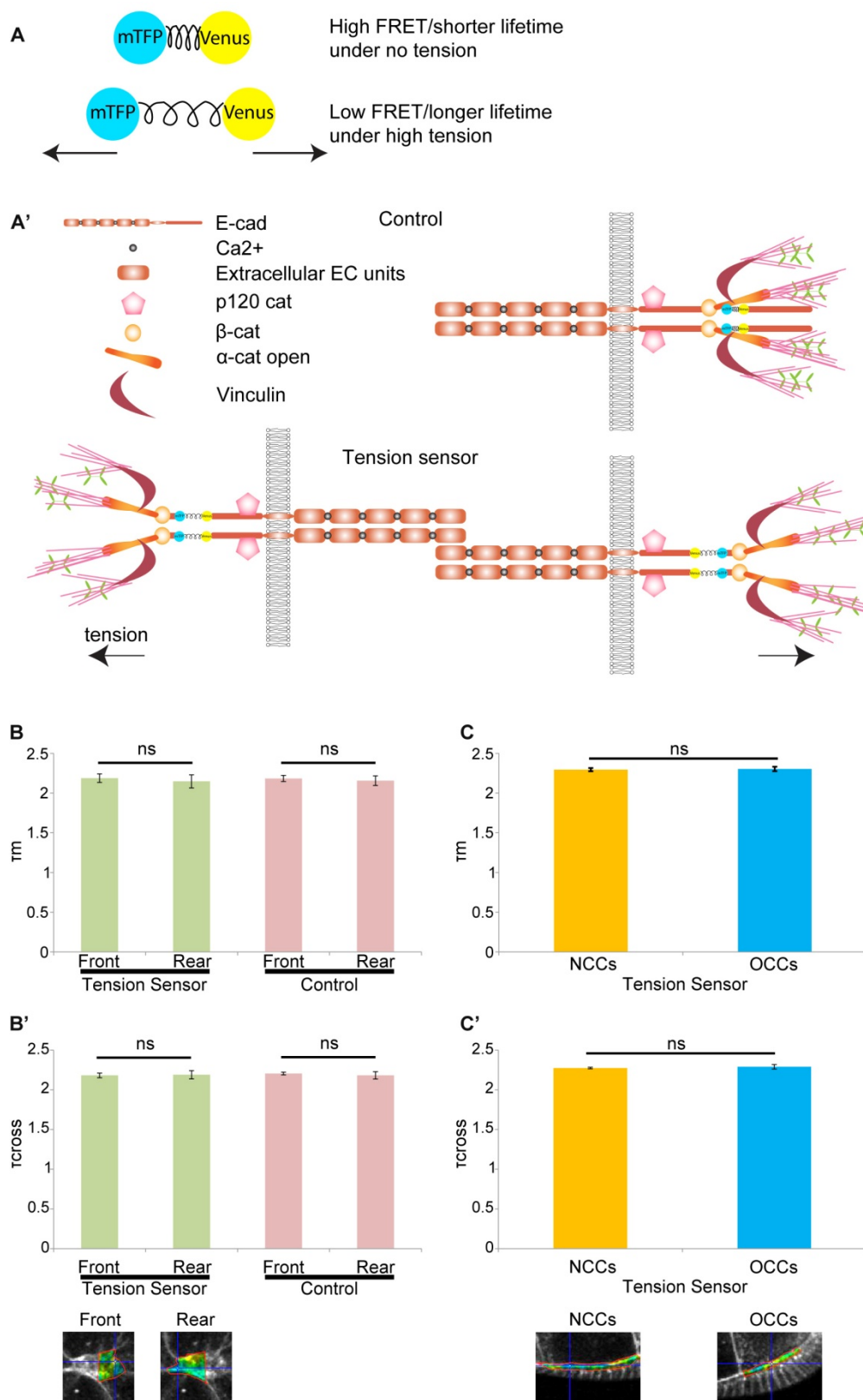


**Figure 19** Fluorescence life-time analysis using a DE-Cad FRET based tension sensor does not reveal differences in tension in the junctions of NCCs and OCCs

(A-A') Schematic representation of the FRET based tension sensor (A) and its integration into the DE-Cad intracellular domain at the end of its cytoplasmic tail to be used as a tension-less control or before the force-bearing modules to be used as a tension sensor (A'). Schemes

## RESULTS

adapted from (Cai, Chen et al. 2014). **(B-C')** Bar plots show the lifetimes of mTFP  $\tau_m$  (B, C) and  $\tau_{\text{cross}}$  (B', C') of the border cell cluster front and rear (B-B'), NCC and OCC junctions (C-C') with the tension sensor (n=7, 11) in (B-B', C-C' respectively) and tension-less control (n=5) in (B-B'). Details of quantifications in section 6.5.3 and Table 20, Table 21. Images under the plots show representative ROIs (red outlines, colored interior) chosen for the front and rear in the border cell cluster and NCC and OCC junctions respectively.

### 3.4.2 Laser ablation experiments reveal differences in tensile forces on adherens junctions during stages 6 to 10

Next, we performed laser ablation of AJs and the apico-medial cortex to measure tensile stress on the apical surface of the epithelium which contacts the growing germline. In laser ablation experiments, a high-power laser is used to ablate a region in the cell. If this region is under tensile stress, the magnitude of initial recoil velocity post-cut is directly proportional to the net force and the stiffness of the junctions (Davidson 2011, Sugimura, Lenne et al. 2016).

We first wanted to identify differences in the tensile stress on junctions between stages 6 and 9 correlating with the shift in Myo II localization and onset of corrugations. When we performed circular cuts in the apico-medial cortex in the egg chambers at stage 6 and 9, we did not find any differences in initial recoil velocities. Similar recoil velocities at stage 6 and 9 upon cortical ablation suggest that tensile stress loaded on the apical surface is similar despite the change in apico-medial Myo II localization (Figure 20A, E). However, when we performed linear cuts through AJs, we found that the initial recoil velocity is higher for junctions at stage 6 if compared to junctions of all columnar-fated cells at stage 9 (Figure 20B, F). Contrary to the expectation that stretching forces on epithelial cells increase as the germline grows in volume and surface area, which would place the junctions under higher tension, we observe that the tension on AJs is decreasing between stage 6 and 9. This suggests that all follicle cells are initiating a mechanism to reduce the overall tensile stress on the epithelium when the germline is growing.

Biologically, differences in AJ tension between stage 6 and 9 can be explained by differences in external forces acting on the junctions, differences in internal resistive contractile forces or by differences in dissipation of stress via addition of material to the junctions. These possibilities align with the exclusion of Myo II from the AJs and increasing AJ length at stage 9 which potentially enables the cells to decrease the internal contractile forces that resist expansion of the germline. By decreasing the AJ tension as the germline surface expands, the follicle cells are becoming more suitable to adapt their surface area to that of the growing germline.

The decrease in AJ tension throughout the epithelium between stages 6 and 9, however, does not explain the presence of cuboidal and columnar cells and transition from cuboidal to columnar cell shapes between stages 6 and 9. We thus compared the apico-medial cortical tension and junctional tension between NCCs and OCCs at stage 9. We observed that there was no difference in the recoil velocities of the cortical cuts, whereas recoil velocities after cuts through AJs were higher in NCCs than OCCs (Figure 20C-F). Importantly, higher tension in AJs of NCCs aligns with higher levels of Myo II in the apico-medial cortex of NCCs if compared to OCCs. This suggests that although Myo II is excluded from the junctions into the apico-medial cortex, it remains tethered to the junctions.

Combined, these observations demonstrate that Myo II exclusion from AJs potentially facilitates a decrease in total tensile stress on the AJs and promotes expansion of the apical surface of columnar-fated cells to match the surface area of the growing germline. However, higher tension on NCC AJs if compared to OCC AJs suggest that a nurse cell contact specific increase in levels of Myo II and adhesion proteins reinforces AJs against external forces from the germline and surprisingly, this correlates with cuboidal shape. Conversely, relatively low AJ tension in OCC correlates with lower levels of Myo II, adhesion proteins and the appearance of columnar shape.

## RESULTS

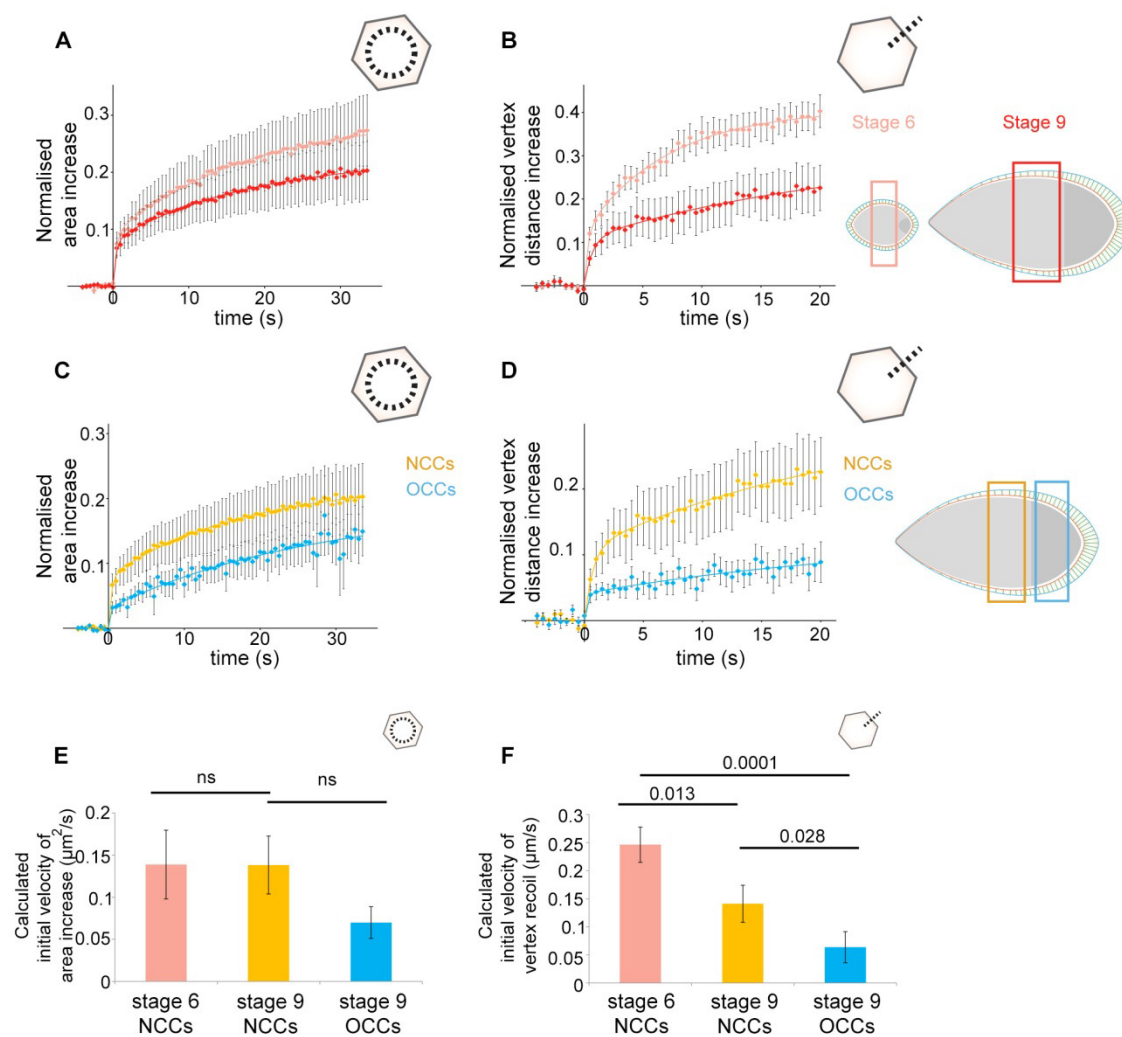


**Figure 20 Laser ablation analysis of junctions and medial cortices in FCE**

(A, C) Graphs display the normalized average apical cell area increase upon laser ablation of the apical-medial cortex as a function of time relative to ablation (pre-ablation  $t=-4\text{s}$  to  $0\text{s}$  and post-ablation  $t=0.5\text{s}$  onwards). Individual data points display  $\text{mean} \pm \text{SEM}$ . The solid lines in the graphs represent a double exponential fit applied to the curves. Parameter estimation and goodness of fit are described in Table 29. Stage 6 (pink,  $n=10$ ), stage 9 (red,  $n=10$ ), NCC (orange,  $n=9$ ), OCC (blue,  $n=9$ ). (B, D) Graphs display the normalized average increase in distance  $\pm \text{SEM}$  and a double exponential fit between vertices upon laser ablation of AJs ( $t=0$ ) as a function of time. Stage 6 (pink,  $n=10$ ), stage 9 (red,  $n=10$ ), stage 11 (brown,  $n=8$ ), NCC (orange,  $n=10$ ), OCC (blue,  $n=10$ ). Cellular and egg chambers schemes illustrate position of laser cuts (black dotted lines). (E, F) Calculated initial velocity of normalized apical cell area increase (E) and initial recoil velocity of vertices (F) at stage 6 NCCs (pink), stage 9 NCCs (orange) or stage 9 OCCs (blue). Graphs display  $\text{mean} \pm \text{SEM}$ . Two-sample t-test was performed. Details of quantifications and analysis in section 6.5.4 and Table 16-18.

### 3.5 Reduction of Myosin and AJs sensitizes the NCCs to greater shape deformation than OCCs

#### 3.5.1 Reduction of Myo II and its upstream activator deforms NCCs more than OCCs

Since the cuboidal cells in stage 9 have higher junctional tension if compared to columnar cells, we wondered how Myo II acts to maintain cuboidal cell shape. To test the role of Myo-II in the maintenance of follicle cell shapes, we performed an RNAi mediated knockdown of an upstream regulator of MRLC, *rok* (Figure 21A). When the entire epithelium has reduced expression of *rok*, NCCs flatten out much more than OCCs at stages 6-9 if compared to WT NCCs and OCCs respectively (Figure 22A-D''', quantifications in Figure 26G-H'). This observation could be further validated by analysis of the hypomorphic MRLC allele *sqhl* and follicle cell specific expression of RNAi targeting MRLC (Figure 22 E-I', Figure 23A-H'). This suggests that NCCs are more sensitive to the loss of Myo II if compared to OCCs. This phenotype aligns with the observation of higher levels of Myo II in the NCC cortex and higher tension on NCC junctions if compared to the OCCs. Importantly, it also suggests that reducing total levels of Myo II is not sufficient to interfere with columnarisation of OCCs. Moreover, as the oocyte grows and meets NCCs, no history of flattening of former NCCs, now OCCs, is ever visible. This implies that flattening of NCCs is reversible when they come into contact with the oocyte. Thus, Myo II is neither needed for columnarisation of the OCCs nor for the recovery of columnar shapes from flattened NCCs. Instead it prevents the over-expansion of the NCCs and stabilizes cuboidal shape aspect ratios. This also implies that columnar OCC shape is acquired by relaxing tensile stress loaded on the junctions when the cells are NCCs.

We next examined the phenotypes upon genetic manipulation of AJ proteins. Mosaic FCE clones of a null allele of DE-Cad (*shg*), did not give rise to 3-D cell shape defects (Figure 24A-F'). The lack of a discernable shape phenotype is most likely due to upregulation of N-Cad compensating for the loss of DE-Cad, as described previously (Figure 24D-F') (Loyer, Kolotuev et al. 2015). Thus, we analyzed mosaic clones of  $\beta$ -cat or expressed an RNAi construct targeting  $\alpha$ -cat in the FCE, which would disrupt both DE-Cad and N-Cad mediated adhesion at AJs (Figure 21B) (Brasch, Harrison et al. 2012, Takeichi 2014, Roper 2015). In both cases, the shape of NCCs was strongly affected. NCCs flattened with dome-shaped apical surfaces, but posterior-most OCCs over the oocyte were columnar (Figure 23I-L', Figure 24G-L'). At later stages, when misshaped NCCs had come into contact with the oocyte, partial recovery of their columnar heights was observed (Figure 23K-N'). The poorer recovery of columnar shape of NCCs which become OCCs as the oocyte grows underneath them indicates

## RESULTS

the detrimental effect of losing the ability to sense mechanical coupling when functional AJs are lost compared to when only contractility is reduced using *rok* RNAi. NCCs with loss of adhesion have disrupted relaxation of tensile stress on junctions as the oocyte encounters them. In contrast, posterior-most OCCs which never touched nurse cells columnarize normally. This suggests that columnarisation is not dependent on maintenance of AJs when the follicle cells have never seen nurse cells. However, AJs are important for cells which previously were in contact with the nurse cells and now contact the oocyte. As proper epithelial polarity is needed for AJ formation and apical actomyosin (Tepass 2012), we found that the FCE specific expression of RNAi targeting apical polarity proteins like *aPKC* and *crb*, gave rise to flattening NCC phenotypes suggesting that the apical surface is essential for maintaining the cuboidal aspect ratio of NCCs (Figure 24M-P').

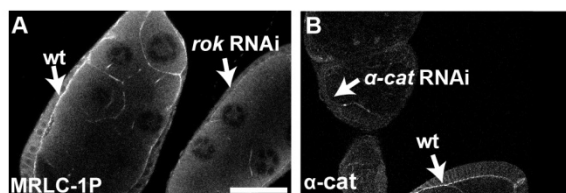


**Figure 21 RNAi efficiency tested with antibodies**

(A-B) Medial sections of egg chambers of wt or follicle cell specific expression of *rok* RNAi (A), *α-cat* RNAi (B) genotypes indicated by white arrows showing reduction in MRLC-1P (A) and  $\alpha$ -cat (B). Scale bar = 100 $\mu$ m. (B) Image taken by AKC.

In addition to the change in aspect ratio of Myo II and *rok* deficient NCCs through apical surface area expansion, these NCCs also present with a loss of corrugations and hence straighter AJs (Figure 22B, D, H). This indicates that contractile cortical network maintains AJs in a corrugated state. The loss of corrugations upon apical surface expansion further implies that corrugations potentially serve as a reservoir of AJs material that allows cells to expand their surface area in response to external germline forces.

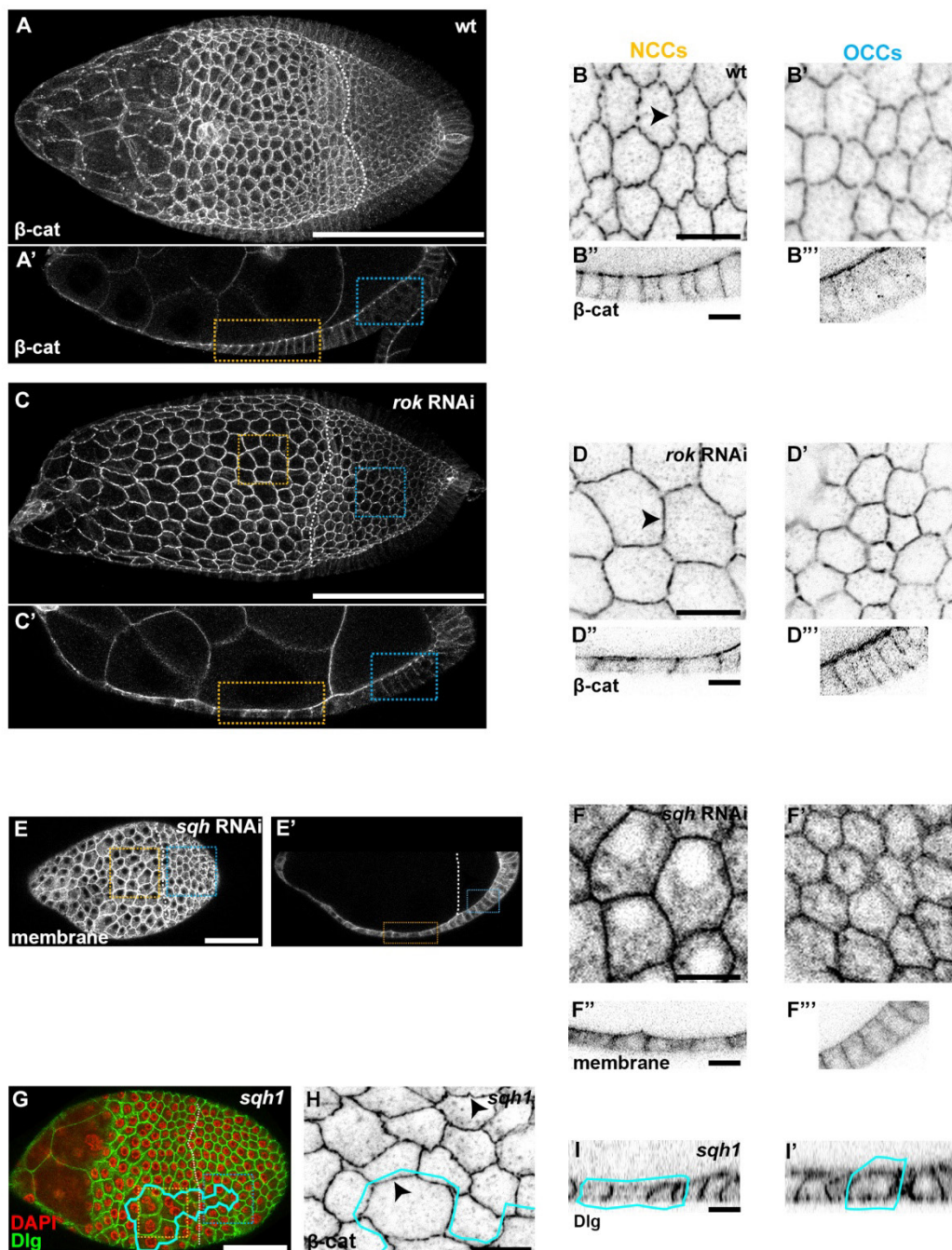


**Figure 22 Regulators of actomyosin contractility are required to prevent NCC flattening**

(A-I') Maximum projections for *en face* view of AJs (A, B-B', C, D-D', E, F-F', G, H) and medial sections (A', B''-B''', C', D''-D''', E', F''-F''', I-I') of wild type egg chambers (A-B''') or those with epithelial expression of Rok (*rok* RNAi (C-D'''), MRLC (*sqh* RNAi (E-F''') or mosaic clones of MRLC hypomorph (*sqh1*) (G-I') stained for  $\beta$ -cat, membrane marker or Dlg. Yellow (NCC) and blue (OCC) frames in (A-A', C-C', E-E', G) are magnified to visualize apical cell areas in (B-B', D-D', F-F') and cell heights in (B''- B''', D''-D''', F''-F''', I-I'). Black arrowheads (B, D and H) indicate corrugations in wild type, reduced corrugations in *rok* RNAi and *sqh1* NCCs. Cyan lines outline homozygous clones for the respective mutants. Cell areas and heights of mosaics clones should be compared with the neighboring cells outside the cyan outlines. Scale bar A-A', C-C' = 100  $\mu$ m, E-E', G = 50  $\mu$ m and B-B''', D-D''', F-F''', H-I' = 10  $\mu$ m. Images for *sqh* RNAi taken by Caroline Sønsteby.

## RESULTS

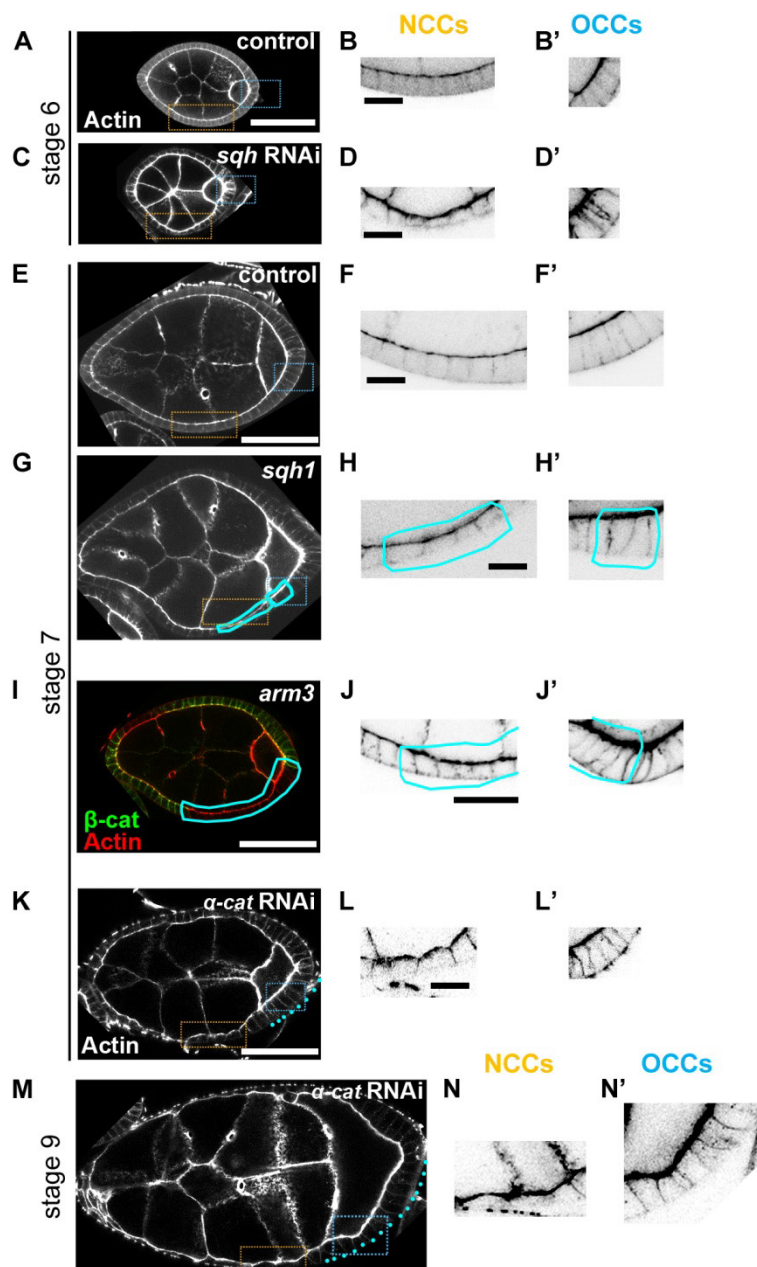


**Figure 23** NCCs are more sensitive to deformations when contractility or AJs are perturbed between stage 6 to 10

(A-N') Medial sections of wild type stage 6 (A-B') and stage 7 (E-F') egg chambers and those with epithelial expression of *sqh* RNAi (C-D'),  $\alpha$ -*cat* RNAi (K-N') or mosaic clones of *sqh*<sup>1</sup> (G-H') and  $\beta$ -*cat* (*arm*<sup>3</sup>) (I-J') at stages 6,7 or 9. Egg chambers were stained for F-actin (grey in A-H', J-N', red in I) or  $\beta$ -cat (green in I). Regions framed by orange (NCC) and blue (OCC) boxes in (A, C, E, G, K) are shown at higher magnification on the right. Cell heights should be compared with those of wild type cells in (B-B', F-F'). Cyan dots in (K, M) represent the number of epithelial cells in contact with the oocyte at stage 7 (K, 8 OCCs) or 9 (M, 15 OCCs). Excessive flattening of many mutant NCCs is reversible, mutant cells columnarize once they encounter the expanding oocyte at later stages. Scale bar (A, C, E, G, I, K, M) = 50  $\mu$ m, (B-B', D-D', F-F', H-H', J-J', L-L') = 10  $\mu$ m. *sqh* RNAi images taken by Caroline Sønsteby.

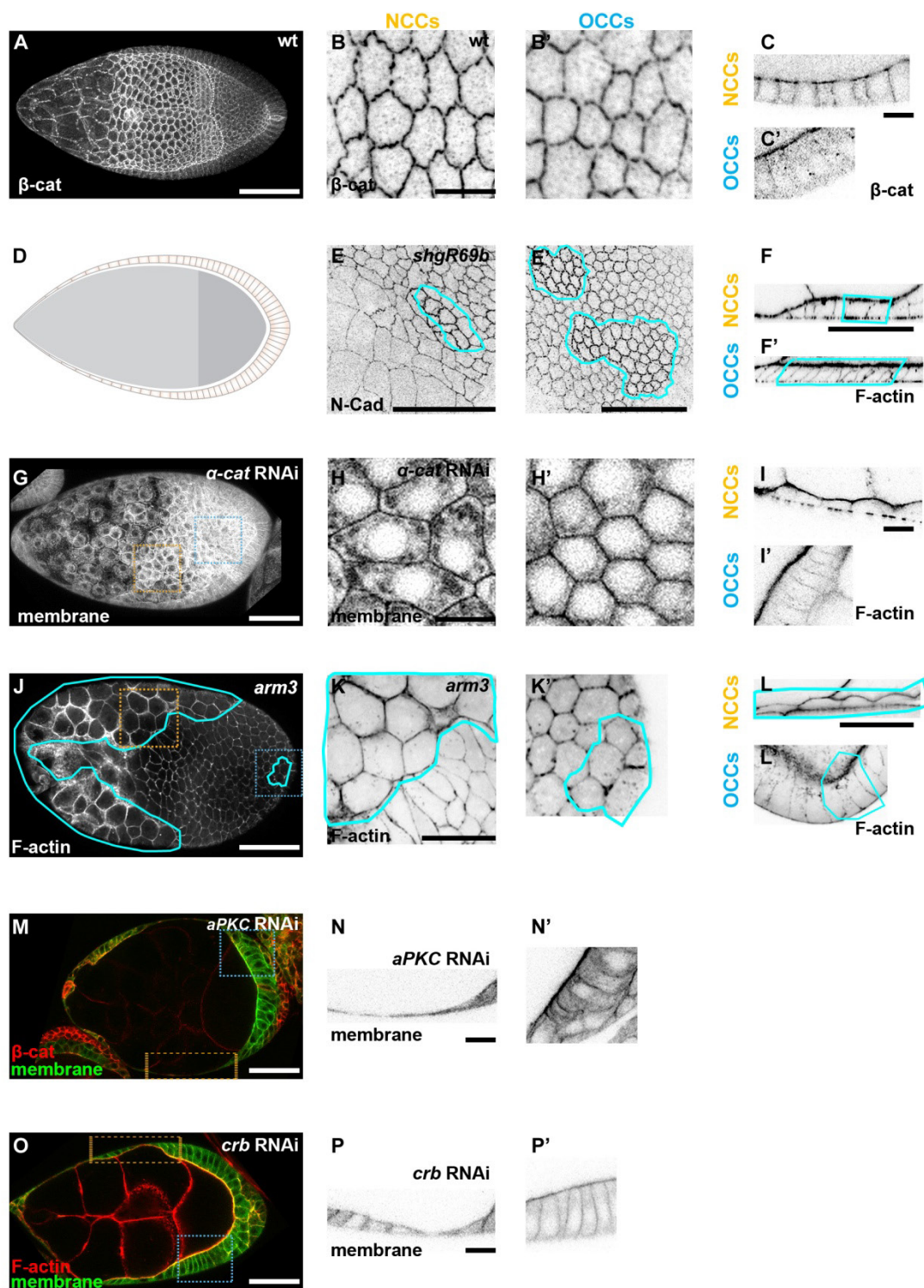


**Figure 24** Junctional catenins and apical polarity factors are required to prevent NCC flattening

(A-P') Maximum projections for *en face* view of AJs (A, B-B', E-E', G, H-H', J, K-K') and medial sections (C-C', F-F', I-I', L-L', M-P') of wild type egg chambers or those with FCE expression of *α-cat* RNAi, mosaic clones of *arm3*, *aPKC* RNAi and *crb* RNAi stained for  $\beta$ -cat, plasma membrane or F-actin. Orange (NCC) and blue (OCC) frames (G, J, M, O) are magnified to visualize apical cell areas (B-B', E-E', H-H', K-K') and cell heights (C-C', F-F', I-I', L-L', N-N', P-P'). Cyan lines outline homozygous clones for the respective mutants. Cell areas and heights of mosaic clones should be compared with the neighboring cells outside the cyan outlines. Scale bar A, E-F', G, J, M, O = 50  $\mu$ m and 10  $\mu$ m for all other panels.

## RESULTS

### 3.5.2 Increasing corrugations in AJs promotes NCC shape deformation

Next, we wondered if corrugations and the decrease in tension on AJs from stage 6 to 9 are initiated by the exclusion of Myo II from AJs and its enrichment into the apico-medial cortex. Previous reports have shown that Canoe (*cno*, Afadin in mammals) is an important coupler of the actomyosin cortex to the adherens junctions (Sawyer, Choi et al. 2011). Promisingly, we observed that Cno localizes to the AJs at stage 6, and is progressively lost from junctions by stage 9, correlating with a shift in Myo II localization from junctions to the apico-medial cortex (Figure 25A, B). However, overexpression of Cno did not recruit the apical-medial ring-like cortex of Myo II back to AJs (Figure 25C, D). Therefore, absence of Cno is not sufficient to explain exclusion of Myo II from the junctions. Thus, it could not be tested if Myo II shift initiates onset of corrugations, but only that Myo II is required to maintain them.

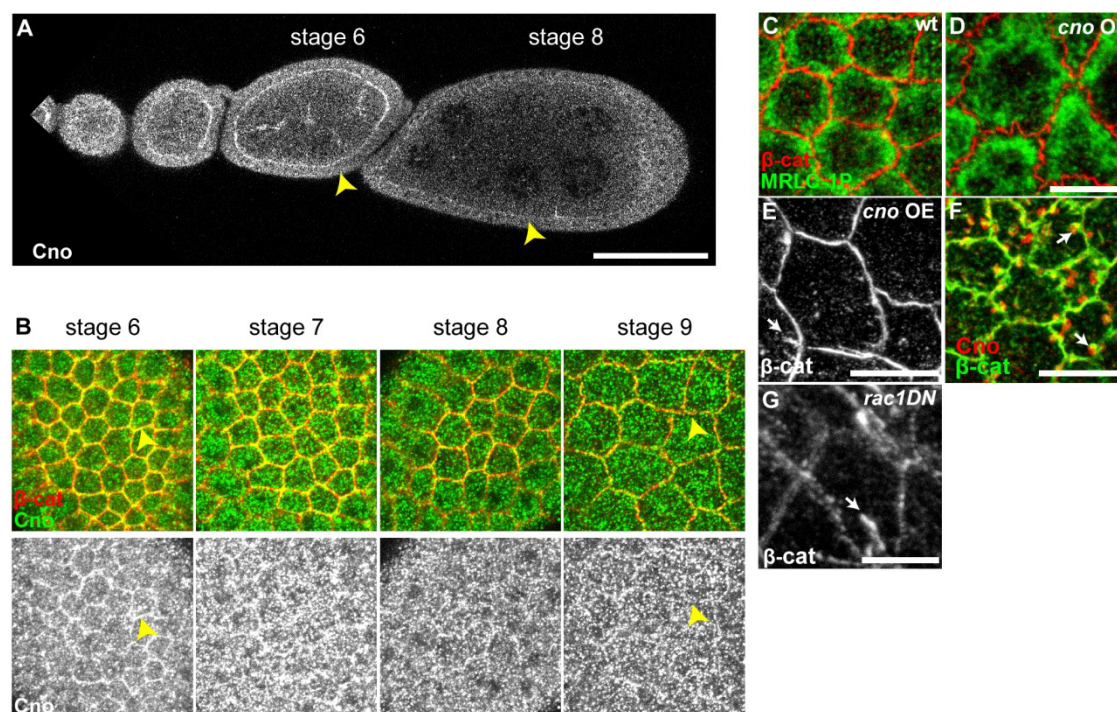


**Figure 25 Canoe overexpression does not relocate excluded Myo II onto the junctions.**

(A) Medial sections of an ovariole with egg chambers from an early stage (only stage 6 and 8 are marked) stained with Cno antibody. Yellow arrowheads point to the loss of FCE signal on their apical surface at stage 8 compared to stage 6. (B) *En face* junctional views of wt egg chambers stained with  $\beta$ -cat (red), Cno (green in top panel, grey in bottom panel). Yellow arrowheads point to the loss of junctional Cno signal at stage 9 compared to stage 6. (C-D) *En face* junctional views of wt (C) and FCE specific overexpression (OE) of Cno (*cno OE*) (D) stained with  $\beta$ -cat (red) and MRLC-1P (green). (E-G) *En face* junctional views of egg chambers with FCE specific expression of *cno* (E, red in F) and dominant negative Rac1 (*Rac1DN*) (F) stained with  $\beta$ -cat. White arrows in E, G point to extensions from junctions reflecting mis-regulated turnover of AJ material and in F point to accumulation of  $\beta$ -cat in vesicle-like structures labelled with Cno. Scale bar A = 100  $\mu$ m, B-G = 10  $\mu$ m.

Interestingly, the Cno over-expressing epithelium also exhibits flattening of NCCs despite the presence of apico-medial Myo II. However, unlike Myo II deficient cells, Cno over-expressing cells do not lose corrugations even upon extensive NCC flattening (Figure 26A-D''', G-H'). This implies that Cno over-expressing cells have extra AJ material that promotes expansion of the apical surface areas of the NCCs. Indeed, Cno over-expressing OCCs, which columnarize normally, display hypercorrugations extending as long folds from AJs into the apical surface of the cells (Figure 26D'). Taken together, Cno overexpression appears to hinder proper turnover of AJs by its presence on junctions instead of recruiting Myo II back to the junctions (Figure 25E, F). We identified an additional molecular regulator of AJs, Rac1, which modified the aspect ratio of NCCs. Like Cno overexpression, expression of a dominant negative Rac1 in the FCE leads to junctional folds and extreme apical expansion of NCCs (Figure 25G, Figure 26E-H'). However, once dominant negative Rac1 NCCs turn into OCCs, they reduce their apical areas and increase in heights like WT cells.

Thus, an absolute increase in adherens junction material is not sufficient to promote expansion of the FCE surface area in response to the growth of the germline, as OCCs acquire columnar shape despite hypercorrugations. We speculate that by altering the levels of AJ material in corrugating junctions, cells can change the extent of response to external forces arising from the germline. This suggests that corrugations may serve as a reservoir of junctional material that promotes apical surface area expansion during stages of germline surface expansion and other forces specifically arising at site of nurse cell contacts.

The selective sensitivity of NCCs to genetic modification of actomyosin contractility and AJ regulation indicates that nurse cell contact derived forces are stronger compared to those exerted by the oocyte. Thus, the higher levels of Myo II and AJ components in NCCs may be required to maintain cuboidal aspect ratio by resisting flattening induced by nurse-cell derived forces. The higher tension of the NCC AJs if compared to OCC AJs, can be explained by a contractile resistance mounted by apico-medial Myo II acting on AJs to prevent excessive expansion of the apical area of the NCCs to nurse cell specific forces. Conversely, lower AJ tension, lower levels of Myo II and AJ proteins in the OCCs and the lower sensitivity to deformation upon loss of Myo II and AJ suggest that OCCs are not seeing as much oocyte-derived forces as the NCCs from nurse cells.

## RESULTS

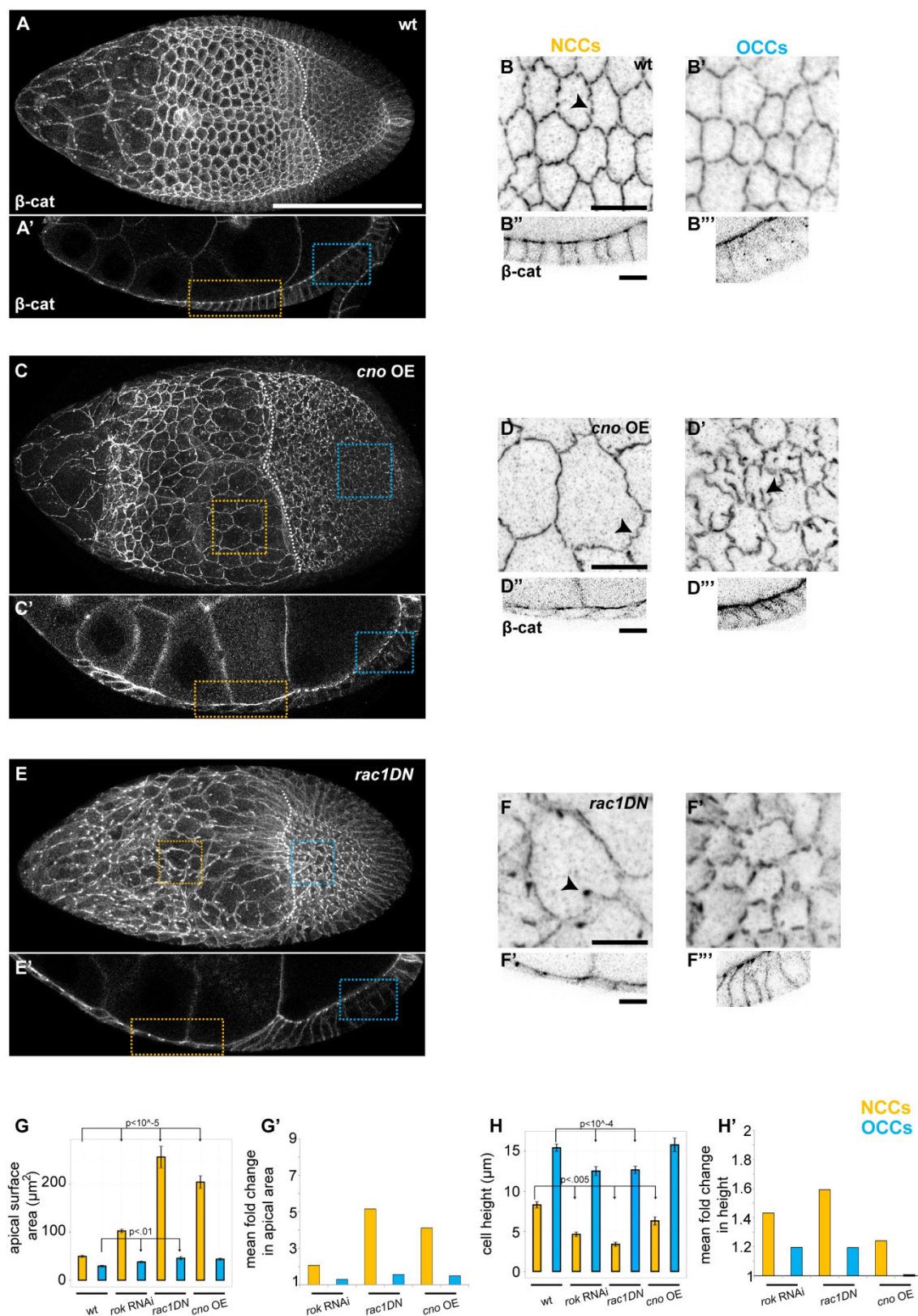


**Figure 26** Increasing junctional corrugations specifically promotes NCC flattening

**(A-F'')** Maximum projections for *en face* view of AJs (A, B-B', C, D-D', E, F-F') and medial sections (A', B''-B''', C', D''-D''', E', F''-F''') of wild type egg chambers or those with FCE expression of *cnoOE* and *Rac1DN* stained for  $\beta$ -cat. Yellow (NCC) and blue (OCC) frames (A-A', C-C', E-E') are magnified to visualize apical cell areas (B-B', D-D', F-F') and cell heights (B''-B''', D''-D''', F''-F'''). Black arrowheads (B, D-D', F) indicate corrugations in wild type,

hypercorrugations in *cno* OE and *Rac1 DN* NCCs. (G-H') Mean apical areas (G), cell heights (H)  $\pm$  SEM and fold area change (G') or fold height change (H') relative to wild type for NCCs (yellow) and OCCs (blue) upon *rok* RNAi, *Rac1DN* and *cnoOE* in the epithelium. See Table 12 and Table 13 for quantification and sample sizes. WMW-tests were performed. Scale bar (A-A', C-C', E-E') = 100 $\mu$ m, 10 $\mu$ m for all other panels. *Rac1DN* images taken by VW.

## 3.6 Organ level consequences of NCC shape deformation

### 3.6.1 NCC-OCC transitions are delayed upon aberrant NCC flattening

Next, we wanted to assess the organ level consequences of excessive NCC flattening upon reducing contractility or increasing junctional material. Upon analyzing the fate of *sqh* RNAi, *rok* RNAi, *cnoOE* or *Rac1DN* expressing egg chambers, we observed that *cnoOE* and *Rac1DN* expressing egg chambers display the germline sizes of stage 10 egg chambers, while NCCs are still contacting nurse cells (Figure 27A-C, I). This is further confirmed by measuring the nurse cell to oocyte area ratios of morphological stage 9 of *cno*, *rok* and *sqh* expressing egg chambers, which are closer to stage 10 wildtype ratios (Figure 27J).

This suggests that completion of NCC cell shape transition is delayed while the germline continues to grow in volume, due to the disruption of NCC contractility and junctional length. Completion of cell shape transitions is achieved when all NCCs contact the oocyte as the oocyte expands underneath them. A delay in NCCs coming into contact with the oocyte occurs when NCCs flatten excessively, shifting their relative positions anteriorly, away from the oocyte. The failure to complete the positioning of NCCs over the oocyte causes columnar-fated cells to still be positioned over the nurse cells reminiscent of stage 9 shape gradient even as the germline continues to growth and attain stage 10A sizes. This ultimately leads to degeneration of egg chambers when they reach sizes larger than stage 9 (Figure 27D-H). Combined, these observations indicate that NCC contractility and tightly regulated levels of AJ material serve to maintain a fixed relative position of NCCs with respect to all columnar fated cells to ensure their final positioning over the expanding oocyte. Furthermore, the delay in completion of cell shape transitions due to flattening NCCs reveals functional importance of maintenance of cuboidal shape.

## RESULTS

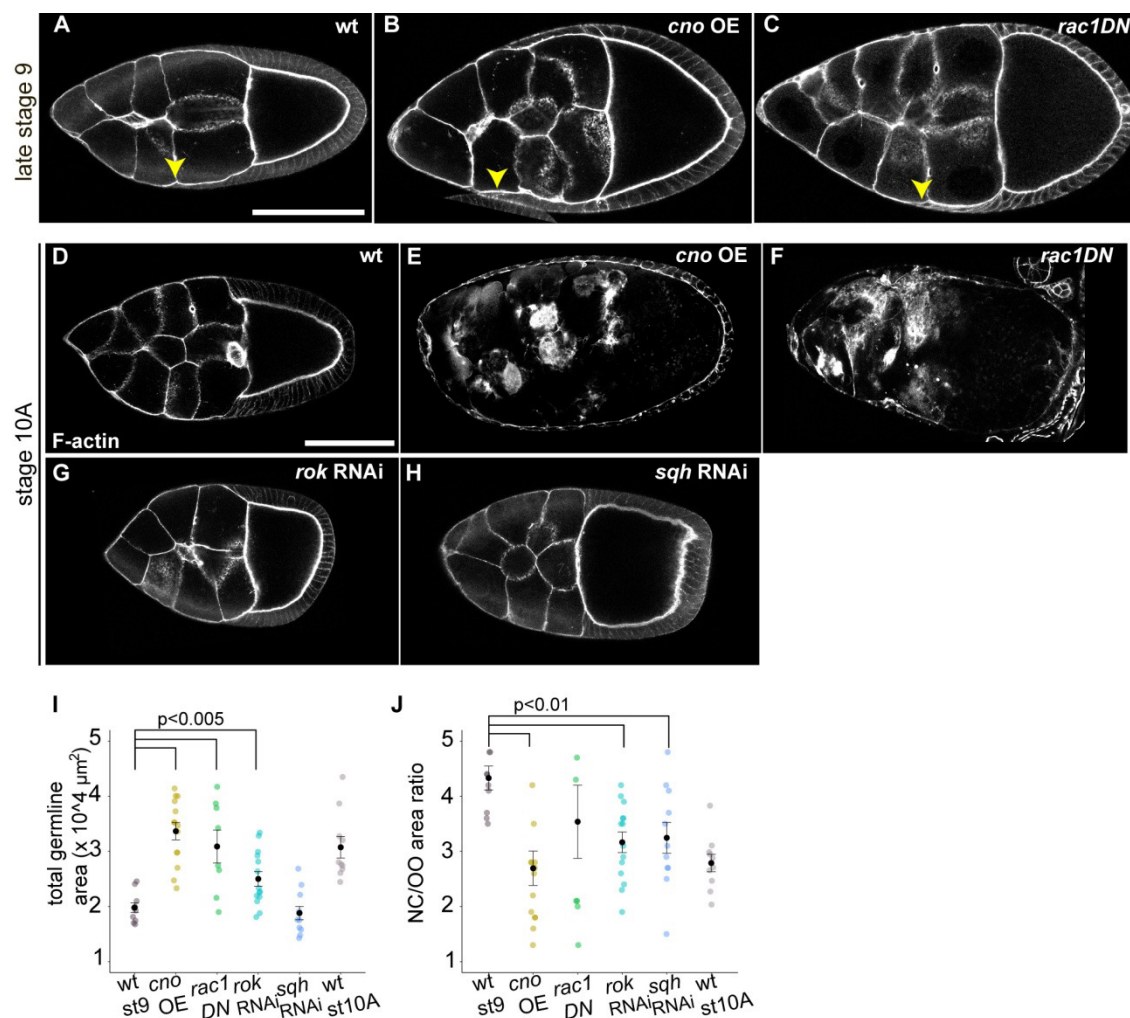


**Figure 27 Organ-level consequences of NCC flattening on disruption of contractility and AJ regulators**

(A-C) Medial sections of morphological late stage 9 egg chambers, either wild type (A) or with epithelial expression of *cno*OE (B) or *Rac1DN* (C). Yellow arrowheads point to most anterior NCCs. (D-H) Medial sections of a stage 10A wild type egg chamber (D) or degenerating egg chambers with epithelial expression of *cno* (E) or *Rac1DN* (F) or normally developing stage 10A egg chamber with epithelial expression of *rok* RNAi (G) or *sqh* RNAi (H) stained for F-actin. (I, J) Total germline area (I) or nurse cell-to-oocyte area ratios (J) in medial sections of wild type egg chambers (wt, stage 9 or 10A) or with epithelial expression of *cno*OE, *Rac1DN*, *rok* RNAi or *sqh* RNAi.  $n \geq 8$  egg chambers for all conditions. Scale bar = 100  $\mu$ m. (I-J) quantifications done by AKC. WMW-tests were performed. Quantifications in Table 23 and Table 24.

### 3.6.2 Anterior expansion of the oocyte is delayed at tears in NCC

We wondered if the anterior membrane of the oocyte was interacting with the apical surface of the NCCs during anteriorly directed oocyte growth. This idea was very compelling, given that we observed a pronounced enrichment of Crb on the anterior surface of the oocyte forming a gradient to the posterior oocyte pole. Crb is known to promote trans-homophilic interactions and regulate actin and spectrin cytoskeletal network (Figure 28A) (Roper 2012,

Fletcher, Elbediwy et al. 2015). Importantly, Crb localization became enriched on the oocyte anterior membrane from stage 7 onwards and was cytoplasmic prior to this (Figure 28A), thus correlating with increased growth rate of the oocyte from stage 7 onwards if compared to the nurse cell compartment (Kolahi, White et al. 2009). However, the cytoplasm to membrane translocalization of Crb occurred even upon genetic reduction of Crb in the FCE (Figure 28B-C). Interactors of Crb implicated in regulation of cellular mechanics including Actin, Phospho-Moesin,  $\alpha$ -spectrin and  $\beta_H$ -spectrin (Medina, Williams et al. 2002, Bulgakova and Knust 2009), also localized on the oocyte membrane but not Sdt, a canonical binding partner important for cell polarity (Bulgakova and Knust 2009, St Johnston and Sanson 2011) (Figure 29A-D). Thus, Crb was a very alluring candidate to potentially serve as a mechanical transmembrane coupler between NCCs and the anterior oocyte membrane, allowing the oocyte to move anteriorly and displace the contact of nurse cells with the overlying FCE (Figure 29E-E').

## RESULTS

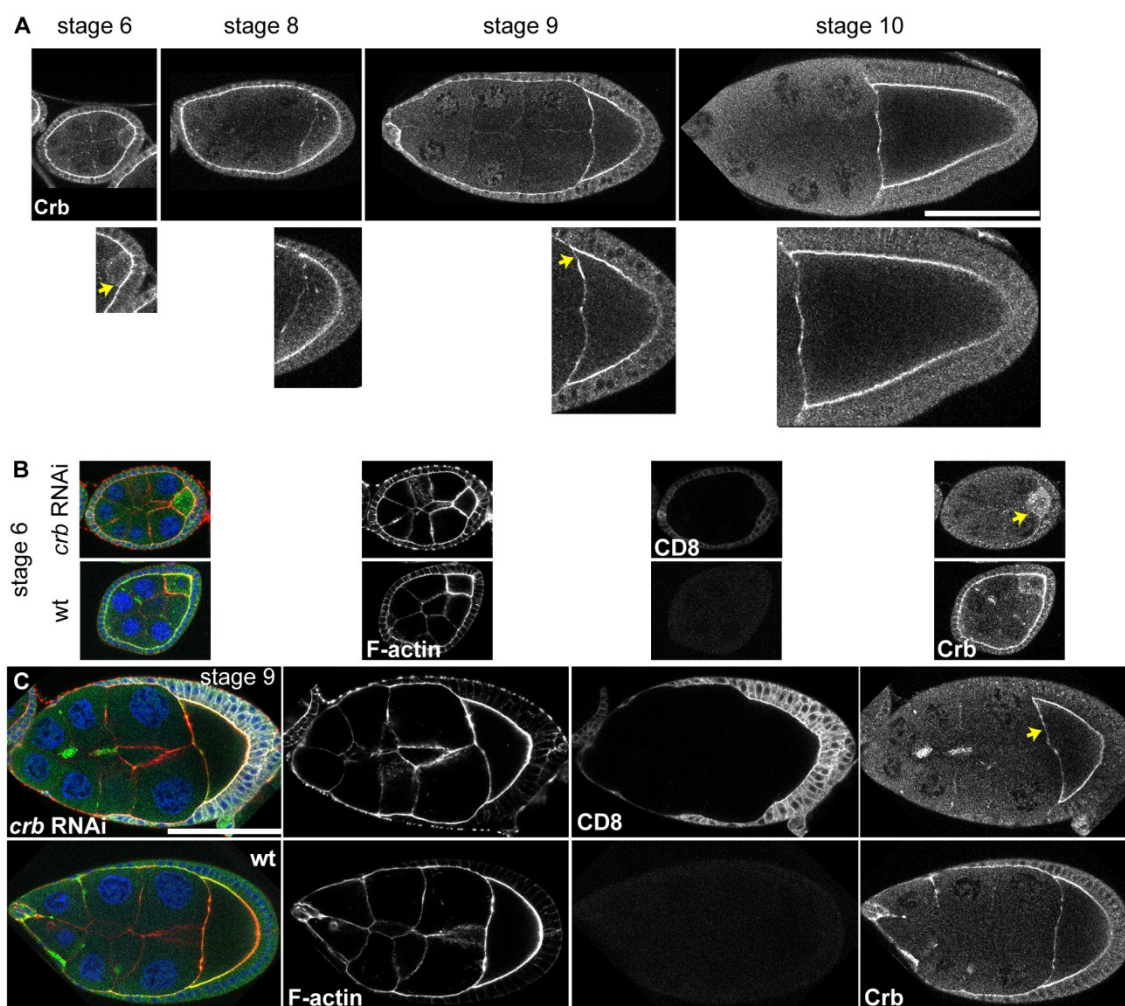


**Figure 28 Crb localisation on the oocyte membrane**

(A) Medial section views of egg chambers stained with Crb and magnified views of oocyte with its Crb localization below. (B-C) Medial sections of egg chambers at stage 6 and 9 with FCE specific expression of Crb (*crb*) RNAi and wt egg chambers. Yellow arrows show the relocalization of cytoplasmic Crb signal at stage 6 in the oocyte onto the surface of the oocyte at stage 9 in both wildtype and *crb* RNAi. Scale bar = 100µm.

To test this hypothesis, we first generated germline *crb* null (*crb11a22*) egg chambers and checked if the oocyte grew to wildtype size. However, we could not observe development of egg chambers beyond stage 8 when the germline was Crb deficient (Figure 30A). Thus, we analyzed a Crb hypomorph allele (*crbD88-3*), Crb ERLI (*crb8F105*, polarity deficient) and Crb FERM (*crbY10A*, mechanical interaction deficient) domain mutants (Klose, Flores-Benitez et al. 2013) as well as expression of *crb* RNAi (not shown) in the germline to check if they revealed a phenotype where anterior expansion of the oocyte was inhibited. Crb ERLI germline mutant egg chambers degenerate at stage 9, but the oocyte appears to have grown as expected (Figure 30B). Additionally, no effect on the anterior expansion of the oocyte was visible in other mutant conditions. Moreover, oocytes in stage 10 egg chambers were comparable in shape and size to wild type egg chambers when they survived (Figure 30C). Taken together, germline

mutants for a null allele of Crb and polarity deficient allele degenerate by stage 9, suggesting a role for Crb in the germline and oocyte development. It is, however, not the hypothesized interactions of the oocyte membrane and the FCE through Crb, since germlines deficient in Crb mechanical interaction domain can grow and complete cell shape transitions.

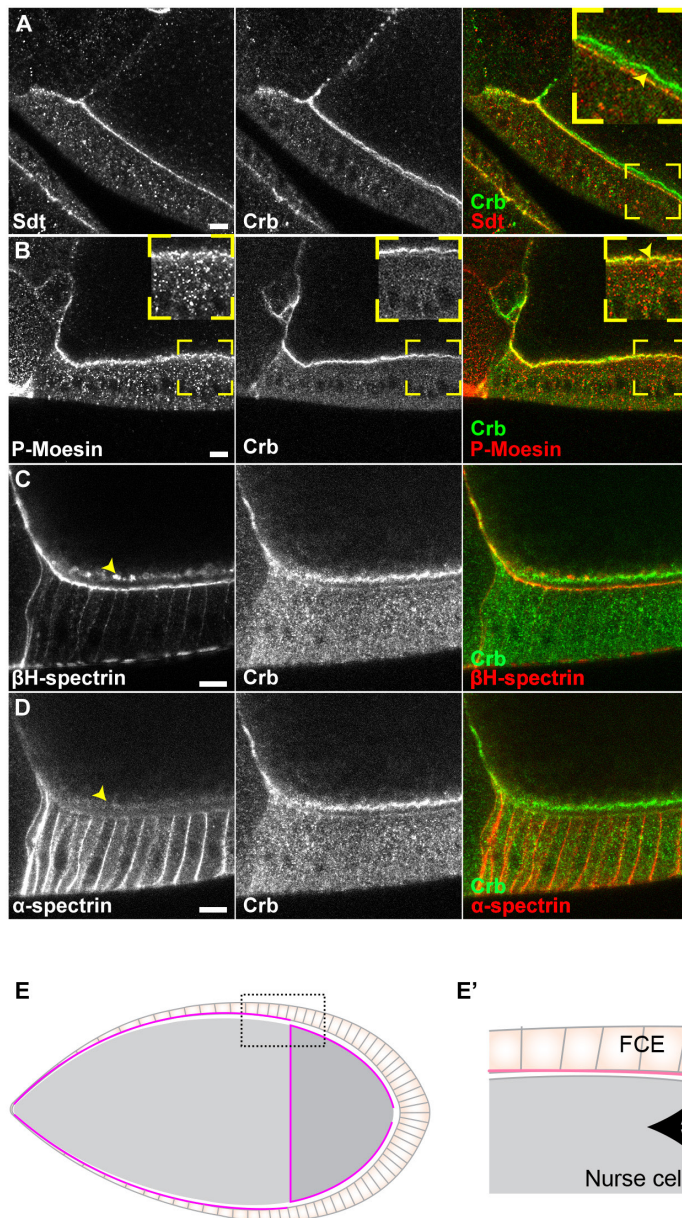


**Figure 29 Localization of Crb and its binding partners on oocyte membrane**

(A) Sdt, a polarity binding partner of Crb is found in the FCE but not on the oocyte membrane (magnified insets). Other binding partners of Crb, Phospho-Moesin (magnified insets) (B),  $\beta$ <sub>H</sub>-spectrin (C) and  $\alpha$ -spectrin (D) are found on the oocyte membrane. Yellow arrowheads point to the oocyte membrane signals. Scale bar = 10  $\mu$ m. (A) images taken by Simone Wendlinger.

## RESULTS

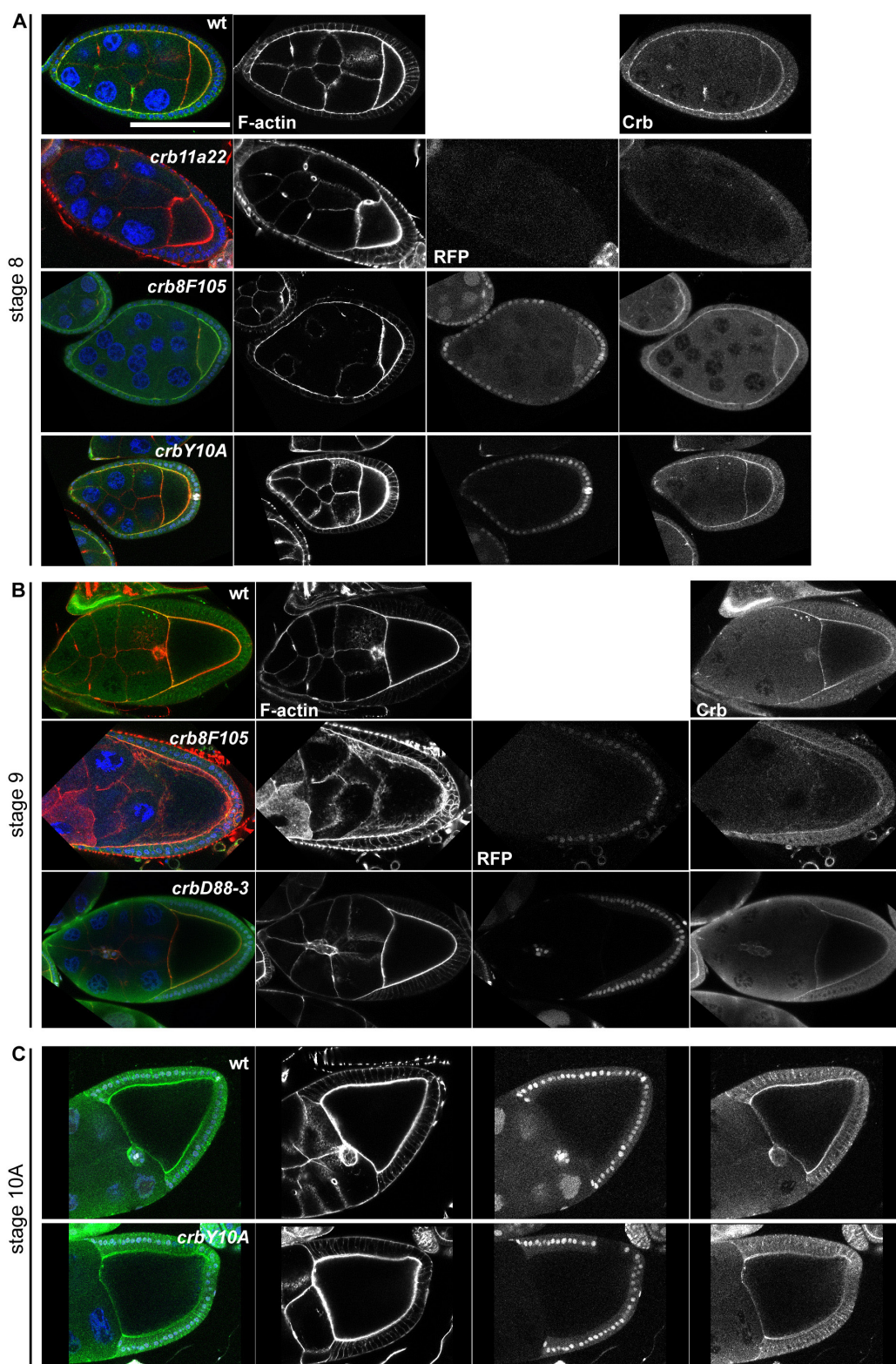


**Figure 30 Crb hypomorph and cytoskeleton-binding domain deficient germline mutants have normal oocyte anterior membrane extension**

(A-C) Medial section of wt, *crb8F105*, *crbY10A* and *crbD88-3* germline mutant egg chambers at stages 8 (A), 9 (B) and 10A (C) stained with Crb, F-actin and labeled with clonal marker RFP. RFP negative nuclei in the germline are homozygous mutants for the above genotypes. Scale bar 100  $\mu$ m.

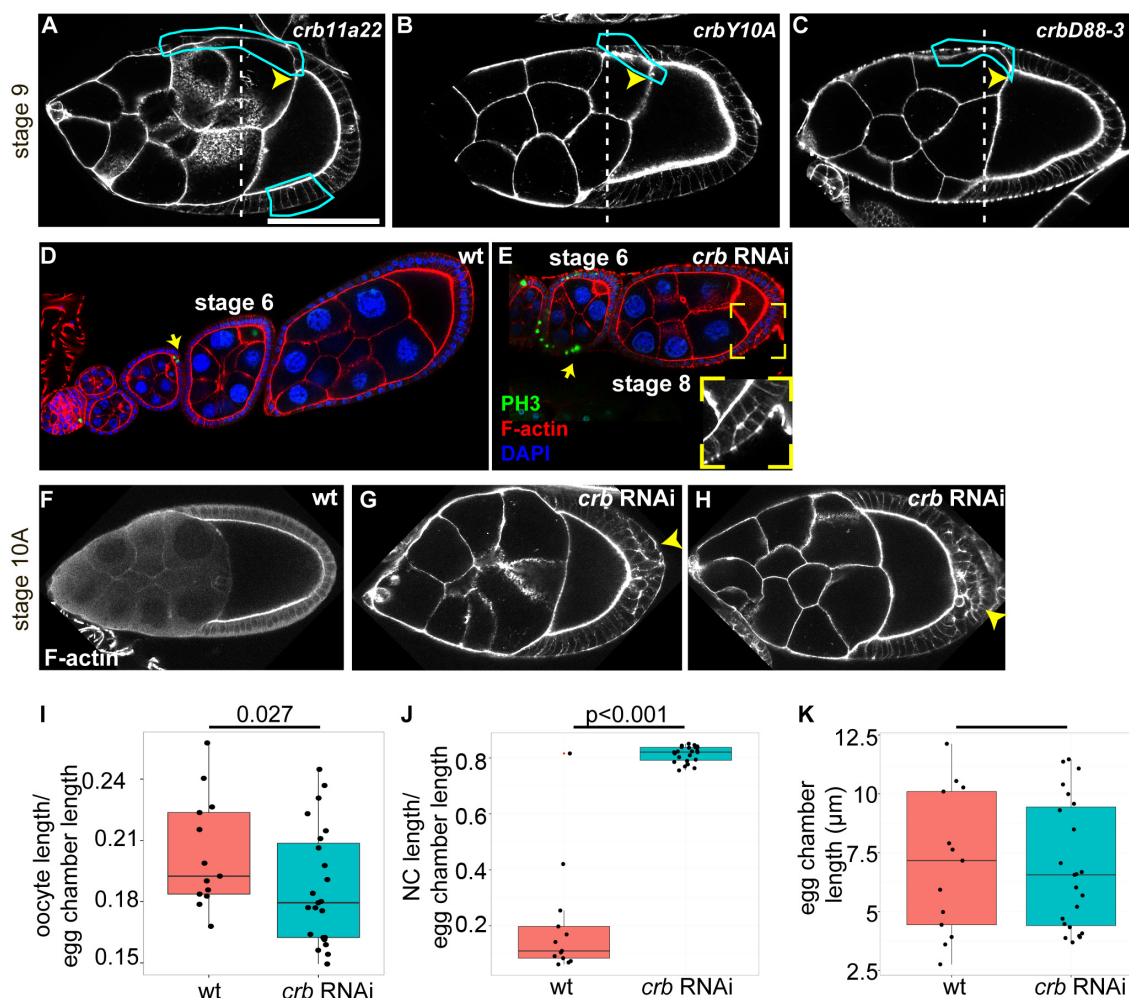


**Figure 31 FCE integrity and number of columnar-fated cells are important for final oocyte size.**

(A-C) Medial sections of *crb11a22*, *crbY10A* and *crbD88-3* mosaic clone egg chambers stained with F-Actin. Yellow arrowheads point to the delayed oocyte anterior membrane where there is an epithelial tear in NCC clones (cyan outlines, compare to equivalent position on the opposite side where NCCs are intact). White dashed line indicates where the oocyte anterior membrane should have been as on the opposite side. (D-E) Medial sections of wt (D) and *crb RNAi* (E) expressing egg chambers show the lack of phospho-histone3 (yellow arrows), a cell division marker after stage 6 in both cases. Yellow bracket is magnified to show multilayering in a stage 8 *crb RNAi* FCE despite the absence of excessive cell divisions. (F-H) Medial sections of stage 10A wildtype (F) and two examples of *crb RNAi* egg chambers (G-H) with smaller oocyte after the completion of cell shape transitions. Yellow arrowheads point to the multilayering in the FCE that decreases the number of cells available for the oocyte to slide under and hence a smaller oocyte. (I-K) Graphs showing the oocyte length ratio to total egg chamber length ratio (I), nurse cell length to total egg chamber length ratio (J) and total egg chamber lengths (K) in wt and FCE expressing *crb RNAi*. Individual data points (n=13 for wt n=21 egg chambers for *crb RNAi*). Box plot with median values are depicted. WMW test was performed. Quantifications in Table 25. Scale bar = 100  $\mu$ m.

Mosaic clones of severe *Crb* alleles in NCCs flattened and upon reaching of limit of flattening displayed discontinuities with the neighboring wildtype cells which we call tears in the epithelium (Figure 31A). Surprisingly, anterior expansion of the oocyte was blocked at the posterior edge of the NCC tear in *Crb* null allele (*crb11a22*), hypomorph allele (*crbD88-3*), and

## RESULTS

Crb FERM (*crbY10A*, mechanical interaction deficient) mosaic clones (Figure 31A-C). As clones for other epithelial regulators such as aPKC (see section 3.7, Figure 33E-E') also caused NCC tearing and stalling of oocyte expansion, we suggest that maintaining an intact epithelium at the nurse cell–oocyte interface is essential for the oocyte to expand properly, rather than specific Crb function in oocyte growth. Interestingly, upon follicle cell specific expression of *crb* RNAi the epithelium remains intact without evidence of NCC tearing. Instead, the epithelium over the oocyte multilayers in the absence of excessive cell divisions, implying the total number of columnar-fated cells that the oocyte contacts are reduced (Figure 31D, E). Indeed, the final size of the oocyte is smaller if compared to wildtype egg chambers (Figure 31F-I), while the nurse cell compartment is larger, and the total germline size is comparable to wildtype egg chambers (Figure 31J-K). This suggests that the growth and final size of the oocyte is tightly dependent not only on the presence of an intact apical surface of the epithelium but also on total number of columnar-fated cells that are available for the oocyte to contact.

### 3.6.3 Summary of consequences of NCC deviation from cuboidal shape

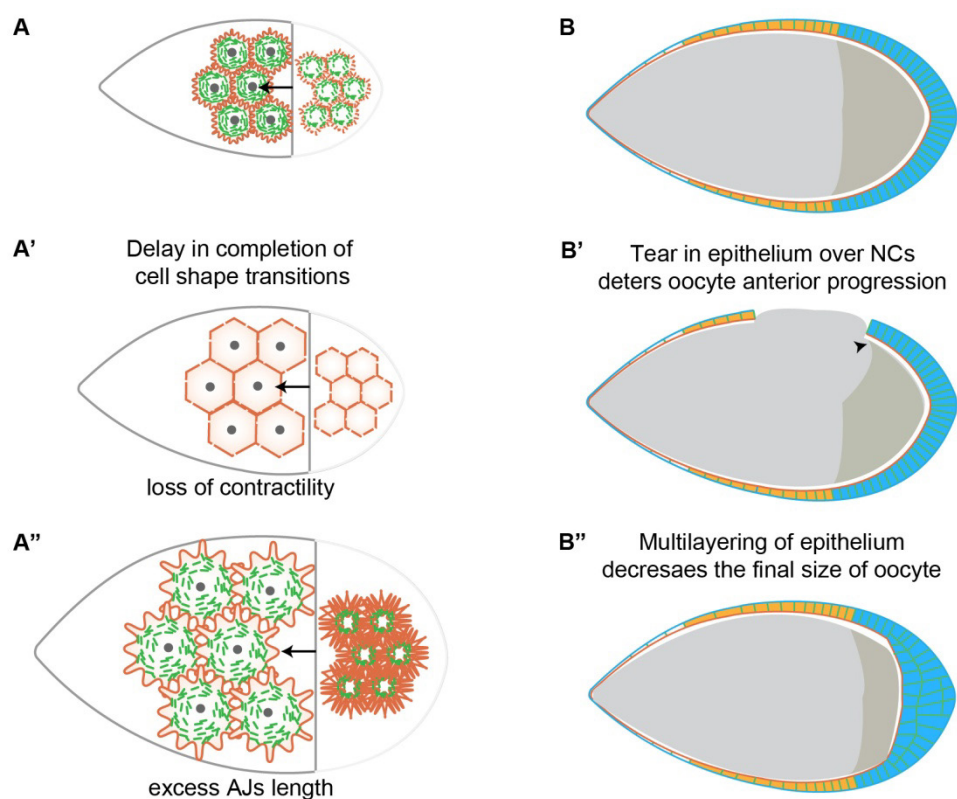


**Figure 32 Summary of consequences of NCC deviation from cuboidal shape**

**(A-A'')** Excess flattening of NCCs in case of loss of contractility (A') or excess length of AJs (A'') leads to a delay in completion of cuboidal to columnar cell shape transitions. This can be visualized when the center of masses of individual NCCs are marked as in the wildtype case (A) and when the NCCs are excessively flattened (A'-A''). The center of masses of excessively flattened NCCs shifts anteriorly, thus delaying the oocyte anterior membrane (black arrows) meeting the last row of NCCs that need to columnarize. **(B-B'')** An intact epithelium (B) is

necessary to prevent the oocyte anterior membrane from stalling (B', black arrowhead). In the case of multilayering of the epithelium, without a change in the total number of columnar-fated cells, the number of cells the oocyte encounters as it progresses anteriorly decreases, thus impeding its growth to its regular size (B", compare dark grey areas of B and B").

### 3.7 Nurse cell cluster elongation is aided by NCCs

The observation that wild type NCCs and even *cno*-overexpressing NCCs with excessive junctional material reduce their apical surface area and columnarize efficiently once in contact with the oocyte indicates that nurse cells may exert stretching forces on the overlying NCCs, while OCCs may be insulated from such external forces. So, we wondered what properties of the nurse cells at a tissue level promoted deformations and ectopic flattening NCCs when their contractility is disrupted or more junction material is added. Nurse cell derived forces acting on NCCs arise potentially from nurse cell growth, shape or geometrical positioning in the egg chamber. Germline growth between stage 8 and 10A is in part driven by a 1.8-fold increase in nurse cell cluster surface. All columnar-fated cells also increase their apical surface area by 1.5-fold (Fig 1C) (Kolahi et al, 2009), consistent with the notion that expansion of their surface areas matches the germline surface area expansion during these stages. Thus, the 2 to 5-fold increase observed in NCC apical surface areas upon loss of MyoII and AJ function may reflect an enhanced ability of these mutant NCCs to expand in concert with the increasing nurse cell surface area but may not be sufficiently accounted for by nurse cell growth and expansion of the surface area alone (Figure 26G').

One additional factor contributing to the mutant NCC deformations could be the geometric positioning of these cells at the maximum DV germline radius, which incidentally coincides with nurse cell position throughout stage 6 to 10. This explains why we observe mild NCC deformations at stage 6 and 7 at positions of maximum DV germline radius when Myo II and AJ function is disrupted (Figure 23). It suggests that the geometric position of NCCs within the egg chamber in addition to nurse cell growth, rather than intrinsic NCC cell properties, sensitize NCC to flattening when MyoII or AJ functions are perturbed. Intriguingly, when the oocyte is misplaced to a central position coinciding with the maximum DV radius in the egg chamber, the relative shape of OCCs is still more columnar if compared to NCCs at the same radial position (Figure 10A-B"). This suggests that while geometric positioning of NCCs at the maximum DV germline radius contributes to the sensitivity of mutant NCC to flatten, additional factors influence this behavior.

Thus, we wondered whether the native nurse cell shape may contribute to forces felt on the apical surfaces of NCCs located at the maximal radius of the D/V germline axis. To test this

## RESULTS

idea, we first investigated what shape nurse cells would acquire in the absence of external constraints to infer the native nurse cell shape.

To remove constraints imposed by the basement membrane, we treated micro-dissected egg chambers with collagenase. First, we analyzed the shape of nurse cells at stage 10A after removal of the basement membrane. At this stage, nurse cells are only covered by squamous epithelial cells minimizing constraints imposed by follicle cells. We observed bulging of individual nurse cells and a shortening of the nurse cell cluster length (AP) to width (DV) axes ratio into a rounder shape (Figure 33A-C') (Chlasta, Milani et al. 2017). This suggests that the shape of individual nurse cells and the nurse cell cluster are constrained primarily by the basement membrane at stage 10A from adopting round shapes. Spheres present the least surface area for the same volume amongst all 3-D shapes. Thus, it appears as if individual nurse cells tend to acquire a surface area minimizing rounder shape and hence promote overall nurse cell cluster shape to be rounder. Surface minimization is driven by high surface tension, which could be driven by MyoII contractility in the nurse cell cortex. Indeed, Myo II localization is higher in the nurse cell cortex if compared to the oocyte cortex (**Error! Reference source not found.A**).

When collagen was removed in stage 8 egg chambers, neither epithelial nor nurse cell shape changed, despite disruption of basal actin filament polarity (Figure 33D-D'). This suggests that the basement membrane and basal actin polarity are not acutely required to determine epithelial or nurse cell shape at stage 8. This indicates that the apical surface of the epithelium in direct contact with nurse cells is the most likely determinant of epithelial cell, nurse cell, nurse cell cluster and thus egg chamber shape. To provide more evidence for this idea, we wanted to eliminate NCCs and assess the unconstrained nurse cell shape at stage 8/9. RNAi-mediated knockdown of the apical determinant aPKC caused extreme NCC flattening and cell-cell contacts to tear, coinciding with bulging of nurse cells into the epithelium (Figure 33E). To prove that nurse cells were not just passively filling space, we acutely removed the basement membrane by collagenase treatment. We observed pronounced bulging of nurse cells out of epithelial gaps (Figure 33E'), suggesting that nurse cells may be subject to forces, such as high surface tension, that promote bulging. This is furthermore supported by nurse cell bulging in anterior positions of collagenase-treated wild type egg chambers where epithelial cells flattened by mid-stage 9 (Figure 33F-F').

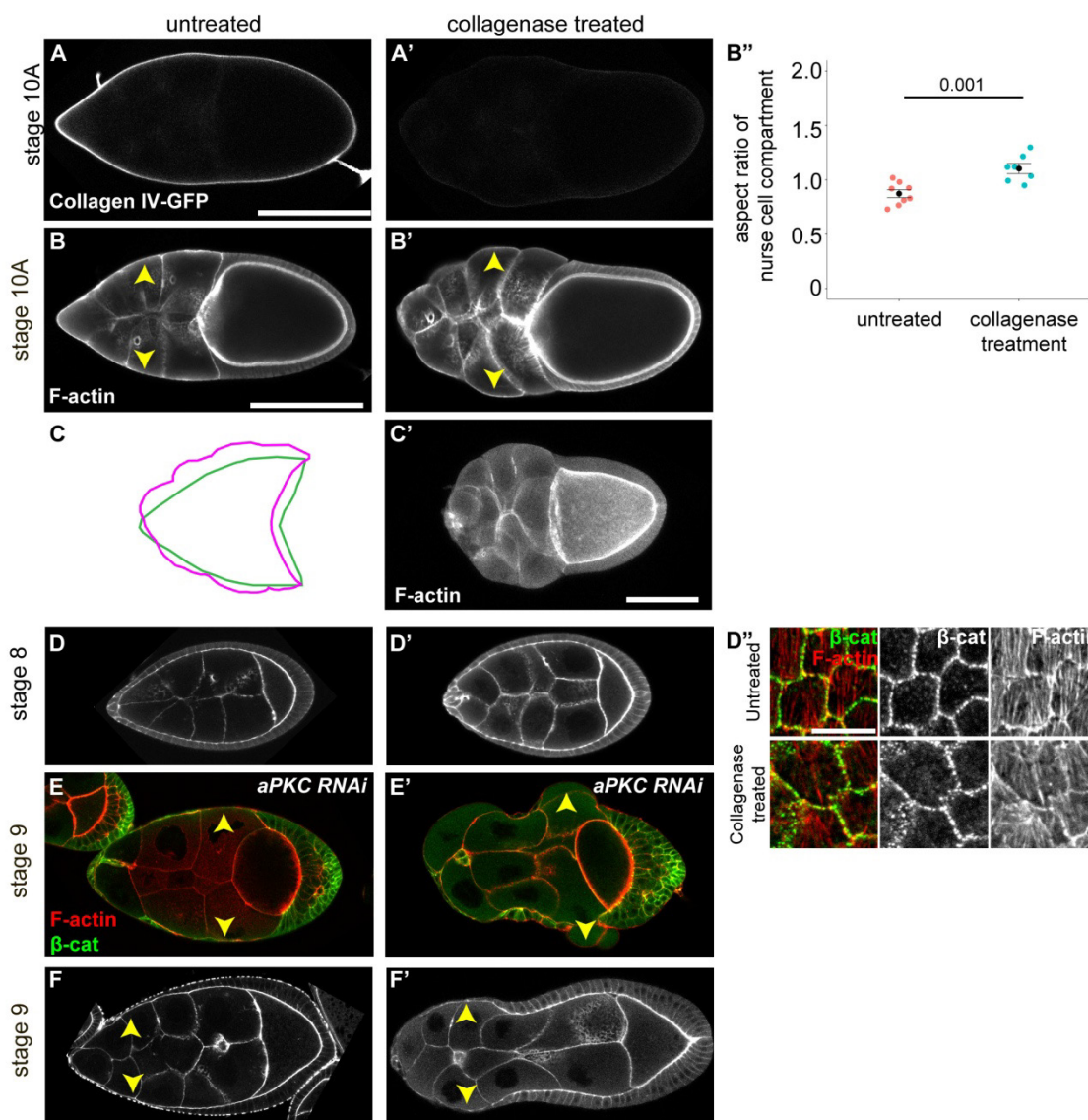


**Figure 33 NCC are required to withstand nurse cell derived-forces and to promote egg chamber elongation**

(A-B') Medial sections of egg chambers untreated (A, B) and treated with collagenase at stage 10A (A', B'). Expression of Collagen IV-GFP (A, A') visualizes degradation of the extracellular matrix by collagenase treatment (A'). (B'') Length-to-width aspect ratios of nurse cell compartments of stage 10 egg chambers untreated (n=8) and upon collagenase treatment (n=7). WMW test was performed. (C-C') Overlay of nurse cell cluster outlines of untreated (green) and collagenase-treated (magenta) (C) of egg chambers shown in (A-B') illustrates shape change of the nurse cell cluster. An additional example of pronounced nurse cell cluster rounding upon collagenase treatment is shown in (C'). (D-D') Medial (D-D') and *en face* section of the basal surfaces (D'') of untreated and collagenase treated stage 8 egg chambers stained for  $\beta$ -cat (green) and F-actin (red). Note disrupted basal actin filaments and their polarity upon collagenase treatment. (E-E') Medial sections of egg chambers untreated and treated with collagenase at stage 9 stained for F-actin and  $\beta$ -cat expressing *aPKC RNAi* in the epithelium. Yellow arrowheads point to nurse cell bulging (E) and the more pronounced rounding of nurse cells upon collagenase treatment where tears in the epithelium are present (E'). (F-F') Medial sections of stage 9 egg chambers untreated and treated with collagenase. Yellow arrowheads point to nurse cell bulging upon collagenase treatment in the anterior where the cells are already flattened. Scale bar (A-F') = 100  $\mu$ m, (D'') = 10  $\mu$ m. Quantifications in Table 27.

## RESULTS

Combined these observations indicate that the apical surface of cuboidal NCCs at stages 8 and 9 prevents nurse cells and the nurse cell cluster from ‘bulging’ into a rounder shape and. In support of this hypothesis, we found that NCC flattening in *cnoOE* and *Rac1DN*-expressing epithelia coincided with bulging of individual nurse cells into the apical NCC surface (Figure 34A-A’). Moreover, we observed pronounced aspect ratio changes in nurse cell cluster shape upon expression of *cnoOE* or *Rac1DN* in the follicle epithelium (Figure 34A’’). Thus, total nurse cell cluster shape at stage 9 is determined by the combined actions of circumferential contractility arising from NCCs and basement membrane stiffness at anterior flattening cells (Crest, Diz-Munoz et al. 2017).

This suggests that while a decrease in junctional tension may mediate adaptation to germline surface area increase, contact-dependent enrichment of E-cad and Myo II in the apical domains of NCCs suppresses rounding of individual nurse cells and imposes circumferential constriction along the DV axis on nurse cells to ensure nurse cell cluster and thus egg chamber elongation during stages 8/9. Thus, the constraint of nurse cells by NCCs could contribute to the external forces acting on the NCCs if compared to the OCCs. Loss of actomyosin function or increasing the amount of junctional material disrupts the balance between contractility and adhesion that maintains the right amount of resistance in the apical surface and hence maintains cuboidal shape of NCCs by resisting the tendency of the nurse cell cluster to round up.

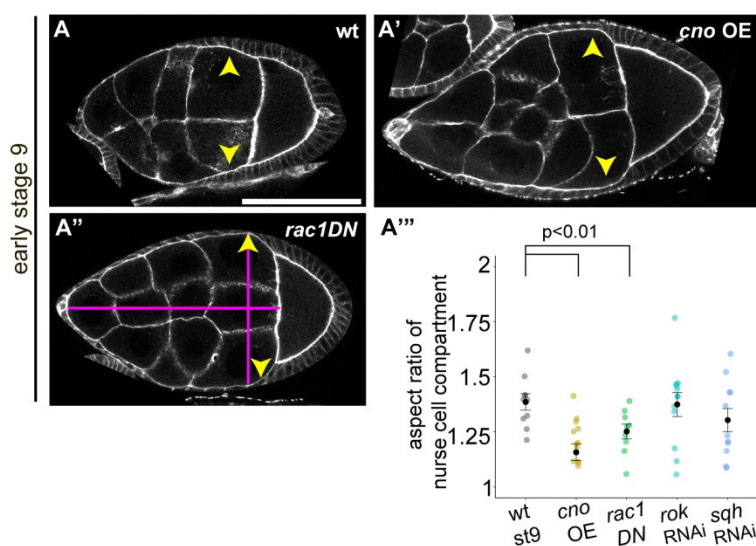


**Figure 34 Bulging of nurse cells is constrained in the DV axis by NCC cell shape**

(A-A’’) Medial sections of morphologically stage 9 egg chamber, either wild type (A) or with epithelial expression of *cnoOE* (A’) or *Rac1DN* (A’’) stained for F-actin and  $\beta$ -cat. Yellow arrowheads point to nurse cell bulging at NCC positions. Length-to-width aspect ratio (A’’’. magenta lines) of nurse cell compartments for wild type egg chamber (wt, stage 9) or with epithelial expression of *cno*, *Rac1DN*, *rok* RNAi or *sqh* RNAi.  $n \geq 9$  egg chambers for any condition. WMW-tests were performed. Scale bars = 100 $\mu$ m. (A’’’) measurements done by AKC. Quantifications in Table 26.

### 3.8 Different properties of nurse cells surfaces compared to the oocyte surface promote sensitivity of mutant NCCs to flattening

Interactions of the apical epithelial surface with nurse cells or oocyte must mediate sensing of germline surface area expansion, as well as propensity of individual nurse cell and the nurse cell cluster to round. We wondered if interaction with the nurse cell surface and oocyte surface may be different, explaining the different sensitivity of mutant NCCs to flatten. Indeed, we observed high F-actin levels in the oocyte cortex whereas Myosin II was enriched in nurse cells, indicating that nurse cell and oocyte cortices differ in molecular composition (**Error! Reference source not found.A, B**).

We investigated the possibility that a specific type of adhesive coupling between NCC and nurse cells transmitted the external forces arising from the nurse cells. Importantly, we could not find any evidence for cadherin-mediated adhesion between nurse cells and NCCs at stage 9. RNAi mediated double-knockdown of N-cad and E-cad in the germline did not disrupt epithelial cell shape transitions (**Error! Reference source not found.C**). Therefore, while E-cad regulates certain aspects of early stage epithelia-germline interactions (Godt and Tepass 1998, Gonzalez-Reyes and St Johnston 1998), no role for adhesion between NCCs and nurse cells at these stages may exist. In agreement with this genetic data, electron micrographs of the NCC-NC interface did not reveal pronounced adhesion-like structures. Instead a gap is visible between NCC and the nurse cell surfaces (**Error! Reference source not found.D, D', D''**). However, the physical gap between OCCs and the oocyte was larger than between NCCs and nurse cells suggesting differences in interaction strength (**Error! Reference source not found.D, D', D''**).

## RESULTS

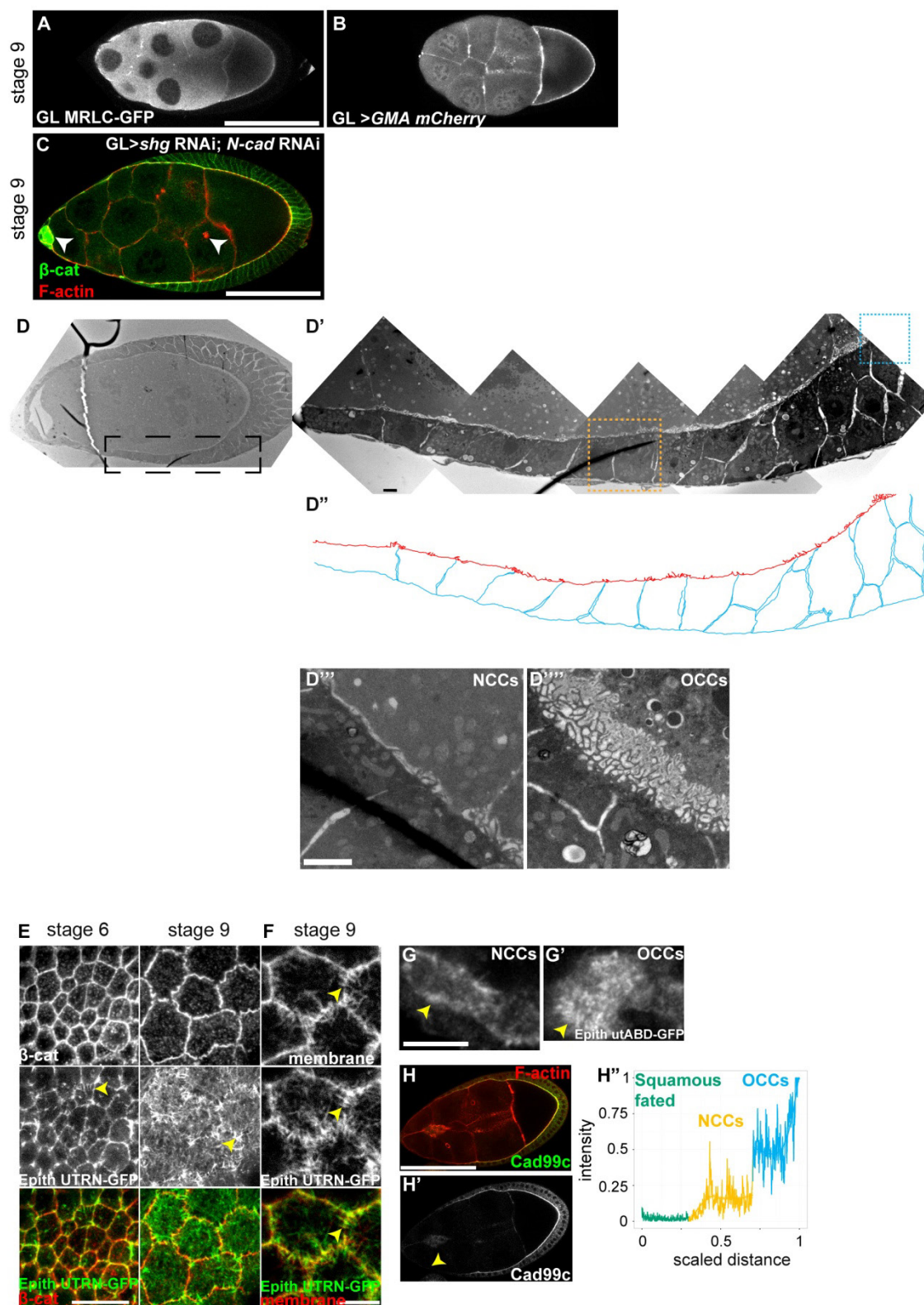


**Figure 35 E-cad adhesion does not mediate NC-NCC interactions and apical protrusions are features of NCC apical domain**

(A-B) Medial sections of stage 9 egg chambers labelled with germline (GL) specific expression of MRLC-GFP (A) and GMA-mCherry (B). (C) Medial section of an egg chamber with RNAi mediated double-knockdown of N-cad (N-cad) and E-cad (shg) in the germline (GL) stained for  $\beta$ -cat (green) and F-actin (red). Note lack of  $\beta$ -cat signal on nurse cell-nurse cell and oocyte junctions indicating efficient knock-down of cadherin-mediated adhesion. Arrowheads point to

floating ring canal (right) and delayed border cell migration characteristic of loss of cadherin-mediated adhesion (Loyer, Kolotuev et al. 2015). Egg chamber displays normal transition of epithelial cell shapes. **(D-D''')** Transmission electron micrographs of an early stage 9 egg chamber. Black box in (D) is shown at higher magnification in (D'). Manual tracing of apical surface (red) and basolateral surfaces (blue) is shown in (D'') to better visualize that apical protrusions occur preferentially near FCE cell-cell contacts. Orange and blue squares in (D') frame NCC and OCC positions shown at higher magnifications in (D''') and (D'''), respectively. Note the difference in distance between apical epithelial surface and germline surface in NCC and OCC positions (D''', D'''). **(E-F)** En face junctional sections in an egg chambers at stage 9 labeled with  $\beta$ -cat (E, grey in top row panel, red in bottom row panel) or epithelial cell specific expression of plasma membrane marker mCD8-tomato (F, grey in top row panel, red in bottom row panel) and of utABD-GFP (E, F grey in middle panel, green in bottom row panel). Yellow arrowheads in E show short filaments radiating from the cell-cell boundaries and in F indicate an example of where actin overlaps with plasma membrane signals suggesting that it represents a filopodia-like protrusion. **(G-G')** En face apical sections of epithelium in an egg chamber at stage 9 with epithelial cell specific expression of utABD-GFP in NCCs (G) and OCCs (G'). Yellow arrowheads point to apical protrusions in NCCs and microvilli in OCCs. **(H-H')** Medial section of stage 9 egg chamber expressing Cad99C-GFP (green in H, grey in H') and stained for F-actin (red in H). Yellow arrowhead in H' indicates the lack of signal in squamous-fated cells. Line profile of Cad99C-GFP fluorescence intensities at the apical/junctional domain in the egg chamber is shown in (H''). Note that apical NCC protrusions are shorter and less numerous in G than apical OCC protrusions in G' representing Cad99C positive microvilli (Schlichting, Wilsch-Brauninger et al. 2006). Scale bar (A-C) = 100  $\mu$ m, (D'-D''') = 2  $\mu$ m, (E) = 10  $\mu$ m, (F) = 5  $\mu$ m. Electron micrographs taken by MR, trace drawn by AKC, (C, G-G') images taken by VW.

Interestingly, our electron micrographs revealed apical protrusions arising from NCC predominantly at sites of epithelial cell-cell contacts (**Error! Reference source not found.D'-D''**). In confocal sections of the apical surface of follicle cells expressing the actin marker *utABD-GFP*, we observed small radiating filaments in the junctional plane (**Error! Reference source not found.E**). These filaments are often covered with plasma membrane suggesting that there is a population of the F-Actin filaments which is present in membranous protrusions visible in electron micrographs (**Error! Reference source not found.F**). These filopodia-like protrusions are visible exclusively in NCCs and not in OCCs, where micro-villi decorate the entire apical surface (**Error! Reference source not found.D''', G-G'**). These microvilli are labelled by markers like Cad99c which is seen at high levels on the OCCs surfaces whereas NCCs have lower levels (**Error! Reference source not found.H-H'**). Therefore, some form of direct interactions between the NCCs and the nurse cells may be mediated by these apical membrane protrusions. Intriguingly, expressing germline specific actin marker like *GMacherry* reveals an imprint of NCC protrusions on the NC cortex. These imprints are absent on the oocyte, reinforcing the idea that apical protrusions mediate interactions between NCCs and nurse cells (Figure 36A-C'). However, germline specific Myo II expression using *sqh* GFP did not reveal a strong imprint (Figure 36D-F'). Thus, the nature of these interactions (biochemical or biomechanical signaling) between apical membrane protrusions of the NCCs with the nurse cells remains an open question.

## RESULTS

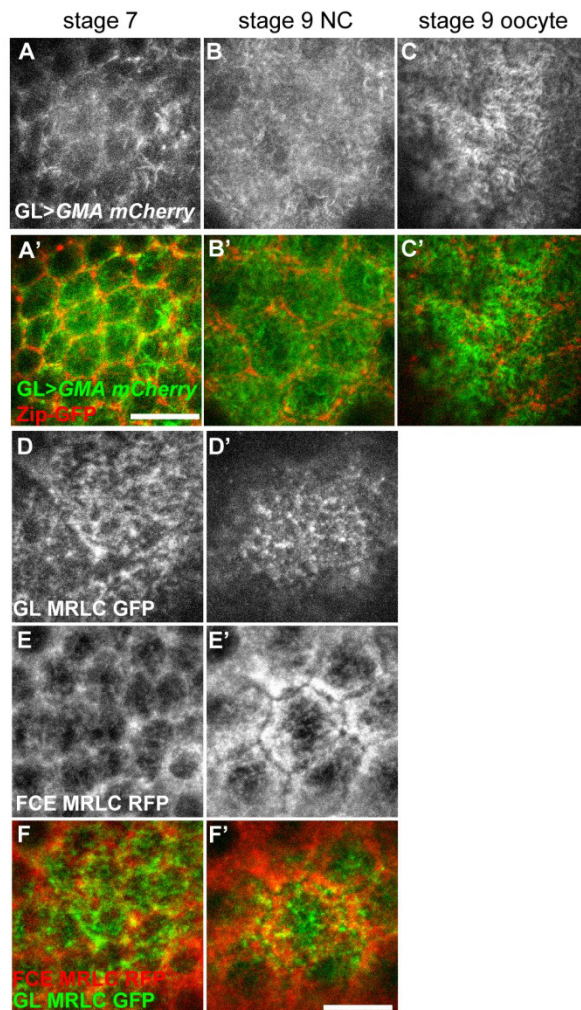


**Figure 36 Interactions between the nurse cells and NCCs are stronger than between the oocyte and the OCCs**

(A-C') *En face* section of epithelial-germline interface of egg chambers at stages 7 (A, A') and 9 (B-C') expressing the actin tracer GMA-mCherry (grey in A, B, C green in A', B', C') in the germline and Zip-GFP (red in A', B', C') in the entire egg chamber (efficiently marking epithelial cell outlines). Nurse cell cortices (A, B) at stages 7 and 9 show an imprint organized as NCC apical shapes with enriched actin filaments along NCC junctional outlines and a clearance in the apical center. The oocyte cortex (C) displays a homogeneous actin filament network. (D-F') *En face* section of epithelial-germline interface of egg chambers at stages 7 and 9 with GL specific MRLC GFP (grey in D-D', green in F-F') and FCE specific MRLC RFP (grey in E-E', red in F-F') expression with no imprint of the FCE Myo II on the GL cortex. Scale bar (A-F') = 10  $\mu$ m.

## 4 Discussion

With this work we show that 3D epithelial cell shape transitions are coordinated with external forces arising from expansion of a closely apposed tissue by globally regulating tensile stress in adherens junctions and by locally reinforcing junctions and contractility to resist deformation by high external forces.

When the egg chamber grows between stages 6 to 9, there is a reduction in tensile stress on the AJs in the epithelium. This decrease in AJ tension correlates with remodeling and elongation of AJs and exclusion of Myo II from AJs. This ‘relaxed’ state of the epithelium still exhibits cuboidal and columnar cell shapes that correlate strongly with the type of germline cell surface the epithelium contacts. We suggest that as a default, posterior and main body FCE acquire a columnar shape, which is promoted upon contact with the oocyte. In contrast, columnar shape is suppressed by contact with nurse cells and results in cuboidal shape, as cells deform in response to nurse cell derived forces. Despite overall relaxation in tissue tension, the AJs of cuboidal cells experience higher tensile stress if compared to AJs of columnar cells. We show that contractility and AJ levels are reinforced in cuboidal cells to prevent excessive deformation from nurse cell derived forces. Thus, deformation from cuboidal shape in NCCs into more flattened cell shapes occurs upon genetically altering AJ length or levels of contractility. In contrast, upon changing AJ length and contractility, columnar cells deform less and suggest that lower external force from the oocyte cortex acts on them. We suggest that the source of external forces from the nurse cells, in addition to growth-related surface area expansion, is the intrinsic tendency of individual nurse cells to round up due to high surface tension. This leads to rounding up of the entire nurse cell compartment and, thereby, expansion of the medial radius of egg chambers at stage 9. Finally, reinforcement of AJ and contractility in NCCs has two-fold importance: - (1) it elongates the overall shape of the egg chamber, as in the absence of this reinforcement, the overall shape of the egg chamber is rounder; (2) it prevents excessive flattening of the NCCs and their relative positional shift towards the anterior of the egg chamber, which delays the completion of the cell shape transitions and hence further development of the egg chamber.

### **4.1 Decrease in tensile stress on the AJs accommodates germline growth**

#### **4.1.1 How is decrease in tensile stress on AJs achieved?**

During steady growth of the germline between stages 6 to 10, the increase in surface area of the germline expansion is accommodated by an increase in surface area of the FCE (Kolahi, White et al. 2009). We demonstrate that during these stages the tensile force on the epithelial junctions decreases, suggesting that the epithelium is relaxing to accommodate the overall germline growth as opposed to uniformly resisting expansion forces from the germline (Figure 37).

In the time frame of AJ recoil velocities measured, junctions typically behave as linear elastic solids. This means that the stress exerted on them is directly proportional to the elastic modulus of the junctions and the strain on the junctions. Two biological factors that can contribute to the elastic modulus and strain on junctions are the contractile cytoskeleton and the junctional composition. Thus, reduction of contractile forces can reduce elastic behavior of the junctions. Similarly, addition of junctional material to AJs can enable cells to relieve strain on junctions as the follicle cell surface area expands from stage 6 to 9. In agreement with this hypothesis, we show that the FCE undergoes Myo II exclusion from the junctions during stages 6 to 9. Coinciding with this, AJs disproportionately increase their junctional lengths which become visible as corrugations. Resistance to external stretch forces from growth of another part of the epithelium has been shown to be mounted on junctions by Myo II (Mao and Baum 2015). Typically, Myo II localization is seen on AJs in epithelial cells and studies show that the resistance of these cells decreases when Myo II is reduced (Legoff, Rouault et al. 2013, Mao, Tournier et al. 2013). In contrast, other studies show that epithelial relaxation is important for brain ventricular morphogenesis in *Xenopus* by decreasing Myo II activity in the tissue that depends on increasing expression of Myo II phosphatases at specific developmental stages (Gutzman and Sive 2010). We suggest that excluding Myo II uniformly from AJs throughout the epithelium and lengthening AJs establishes the epithelium in a relaxed state - primed to respond to the external forces derived from germline growth (Figure 37A').

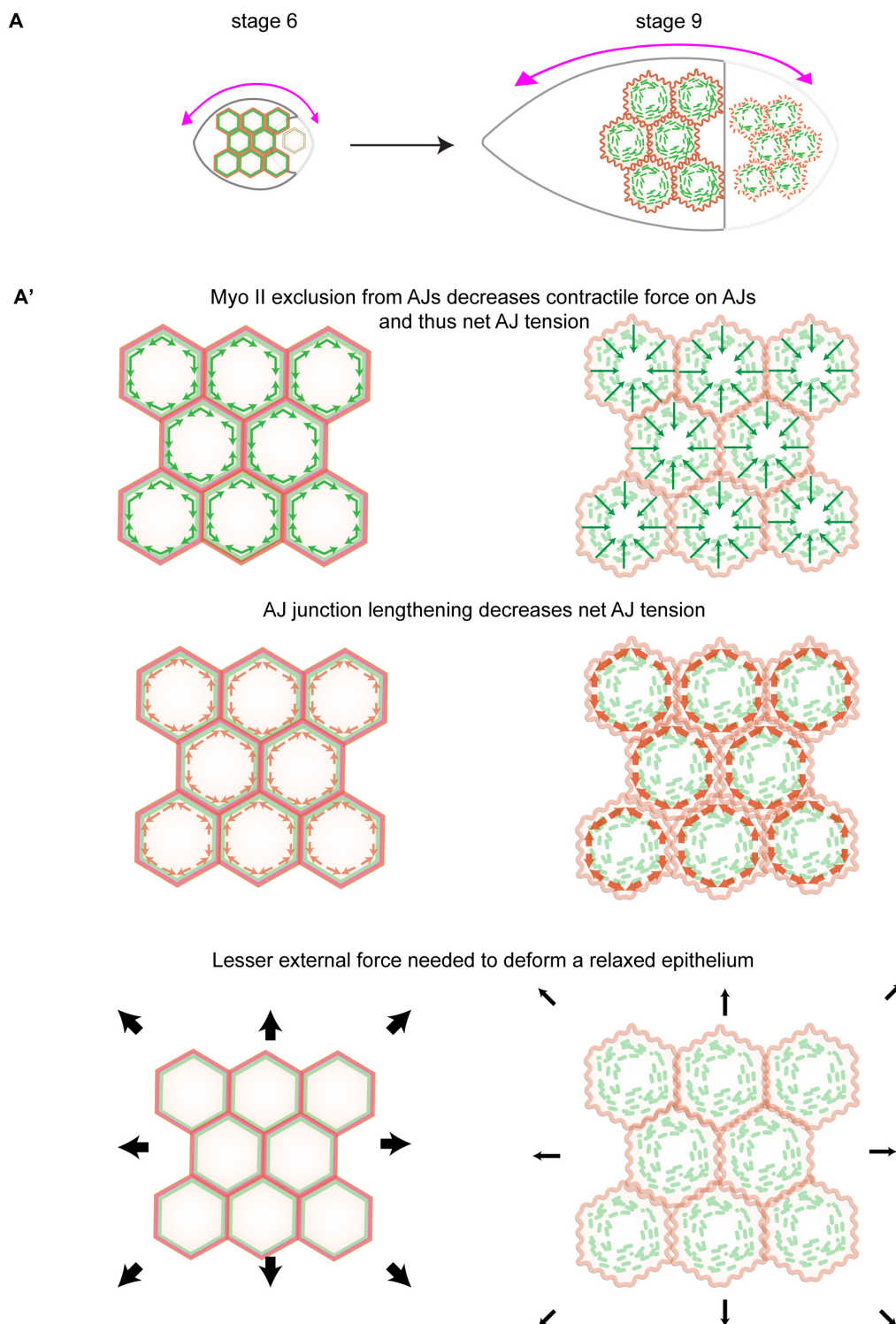


**Figure 37 Epithelium tension relaxation during stages of germline surface area expansion by junctional lengthening and Myo II exclusion**

(A) Scheme of egg chamber developing from stage 6 to stage 9 with germline growth shown in pink arrows. (A') The tensile stress on the AJs in the epithelium decreases by shifting Myo II from the AJs and decreasing inward contractile forces and increasing AJ length to relieve tensile stress on AJs by promoting higher adhesive forces. Thus, the magnitude of external forces (black arrows) potentially needed to deform the epithelium in this arrangement to the same extent is lesser. This relaxation in the epithelium to deformation by external forces allows it to expand its surface area to accommodate the surface area expansion of the germline.

## DISCUSSION

Since junctional corrugations and Myo II exclusion coincide temporally, we wanted to assess the possibility of a causative link between the two events. Junctional loss of Myo II has been shown to lead to wiggly, corrugating junctions during dorsal closure (Blanchard, Murugesu et al. 2010). Previous work has shown Afadin to be important to anchor Myo II on AJs (Sawyer, Harris et al. 2009, Sawyer, Choi et al. 2011). While we see a decrease in Afadin levels on AJs between stages 6 to 10, we could not relocalize Myo II back to the junctions upon its overexpression. Intriguingly, the junctions became hypercorrugated upon Afadin overexpression while still maintaining apico-medial Myo II. Total corrugated AJ length may set the upper limit for apical area expansion beyond which the risk of epithelial tearing in response to external forces might be high. Thus, having a surplus of junctional material as in Afadin overexpression may shift cells into a state of greater relaxation of AJs, driving excessive apical surface expansion to nurse cell derived forces, even when the contractile machinery is in place to counteract it. In contrast, the extent of apical surface area expansion upon genetically reducing contractility is limited by normal corrugated junction length. This explains the milder tissue and organ level phenotypes upon ROCK and MRLC genetic perturbations. Further, this invokes the possibility that altering E-Cad trafficking could promote junctional corrugations and initiate relaxation of tension at AJs. Initiating tensile relaxation could feed-forward to exclude Myo II from junctions, as MyoII is known to be recruited to junctions under high tension (Chanet, Miller et al. 2017). Previous work has suggested roles for Afadin in regulating trafficking to junctions via control by GTPases like Rap1 (Roeth, Sawyer et al. 2009, Mateus, Gorfinkiel et al. 2011, Sherrard and Fehon 2015). Molecular mechanisms that regulate AJ corrugations would be important to investigate and should include further testing of the role of Rap1 and Afadin in trafficking E-Cad. Importantly, Rac1DN expression in the epithelium also resembles Afadin overexpression. While a role for Rac1 in E-Cad trafficking has been described in mammalian cells (Akhtar and Hotchin 2001), how Rac1 promotes corrugations in the fly remains an open question.

The signal initiating a uniform program in the FCE to decrease tensile stress is not known yet. One possibility could be that germline growth provides such a signal to the FCE. However, we do not observe a decrease in corrugations in small *dic* or *egl* germline mutants (not shown). Another possibility could be that growth of epithelial cells promotes the decrease in tensile stress. Growth of the epithelium between stage 6 to 9 is coupled to three rounds of endoreplication (Shcherbata, Althausen et al. 2004). Future experiments that manipulate the endoreplication state with Cyclin E or size of the FCE with dAKT and hence the growth of the FCE could throw light on this possibility (Lilly and Spradling 1996, Cavaliere, Donati et al. 2005, Jia, Huang et al. 2015).

#### 4.1.2 Junction excluded Myo II exerts forces on junctions

Myo II is typically tethered to junctions via F-actin cables that run in parallel to junctions. This actomyosin network parallel to the junctions can exert strong contractile forces on AJ belts. Despite junctional exclusion, Myo II continues to mediate contractile forces as the tension on the junctions only decreases when the shift occurs. Previous studies have shown that medial Myo II can be tethered to the junctions by radial actin filaments generating radial contractility (Martin, Gelbart et al. 2010, Coravos and Martin 2016, Weng and Wieschaus 2016). Indeed, in the case of FCE, the apical-medial Myo II also appears to be tethered to junctions, as its level can modulate the extent of tensile forces on the junctions and loss of Myo II leads to expansion of the cells and decrease of corrugations. However, unlike reports of oscillatory medial Myo II networks as described in embryogenesis (Martin, Kaschube et al. 2009), we think the apico-medial Myo II is less dynamic. We do not see variable distributions of the medial Myo II cortex across several experiments in fixed tissues which would be expected if there are strong oscillations. Furthermore, recent work in the egg chamber has shown that while the Myo II network is oscillatory at stages 3-6, oscillations dramatically decrease from stage 7 and are lost by stage 9 (He, Wang et al. 2010, Alegot, Pouchin et al. 2018).

Combined, corrugations appear to be maintained by stable radial contractility exerted by the apico-medial Myo II during stages of steady germline growth. It is possible that because of radial Myo II rearrangement and onset of AJ corrugations, the net internal contractile force per unit of junction decreases compared to when Myo II primarily localizes to junctions. One can speculate that this radial arrangement enables the epithelium to respond to germline derived external forces more easily and is energetically favorable during development of the egg chamber. Physical models of epithelia with different arrangement of contractile network — parallel to the junctions versus radial during apical surface area expansion of cells could elucidate energy-minimizing configurations of the contractile network relative to the junctions.

Thus, we show that a cellular rearrangement of contractility and junctional architecture can prime cells for decreasing tensile stress on junctions. Future studies can elucidate the molecular linkers between the radial contractile network and the junctions in this epithelium. Apart from Arf GEFs and myosin phosphatases which have been implicated in modulation of the extent of contractility exerted on junctions, no other molecular players for this contractile arrangement are known (Gutzman and Sive 2010, West, Zulueta-Coarasa et al. 2017).

### **4.1.3 Dumping stage of egg chambers show complete loss of tensile stress in AJs**

In line with decreasing tension in the junctions as the germline grows, we also observe that junctional recoil velocities drop to undetectable levels during rapid nurse cell dumping stages 11-12 (Figure 38A). This process is very fast lasting typically 30 minutes and the columnar cells rapidly flatten uniformly to accommodate the massive surface area expansion of the oocyte (Figure 38B). Thus, complete loss of stress on the junctions may be favorable for these changes and suggest that the FCE is fully relaxed to the germline surface expansion. Aligning with the surface area expansion of the FCE, the AJs expand from extreme corrugations into straight junctions (Figure 38C).

### **4.1.4 Limitations of recoil velocity measurements in understanding biomechanical properties of epithelia**

The laser ablation recoil curves were fit to a double-exponential curve as shown previously. Velocities of initial recoil could be well estimated for stage 6 and stage 9 NCCs because of good fitting parameters (Figure 38D, E). However, the fit parameters for the stage 9 OCCs were poorly estimated. This suggests that the recoil curves for stage 9 OCCs behave differently. We thus calculated the initial recoil velocities by assuming the linear phase of recoil lasts up to 0.5 s after the laser cut (the limit of our temporal resolution with this set up).

The final cell surface areas after circular cortical cuts and final vertex distances upon junctional cuts are different from each other in all stages and at different positions (Figure 38F, G). The final areas and distances are affected by the initial recoil velocity as well as viscoelastic effects of the cortex which in turn can also depend on the magnitude of initial recoil velocities. It has been beyond the scope of this study to understand the contributions of the latter to the final distances the vertices and areas relax to. The differences in final distances because of differences in the initial junctional recoil velocities are logically foreseeable. However, it is unclear how circular cortical cuts with similar initial recoil velocities can have different final areas. Some studies focusing on laser ablation discuss the influence of viscoelastic properties of cells on recoil velocities in detail and these properties should be kept in mind for future experimental designs using laser ablation approaches (Hutson, Tokutake et al. 2003, Mayer, Depken et al. 2010, Davidson 2011).

## 4.2 Epithelial cell shapes in a relaxed epithelium

### 4.2.1 Cuboidal cell shape is a result of local resistance to nurse cell derived forces mediated by actomyosin contractility

Although the junctional tension relaxation program initiates uniformly in the epithelium, germline contact-dependent differences are seen in the epithelium. The epithelium can be divided into two populations of cells. One population, the squamous-fated cells acquires squamous cell shape dependent on a developmental fate (Xi, McGregor et al. 2003, Brigaud, Duteyrat et al. 2015). Indeed, squamous cells can form independent of the germline cell type they are in contact with (Gonzalezreyes, Elliott et al. 1995). We call the complementary set of cells in the epithelium the columnar-fated cells which do not have one specific known developmental fate pre-pattern that assigns their shape (discussed further in section 4.2.3). Instead columnar-fated cells appear columnar by stage 10, when they contact the oocyte. In the intermediate stages, i.e. between stage 6 and 9, they appear columnar only when the oocyte expands underneath them, whereas they appear cuboidal when still in contact with nurse cells. Thus, cuboidal and columnar cell shapes are dependent on germline-contact despite uniform reorganization of junctions and cytoskeleton of all cells. This suggests that there are germline-contact dependent differences in forces felt on the overlying epithelium. Concomitantly, the tensile forces on NCC junctions are higher than on OCCs junctions. Contact-dependent differences include higher levels of Myo II, AJ proteins and more pronounced corrugations in NCCs when compared to the OCCs. Indeed, NCCs are more sensitive to deformation upon the loss of Myo II, AJ proteins or promoting junctional corrugations and shift their aspect ratios to a flatter cell shape. The OCCs on the other hand, do not experience aspect ratio deviations from columnar shape upon similar genetic manipulations. The shift to flatter cell shapes of NCCs reveals that they relax to external nurse cell derived forces. The lack of flattening deformation in columnar OCCs, suggests that oocyte derived forces are weaker. Furthermore, it indicates that the forces from nurse cells are resisted by the greater levels of Myo II in the NCCs. Thus, cuboidal cells are obtained by balancing the relaxation of the epithelium to stronger nurse cell derived forces via contractility mediated resistance resulting from recruiting more medial Myo II, which puts the junctions of cuboidal cells in a more enhanced tensile state than columnar cells.

## DISCUSSION

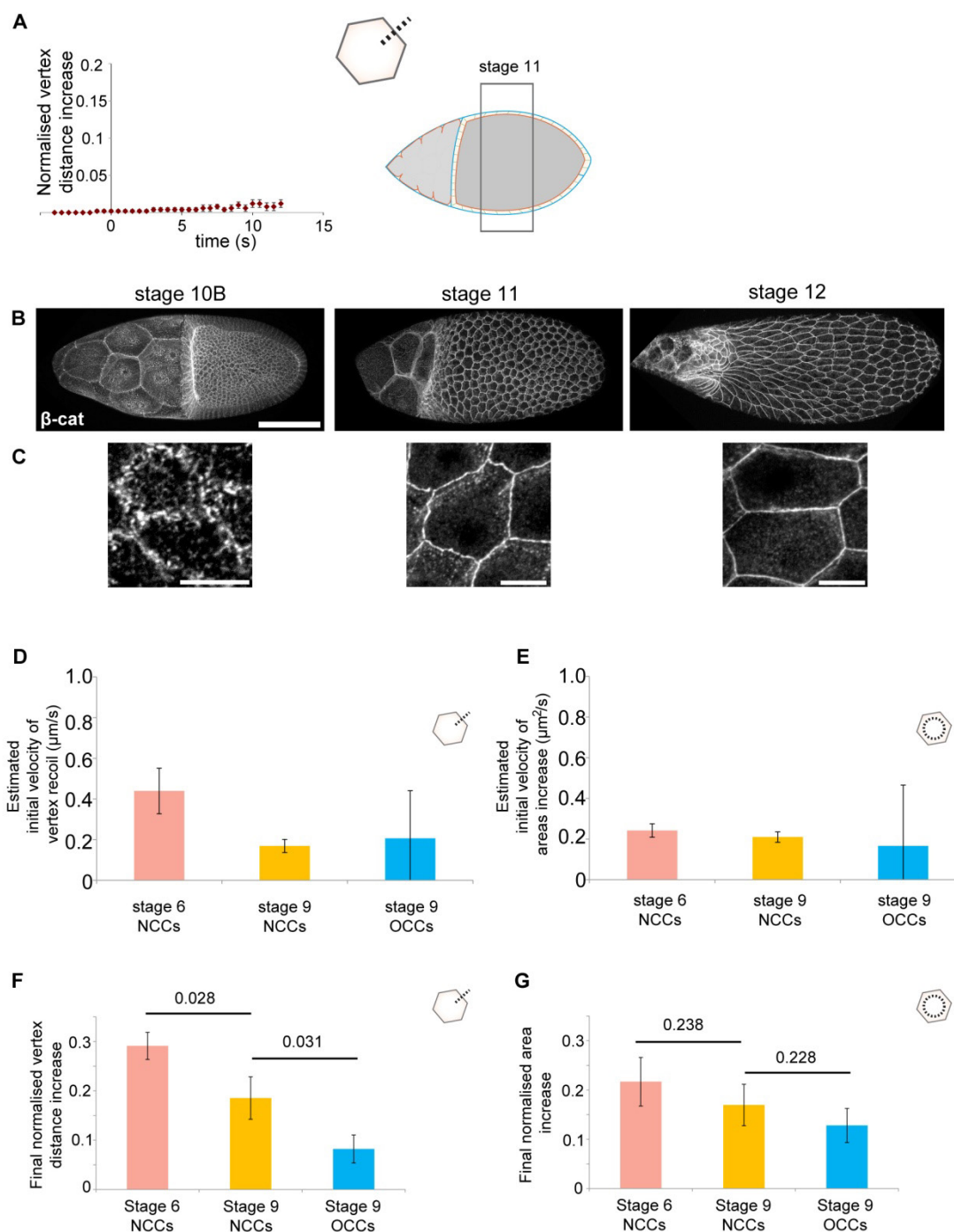


**Figure 38 Complete loss of junctional tension during nurse cell dumping**

(A) Graph displays the normalized average increase in distance $\pm$ SEM upon laser ablation of AJs ( $t=0$ ) as a function of time at stage 11 ( $n=8$ , Table 16). Cellular and egg chamber schemes illustrate position of laser cuts (black dotted lines). (B) *En face* junctional view at stages 10B-12. Note the increasing area of columnar-fated cells. Images taken by VW. (C) *En face* junctional sections of egg chambers between stages 10A and 12 stained for  $\beta$ -cat. Note the conversion from extremely corrugated and discontinuous junctions at stage 10B to straight junctions in epithelial cells at stages 11-12. (D-E) Estimated initial velocity  $v_0$  (see section 6.5.4) of normalized junctional vertex recoil (D) and area increase (E) upon junctional (D) and cortical (E) ablations in stage 6 NCCs (pink), stage 9 NCCs (orange) or stage 9 OCCs (blue) are plotted. (F, G) Final normalized vertex distances reached upon junctional ablations (F) and final normalized areas measured upon cortical ablations (G). Graphs display mean $\pm$ st. error in (D, E) and mean $\pm$ SEM in (F, G). Welch Two Sample t-test was performed in F and G. Scale bar (B) = 100  $\mu\text{m}$ , (C) = 10  $\mu\text{m}$ .

#### 4.2.2 Columnar cell shape is not generated by apical contractility

In contrast to NCCs, OCCs acquire their columnar shape in the absence of strong germline-derived forces arising from the oocyte when compared to nurse cells. Further, NCCs that have deformed into flatter shapes upon *sqh* and *rok* loss of functions are able to recover their lateral height and decrease their apical areas when the oocyte expands underneath them, and they lose contact with nurse cells. This suggests that the default shape of cells is indeed columnar which is promoted by reduced germline-derived forces from the oocyte growth. Additionally, upon genetic manipulation of genes essential for germline development (Huynh, Petronczki et al. 2001), we observe that germlines are small because of their impaired development and shape of the follicle cells is more columnar over the nurse cells indicating that growth of the nurse cells is indeed important to suppress columnar cell shape (Figure 39A).



**Figure 39 Small germline has columnar cells over the nurse cells**

(A) Medial section of egg chambers with germline deficient in Baz, shown to be important for germline development (Huynh, Petronczki et al. 2001). Cyan arrowhead points to columnarized cells over the nurse cells.

OCCs have lower levels of apical Myo II, junctional materials, and lower junctional tension levels if compared to NCCs while acquiring columnar form. This confirms as previously suggested that apical contractility is not required for the onset of columnarisation (Kolahi, White et al. 2009). Others suggest membrane trafficking is redirected in columnar cells (Dunst, Kazimiers et al. 2015). Aligning with this work, we have preliminary observations hinting towards trafficking mechanisms that promote columnarisation as secretory pathway proteins relocalize specifically in the OCCs. Rab11 relocalizes to the lateral membrane, whereas the exocyst proteins Sec6, Sec10 and RabX1 shift towards the apical surface in OCCs (Figure 40A-

## DISCUSSION

D'). Moreover, differential sensitivity of NCCs to disruption of endocytic turnover of AJ proteins like DE-Cad and  $\beta$ -cat is visible by characterising a *shi<sup>TS</sup>* mutant FCE. We observe that *shi<sup>TS</sup>* mutant NCCs display a greater accumulation of AJ proteins in the lateral cell membranes than OCCs, suggesting the AJ material trafficking is also altered in a germline contact-dependent manner (Figure 40E-E').

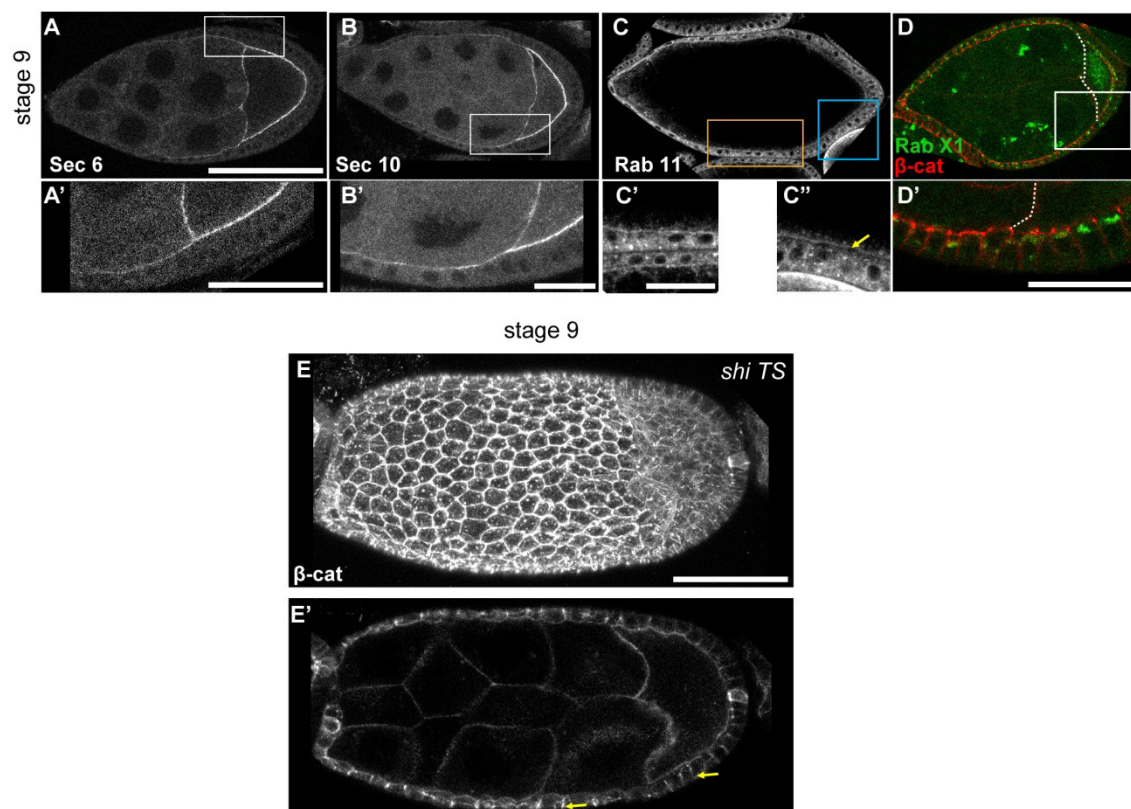


**Figure 40 Reorganisation of trafficking components potentially by germline contact-dependent cues could promote OCC columnarisation**

(A-D') Medial section of egg chambers expressing Sec6-GFP (A, A'), Sec10-GFP (B, B'), Rab11-GFP (C-C'') and RabX1-YFP (green in D, D'). White boxes (A, B, D) are shown at higher magnifications in (A', B', D'). Orange and blue boxes (C) represent NCC and OCC positions shown at higher magnifications in C' and C'', respectively. Yellow arrow (C'') indicates the sharp drop in apical intensity of Rab11-GFP in OCCs. (E-F') *En face* (E) and medial section (F) of *shi<sup>TS</sup>* egg chamber at stage 9, showing the effect higher levels of NCC  $\beta$ -cat accumulated on the lateral membrane and comparatively lower levels of lateral accumulation on the OCCs (compare yellow arrows at NCC and OCC positions). Scale bar (A-D) = 100  $\mu$ m, (A', E-E') = 50  $\mu$ m, (C'-C'', D') = 20  $\mu$ m, (B') = 10  $\mu$ m. (A-D') images taken by AKC.

At a molecular level alpha-spectrin and integrins have been implicated in the growth of the lateral membrane (Ng, Selvaraj et al. 2016). The heterodimeric integrin complex is made of either  $\beta$ PS or  $\beta_v$  integrin subunits with one  $\alpha$ PS integrin subunits. In the egg chamber, 4  $\alpha$ PS genes ( $\alpha$ PS 1, 2, 3, 4) are expressed at different spatio-temporal positions during development of the egg chamber and heterodimerize with  $\beta$ PS (Dinkins, Fratto et al. 2008). Of these  $\alpha$ PS1 and  $\alpha$ PS2 have been more extensively studied and have been shown to have differential roles

during development. The  $\alpha$ PS1- $\beta$ PS integrin heterodimeric complex is the most prevalent complex between stages 6 to 10A (Delon and Brown 2009).

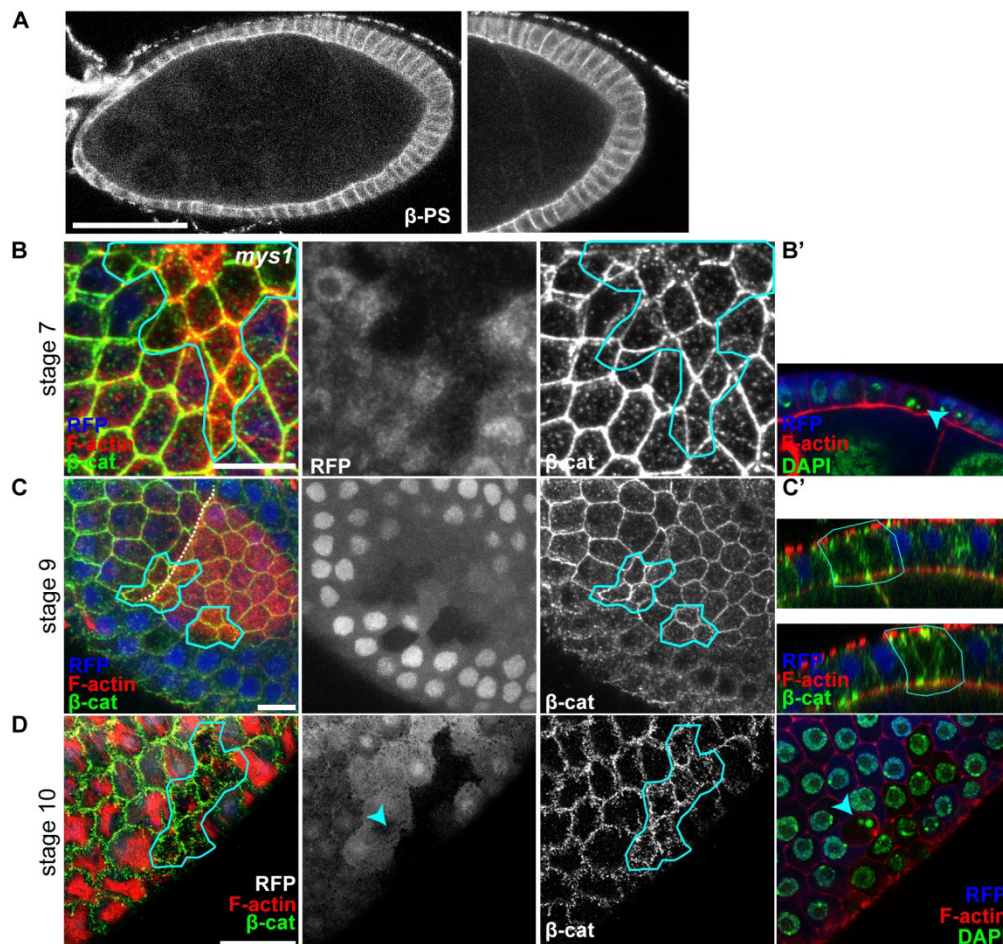


**Figure 41 Volume of follicle cells decreases in  $\beta$ -PS deficient cells**

(A) Medial section of egg chamber labeled with  $\beta$ -PS integrin. Note the strong lateral signal in the FCE. (B-D) *En face* junctional views of stage 7 NCCs, stage 9 NCCs and OCCs and stage 10 OCCs with cyan outlines for *mys*<sup>1</sup> homozygous mosaic clones. Compare areas of the mutant cells in B-D with the neighboring cells. They are smaller. Also compare heights of the mutant cells in C' with the neighboring cells. They are comparable. Cyan arrowheads in B' and D indicate condensed nuclei in rounded cells characteristic of dying cells. Scale bar in A = 50  $\mu$ m, B-D=10  $\mu$ m

Interestingly,  $\beta$ PS integrin is localized to the lateral cell membranes in the FCE (Figure 41, (Dinkins, Fratto et al. 2008)). Effects of removing  $\beta$ PS (*mysospheroid*, *mys*) in mosaic clones include a decreased apical and basal area in early and late stages in both NCCs and OCCs (Figure 41B-D). However, there is no strong effect on the lateral height of mutant cells (Figure 41C'). This suggests that the volume of  $\beta$ PS deficient cells is reduced. Work of Ng *et al* also shows that the volume of  $\beta$ PS-integrin deficient cells is reduced when the entire epithelium is deficient for integrin (Ng, Selvaraj et al. 2016). However, their apical areas are comparable to wildtype cells and heights are reduced. This discrepancy in area reduction in mosaics versus

## DISCUSSION

height reduction upon global  $\beta$ PS-integrin reduction is likely due to more pronounced tissue level effects in the latter. The shorter cell heights likely compensate for the reduced volumes of all cells so that flatter cells still maintain integrity of the epithelium as it accommodates germline growth. Nevertheless, loss of  $\beta$ PS integrin function appears to decrease the volume of epithelial cell by impairing cellular growth. One possibility is that  $\beta$ PS-integrin signals into cellular growth and endocycle pathways. In some instances, we observe  $\beta$ PS integrin deficient cells are rounding up basolaterally and contain condensed nuclear fragments reminiscent of apoptotic cells (Figure 41B', D). Therefore, cellular mechanisms that can control the lateral heights of columnar cells could strongly be coupled to the growth of cells. In support of this idea, some studies in sea urchins have shown lateral Fas II mediated adhesion is important for columnarisation and studies in flies show that removal of Fas II can shorten lateral membranes (Szafranski and Goode 2004, Gomez, Wang et al. 2012)). It would be interesting to decipher the role of such SJ proteins in epithelial cells in zippering up lateral membrane to promote columnar shapes of cells.

Since columnarisation appears to be controlled by growth and lateral membrane extension, the intriguing question of what sets the limit of apical areas as these columnar cell form, arises. The apical area of columnar cell is obtained by relaxing the tension they experienced while in contact with the nurse cells. However, what limits the size of the final apical area of columnarizing cells is unknown. Again, this limit maybe partially be controlled by cell growth as visible in integrin mutant cells. Interestingly, the apical area limit can be changed when neighboring cells are spread out, as is the case in severe phenotypes seen for  $\beta$ -cat (*arm<sup>3</sup>*) mosaics (Figure 42A, B). In *arm<sup>3</sup>* mosaic FCE, neighboring wildtype cells have reduced apical areas and appear pseudostratified to accommodate the expanded surface of *arm<sup>3</sup>* cells. Thus, mechanisms that impinge on sensing the available space and intrinsic cellular growth rates would be interesting to investigate in the future to understand how apical areas of columnar cells are determined.

Extensile behavior as opposed to contractile behavior of the actomyosin cytoskeleton has been shown to be possible in *in silico* studies dependent on the arrangement and crosslinking of polar actin filaments (section 1.3.1, (Gardel, Kasza et al. 2008)). The presence of such networks in the apical cortex of the columnar cells could potentially set the dimensions of the apical area by limiting persistent shrinkage of the apical area of cells smaller than what is observed in columnar cells of FCE. Another possible mechanism driving columnarisation could be pushing forces from NCCs on OCCs to acquire columnar shapes. However, currently known mechanisms of pushing forces generated by filopodia-like protrusions in cells (Ladoux and Mege 2017) do not appear sufficient in magnitude to maintain an increasing number of cells in

columnar shape through development of egg chamber. Furthermore, we have seen no expansion of apical areas of columnar cells when potential pushing forces from NCCs are lost when an epithelial tear appears between NCCs and OCCs (Figure 31A).

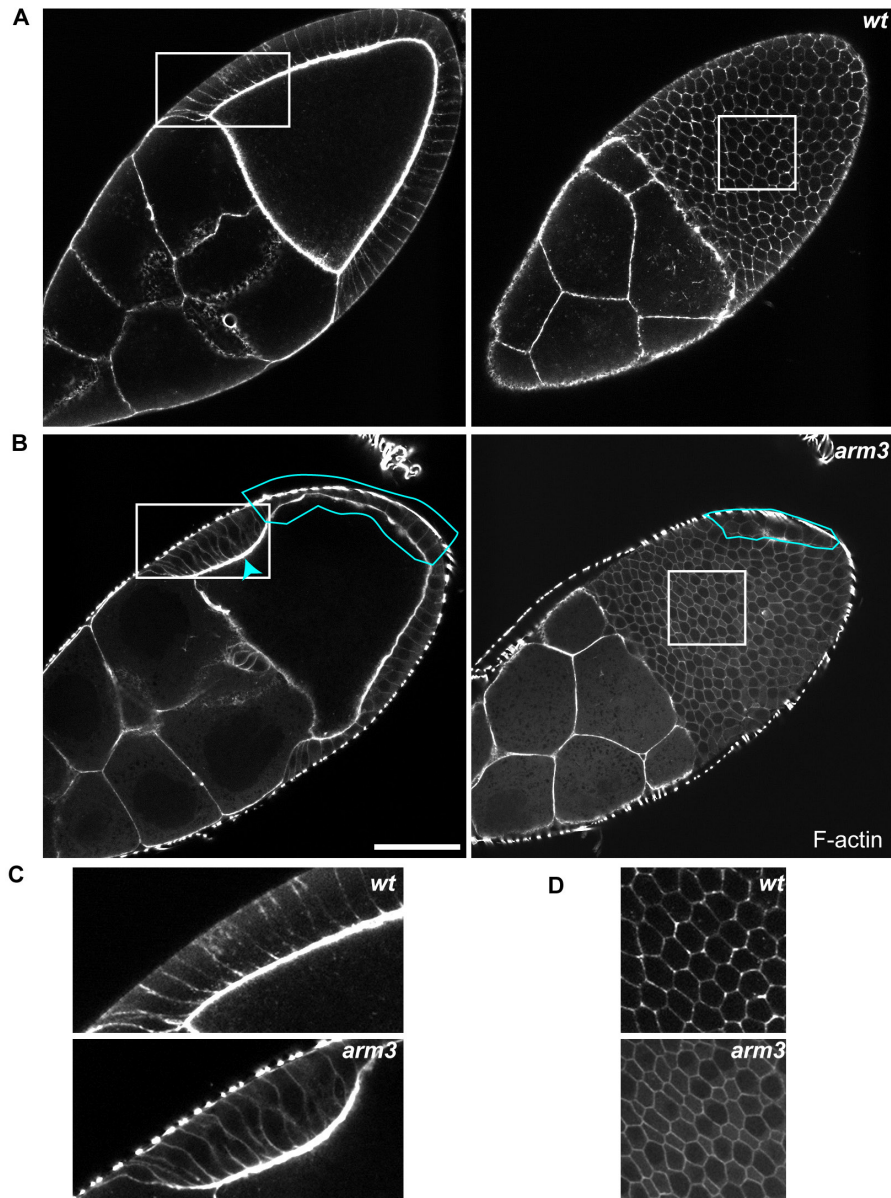


**Figure 42** What sets the limit of apical area in columnar-fated cells?

(A-B) Medial and *en face* sections of wildtype (A) and *arm*<sup>3</sup> mosaic clones (cyan outline) which acquire a dome-like shape with wider areas compared to neighboring cells. Cyan arrowhead points to wildtype cells which appear pseudostratified (false appearance of stacking of multiple layers of cells, even though they are in a monolayer) on the side of the clone compared to *wt* egg chamber where they are more columnar in appearance. (C-D) White boxes in A and B are magnified to show the cell heights (C) and areas (D). Note in *arm*<sup>3</sup> heterozygous neighbors, the organization of the cells with different cross-sectional areas as they squeeze to accommodate in the available space. Scale bar = 50  $\mu$ m.

### **4.2.3 Is there a developmental signal that controls columnar-fate?**

We currently have no evidence that the known main-body fate and posterior cell fates are important for columnar shapes to arise. EGFR signaling is known to suppress the squamous fate in posterior cells. However, EGFR signal implicated in posterior specification in follicle cells is not activated in all cells which become columnar (Horne-Badovinac and Bilder 2005, Wu, Tanwar et al. 2008) indicating that it is not required for columnar shapes to arise over the oocyte. Another candidate specifying columnar shape was Brinker, which is repressed by TGF $\beta$  pathway active in the squamous-fated cells. However, not all columnar-fated cells express Brinker (data not shown, (Chen and Schupbach 2006)). Thus, so far, no columnar fate specifying developmental patterning signal could be identified. Further, if such a development fate exists, it is not sufficient to generate columnar shape, since nurse cell contact suppresses it (discussed in section 4.3.1).

### **4.2.4 Squamous cell shape**

The anterior squamous-fated cells also exclude Myo II and form corrugations suggesting that relaxation of tensile stress occurs at their AJs too. However, they additionally express developmental fates that promote cell flattening independent of nurse cell or oocyte contact (Gonzalezreyes, Elliott et al. 1995). Squamous shape can be viewed as cell shape that has relaxed completely in response to external forces from nurse cell growth as a consequence of developmental fate mediated cytoskeletal relaxation. Cellular mechanisms may impinge on loosening the cytoskeleton and sliding movement over the basement membrane, suggested by decreased levels of Cher, a filament forming Actin remodeler and increased levels of the basement membrane protein Perlecan in anterior cells. Ongoing work in the lab is elucidating these mechanisms.

## **4.3 Sources of external forces during germline growth**

### **4.3.1 Nurse cell and oocyte cortices are different**

A key limitation of this model system was the inability for us to measure the magnitude of forces exerted by the germline on the overlying epithelium and how it affects the cuboidal cell shape. Egg chambers with genetically reduced germline sizes presented columnar cells over the nurse cells and indicate that germline growth and surface area expansion are the primary source of forces on the overlying NCC epithelium mounting a high tension at their AJs (Figure 39).

We show that there are several possibilities for why nurse cells exert stronger forces on the epithelium in comparison to the oocyte. The cortex of the nurse cells is constituted differently compared to the oocyte. The Actin cortex of the nurse cells is not dense as the oocyte

cortex. In addition, the physical distance between the epithelial and the nurse cells surfaces is lesser when compared to the distance between the epithelial and the oocyte surface. Despite the closer apposition of the epithelium to the nurse cells, we could not find evidence for DE-Cad mediated adhesion between the two surfaces to transmit forces. Furthermore, the rounding up of individual nurse cells and hence of the nurse cell compartment can contribute to forces acting on the NCCs, in addition to germline growth. Higher Myo II levels in the nurse cell cortex when compared to the oocyte also supports our conclusion that nurse cell surfaces are dominated by contractility mediated surface minimization. Future experiments need to decipher the signals between nurse cells and the overlying NCCs to mediate effective transmission of these forces. Since we observe that the nurse cell actin cortex has a spike-like Actin imprint of the filipodia extending from the junctional domains of NCCs, the possibility of unidentified biomechanical linkages or a biochemical signal is not ruled out.

In contrast, the dense Actin filament cortex of the oocyte may confer stiffness and the larger physical distance between epithelial and oocyte surfaces compared to epithelial and nurse cell surfaces can potentially decrease the net forces from the surface area expansion due to germline growth that are perceived by the epithelium between stages 6-10A. Intriguingly, the dense Actin cortex of the oocyte and the physical distance between epithelial and oocyte surfaces in stages of nurse cell dumping does not prevent the transmission of forces to the overlying epithelium to promote their flattening. Future molecular characterization of the Actin cortex remodelers (Dahlgard, Raposo et al. 2007) or other oocyte-intrinsic signaling that can potentially change oocyte cortex stiffness in a developmentally programmed manner would be interesting to investigate.

#### **4.3.2 Mechanosensing forces from nurse cells to generate resistance in NCCs**

We conclude that Myo II levels are increased in NCCs as a reaction to nurse cell contact and drop as soon as NCCs come in contact with the oocyte. So how do nurse cells mount a tensile stress mediated by Myo II onto the junctions of the NCCs? Little is known about mechanosensory feedback upon stretch forces in epithelial cells to reinforce Myo II levels. We observed Actin-rich apical spikes in NCCs predominantly at their cell-cell junctions, which could help in mediating a signal from the nurse cell cortex to the apical surface of the epithelium. These spikes could presumably relay a mechanical signal that induces greater stretch in NCC junctions. The apical spectrin network could be instrumental in this process. The spectrin cytoskeleton is known to be a stretch-sensitive cytoskeleton (Deng, Wang et al. 2015, Fletcher, Elbediwy et al. 2015). We show  $\beta_H$ -spectrin behaves like Myo II and shifts out of the junctions. One can speculate that a stretched spectrin cytoskeleton is able to recruit more Myo II

## DISCUSSION

into the apical-medial Myo II network, thus increasing levels of Myo II over the NCCs. Experiments that can identify the levels of stretch on the spectrin cortex by using FRET-tension sensors would be interesting and would help to understand the contribution of spectrin as a mechanosensory cytoskeleton (Krieg, Stuhmer et al. 2017). New scaffolding proteins like Big bang, bind both Myo II and spectrin and have been recently identified to localize in the apical cortex. Such scaffolding proteins could be instrumental in relaying stretch signals from the spectrin cortex to tune the resistance response mounted by Myo II mediated contractility (Forest, Logeay et al. 2018, Tsoumpekos, Nemetschke et al. 2018).

### **4.4 Organ shape is modulated by local contractility in the epithelium**

#### **4.4.1 Local apical contractility from NCCs constrains the nurse cell compartment into elongation**

A lot of work on the egg chamber has focused on understanding how the egg chamber attains its shape. During its development, it undergoes elongation from a near perfect sphere to an ellipsoid with a drop-like anterior tip which post- dumping transforms into a uniform ellipsoidal shape of the mature oocyte. Different stages appear to require different mechanisms to sculpt the egg chamber shape. In the early stages 3-5, recent work implicates the Jak-Stat pathway in shaping the egg chamber (Alegot, Pouchin et al. 2018). Stages 6-8 have been shown to require a polarized basement membrane (Haigo and Bilder 2011) and an atypical Cadherin Fat2 mediated basal F-Actin organization (Aurich and Dahmann 2016). At late stage 9 and 10A, basal Myo II oscillations have been implied to reinforce the DV axis constriction of the egg chamber to generate a corset-like constriction on the DV axis. Increased anterior basement membrane stiffness at stage 8-9 has also been implicated in overall egg chamber shape (He, Wang et al. 2010, Crest, Diz-Munoz et al. 2017). We could exclude the effect of early egg chamber elongation on cell shape gradients and transitions because round egg chambers generated by genetic manipulation of *fat2* still show cuboidal and columnar shapes (Figure 43A-A”). We demonstrate here that interim constraint on the nurse cells from reinforced contractility by enrichment of Myo II and E-cad/ $\beta$ -cat on apical NCC surfaces is important during early to late stage 9 to maintain the overall egg chamber shape. Genetic reduction of contractility or increasing extent of corrugations causes the nurse cells to bulge, nurse cell cluster to round up and change the overall aspect ratio of the egg chamber. Thus, NCC contractility compresses the nurse cell cluster into a more elongated shape during stage 9 (Figure 44A’, B’, C’).

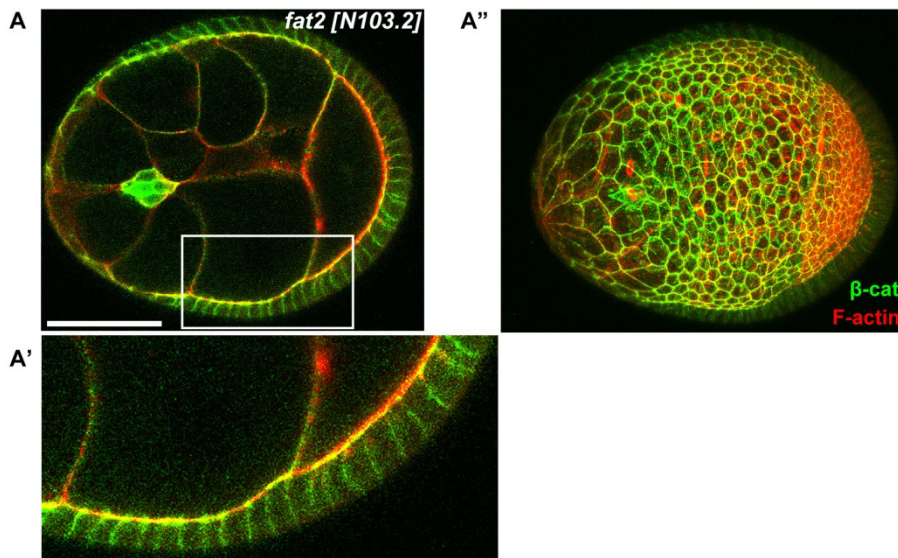


**Figure 43 Round egg chambers show cuboidal-columnar cell shape gradient dependent on germline contact**

(A-A'') Medial sections (A-A') labeled with F-Actin and  $\beta$ -cat shows that round egg *fat2* mutant egg chamber shows a gradient in cell shape. White box in A is magnified in A'. (A'') *En face* junctional view of the same egg chamber shows the gradient in cell shape areas. Scale bar = 50  $\mu$ m.

#### 4.4.2 Completion of cuboidal to columnar shape transitions relies on balance of localized increase in tensile stress and AJ length in NCCs

For the egg chamber to complete cell shape transitions by stage 10A, i.e. when the oocyte has expanded underneath all NCCs, the relative position of the NCCs with respect to the distance from the posterior oocyte pole should be maintained throughout. When the NCCs ectopically flatten due to hypercorrugations upon targeted overexpression of *cno* and *Rac1DN*, their positions relative to the oocyte shifts dramatically towards the anterior pole. This means the rate of oocyte expansion is insufficient for the oocyte to establish contact with the more anteriorly shifted NCCs, thus leading to a delay and even a failure to finish the transitions. Ectopic NCC flattening is also visible in *rok* and *sqh* mutant FCE but to a milder degree if compared to NCC area changes upon junctional length alterations by targeted overexpression of *cno* and *Rac1DN* (discussed in section 4.1.1). This could explain the ability of *rok* and *sqh* mutant FCE to complete the transitions. Thus, the levels of corrugations and contractility very finely balance the apical area size of the cuboidal NCCs in wildtype egg chambers, such that the oocyte can expand underneath the NCCs without delay (Figure 44A, B, C). Therefore, the growth of the germline alone cannot promote proper cell shape transitions. The regulation of epithelial relaxation by corrugations and reinforced contractility is vital to smoothly finishing the transitions. A possible reason for why the egg chambers degrade when there is a delay in

## DISCUSSION

establishing NCC contacts with the oocyte is the presence of a checkpoint, which assesses if the oocyte has encountered the last row of the columnar-fated cells.

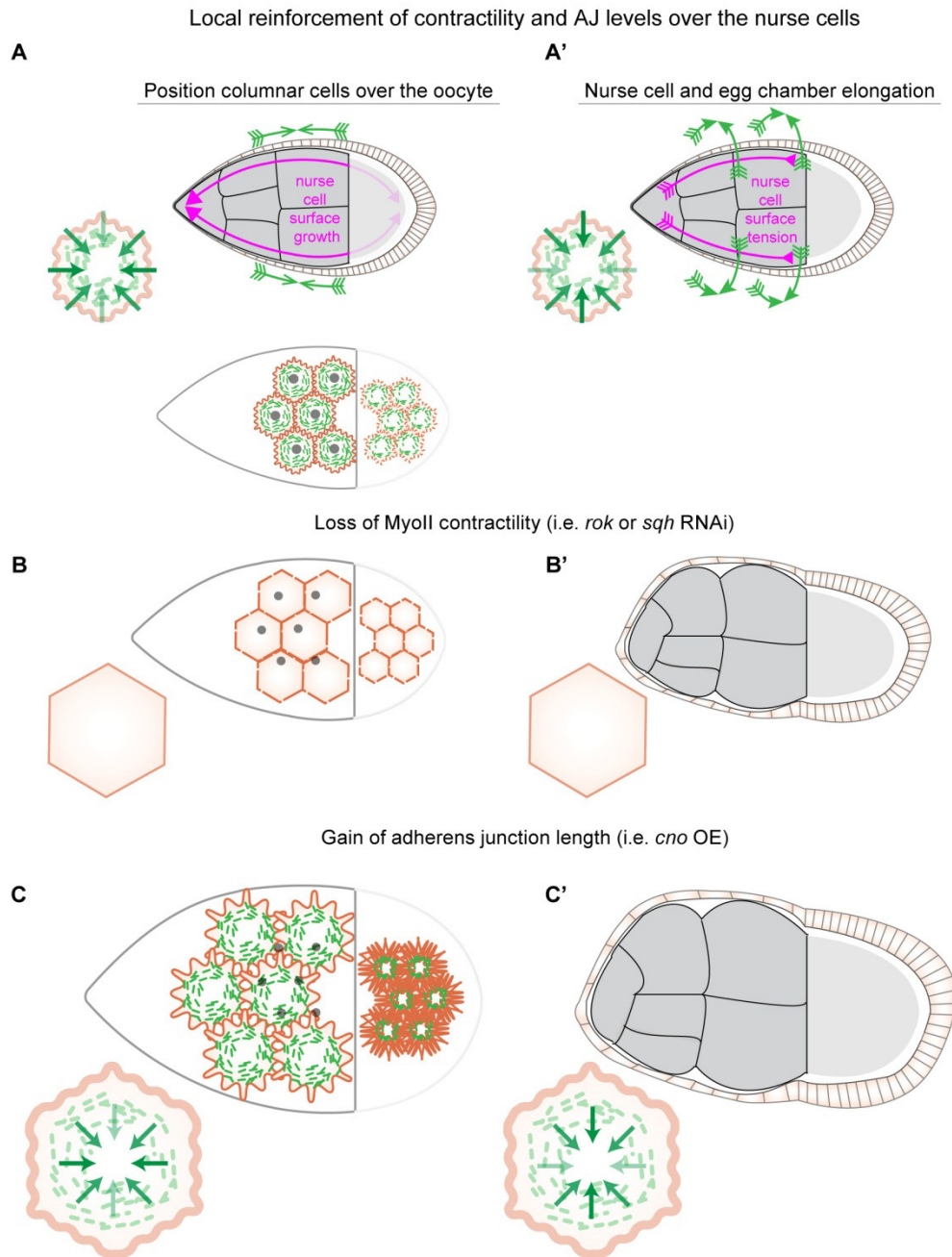


**Figure 44 Balance of local contractility and junction length over the nurse cells controls cell shape transitions and egg chamber shape**

(**A, B and C**) The growth derived surface expansion forces are stronger from the nurse cells compared to the oocyte (pink arrows in **A**) which reinforces the levels of the junction excluded Myo II and junction levels in the NCCs. This reinforcement is important, because in the absence of the Myo II (**B**) or gain of AJ length (**C**), the NCCs flatten more anteriorly. Thus, the position of the cells relative to the oocyte has shifted anteriorly, delaying the completion of cell shape transitions (grey dots mark where their centers of masses should have been, see **B**). The green arrows in cell and egg chamber schemes indicate the dominant AP contractile force vectors that are important to prevent this anterior shift, which are absent in Myo II loss (**B**) or insufficient to resist expansion from excess junction material upon gain of junctions (**C**). (**A', B' and C'**) The nurse cell surface tension tends to round them (pink inward pointing arrows) which are resisted by the NCC Myo II reinforcement with dominant DV contractile force vectors. This resistance is lost in Myo II reduction (**B'**) or upon increasing the length of the AJs (**C'**), resulting in their bulging and rounder overall egg chamber shape.

## 5 Conclusion

With this work, we show that an autonomous cellular program primes the epithelium to relax to external forces exerted on it. The external forces from a neighboring tissue that grows and expands its surface area and its intrinsic shape can reinforce local resistance even as the overall epithelium relaxes. This balance of resistance and relaxation to external forces result in cuboidal and columnar cell shapes. We demonstrate that AJ lengthening and junctional exclusion of Myosin II facilitates epithelial tension relaxation to germline growth related forces. Furthermore, in this relaxed state, we provide evidence that cortical Myosin II coupled to AJs maintains cuboidal cell shape by locally resisting germline growth and shape related forces and facilitates cuboidal- columnar cell shape transition. Finally, we show that the local resistance in the epithelium to the external germline forces, in turn guides the shape of the germline and hence the overall egg chamber. These processes arise from a cell-autonomous epithelium relaxation program and a superimposed non-autonomous signal inducing local resistance to external forces from the germline.

Clearly dissecting the mechanical contributions of the cell autonomous mechanisms from that of the external forces from the germline has been a limitation in this study. Furthermore, cleaner mechanical perturbation methods are needed to measure external forces and to understand the biomechanical properties like stiffness of the epithelium and how it is modulated in development. In this work, we only discuss tensile stress as the cumulative result of forces on junctions and stiffness of junctions. Dissecting individual role of these factors has not been possible. Nevertheless, this work provides a foundation in understanding organ sculpting when epithelial tissue interacts with a non-epithelial tissue during development and has strong relevance in metazoan development and disease. Finding evidence of epithelial relaxation programs in epithelial tissues in different organs and model organisms could be vital in understanding how they maintain their integrity despite so many external stresses exerted on them during organogenesis. Further, the identification of proteins and signaling mechanisms that are important to fine-tune actomyosin contractility and adherens junction remodeling to balance the intrinsic force-generating ability of cells against external forces to result in morphogenetically relevant amount of forces for epithelial cell shape changes remains an open field of research.

## 6 Materials and Methods

### 6.1 Fly husbandry and genetic manipulation systems

All stocks and experimental crosses were maintained on standard fly food at 18 °C or 25 °C. Two genetic tools now prolifically used in fly genetics were routinely employed in this work. For detailed genotypes used in this study refer to Table 1. For *shil*<sup>TS</sup> temperature sensitive mutants, females reared at 18 °C were given 1-hour heat shock at 30 °C and dissected immediately.

#### a FLP-FRT system

This approach is used to generate mosaic tissues with homozygous mutant cells and heterozygous cells which are aphenotypic. It is based on a site-specific (FRT recombination target sites) mitotic recombination induced by a yeast recombinase called flippase (FLP). An FRT site has been introduced near a mutation of interest on a chromosome arm and another FRT site carries a wildtype copy of the gene with a clonal marker like GFP. The two FRT sites are brought together in the progeny of fly strains carrying each FRT site individually. In addition, one of the strains carries the flippase which is expressed under spatio-temporal control of a chosen promoter. In our case, the flippase is under the control of a heat-shock promoter that allows expression of the flippase upon a 37°C heat-shock. When the flippase is produced in mitotically active cells, recombination is induced at the FRT sites which leads to the generation of patches of cells which are either homozygous for the mutant or homozygous for the clonal marker or cells which remain unrecombined. Thus, follicle epithelial mosaic clones are generated by mitotic recombination occurring until stage 6. Flippase expression was induced in young adult females (typically 1-3 days after eclosion) using a heat-shock for 1 h at 37°C. For germline clones, flippase expression was induced in larvae when the germline stem cells are still mitotically active, at 96 hr after egg-lay (AEL) and again at 120 hr AEL for 1 hour at 37°C. The flies were fed yeast paste for 48 to 72 hr before dissection (Golic and Lindquist 1989, Xu and Rubin 1993, Cox, Lu et al. 2001)

#### b Gal4/UAS expression system

This system utilizes the yeast UAS promoter element that is activated by binding of transcriptional activator Gal4. The UAS elements are upstream of a transgenic overexpression

## MATERIALS AND METHODS

sequence or an RNAi element for a gene of interest. The Gal4 expression can be controlled in a tissue-specific manner by placing it downstream of tissue specific promoters. Thus, when Gal4 is expressed in a tissue during development, it can activate the expression of the RNA interference or overexpression for one or more genes of interest. In this study, the typical tissue specific promoter for the follicle cell epithelium is one associated with *traffic-jam* gene and for the germline is a combination of *otu* and *nanos* gene promoter elements.(Brand and Perrimon 1993)

### 6.2 Dissection and immunohistochemistry of egg chambers

Ovaries were dissected and fixed in 4% formaldehyde/PBS for 15 min at 22°C. Washing was performed in PBS + 0.1 Triton X-100 (PBT) for 15 min. Ovaries were incubated with primary antibodies in PBT overnight at 4°C (Table 2). No blocking was used. We tested antibodies stained membrane and cytoskeleton structures better without blocking. Unspecific binding of both mono- and poly- antibodies could also be tested to be minimal (for e.g., see Figure 21). Ovaries were incubated with secondary antibodies (coupled to Alexa Fluorophores, Table 3), DAPI (0.25 ng/μl) and Phalloidin (Table 3, Table 4) for 2 h at 22 °C. Egg chambers were mounted using Molecular Probes Antifade Reagents (Table 4). Samples were imaged using a Leica TCS SP5 or SP8 confocal microscopes (Table 5). Samples were processed in parallel and images were acquired using the same confocal settings, if fluorescence intensities had to be compared. Images were processed and analyzed using Fiji (ImageJ 1.48b).

### 6.3 Electron microscopy

Isolated ovarioles were incubated in Schneider's medium containing 2.5% glutaraldehyde and 2% paraformaldehyde for 30 min, followed by incubation in PHEM buffer with fixatives for additional 30 min. Samples were flat embedded in 2% low melting agarose and placed at 4 C° for 10 minutes until polymerization. Blocks of agarose were transferred to PHEM buffer with fixatives at 4°C overnight. Post-fixation, embedding, and imaging were performed as described in (Schuessel, Hoernstein et al. 2016).

### 6.4 Live imaging culture conditions

Individual ovarioles were dissected out of the muscle sheet and were mounted with a minimal volume of Schneider's medium supplemented with Insulin and FBS as previously described (He, Wang et al. 2011), on a standard microscope slide with spacers fashioned from double-sided tape and covered with a coverslip and sealed with Halocarbon oil. FLIM and laser ablation experiments were performed on freshly dissected ovariole samples prepared every 20 minutes.

### 6.4.1 FLIM imaging

Live egg chambers expressing DE-Cad (TS) and DE-Cad (TS control) (Borghi, Sorokina et al. 2012, Cai, Chen et al. 2014, Gayrard and Borghi 2016) were imaged using the Leica TCS SP5 MP-FLIM setup, equipped with 40X/oil objective, 2-photon excitation at  $\lambda=885$  nm, 1.4W, 80 MHz laser power for exciting mTFP. Emission spectral window of 463-501 nm was used to capture emission of mTFP. 256X256 pixel area images are acquired for 90 s at 3 s intervals for sufficient number of photons to be acquired for life-time analysis (typically in the order of 103 photons) without photobleaching the sample.

### 6.4.2 Laser ablation

Laser ablations on live egg chambers expressing *shg-GFP* (Huang, Zhou et al. 2009) were performed using the inverted microscope set up described previously (Farhadifar, Roper et al. 2007). 32 pulses/ $\mu\text{m}$  of the laser at 1000 Hz,  $\lambda=355\text{nm}$  was applied at a length of 0.22  $\mu\text{m}$  for cell-cell junction ablations. For medial cortex ablations, circular cuts were made with a radius varying from 0.13 to 0.29  $\mu\text{m}$  depending on the size of the apical area. Images were taken every 0.5 s for up to 40 s.

### 6.4.3 Collagenase treatment of egg chambers

Individual ovarioles were dissected from the surrounding muscle sheet and were incubated in Schneider's medium supplemented with 1000 Units/ml collagenase (CLSPA; Worthington Biochemical Corp) for up to 30 minutes, rinsed in 1X PBS three times and then fixed and immunostained as described above individually in an 8-well tissue culture dish.

## 6.5 Image Analysis and Quantification using Fiji

All images and movies were analyzed in FIJI (ImageJ 1.48b) (Schindelin, Arganda-Carreras et al. 2012), unless otherwise stated. Graphs were generated with Microsoft Excel 2007 and R version 3.2.0. Statistical tests were performed in R 3.2.0. Data sets were checked for normality of distribution with Shapiro test and homogeneity of variances by applying Bartlett's or Levene's test. Statistical test used in each analysis is indicated in figure legends.  $\alpha$  value for statistical analysis was set to 0.05 ( $\alpha = 0.05$ ).

### 6.5.1 Quantification of cell areas, heights and corrugations

Apical epithelial cell areas were measured at the level of AJs using the polygon tool. Heights were measured using the line tool in a medial cross-section of the egg chambers. Junctional corrugations were quantified by forming a ratio of (1) junction length obtained by directly tracing the  $\beta$ -cat signal between two vertices using the segmented line tool and (2) the distance between the same vertices obtained by using the straight-line tool. This value would

theoretically = 1 when the junction is a straight line between 2 vertices and >1 when (1) > (2). Junctional roughness is defined as junctional corrugation minus 1.

### 6.5.2 Fluorescence intensity quantification

Measurement of fluorescence intensity traces for junction and cytoskeleton markers were drawn using line tools in FIJI. The surface occupied by squamous fated cells was approximated by a line of the same length as that was obtained for OCCs in the same egg chamber. The remaining segment between ‘squamous-fated’ and OCC cells was denoted as NCCs (only for quantifications in Figure 12, Figure 13, Figure 34).

### 6.5.3 mTFP fluorescence life-time analysis

For performing the life-time analysis, fluorescence decay curves were calculated by Time-Correlated Single Photon Counting (TCSPC) in the built-in Leica software. A one-component exponential decay function is fit to a “hotspot” in the ROI (Figure 45A). The hot-spot was chosen in the ROI such that the  $\chi^2$  value of its fit is close to 1 and a good background correction called Instrument Response Function (IRF) can be generated. The fit equation for the decay curve is of the form

$$I(t) = I_0 * e^{-(t/\tau)}, \text{ where } \tau \text{ is the lifetime of the mTFP in this case.}$$

4 pixels are binned around the hot spot to calculate the fit. A time range along the decay axis is chosen that best describes the decay of fluorescence in the hot-spot. A threshold is chosen to suppress dark pixels from being used in the fitting.  $\tau_m$  is obtained from the fit of decay at the hotspot (Figure 45A, B). Further, a decay matrix is calculated to obtain the life-times of different positions in the ROI. An unweighted (by pixel intensity) histogram is generated of the frequency of number of pixels with specific life-times.  $\tau_{\text{cross}}$  approximates the average life-time from the histogram in the ROI (Figure 45C).

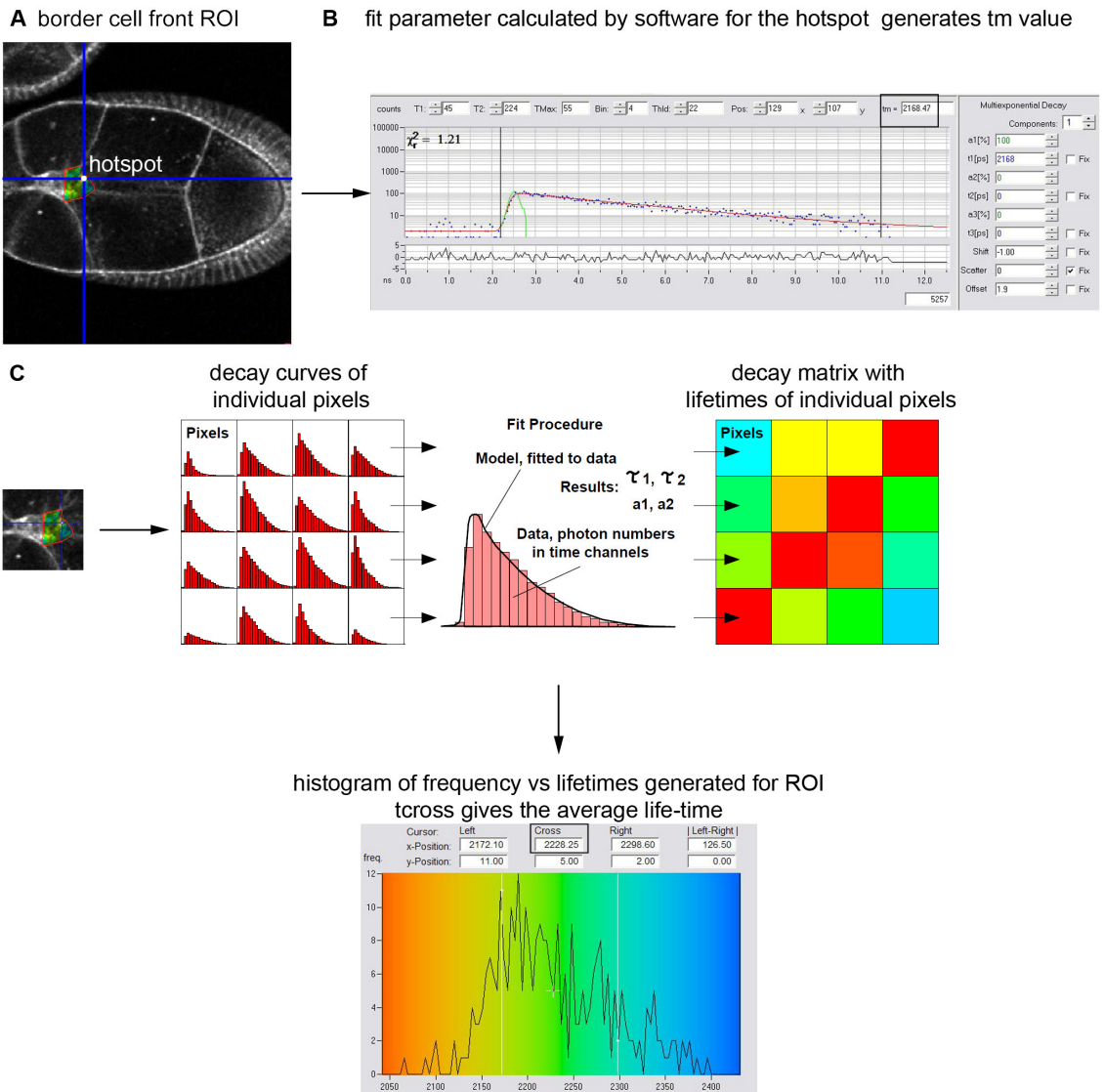


**Figure 45 FLIM data analysis**

(A) A representative FLIM image with the border cell front as the ROI. The hotspot is indicated as a white circle. (B) The fit parameters are calculated by the Leica software and  $\tau_m$  (black box) is generated. (C) For all the pixels in the ROI, fluorescence decay curves are generated and converted into a matrix with  $\tau$  values for individual pixels. These are then plotted as a histogram of the frequency of occurrence of specific lifetimes.  $\tau_{\text{cross}}$  (black box) estimates the average life-time for the ROI. (C) adapted from Leica MP-FLIM and D-FLIM handbook.

#### 6.5.4 Analysis of vertex displacement, cortical area changes and initial recoil velocities after laser ablation

For ablation of adherens junctions, a kymograph of the adherens junctions between the two vertices was generated. The vertices of the ablated junction were tracked pre-and post-ablation and distances between the vertices were obtained for each time point over the period of recording (Figure 46A-A’). For ablation of the apical-medial cortex, macros were written to segment cellular junctions and obtain areas of the cells which underwent ablation. The segmentation output was manually curated if necessary (Figure 46B-B’).

For each ablation in an egg chamber, at any post-ablation time point the change in distance between the vertices (line cuts) or area (circular cuts) relative to the average distance or average pre-ablation area from 10 pre-ablation time points was obtained. These vertex distance and area changes were normalized to the average junction length or area across all the samples. Finally, the mean relative vertex distance and area changes were plotted as a function of time. Initial velocities calculated in Figure 20 were obtained by calculating the slope of the curve between  $t=0$  and  $t= 0.5$  s which is approximately the linear phase of the curves. The SEM was calculated by the method of propagation of uncertainty. A double exponential fit (Farhadifar, Roper et al. 2007, Landsberg, Farhadifar et al. 2009) was applied to estimate the initial velocity of the average curves:  $d(t) = d_1(1 - e^{-t/T_1}) - d_2(e^{-t/T_2} - e^{-t/T_1})$ , where  $T_1$  is the slow relaxation time and  $T_2$  is the fast relaxation time of the vertices of ablated cell bonds.  $d_1$  is the final change of distance between vertices of ablated cell bonds at  $t \rightarrow \infty$  and  $d_2$  is the change in distance due to fast relaxation only. The fit parameters were calculated, and the standard error was determined (Table 28). The initial velocity  $v_0$  was obtained by solving this equation:  $v_0 = d_1/T_1 - d_2(1/T_1 - 1/T_2)$  as previously described (Landsberg, Farhadifar et al. 2009). The standard error of  $v_0$  was determined by using the method of propagation of uncertainty. The velocities estimated for the OCCs have a very large standard error and the fit parameters for cuts in the OCCs are a poorly estimated (Table 29). Thus, we present initial velocities (Figure 20) obtained by calculating the slope of the curve between  $t=0$  and  $t= 0.5$  s which is expected to approximately cover the linear phase of the curves (Mayer, Depken et al. 2010).

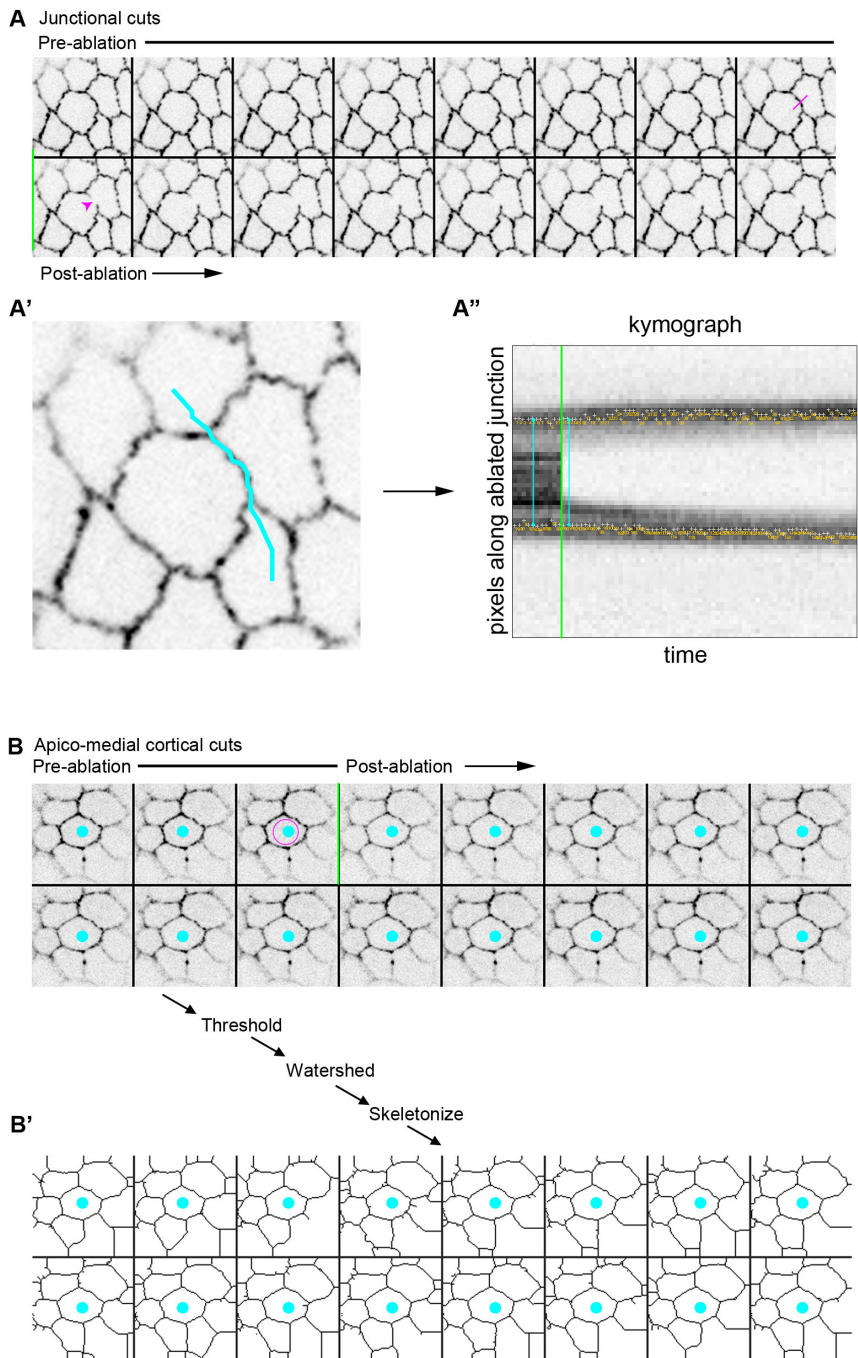


**Figure 46 Laser ablation data analysis**

**(A-A'')** Vertex recoil analysis. Montage of time lapse images (interval of 0.5s) pre-ablation, time of ablation (green line) and post-ablation are shown. Magenta line marks the junction that was ablated and can be tracked by the magenta arrowhead post-ablation. **(A')** A single image from the time lapse shown with a cyan line drawn across the vertices of the junction ablated in (A). **(A'')** A kymograph of the line drawn in (A') which tracks the position of the pixels on this line with time. The distance between vertices can be tracked pre- and post- ablation for every time interval. Shown here are two representative vertex distances (cyan lines), green line represents time point of ablation. **(B-B')** Apico-medial cortical cuts. Montage of time lapse images (interval of 0.5s) pre-ablation, time of ablation (green line) and post-ablation are shown. The cell cortex that was ablated can be tracked with the cyan dots and the magenta circle marks the region of ablation (B). The images are thresholded, passed through watershed and skeletonizing algorithms to obtain segmented cell outlines whose areas then can be measured through time (B').

### 6.5.5 Germline aspect ratio measurements

Using the line tool in FIJI, the maximum width (W) and the maximum length (L) of the nurse cell compartment in a medial section of stage 10 egg chambers was measured and the ratio of width to length was obtained. Total lengths of germline were obtained by measuring a line along the AP axis.

### 6.5.6 Germline area and nurse cell-oocyte area ratio measurements

Using the Polygon tool in FIJI, the traces of the nurse cell compartment and oocyte were generated in the medial section of the egg chambers. Both areas were summed for total germline area and used as a proxy for volume of egg chamber. Ratio of nurse cell to oocyte for relative size was obtained.

## 6.6 Fly stocks

**Table 1 Fly stocks: All fly stocks used in this study are listed with their source.**

BL-Bloomington Stock Center, Indiana, VDRC – Vienna Drosophila Resource Center.

<i>Stock</i>	<i>Source</i>
<i>w[118]</i>	BL3605
<i>TJ-GAL4, Mef20-GAL80/CyO (float)</i>	Sally Horne Badovinac
<i>TJ-GAL4, UAS-CD8tom; UAS-Dcr2/TM6C</i>	David Bilder
<i>MTD GAL4-P{otu-GAL4::VP16.R}1, w[*]; P{GAL4-nos.NGT}40; P{GAL4::VP16-nos.UTR}CG6325[MVD1]</i>	BL 31777
<i>ubiGFP FRT101; e22C-GAL4, UAS-FLP/CyO line C</i>	Joe Lipstick
<i>ubi-mRFP, hsFLP [122], FRT19A/FM7</i>	Joe Lipstick
<i>hsflp [122]; Sp/CyO, ubi-GFP; FRT82B ubi-mRFP/TM6c</i>	Elizabeth Knust
<i>FlyFos (mirr::TT-GFP-NLS-FLAG )</i>	VDRC 318430
<i>dpp-LacZ [10638]/CyO; Dr/TM6c</i>	David Bilder
<i>Sp/CyO; pointed LacZ (998/12) /TM6c</i>	Doug Harrison
<i>w; vkg-GFP; FRT80 fat2 [N103.2] / TM6c</i>	Sally Horne-Badovinac
<i>Sp/CyO; Acf1 [1] /TM6c</i>	Peter Becker
<i>UAS-shg-RNAi</i>	BL38207
<i>kst::GFP</i>	BL60193
<i>ed::GFP [MI01552] / SM6a</i>	BL34211
<i>sqh-Rok::GFP</i>	BL52289
<i>cher::GFP-ST-F [MI07480]/TM3 Sb, Ser</i>	BL60261
<i>trol::GFP-ST-F [M104580]</i>	BL60214
<i>baz&gt;GFP (CC01941, I)</i>	Flytrap CC01941
<i>zip&gt;GFP (CC01626, II)</i>	Flytrap CC01626
<i>sqh:sqh-GFP/ CyO; Dr/TM6c</i>	David Bilder
<i>hsflp; FRT40A sqh:GFP/CyO ubi GFP; Dr/Tm6c</i>	Yohanns Bellaiche
<i>FRT40A sqh:RFP/CyO</i>	Yohanns Bellaiche
<i>UASp-Utrophin-GFP / TM3</i>	Katja Röper
<i>UAS-rok-RNAi (JF03225/III)</i>	BL28797

<i>FRT9-2 baz [Xi106] /FM7</i>	Andreas Wodarz
<i>ovo[D2], FRT9-2/C(1)DX, y[1] f[1]/Y; hsFLP38</i>	BL 1843
<i>UAS-sqh RNAi (HMS00830/III)</i>	BL33892
<i>FRT101 sqh[1]/FM</i>	Muriel Grammont
<i>UAS-alpha-cateninRNAi (107298/KK/II)</i>	VDRC 107298
<i>UAS-aPKC RNAi (HMS01320/III)</i>	BL34332
<i>UAS-crb RNAi (GD/39177/II) ; MKRS/TM6n</i>	Elizabeth Knust
<i>UAS-cno/CyO; UAS-cno/Tm3 Ser</i>	Ana Carmena
<i>w; UAS GFP::Cno</i>	Ana Carmena
<i>UAS-Rac1<sup>N17</sup></i>	BL6292
<i>Cad99C::GFP</i>	BL 44967
<i>FRT80B ubi-PH::GFP/TM6b</i>	Yohanns Bellaïche
<i>DEcad::GFP/CyO</i>	BL60584
<i>w;FRT82B crb [D88-2] /TM6b</i>	Elizabeth Knust
<i>w;FRT82B crb [D88-3] /TM6b</i>	Elizabeth Knust
<i>w; FlyFos crb [Y10A] /CyO</i>	Elizabeth Knust
<i>w;FRT82B crb [8F105] /TM6b</i>	Elizabeth Knust
<i>FRT 82B crb [11A22] / TM6b</i>	Elizabeth Knust
<i>vkg&gt;GFP (CC00791, II)</i>	Flytrap CC00791
<i>UAS-GMA-Cherry / Cyo; Dr/TM6c</i>	Frank Schnorrrer
<i>UAS-Ncad-RNAi (1093/GD/II)</i>	VDRC1093
<i>w*; snaSco/CyO; P{Ubi-shg-tension-sensor}3/MKRS</i>	BL58365
<i>w*; snaSco/CyO; P{Ubi-shg-tension-sensor-control}3</i>	BL58368
<i>sec6::GFP</i>	VDRC318479
<i>sec10::GFP</i>	VDRC 318483
<i>RabX1::eYFP</i>	BL 62562
<i>Rab11::eYFP</i>	BL 62549
<i>FRT19A mys [1]/Fm7c</i>	BL23862
<i>shi[ts1]</i>	BL7068
<i>FRT101 arm3</i>	Also called <i>armXP33</i> (Peifer and Wieschaus 1990)
<i>hsflp[122]/+;FRT42D ubi-GFP/</i>	David Bilder
<i>FRT42D shgR69b</i>	Ulrich Tepass

## 6.7 Antibodies

### 6.7.1 Primary antibodies

**Table 2 Primary antibodies: Antigen, Source, Catalog number, Dilution and Manufacturer**

<i>Antigen</i>	<i>Source</i>	<i>Cat #</i>	<i>Dilution</i>	<i>Manufacturer/ Provided by</i>
MRLC-1P	Guinea pig	--	1:400	Robert Ward
β-catenin	Mouse	N27A1	1:100	DSHB
DE-cadherin	Rat	DCAD2	1:50	DSHB
GFP	Rabbit	G10362	1:200	Thermo Fisher
RFP	Rat	5F8	1:20	Heinrich Leonhardt,ChromoTek
Dlg	Mouse	4F3	1:100	DSHB

## MATERIALS AND METHODS

N-Cad	Rat	DN-EXH8	1:20	DSHB
Crb	Rat	--	1:2000	Elizabeth Knust
PKC $\zeta$	Mouse	H-1, sc-17781	1:50	Santa Cruz
$\beta$ -gal	Mouse	Z378B	1:1000	Promega
P-	Rabbit	3149P	1:250	Cell Signaling
Ezrin/ERM(T567)				
Cno	Rabbit	--	1:400	Ana Carmena

### 6.7.2 Secondary antibodies and Phalloidin

Table 3 Secondary antibodies: Antigen, Conjugate, Source, Dilution and Manufacturer

<i>Antigen</i>	<i>Conjugate</i>	<i>Source</i>	<i>Dilution</i>	<i>Manufacturer/ Provided by</i>
Mouse (pre-cleared)	Alexa 488	Goat	1:400	Abcam
	Alexa 555	Donkey		
	Alexa 647	Goat		
Rat	Alexa 488	Goat	1:400	Life Technologies GmbH, Darmstadt
	Alexa 555	Goat		
	Alexa 647	Goat		
Rabbit	Alexa 488	Goat	1:400	Life Technologies GmbH, Darmstadt
	Alexa 555	Goat		
	Alexa 647	Goat		
Guinea pig	Alexa 647	Goat	1:400	Life Technologies GmbH, Darmstadt
Phalloidin	Alexa 488		1:100	Life Technologies GmbH, Darmstadt
	Alexa 647		1:100	
	TritC		1:400	

### 6.8 Consumables

Table 4 Buffers and reagents

<i>Buffer/Reagent</i>	<i>Manufacturer</i>
DAPI	Sigma-Aldrich Chemie GmbH, Munich
Paraformaldehyde	Science Services GmbH, Munich
PBS	Sigma-Aldrich Chemie GmbH, Munich
Triton-X 100	Sigma-Aldrich Chemie GmbH, Munich
Schneider's medium	
Shields and Sang medium	Sigma-Aldrich Chemie GmbH, Munich
SlowFade® Antifade Kit (Cat# S2828)	Life Technologies GmbH, Darmstadt
SlowFade® Gold Antifade reagent (Cat# S36936)	Life Technologies GmbH, Darmstadt
Collagenase (CLSPA, Cat# LS005275)	Worthington Biochemical Corporation, Lakewood

## 6.9 Equipment

### 6.9.1 Microscopes

Table 5 Microscopes with key equipment

<b>Microscope &amp; Manufacturer</b>	<b>Equipment</b>
Stereoscopic Zoom Microscope <b>SMZ745</b>	SMZ745 zooming body with C-PS plain focusing stand <b>Eyepiece:</b> C-W10XB, 10x/22 <b>Light source:</b> KL 1500 LCD with flexible guides (Schott AG) Halogen lamp 15V.150Wm Type 6423FO (Philips)
Confocal laser scanning microscopes <b>Leica TCS SP5</b>	<b>Lasers:</b> Continuous: Diode laser $\lambda=405\text{nm}$ , Argon laser $\lambda=458,476,488,514\text{ nm}$ DPSS Laser $\lambda=561\text{nm}$ , 10mV HeNe Laser $\lambda=633\text{nm}$ <b>Objectives:</b> HCX PL APO Lambda Blue 20x/0.7 oil HCX PL APO Lambda Blue 63x/1.4 oil <b>Emission filters:</b> spectrally adjusted <b>Detectors:</b> GsAsP hybrid detectors, PMTs
<b>Leica TCS SP8</b>	<b>Lasers:</b> Pulsed: visible White light laser, power =1.5mW, $\lambda=470 - 670\text{nm}$ with integrated pulse picker = 78, 39, 19.5, 9.75MHz) Continuous: UV Diode, power = 50mW, $\lambda=405\text{nm}$ <b>Objectives:</b> HC PL APO 20x/0.75 multi imm HC PL APO CS2 40x/1.30 oil HC PL APO CS2 63x/1.40 oil <b>Emission filters:</b> spectrally adjusted <b>Detectors:</b> GsAsP hybrid detectors, PMTs
<b>Zeiss LSM880</b>	<b>Lasers:</b> Continuos: Diode laser $\lambda=405\text{nm}$ , Argon laser $\lambda=458,476,488,514\text{ nm}$ DPSS Laser $\lambda=561\text{nm}$ , 10mV HeNe Laser $\lambda=633\text{nm}$ <b>Objectives:</b> C-Achroplan 40x/0.80 oil Plan-Apochromat 63x/1.4 oil

---

*Emission filters:* Band pass filters  
*Detectors:* PMTs

---

### 6.9.2 Other technical equipment

Table 6 Technical equipment

<i>Equipment</i>	<i>Manufacturer</i>
Incubator (18 °C), Percival	CLF Plant Climatics GmbH, Wertingen
Incubator (25 °C), Mir-154,	Panasonic Biomedical Sales, Europe
Nutating mixer	VWR International GmbH, Darmstadt
Vortex mixer	Scientific Industries, Inc., New York
Water bath	Julabo GmbH, Seelbach
Coverslips	Gerhard Menzel GmbH, Braunschweig
Dissection dishes	Science Services GmbH, Munich
Double sided tape #5338	tesa
Forceps	Fine Science Tool, Dumont, Switzerland
Immersion oil 518F	Carl Zeiss, Jena
Microscope slides	Carl Roth GmbH +Co. KG, Karlsruhe
Transparent nail polish	
Reaction tubes, Rotilab®	Carl Roth GmbH +Co. KG, Karlsruhe

### 6.9.3 Software

Table 7 Softwares

<i>Software</i>	<i>Developer</i>
Office Suite 2007, 2016	Microsoft
Adobe Photoshop CS5.1	Adobe Systems
Adobe Illustrator CS5.1	Adobe Systems
R	Ross Ihaka, Robert Gentleman , University of Auckland
RStudio 3.2.0	Joseph J Allaire
ImageJ 1.48b	Wayne Rasband, National Institutes of Health

## References

- Akhtar, N. and N. A. Hotchin (2001). "RAC1 regulates adherens junctions through endocytosis of E-cadherin." Molecular Biology of the Cell **12**(4): 847-862.
- Alegot, H., P. Pouchin, O. Bardot and V. Mirouse (2018). "Jak-Stat pathway induces *Drosophila* follicle elongation by a gradient of apical contractility." Elife **7**.
- Aurich, F. and C. Dahmann (2016). "A Mutation in *fat2* Uncouples Tissue Elongation from Global Tissue Rotation." Cell Rep **14**(11): 2503-2510.
- Banerjee, S., A. D. Sousa and M. A. Bhat (2006). "Organization and function of septate junctions: an evolutionary perspective." Cell Biochem Biophys **46**(1): 65-77.
- Bastock, R. and D. St Johnston (2008). "*Drosophila* oogenesis." Curr Biol **18**(23): R1082-1087.
- Bate, M., Martinez Arias, M., Ed. (1993). The development of *drosophila melanogaster*.
- Bauer, R., B. Loer, K. Ostrowski, J. Martini, A. Weimbs, H. Lechner and M. Hoch (2005). "Intercellular communication: the *Drosophila* innexin multiprotein family of gap junction proteins." Chem Biol **12**(5): 515-526.
- Baum, B. and M. Georgiou (2011). "Dynamics of adherens junctions in epithelial establishment, maintenance, and remodeling." J Cell Biol **192**(6): 907-917.
- Baum, B. and N. Perrimon (2001). "Spatial control of the actin cytoskeleton in *Drosophila* epithelial cells." Nat Cell Biol **3**(10): 883-890.
- Bilder, D. and S. L. Haigo (2012). "Expanding the morphogenetic repertoire: perspectives from the *Drosophila* egg." Dev Cell **22**(1): 12-23.
- Blanchard, G. B., S. Murugesu, R. J. Adams, A. Martinez-Arias and N. Gorfinkiel (2010). "Cytoskeletal dynamics and supracellular organisation of cell shape fluctuations during dorsal closure." Development **137**(16): 2743-2752.
- Borghi, N., M. Sorokina, O. G. Shcherbakova, W. I. Weis, B. L. Pruitt, W. J. Nelson and A. R. Dunn (2012). "E-cadherin is under constitutive actomyosin-generated tension that is increased at cell-cell contacts upon externally applied stretch." Proc Natl Acad Sci U S A **109**(31): 12568-12573.
- Brand, A. H. and N. Perrimon (1993). "Targeted gene expression as a means of altering cell fates and generating dominant phenotypes." Development **118**(2): 401-415.
- Brasch, J., O. J. Harrison, B. Honig and L. Shapiro (2012). "Thinking outside the cell: how cadherins drive adhesion." Trends Cell Biol **22**(6): 299-310.

## REFERENCES

- Brigaud, I., J. L. Duteyrat, J. Chlasta, S. Le Bail, J. L. Couderc and M. Grammont (2015). "Transforming Growth Factor beta/activin signalling induces epithelial cell flattening during *Drosophila* oogenesis." *Biol Open* **4**(3): 345-354.
- Bryant, D. M. and J. L. Stow (2004). "The ins and outs of E-cadherin trafficking." *Trends Cell Biol* **14**(8): 427-434.
- Bulgakova, N. A. and N. H. Brown (2016). "*Drosophila* p120-catenin is crucial for endocytosis of the dynamic E-cadherin-Bazooka complex." *J Cell Sci* **129**(3): 477-482.
- Bulgakova, N. A. and E. Knust (2009). "The Crumbs complex: from epithelial-cell polarity to retinal degeneration." *J Cell Sci* **122**(Pt 15): 2587-2596.
- Cai, D., S. C. Chen, M. Prasad, L. He, X. Wang, V. Choismel-Cadamuro, J. K. Sawyer, G. Danuser and D. J. Montell (2014). "Mechanical feedback through E-cadherin promotes direction sensing during collective cell migration." *Cell* **157**(5): 1146-1159.
- Cancer Research Institute, U. (2017, 30 November 2017). "Types of cancer-  
<http://www.cancerresearchuk.org/what-is-cancer/how-cancer-starts/types-of-cancer>."
- Cavaliere, V., A. Donati, A. Hsouna, T. Hsu and G. Gargiulo (2005). "dAkt kinase controls follicle cell size during *Drosophila* oogenesis." *Dev Dyn* **232**(3): 845-854.
- Chanet, S., C. J. Miller, E. D. Vaishnav, B. Ermentrout, L. A. Davidson and A. C. Martin (2017). "Actomyosin meshwork mechanosensing enables tissue shape to orient cell force." *Nat Commun* **8**: 15014.
- Chen, Y. and T. Schubach (2006). "The role of brinker in eggshell patterning." *Mech Dev* **123**(5): 395-406.
- Chlasta, J., P. Milani, G. Runel, J. L. Duteyrat, L. Arias, L. A. Lamire, A. Boudaoud and M. Grammont (2017). "Variations in basement membrane mechanics are linked to epithelial morphogenesis." *Development* **144**(23): 4350-4362.
- Classen, A. K., K. I. Anderson, E. Marois and S. Eaton (2005). "Hexagonal packing of *Drosophila* wing epithelial cells by the planar cell polarity pathway." *Dev Cell* **9**(6): 805-817.
- Conder, R., H. Yu, B. Zahedi and N. Harden (2007). "The serine/threonine kinase dPak is required for polarized assembly of F-actin bundles and apical-basal polarity in the *Drosophila* follicular epithelium." *Dev Biol* **305**(2): 470-482.
- Conder, R., H. Yu, B. Zahedi and N. Harden (2016). "Corrigendum to "The serine/threonine kinase dPak is required for polarized assembly of F-actin bundles and apical-basal polarity in the *Drosophila* follicular epithelium" [Dev. Biol. 305 (2007) 470-482]." *Dev Biol* **415**(1): 168.
- Coravos, J. S. and A. C. Martin (2016). "Apical Sarcomere-like Actomyosin Contracts Nonmuscle *Drosophila* Epithelial Cells." *Dev Cell* **39**(3): 346-358.
- Coravos, J. S., F. M. Mason and A. C. Martin (2017). "Actomyosin Pulsing in Tissue Integrity Maintenance during Morphogenesis." *Trends in Cell Biology* **27**(4): 276-283.

- Cost, A. L., P. Ringer, A. Chrostek-Grashoff and C. Grashoff (2015). "How to Measure Molecular Forces in Cells: A Guide to Evaluating Genetically-Encoded FRET-Based Tension Sensors." Cell Mol Bioeng **8**(1): 96-105.
- Cox, D. N., B. Lu, T. Q. Sun, L. T. Williams and Y. N. Jan (2001). "Drosophila par-1 is required for oocyte differentiation and microtubule organization." Curr Biol **11**(2): 75-87.
- Crest, J., A. Diz-Munoz, D. Y. Chen, D. A. Fletcher and D. Bilder (2017). "Organ sculpting by patterned extracellular matrix stiffness." Elife **6**.
- Dahlgaard, K., A. A. S. F. Raposo, T. Niccoli and D. St Johnston (2007). "Capu and spire assemble a cytoplasmic actin mesh that maintains microtubule organization in the Drosophila oocyte." Developmental Cell **13**(4): 539-553.
- Davidson, L. A. (2011). "Embryo Mechanics: Balancing Force Production with Elastic Resistance during Morphogenesis." Forces and Tension in Development **95**: 215-241.
- Day, R. N., C. F. Booker and A. Periasamy (2008). "Characterization of an improved donor fluorescent protein for Forster resonance energy transfer microscopy." Journal of Biomedical Optics **13**(3).
- de Beco, S., J. B. Perney, S. Coscoy and F. Amblard (2015). "Mechanosensitive Adaptation of E-Cadherin Turnover across adherens Junctions." Plos One **10**(6).
- Delon, I. and N. H. Brown (2009). "The integrin adhesion complex changes its composition and function during morphogenesis of an epithelium." J Cell Sci **122**(Pt 23): 4363-4374.
- Deng, H., W. Wang, J. Yu, Y. Zheng, Y. Qing and D. Pan (2015). "Spectrin regulates Hippo signaling by modulating cortical actomyosin activity." Elife **4**: e06567.
- Dickinson, D. J., W. J. Nelson and W. I. Weis (2011). "A polarized epithelium organized by beta- and alpha-catenin predates cadherin and metazoan origins." Science **331**(6022): 1336-1339.
- Dinkins, M. B., V. M. Fratto and E. K. Lemosy (2008). "Integrin alpha chains exhibit distinct temporal and spatial localization patterns in epithelial cells of the Drosophila ovary." Dev Dyn **237**(12): 3927-3939.
- Dobens, L. L. and L. A. Raftery (2000). "Integration of epithelial patterning and morphogenesis in Drosophila ovarian follicle cells." Developmental Dynamics **218**(1): 80-93.
- Dray, N., A. Lawton, A. Nandi, D. Julich, T. Emonet and S. A. Holley (2013). "Cell-Fibronectin Interactions Propel Vertebrate Trunk Elongation via Tissue Mechanics." Current Biology **23**(14): 1335-1341.
- Duhart, J. C., T. T. Parsons and L. A. Raftery (2017). "The repertoire of epithelial morphogenesis on display: Progressive elaboration of Drosophila egg structure." Mech Dev **148**: 18-39.
- Dunst, S., T. Kazimiers, F. von Zadow, H. Jambor, A. Sagner, B. Brankatschk, A. Mahmoud, S. Spannll, P. Tomancak, S. Eaton and M. Brankatschk (2015). "Endogenously Tagged Rab Proteins: A Resource to Study Membrane Trafficking in Drosophila." Developmental Cell **33**(3): 351-365.

## REFERENCES

- Eder, D., K. Basler and C. M. Aegerter (2017). "Challenging FRET-based E-Cadherin force measurements in *Drosophila*." Sci Rep **7**(1): 13692.
- Farhadifar, R., J. C. Roper, B. Aigouy, S. Eaton and F. Julicher (2007). "The influence of cell mechanics, cell-cell interactions, and proliferation on epithelial packing." Curr Biol **17**(24): 2095-2104.
- Fletcher, D. A. and R. D. Mullins (2010). "Cell mechanics and the cytoskeleton." Nature **463**(7280): 485-492.
- Fletcher, G. C., A. Elbediwy, I. Khanal, P. S. Ribeiro, N. Tapon and B. J. Thompson (2015). "The Spectrin cytoskeleton regulates the Hippo signalling pathway." Embo Journal **34**(7): 940-954.
- Forest, E., R. Logeay, C. Geminard, D. Kantar, F. Frayssinoux, L. Heron-Milhavet and A. Djiane (2018). "The apical scaffold big bang binds to spectrins and regulates the growth of *Drosophila melanogaster* wing discs." J Cell Biol **217**(3): 1047-1062.
- Gardel, M. L., K. E. Kasza, C. P. Brangwynne, J. Y. Liu and D. A. Weitz (2008). "Mechanical Response of Cytoskeletal Networks." Biophysical Tools for Biologists, Vol 2: In Vivo Techniques **89**: 487-+.
- Gardel, M. L., I. C. Schneider, Y. Aratyn-Schaus and C. M. Waterman (2010). "Mechanical Integration of Actin and Adhesion Dynamics in Cell Migration." Annual Review of Cell and Developmental Biology, Vol 26 **26**: 315-333.
- Gayrard, C. and N. Borghi (2016). "FRET-based Molecular Tension Microscopy." Methods **94**: 33-42.
- Gibson, W. T. and M. C. Gibson (2009). "Cell topology, geometry, and morphogenesis in proliferating epithelia." Curr Top Dev Biol **89**: 87-114.
- Godt, D. and U. Tepass (1998). "*Drosophila* oocyte localization is mediated by differential cadherin-based adhesion." Nature **395**(6700): 387-391.
- Goldstein, B. and I. G. Macara (2007). "The PAR proteins: fundamental players in animal cell polarization." Dev Cell **13**(5): 609-622.
- Golic, K. G. and S. Lindquist (1989). "The FLP recombinase of yeast catalyzes site-specific recombination in the *Drosophila* genome." Cell **59**(3): 499-509.
- Gomez, J. M., Y. Wang and V. Riechmann (2012). "Tao controls epithelial morphogenesis by promoting Fasciclin 2 endocytosis." J Cell Biol **199**(7): 1131-1143.
- Gonzalez-Reyes, A. and D. St Johnston (1998). "The *Drosophila* AP axis is polarised by the cadherin-mediated positioning of the oocyte." Development **125**(18): 3635-3644.
- Gonzalezreyes, A., H. Elliott and D. Stjohnston (1995). "Polarization of Both Major Body Axes in *Drosophila* by Gurken-Torpedo Signaling." Nature **375**(6533): 654-658.
- Goodwin, K., S. J. Ellis, E. Lostchuck, T. Zulueta-Coarasa, R. Fernandez-Gonzalez and G. Tanentzapf (2016). "Basal Cell-Extracellular Matrix Adhesion Regulates Force Transmission during Tissue Morphogenesis." Dev Cell **39**(5): 611-625.

- Grammont, M. (2007). "Adherens junction remodeling by the Notch pathway in *Drosophila melanogaster* oogenesis." J Cell Biol **177**(1): 139-150.
- Gumbiner, B. M. (2005). "Regulation of cadherin-mediated adhesion in morphogenesis." Nat Rev Mol Cell Biol **6**(8): 622-634.
- Gutzman, J. H. and H. Sive (2010). "Epithelial relaxation mediated by the myosin phosphatase regulator Mypt1 is required for brain ventricle lumen expansion and hindbrain morphogenesis." Development **137**(5): 795-804.
- Haigo, S. L. and D. Bilder (2011). "Global tissue revolutions in a morphogenetic movement controlling elongation." Science **331**(6020): 1071-1074.
- Harris, T. J. and M. Peifer (2005). "The positioning and segregation of apical cues during epithelial polarity establishment in *Drosophila*." J Cell Biol **170**(5): 813-823.
- He, L., X. Wang and D. J. Montell (2011). "Shining light on *Drosophila* oogenesis: live imaging of egg development." Curr Opin Genet Dev **21**(5): 612-619.
- He, L., X. Wang, H. L. Tang and D. J. Montell (2010). "Tissue elongation requires oscillating contractions of a basal actomyosin network." Nat Cell Biol **12**(12): 1133-1142.
- Heisenberg, C. P. and Y. Bellaïche (2013). "Forces in tissue morphogenesis and patterning." Cell **153**(5): 948-962.
- Hoffman, B. D., C. Grashoff and M. A. Schwartz (2011). "Dynamic molecular processes mediate cellular mechanotransduction." Nature **475**(7356): 316-323.
- Hoffman, B. D. and A. S. Yap (2015). "Towards a Dynamic Understanding of Cadherin-Based Mechanobiology." Trends Cell Biol **25**(12): 803-814.
- Horne-Badovinac, S. and D. Bilder (2005). "Mass transit: epithelial morphogenesis in the *Drosophila* egg chamber." Dev Dyn **232**(3): 559-574.
- Hoshino, T., T. Sakisaka, T. Baba, T. Yamada, T. Kimura and Y. Takai (2005). "Regulation of E-cadherin endocytosis by nectin through afadin, Rap1, and p120(ctn)." Journal of Biological Chemistry **280**(25): 24095-24103.
- Huang, J., W. Zhou, W. Dong, A. M. Watson and Y. Hong (2009). "Directed, efficient, and versatile modifications of the *Drosophila* genome by genomic engineering." Proc Natl Acad Sci U S A **106**(20): 8284-8289.
- Humphrey, J. D., E. R. Dufresne and M. A. Schwartz (2014). "Mechanotransduction and extracellular matrix homeostasis." Nat Rev Mol Cell Biol **15**(12): 802-812.
- Hutson, M. S., Y. Tokutake, M. S. Chang, J. W. Bloor, S. Venakides, D. P. Kiehart and G. S. Edwards (2003). "Forces for morphogenesis investigated with laser microsurgery and quantitative modeling." Science **300**(5616): 145-149.
- Huxley, H. E. (1969). "The mechanism of muscular contraction." Science **164**(3886): 1356-1365.

## REFERENCES

- Huynh, J. R., M. Petronczki, J. A. Knoblich and D. St Johnston (2001). "Bazooka and PAR-6 are required with PAR-1 for the maintenance of oocyte fate in *Drosophila*." Curr Biol **11**(11): 901-906.
- Hynes, R. O. (2012). "The evolution of metazoan extracellular matrix." Journal of Cell Biology **196**(6): 671-679.
- Izumi, Y. and M. Furuse (2014). "Molecular organization and function of invertebrate occluding junctions." Semin Cell Dev Biol **36**: 186-193.
- Jia, D., Y. C. Huang and W. M. Deng (2015). "Analysis of Cell Cycle Switches in *Drosophila* Oogenesis." Methods Mol Biol **1328**: 207-216.
- Julich, D., G. Cobb, A. M. Melo, P. McMillen, A. K. Lawton, S. G. J. Mochrie, E. Rhoades and S. A. Holley (2015). "Cross-Scale Integrin Regulation Organizes ECM and Tissue Topology." Developmental Cell **34**(1): 33-44.
- Katta, S., M. Krieg and M. B. Goodman (2015). "Feeling force: physical and physiological principles enabling sensory mechanotransduction." Annu Rev Cell Dev Biol **31**: 347-371.
- Klose, S., D. Flores-Benitez, F. Riedel and E. Knust (2013). "Fosmid-based structure-function analysis reveals functionally distinct domains in the cytoplasmic domain of *Drosophila* crumbs." G3 (Bethesda) **3**(2): 153-165.
- Kolahi, K. S., P. F. White, D. M. Shreter, A. K. Classen, D. Bilder and M. R. Mofrad (2009). "Quantitative analysis of epithelial morphogenesis in *Drosophila* oogenesis: New insights based on morphometric analysis and mechanical modeling." Dev Biol **331**(2): 129-139.
- Kowalczyk, A. P. and B. A. Nanes (2012). "Adherens junction turnover: regulating adhesion through cadherin endocytosis, degradation, and recycling." Subcell Biochem **60**: 197-222.
- Krahn, M. P., J. Buckers, L. Kastrup and A. Wodarz (2010). "Formation of a Bazooka-Stardust complex is essential for plasma membrane polarity in epithelia." J Cell Biol **190**(5): 751-760.
- Krahn, M. P., D. R. Klopfenstein, N. Fischer and A. Wodarz (2010). "Membrane targeting of Bazooka/PAR-3 is mediated by direct binding to phosphoinositide lipids." Curr Biol **20**(7): 636-642.
- Krieg, M., J. Stuhmer, J. G. Cueva, R. Fetter, K. Spilker, D. Cremers, K. Shen, A. R. Dunn and M. B. Goodman (2017). "Genetic defects in beta-spectrin and tau sensitize *C.elegans* axons to movement-induced damage via torque-tension coupling." Elife **6**.
- Ladoux, B. and R. M. Mege (2017). "Mechanobiology of collective cell behaviours." Nat Rev Mol Cell Biol **18**(12): 743-757.
- Landsberg, K. P., R. Farhadifar, J. Ranft, D. Umetsu, T. J. Widmann, T. Bittig, A. Said, F. Julicher and C. Dahmann (2009). "Increased cell bond tension governs cell sorting at the *Drosophila* anteroposterior compartment boundary." Curr Biol **19**(22): 1950-1955.
- Laprise, P., K. M. Lau, K. P. Harris, N. F. Silva-Gagliardi, S. M. Paul, S. Beronja, G. J. Beitel, C. J. McGlade and U. Tepass (2009). "Yurt, Coracle, Neurexin IV and the Na(+),K(+)-ATPase form a novel group of epithelial polarity proteins." Nature **459**(7250): 1141-1145.

- Leckband, D. E. and J. de Rooij (2014). "Cadherin adhesion and mechanotransduction." Annu Rev Cell Dev Biol **30**: 291-315.
- Lecuit, T. and P. F. Lenne (2007). "Cell surface mechanics and the control of cell shape, tissue patterns and morphogenesis." Nat Rev Mol Cell Biol **8**(8): 633-644.
- Lecuit, T., P. F. Lenne and E. Munro (2011). "Force generation, transmission, and integration during cell and tissue morphogenesis." Annu Rev Cell Dev Biol **27**: 157-184.
- Legoff, L., H. Rouault and T. Lecuit (2013). "A global pattern of mechanical stress polarizes cell divisions and cell shape in the growing *Drosophila* wing disc." Development **140**(19): 4051-4059.
- Leys, S. P., S. A. Nichols and E. D. Adams (2009). "Epithelia and integration in sponges." Integr Comp Biol **49**(2): 167-177.
- Lilly, M. A. and A. C. Spradling (1996). "The *Drosophila* endocycle is controlled by cyclin E and lacks a checkpoint ensuring S-phase completion." Genes & Development **10**(19): 2514-2526.
- Loyer, N., I. Kolotuev, M. Pinot and R. Le Borgne (2015). "*Drosophila* E-cadherin is required for the maintenance of ring canals anchoring to mechanically withstand tissue growth." Proc Natl Acad Sci U S A **112**(41): 12717-12722.
- Mao, Y. and B. Baum (2015). "Tug of war--the influence of opposing physical forces on epithelial cell morphology." Dev Biol **401**(1): 92-102.
- Mao, Y., A. L. Tournier, A. Hoppe, L. Kester, B. J. Thompson and N. Tapon (2013). "Differential proliferation rates generate patterns of mechanical tension that orient tissue growth." EMBO J **32**(21): 2790-2803.
- Martin-Belmonte, F. and M. Perez-Moreno (2011). "Epithelial cell polarity, stem cells and cancer." Nat Rev Cancer **12**(1): 23-38.
- Martin, A. C. (2010). "Pulsation and stabilization: contractile forces that underlie morphogenesis." Dev Biol **341**(1): 114-125.
- Martin, A. C., M. Gelbart, R. Fernandez-Gonzalez, M. Kaschube and E. F. Wieschaus (2010). "Integration of contractile forces during tissue invagination." J Cell Biol **188**(5): 735-749.
- Martin, A. C., M. Kaschube and E. F. Wieschaus (2009). "Pulsed contractions of an actin-myosin network drive apical constriction." Nature **457**(7228): 495-499.
- Mateus, A. M., N. Gorfinkiel, S. Schamberg and A. M. Arias (2011). "Endocytic and Recycling Endosomes Modulate Cell Shape Changes and Tissue Behaviour during Morphogenesis in *Drosophila*." Plos One **6**(4).
- Mayer, M., M. Depken, J. S. Bois, F. Julicher and S. W. Grill (2010). "Anisotropies in cortical tension reveal the physical basis of polarizing cortical flows." Nature **467**(7315): 617-621.
- Medina, E., J. Williams, E. Klipfell, D. Zarnescu, G. Thomas and A. Le Bivic (2002). "Crumbs interacts with moesin and beta(Heavy)-spectrin in the apical membrane skeleton of *Drosophila*." J Cell Biol **158**(5): 941-951.

## REFERENCES

- Morais-de-Sa, E., V. Mirouse and D. St Johnston (2010). "aPKC phosphorylation of Bazooka defines the apical/lateral border in Drosophila epithelial cells." *Cell* **141**(3): 509-523.
- Murrell, M., P. W. Oakes, M. Lenz and M. L. Gardel (2015). "Forcing cells into shape: the mechanics of actomyosin contractility." *Nat Rev Mol Cell Biol* **16**(8): 486-498.
- Nam, S. C. and K. W. Choi (2003). "Interaction of Par-6 and Crumbs complexes is essential for photoreceptor morphogenesis in Drosophila." *Development* **130**(18): 4363-4372.
- Nanes, B. A., C. Chiasson-MacKenzie, A. M. Lowery, N. Ishiyama, V. Faundez, M. Ikura, P. A. Vincent and A. P. Kowalczyk (2012). "p120-catenin binding masks an endocytic signal conserved in classical cadherins." *J Cell Biol* **199**(2): 365-380.
- Ng, B. F., G. K. Selvaraj, C. Santa-Cruz Mateos, I. Grosheva, I. Alvarez-Garcia, M. D. Martin-Bermudo and I. M. Palacios (2016). "alpha-Spectrin and integrins act together to regulate actomyosin and columnarization, and to maintain a monolayered follicular epithelium." *Development* **143**(8): 1388-1399.
- Orr, A. W., B. P. Helmke, B. R. Blackman and M. A. Schwartz (2006). "Mechanisms of mechanotransduction." *Dev Cell* **10**(1): 11-20.
- Peifer, M. and E. Wieschaus (1990). "The segment polarity gene armadillo encodes a functionally modular protein that is the Drosophila homolog of human plakoglobin." *Cell* **63**(6): 1167-1176.
- Picone, R., X. Ren, K. D. Ivanovitch, J. D. Clarke, R. A. McKendry and B. Baum (2010). "A polarised population of dynamic microtubules mediates homeostatic length control in animal cells." *PLoS Biol* **8**(11): e1000542.
- Pope, K. L. and T. J. Harris (2008). "Control of cell flattening and junctional remodeling during squamous epithelial morphogenesis in Drosophila." *Development* **135**(13): 2227-2238.
- Puech, P. H., A. Taubenberger, F. Ulrich, M. Krieg, D. J. Muller and C. P. Heisenberg (2005). "Measuring cell adhesion forces of primary gastrulating cells from zebrafish using atomic force microscopy." *Journal of Cell Science* **118**(18): 4199-4206.
- Rodriguez-Boulan, E. and I. G. Macara (2014). "Organization and execution of the epithelial polarity programme." *Nat Rev Mol Cell Biol* **15**(4): 225-242.
- Roeth, J. F., J. K. Sawyer, D. A. Wilner and M. Peifer (2009). "Rab11 helps maintain apical crumbs and adherens junctions in the Drosophila embryonic ectoderm." *PLoS One* **4**(10): e7634.
- Roper, K. (2012). "Anisotropy of Crumbs and aPKC Drives Myosin Cable Assembly during Tube Formation." *Developmental Cell* **23**(5): 939-953.
- Roper, K. (2015). "Integration of Cell-Cell Adhesion and Contractile Actomyosin Activity During Morphogenesis." *Cellular Adhesion in Development and Disease* **112**: 103-127.
- Roth, S. and J. A. Lynch (2009). "Symmetry breaking during Drosophila oogenesis." *Cold Spring Harb Perspect Biol* **1**(2): a001891.

- Sawyer, J. K., W. Choi, K. C. Jung, L. He, N. J. Harris and M. Peifer (2011). "A contractile actomyosin network linked to adherens junctions by Canoe/afadin helps drive convergent extension." Molecular Biology of the Cell **22**(14): 2491-2508.
- Sawyer, J. K., N. J. Harris, K. C. Slep, U. Gaul and M. Peifer (2009). "The Drosophila afadin homologue Canoe regulates linkage of the actin cytoskeleton to adherens junctions during apical constriction." Journal of Cell Biology **186**(1): 57-73.
- Schindelin, J., I. Arganda-Carreras, E. Frise, V. Kaynig, M. Longair, T. Pietzsch, S. Preibisch, C. Rueden, S. Saalfeld, B. Schmid, J. Y. Tinevez, D. J. White, V. Hartenstein, K. Eliceiri, P. Tomancak and A. Cardona (2012). "Fiji: an open-source platform for biological-image analysis." Nat Methods **9**(7): 676-682.
- Schlichting, K., M. Wilsch-Brauninger, F. Demontis and C. Dahmann (2006). "Cadherin Cad99C is required for normal microvilli morphology in Drosophila follicle cells." J Cell Sci **119**(Pt 6): 1184-1195.
- Schuessle, C., S. N. Hoernstein, S. J. Mueller, M. Rodriguez-Franco, T. Lorenz, D. Lang, G. L. Igloi and R. Reski (2016). "Spatio-temporal patterning of arginyl-tRNA protein transferase (ATE) contributes to gametophytic development in a moss." New Phytol **209**(3): 1014-1027.
- Schwartz, M. A. (2010). "Integrins and Extracellular Matrix in Mechanotransduction." Cold Spring Harbor Perspectives in Biology **2**(12).
- Schwarz, U. S. and M. L. Gardel (2012). "United we stand: integrating the actin cytoskeleton and cell-matrix adhesions in cellular mechanotransduction." J Cell Sci **125**(Pt 13): 3051-3060.
- Shcherbata, H. R., C. Althausen, S. D. Findley and H. Ruohola-Baker (2004). "The mitotic-to-endocycle switch in Drosophila follicle cells is executed by Notch-dependent regulation of G1/S, G2/M and M/G1 cell-cycle transitions." Development **131**(13): 3169-3181.
- Sherrard, K., F. Robin, P. Lemaire and E. Munro (2010). "Sequential activation of apical and basolateral contractility drives ascidian endoderm invagination." Curr Biol **20**(17): 1499-1510.
- Sherrard, K. M. and R. G. Fehon (2015). "The transmembrane protein Crumbs displays complex dynamics during follicular morphogenesis and is regulated competitively by Moesin and aPKC." Development **142**(10): 1869-1878.
- Spradling, A., Ed. (1993). Developmental Genetics of Oogenesis The development of Drosophila melanogaster  
Cold Spring Harbor Lab, NY.
- St Johnston, D. and B. Sanson (2011). "Epithelial polarity and morphogenesis." Curr Opin Cell Biol **23**(5): 540-546.
- Sugimura, K. and S. Ishihara (2013). "The mechanical anisotropy in a tissue promotes ordering in hexagonal cell packing." Development **140**(19): 4091-4101.
- Sugimura, K., P. F. Lenne and F. Graner (2016). "Measuring forces and stresses in situ in living tissues." Development **143**(2): 186-196.

## REFERENCES

- Suzuki, A. and S. Ohno (2006). "The PAR-aPKC system: lessons in polarity." *J Cell Sci* **119**(Pt 6): 979-987.
- Szafranski, P. and S. Goode (2004). "A Fasciclin 2 morphogenetic switch organizes epithelial cell cluster polarity and motility." *Development* **131**(9): 2023-2036.
- Takeichi, M. (2014). "Dynamic contacts: rearranging adherens junctions to drive epithelial remodelling." *Nat Rev Mol Cell Biol* **15**(6): 397-410.
- Tanentzapf, G. and U. Tepass (2003). "Interactions between the crumbs, lethal giant larvae and bazooka pathways in epithelial polarization." *Nat Cell Biol* **5**(1): 46-52.
- Tepass, U. (2012). "The apical polarity protein network in Drosophila epithelial cells: regulation of polarity, junctions, morphogenesis, cell growth, and survival." *Annu Rev Cell Dev Biol* **28**: 655-685.
- Thompson, B. J., F. Pichaud and K. Roper (2013). "Sticking together the Crumbs - an unexpected function for an old friend." *Nat Rev Mol Cell Biol* **14**(5): 307-314.
- Tsoumpekos, G., L. Nemetschke and E. Knust (2018). "Drosophila Big bang regulates the apical cytocortex and wing growth through junctional tension." *J Cell Biol* **217**(3): 1033-1045.
- Vasquez, C. G. and A. C. Martin (2016). "Force transmission in epithelial tissues." *Developmental Dynamics* **245**(3): 361-371.
- Walther, R. F. and F. Pichaud (2010). "Crumbs/DaPKC-dependent apical exclusion of Bazooka promotes photoreceptor polarity remodeling." *Curr Biol* **20**(12): 1065-1074.
- Wang, Y. and V. Riechmann (2007). "The role of the actomyosin cytoskeleton in coordination of tissue growth during Drosophila oogenesis." *Curr Biol* **17**(15): 1349-1355.
- Wang, Y. C., Z. Khan, M. Kaschube and E. F. Wieschaus (2012). "Differential positioning of adherens junctions is associated with initiation of epithelial folding." *Nature* **484**(7394): 390-393.
- Weng, M. and E. Wieschaus (2016). "Myosin-dependent remodeling of adherens junctions protects junctions from Snail-dependent disassembly." *J Cell Biol* **212**(2): 219-229.
- West, J. J., T. Zulueta-Coarasa, J. A. Maier, D. M. Lee, A. E. E. Bruce, R. Fernandez-Gonzalez and T. J. C. Harris (2017). "An Actomyosin-Arf-GEF Negative Feedback Loop for Tissue Elongation under Stress." *Curr Biol* **27**(15): 2260-2270 e2265.
- Widmann, T. J. and C. Dahmann (2009). "Dpp signaling promotes the cuboidal-to-columnar shape transition of Drosophila wing disc epithelia by regulating Rho1." *J Cell Sci* **122**(Pt 9): 1362-1373.
- Woichansky, I., C. A. Beretta, N. Berns and V. Riechmann (2016). "Three mechanisms control E-cadherin localization to the zonula adherens." *Nat Commun* **7**: 10834.
- Wu, X. D., P. S. Tanwar and L. A. Raftery (2008). "Drosophila follicle cells: Morphogenesis in an eggshell." *Seminars in Cell & Developmental Biology* **19**(3): 271-282.

- Xi, R. W., J. R. McGregor and D. A. Harrison (2003). "A gradient of JAK pathway activity patterns the anterior-posterior axis of the follicular epithelium." Developmental Cell **4**(2): 167-177.
- Xu, T. and G. M. Rubin (1993). "Analysis of genetic mosaics in developing and adult *Drosophila* tissues." Development **117**(4): 1223-1237.
- Yu, W., A. Datta, P. Leroy, L. E. O'Brien, G. Mak, T. S. Jou, K. S. Matlin, K. E. Mostov and M. M. Zegers (2005). "Beta1-integrin orients epithelial polarity via Rac1 and laminin." Mol Biol Cell **16**(2): 433-445.
- Yurchenco, P. D. (2011). "Basement Membranes: Cell Scaffoldings and Signaling Platforms." Cold Spring Harbor Perspectives in Biology **3**(2).
- Zarnescu, D. C. and G. H. Thomas (1999). "Apical spectrin is essential for epithelial morphogenesis but not apicobasal polarity in *Drosophila*." Journal of Cell Biology **146**(5): 1075-1086.
- Zhou, J., H. Y. Kim and L. A. Davidson (2009). "Actomyosin stiffens the vertebrate embryo during crucial stages of elongation and neural tube closure." Development **136**(4): 677-688.
- Zhou, J., S. Pal, S. Maiti and L. A. Davidson (2015). "Force production and mechanical accommodation during convergent extension." Development **142**(4): 692-701.

## 7 Appendix

### 7.1 Genotypes

Table 8 Detailed genotypes of individual images presented in this work

Figure	Genotype
<b>Figure 7</b>	
A	<i>baz::GFP (CC01941, I)</i> <i>zip::GFP (CC01626, II)</i>
<b>Figure 8</b>	
A	<i>w[118]</i> <i>dpp-LacZ [10638]/CyO ; Dr/TM6c</i>
B-E'	<i>pointed(pnt)- LacZ (998/12) /TM6c</i>
F-I'	<i>mirr::GFP</i>
<b>Figure 10</b>	
A-A''	<i>otu-GAL4::VP16.R, w[*]/+;nos.NGT-GAL4/ UAS-shg RNAi; GAL4::VP16-nos.UTR /+</i>
B-B''	<i>Acf1 [1] /TM6c</i>
C-C''	<i>w; vkg-GFP; FRT80.fat2 [N103.2] / "</i>
<b>Figure 11</b>	
A	<i>w[118]</i> for aPKC, Crb, $\alpha$ -spectrin, N-Cad, Dlg, Moe-P, <i>kst::GFP</i> <i>ed::GFP [MI01552] / SM6a</i> <i>sqh-Rok::GFP</i>
B	<i>cher::GFP [MI07480]</i> <i>trol::GFP-ST-F [M104580]</i>
C	<i>baz::GFP (CC01941, I)</i> <i>w[118]</i> for E-Cad, MRLC-2P <i>zip&gt;GFP (CC01626, II)</i> <i>sqh-sqh::GFP/ CyO; Dr/TM6c</i>
<b>Figure 12</b>	
A, D-D'	<i>mirr::GFP</i>
C	<i>otu-GAL4::VP16.R, w[*]/+;nos.NGT-GAL4/ UAS-shg RNAi; GAL4::VP16-nos.UTR /+</i>
<b>Figure 13</b>	
A	<i>baz::GFP (CC01941, I)</i> <i>zip::GFP (CC01626, II)</i>
B-C	<i>sqh-sqh::GFP/ CyO; Dr/TM6c</i>
D	<i>TJ-GAL4, Mej20-GAL80/+;UASp-UtrophinABD::GFP /+</i>
E	<i>hsflp [122]/+; FRT40A sqh::GFP / FRT40A sqh::RFP</i>
J	<i>otu-GAL4::VP16.R, w[*]/+;nos.NGT-GAL4/ UAS-shg RNAi; GAL4::VP16-nos.UTR /+</i>
<b>Figure 14</b>	
A-A''	<i>hsflp [122]/+; FRT40A sqh::GFP / FRT40A sqh::RFP</i>
B-B''	<i>sqh-sqh::GFP/ CyO; Dr/TM6</i>
C-C'	<i>mirr::GFP</i>
<b>Figure 15</b>	
A-D''''', I-I'	<i>w[118]</i>
E-E', H-H'	<i>zip::GFP (CC01626, II)</i>
F-F'	<i>rok::GFP</i>
G-G', J	<i>kst::GFP</i>
<b>Figure 16</b>	

A	w[118]
<b>Figure 17</b>	
A, F-F''	w[118]
B-C'', H-I'	<i>FRT80B ubi-PH::GFP/TM6b</i>
<b>Figure 19</b>	
B-C'	w*; <i>snaSco/CyO</i> ; <i>P{Ubi-shg-tension-sensor}3/MKRS</i> w*; <i>snaSco/CyO</i> ; <i>P{Ubi-shg-tension-sensor-control}3</i>
<b>Figure 19</b>	
A-F	<i>DEcad::GFP/CyO</i>
<b>Figure 19</b>	
A	w[118] and <i>TJ-GAL4, Mef20-GAL80/+; UAS-rok RNAi (JF03225)/+</i>
B	w[118] and <i>TJ-GAL4, UAS-CD8tom / UAS-<math>\alpha</math>-catenin RNAi (107298/KK); UAS-Dcr2/+</i>
<b>Figure 22</b>	
A-B''''	w[118]
C-D''''	<i>TJ-GAL4, Mef20-GAL80/+; UAS-rok RNAi (JF03225)/+</i>
E-F''''	<i>TJ-GAL4, UAS CD8 tom/+; UAS-sqh RNAi (HMS00830)/UAS Dicer</i>
G-I'	<i>FRT101 ubi-GFP/ FRT101 sqh<sup>1</sup>; e22C-GAL4, UAS-FLP/+</i>
<b>Figure 23</b>	
A-B', E-F'	<i>zip&gt;GFP (CC01626, II)</i>
C-D'	<i>TJ-GAL4, UAS CD8 tom/+; UAS-sqh RNAi (HMS00830)/UAS Dicer</i>
G-H'	<i>FRT101 ubi-GFP/ FRT101 sqh<sup>1</sup>; e22C-GAL4, UAS-FLP/+</i>
I-J'	<i>FRT101 ubi-GFP/ FRT101 arm<sup>3</sup>; e22C-GAL4, UAS-FLP/+</i>
K-N'	<i>TJ-GAL4, UAS-CD8tom / UAS-<math>\alpha</math>-catenin RNAi (107298/KK); UAS-Dcr2/+</i>
<b>Figure 24</b>	
A-C'	w[118]
E-F'	<i>hsflp[122]/+; FRT42D ubi-GFP/ FRT42D shg<sup>R69b</sup></i>
G-I'	<i>TJ-GAL4, UAS-CD8tom / UAS-<math>\alpha</math>-catenin RNAi (107298/KK); UAS-Dcr2/+</i>
J-L'	<i>FRT101 ubi-GFP/ FRT101 arm<sup>3</sup>; e22C-GAL4, UAS-FLP/+</i>
M-N'	<i>TJ-GAL4, Mef20-GAL80/+; UAS-aPKC RNAi (HMS01320)/+</i>
O-P;	<i>TJ-GAL4, UAS-CD8tom / UAS-crb RNAi; UAS-Dcr2/MKRS or TM6</i>
<b>Figure 25</b>	
A-C	w[118]
E	<i>TJ-GAL4, Mef20-GAL80/UAS-cno; UAS-cno/+</i>
F	w/+; <i>TJ-GAL4, Mef20-GAL80/+; UAS GFP::Cno/+</i>
G	<i>TJ-GAL4, Mef20-GAL80/+; UAS-Rac1<sup>N17</sup>/+</i>
<b>Figure 26</b>	
A-B''''	w[118]
C-D''''	<i>TJ-GAL4, Mef20-GAL80/UAS-cno; UAS-cno/+</i>
E-F''''	<i>TJ-GAL4, Mef20-GAL80/+; UAS-Rac1<sup>N17</sup>/+</i>
<b>Figure 27</b>	
A, D	w[118]
B, F	<i>TJ-GAL4, Mef20-GAL80/UAS-cno; UAS-cno/+</i>
C, F	<i>TJ-GAL4, Mef20-GAL80/+; UAS-Rac1<sup>N17</sup>/+</i>
G	<i>TJ-GAL4, Mef20-GAL80/+; UAS-rok RNAi (JF03225)/+</i>
H	<i>TJ-GAL4, Mef20-GAL80/+; UAS-sqh RNAi (HMS00830)/+</i>
<b>Figure 28</b>	
A	w[118]
B-C	w[118] <i>TJ-GAL4, UAS-CD8tom / UAS-crb RNAi; UAS-Dcr2/MKRS or TM6</i>
<b>Figure 29</b>	
A, B, D	w[118]
C	<i>kst::GFP</i>
<b>Figure 30</b>	
A-C	w[118] <i>hsflp [122]/+;; FRT82B ubi-mRFP/ FRT82B crb<sup>11A22</sup></i> <i>hsflp [122]/+;; FRT82B ubi-mRFP/ FRT82B crb<sup>8F105</sup></i> <i>hsflp [122]/+;; FRT82B ubi-mRFP/ FRT82B crb<sup>Y10A</sup></i> <i>hsflp [122]/+;; FRT82B ubi-mRFP/ FRT82B crb<sup>D88-3</sup></i>
<b>Figure 31</b>	
A	<i>hsflp [122]/+;; FRT82B ubi-mRFP/ FRT82B crb<sup>11A22</sup></i>
B	<i>hsflp [122]/+;; FRT82B ubi-mRFP/ FRT82B crb<sup>Y10A</sup></i>
C	<i>hsflp [122]/+;; FRT82B ubi-mRFP/ FRT82B crb<sup>D88-3</sup></i>
D-H	w[118]

## APPENDIX

*TJ-GAL4, UAS-CD8tom / UAS-crb RNAi; UAS-Dcr2/MKRS or TM6*

### Figure 33

A-D<sup>''</sup>, F-F<sup>'</sup> *vkg::GFP (CC00791)*  
E-E<sup>'</sup> *TJ-GAL4, Mef20-GAL80/+; UAS-aPKC RNAi (HMS01320)/+*

### Figure 34

A-A<sup>''</sup> *w[118]*  
*TJ-GAL4, Mef20-GAL80/UAS-cno; UAS-cno/+*  
*TJ-GAL4, Mef20-GAL80/+; UAS-Rac1<sup>N17</sup>/+*

### Figure 35

A *hsflp [122]/+; FRT40A sqh::GFP / FRT40A sqh::RFP*  
B *otu-GAL4::VP16.R, w[\*]/+; nos.NGT GAL4/ UAS-GMA::mCherry; GAL4::VP16-nos.UTR /+*  
C *otu-GAL4::VP16.R, w[\*]/+; nos.NGT GAL4/ UAS-N-cad RNAi; GAL4::VP16-nos.UTR / UAS-shg RNAi*  
D-D<sup>'''</sup> *w[118]*  
E *TJ-GAL4, Mef20-GAL80/+; UASp-UtrophinABD::GFP /+*  
F *TJ-GAL4, UAS-CD8tom/+; UASp-UtrophinABD::GFP /UAS-Dcr2*  
G-G<sup>'</sup> *hsflp [122]; Act5C.GAL4 (FRT.CD2), UAS-RFP / UASp-UtrophinABD::GFP*  
H-H<sup>'</sup> *Cad99C::GFP*

### Figure 36

A-C<sup>'</sup> *otu-GAL4::VP16.R, w[\*]/zip::GFP; nos.NGT GAL4/ UAS-GMA::mCherry; GAL4::VP16-nos.UTR /+*  
D-F<sup>'</sup> *hsflp [122]/+; FRT40A sqh::GFP / FRT40A sqh::RFP*

### Figure 37

A *DEcad::GFP/CyO*  
B *w[118]*  
C *FRT80B ubi-PH::GFP/TM6b*

### Figure 38

A *FRT9-2 baz [Xi106]/ ovo[D2], FRT9-2/C(1)DX, y[1] f[1]/Y; hsFLP38/+*

### Figure 39

A-A<sup>'</sup> *sec6::GFP*  
B-B<sup>'</sup> *sec10::GFP*  
C-C<sup>''</sup> *Rab11::eYFP*  
D-D<sup>'</sup> *RabX1::eYFP*  
E-E<sup>'</sup> *shi ts [1]*

### Figure 40

A *vkg::GFP (CC00791)*  
B-D *FRT19A mys [1]/ ubi-mRFP, hsFLP[122], FRT19A*

### Figure 41

A *zip::GFP (CC01626, II)*  
B *FRT101 ubi-GFP/ FRT101 arm<sup>3</sup>; e22C-GAL4, UAS-FLP/+*

### Figure 43

A-A<sup>''</sup> *w; vkg-GFP; FRT80 fat2 [N103.2] / TM6c*

## 7.2 Quantifications

### 7.2.1 Epithelial cell junctional area and height measurements at stage 7 and stage 9

Table 9 FCE cell junctional area measurements at stage 7 and stage 9 in wildtype egg chambers

	Stage 7		Stage 9	
	NCC	OCC	NCC	OCC
	32.504	12.242	40.114	31.173
	25.523	10.488	60.574	42.208
	33.154	13.898	40.114	20.701
	31.173	14.19	56.707	27.306
	32.147	19.515	68.387	38.342
	29.127	13.606	67.34	24.971
	28.12	13.378	55.016	35.845

	26.497	18.124	44.947	16.593
	28.056	19.01	45.833	32.864
	23.25	20.138	58.882	36.167
	32.115	20.943	56.224	37.134
	23.347	27.226	56.063	28.837
	25.977	14.257	48.813	24.648
	34.388	14.982	62.024	33.589
	27.763	13.774	71.287	22.715
	23.601	20.46	57.11	39.55
	19.976	31.978	77.973	37.053
	37.214	32.501	77.248	19.735
	24.89	31.288	64.762	23.923
	20.701	20.32	60.493	19.735
	38.825	28.633	58.238	24.729
	29.481	16.856	51.472	
	32.542		59.607	
	29.642		55.096	
	28.515		74.589	
	23.198		57.271	
	28.354		51.713	
	36.409		53.324	
	56.977		72.898	
	49.992		46.397	
	41.679		41.564	
	47.106		64.279	
	43.18		38.181	
	44.161		62.185	
	51.551		35.362	
	49.126		18.365	
	50.223		24.568	
	52.012		35.684	
			17.802	
			41.967	
			16.593	
			20.46	
			28.031	
			48.33	
			33.026	
			24.326	
			30.69	
<b>Mean</b>	<b>34.01305</b>	<b>19.44577</b>	<b>49.61551</b>	<b>29.4199</b>
<b>SEM</b>	1.627217	1.446229	2.417144	1.699517
<b># cells/ #ECs</b>	<b>38/3</b>	<b>22/3</b>	<b>47/3</b>	<b>20/3</b>

Table 10 FCE cell height measurements at stage 7 and stage 9 in wildtype egg chambers

Stage 7		Stage9	
NCC	OCC	NCC	OCC
6.895	11.002	9.362	7.891
5.9	11.076	12.134	15.61
6.286	11.046	9.604	15.674
5.168	10.966	8.381	17.264
6.345	11.579	8.289	14.117
8.208	10.573	9.434	15.736
6.057	8.632	9.055	16.716
5.774	8.581	6.434	15.985
5.727	9.005	8.077	18.882
6.317	7.947	5.452	17.79
6.728	7.63	10.955	16.889
5.99	8.044	8.25	14.343
9.262	7.719	5.823	14.191
4.833	7.579	7.236	11.702
4.494	8.479	8.766	17.979
4.7	13.145	5.053	19.942
4.353	13.463	1.853	14.986
5.772	12.59	2.417	16.217
4.577	12.487	2.255	16.12
5.021	12.413	2.739	15.674
4.455	11.415	2.336	13.148
5.204	10.672	2.255	12.772
4.965	11.201	1.772	12.997
7.168		1.692	4.028

APPENDIX

	4.73		2.417	4.43
	4.876			4.028
	5.479			4.189
	5.846			4.672
	5.547			5.075
	8.491			5.397
	5.949			4.511
	6.201			4.672
	6.05			5.236
	5.822			
	5.624			
	6.14			
	5.221			
	6.177			
<b>Mean</b>	<b>5.851368</b>	<b>10.31496</b>	<b>6.08164</b>	<b>12.08676</b>
<b>SEM</b>	0.177147	0.400432	0.67048	0.947345
<b># cells/ #ECs</b>	<b>38/3</b>	<b>23/3</b>	<b>25/3</b>	<b>33/3</b>

Table 11 FCE height measurements in egg chambers with misplaced oocytes upon germline specific expression of *shg* RNAi

EC1		EC2		EC3		EC4		EC5		EC6	
NCC	OCC	NCC	OCC	NCC	OCC	NCC	OCC	NCC	OCC	NCC	OCC
8.716	11.731	6.696	13.464	5.713	7.035	6.918	11.03	5.926	10.167	6.459	10.845
7.723	11.731	7.953	11.501	5.593	9.364	6.8	10.473	6.25	9.241	7.791	11.368
4.811	9.854	7.672	11.433	6.101	9.364	5.87	12.764	5.767	8.275	7.288	11.317
5.609	11.107	7.621	10.161	4.623	8.427	4.655	9.313	5.688	9.966	6.168	10.376
6.883	11.795	6.068	11.662	5.371	7.749	6.025	12.195	8.281	10.058	8.534	11.676
5.326	12.419	5.29	10.649	5.676	8.548	4.782	13.986	6.65	9.687	6.99	14.029
4.591	10.432	9.632	10.184	5.676			10.51	6.378			10.817
5.099	11.239	9.219	10.266					7.444			11.152
6.026	11.724	7.735	10.992					6.049			
4.671			9.797					6.741			
3.948											

#NCC cells/ # ECs = 49/6, #OCC cells/ # ECs = 46/6

Table 12 Cell junctional area measurements in FCE specific knockdown and overexpression of different genes at stage 9

<i>wt</i>		<i>rok</i>		<i>Rac1DN</i>		<i>cnoOE</i>	
NCC	OCC	NCC	OCC	NCC	OCC	NCC	OCC
40.114	31.173	108.919	38.96	184.626	67.879	179.372	33.405
60.574	42.208	108.008	38.139	186.068	42.691	163.567	46.041
40.114	20.701	107.103	27.158	204.873	56.28	296.16	36.195
56.707	27.306	83.903	38.863	340.152	42.004	170.353	34.027
68.387	38.342	100.856	37.061	383.185	36.691	238.202	35.977
67.34	24.971	114.531	44.655	260.465	32.063	215.612	55.168
55.016	35.845	87.585	44.655	254.405	38.838	159.79	49.934
44.947	16.593	100.484	37.369	273.968	44.325	181.091	36.946
45.833	32.864	123.171	48.465	306.078	50.91	172.605	35.618
58.882	36.167	90.439	31.942	166.9		115.859	35.387
56.224	37.134		35.509			280.209	54.668
56.063	28.837		33.912			199.968	52.012
48.813	24.648					267.74	53.571
62.024	33.589					240.723	49.299
71.287	22.715					178.262	48.433
57.11	39.55						
77.973	37.053						
35.362							
18.365							
24.568							
35.684							
17.802							
41.967							
16.593							
20.46							
28.031							
48.33							
33.026							
24.326							
30.69							

<b>Mean</b>	<b>40.61551</b>	<b>29.4199</b>	<b>102.4999</b>	<b>38.05733</b>	<b>256.072</b>	<b>45.74233</b>	<b>203.9675</b>	<b>43.77873</b>
<b>SEM</b>	2.417144	1.658559	3.923299	1.692944	22.76649	3.670064	13.1481	2.195128
<b>#cells/ #ECs</b>	<b>47/3</b>	<b>21/3</b>	<b>10/2</b>	<b>12/2</b>	<b>10/2</b>	<b>9/2</b>	<b>15/3</b>	<b>15/3</b>

Table 13 Cell height measurements in FCE specific knockdown and overexpression of different genes at stage 9

	<i>wt</i>		<i>rok</i>		<i>Rac1DN</i>		<i>cnoOE</i>	
	NCC	OCC	NCC	OCC	NCC	OCC	NCC	OCC
	8.027	15.273	4.43	8.811	2.62	15.886	9.854	10.181
	9.215	15.61	3.415	14.86	5.887	15.989	7.168	15.016
	11.877	16.275	3.415	15.439	4.477	14.361	8.769	13.909
	8.151	18.535	3.874	16.916	3.416	12.816	6.934	13.138
	5.378	13.5	2.554	11.645	3.155	14.494	9.651	11.249
	7.464	7.891	4.615	12.013	2.834	12.221	4.953	16.341
	8.402	15.61	2.554	9.231	1.808	12.673	5.846	15.137
	9.362	15.674	6.007	12.004	2.901	13.102	3.015	16.402
	12.134	17.264	5.291	15.491	3.905	17	6.007	12.445
	9.604	14.117	3.739	16.818	2.619	15.034	6.011	11.929
	8.381	15.736	4.769	12.93	4.452	11.018	6.011	15.735
	8.289	16.716	5.775	13.442	4.884	13.645	5.375	18.486
	9.434	15.985	5.704	15.289	2.547	10.261	3.011	22.219
	9.055	18.882	6.856	13.252	2.763	13.162	7.782	21.102
	6.434	17.79	4.89	8.104	2.797	13.582	3.844	21.211
	8.077	16.889	7.479	9.481	3.089	8.392	8.663	17.721
	5.452	14.343	7.249	11.47		11.722	4.092	16.1
	10.955	14.191	2.718	13.076		9.006		
	8.25	11.702	6.487	8.976		11.164		
	5.823	17.979	5.291	8.167		9.541		
	7.236	19.942	4.077	14.128		11.884		
	8.766	14.986	3.368	14.75		12.364		
	5.053	16.217	3.799	14.161		11.755		
		16.12	3.977	9.936				
		15.674	2.903					
		13.148	4.37					
		12.772	5.802					
		12.997	4.196					
<b>Mean</b>	<b>8.296478</b>	<b>15.42207</b>	<b>4.628714</b>	<b>12.51625</b>	<b>3.384625</b>	<b>12.6553</b>	<b>6.293294</b>	<b>15.78359</b>
<b>SEM</b>	0.39535	0.461243	0.264679	0.56191	0.265216	0.46429	0.523477	0.858532
<b>#cells/ #ECs</b>	<b>23/3</b>	<b>28/3</b>	<b>28/3</b>	<b>24/3</b>	<b>16/3</b>	<b>23/3</b>	<b>17/3</b>	<b>17/3</b>

7.2.2 Junction corrugation and roughness measurements

Table 14 Junction corrugation measures at stage 6 and stage 9

Corrugations		
	stage 6	stage 9
	1	1.106
	1.01	1.037
	1.02	1.06
	1.06	1.102
	1	1.067
	1	1.061
	1.06	1.079
	1.01	1.071
	1	1.039
	1.01	1
	1.01	1.103
	1.02	1.079
	1.01	1.022
	1.01	1.117
	1.03	1.042
	1.01	1.166
	1	1.066
	1	1.015
	1	1.021
	1.02	1.107
	1	1
	1.02	1.161
	1.02	1.106
	1.02	1.021
	1	1
	1.02	1.064
	1.02	1.133
	1	1.061
	1.01	1.06
	1	1.083
	1	1.052
	1.03	1.087
	1	1.026
	1.07	1.037
	1	1.129
	1	1.053
	1.05	1.025
	1	1.08
	1.24	1.053
	1.03	1.067
	1.01	1
	1	1.223
	1	1.059
	1.01	1.132
	1	1.034
	1.06	1.019
		1.112
		1.088
		1.085
		1.098
		1.018
		1
		1.004
		1.018
		1.023
		1.002
		1.073
		1.142
		1.049
		1.047
		1.049
		1.124
		1.118
		1
		1.061
<b>Mean</b>	<b>1.019348</b>	<b>1.065169</b>
<b>SEM</b>	0.005624	0.005885
<b># edges/ #ECs</b>	<b>46/3</b>	<b>65/3</b>

Table 15 Junction corrugations in NCCs and OCCs at stage 9

	EC1		EC2		EC3		EC4	
	NCC	OCC	NCC	OCC	NCC	OCC	NCC	OCC
1.067437	1.025492	1.071171	1.031763	1.143281	1.056313	1.311068	1.041761	
1.02962	1.007079	1.124847	1.069989	1.045576	1.011064	1.082036	1.010627	
1.01652	1.038541	1.072199	1.13137	1.021975	1.065702	1.020415	1.050796	
1.022111	1.000876	1.046769	1.074027	1.103012	1.058718	1.043665	1.024623	
1.105203	1.024034	1.045798	1.110666	1.168235	0.998233	1.016157	1.019762	
1.08498	0.994224	1.129044	1.001629	1.189677	1.008391	1.02747	1.017995	
1.024663	1.063063	0.998147	1.030673	1.008355	1.024912	1.027244	1.060226	
1.049309	1.003075	1.073397	1.087539	1.035154	1.002754	1.057986	1.041695	
1.051774	1.046487	1.064093	1.104575	1.080479	1.047376	1.039127	1.087169	
1.046195	1.136164	1.031488	1.007966	1.070805	1.026241	1.082419	1.021517	
1.032578	1.112835	1.020202	1.052521	1.104167	1.034567	1.182874	1.042415	
1.106014	1.015547	1.017648	0.992659	1.074281	1.029703	1.068707	1.037719	
1.11299	1.004773	1.098395	1.009747	1.082708	1.047322	1.053819	1.001587	
1.016089	1.036872	1.034537	1.024322	1.066833	1.109556	1.012921	1.252765	
1.157158	1.065242	1.072011	1.018401	1.087389	1.030634	1.441279	1.038402	
1.073289	1.025604	1.005039	1.053633	1.160526	1.072201	1.036645	1.038238	
1.095183	1.00936	1.031117	1.064896			1.059451	1.086207	
1.141973	1.096883	1.001714	0.989091			1.09821	1.024851	
1.060144	1.046983	1.236323	1.047408			1.317591	1.013504	
1.02056	1.06489	1.116051	1.010379			1.08997	1.038034	
1.10414	1.051659	1.194231	1.071862			1.164865	1.047619	
1.117088	1.009658	1.127858	1.004272			1.191314	1.021825	
1.028031	1.020551	1.216908	1.066339			1.075095	1.004049	
	1.021725	1.111867	1.057163			1.142027	1.048193	
1.137098	1.053105	1.467309				1.008185	1.007269	
1.093979	1.048512	1.127942				1.060615	1.018452	
1.12855		1.03238				1.208551	1.032271	
1.084516						1.027671	1.000859	
1.136025						1.213855	1.041631	
						1.064579		
						1.035035		
						1.024358		
						1.262187		
<b>Mean</b>	<b>1.074532</b>	<b>1.039355</b>	<b>1.095129</b>	<b>1.04637</b>	<b>1.090153</b>	<b>1.03898</b>	<b>1.107497</b>	<b>1.040416</b>
<b>SEM</b>	0.008257	0.006929	0.018852	0.007979	0.0132	0.007318	0.018346	0.008581
<b># edges</b>	29	26	27	24	16	16	33	29

## 7.2.3 Laser ablation data analysis

Table 16 Vertex displacement analysis

Time	average normalised junction length				SEM normalized junction length			
	Stage 6 NCC	Stage 9 NCC	Stage 9 OCC	Stage 11 OCC	Stage 6 NCC	Stage 9 NCC	Stage 9 OCC	Stage 11 OCC
-4	-0.00308	-0.00354	0.007442	4.79E-17	0.009583	0.00649	0.004341	3.36E-17
-3.5	-0.00308	0.00531	0.002703	4.79E-17	0.004865	0.005628	0.009014	3.36E-17
-3	0.003077	0.000877	-0.00633	4.79E-17	0.007346	0.002047	0.007457	3.36E-17
-2.5	0.009231	0.009692	0.00274	4.79E-17	0.012346	0.006083	0.008616	3.36E-17
-2	0.009231	0.009607	-0.00181	4.79E-17	0.009583	0.006371	0.010032	3.36E-17
-1.5	-0.00308	0.000873	-0.00182	4.79E-17	0.00559	0.002038	0.005718	3.36E-17
-1	-0.00308	0.000881	0.016364	0.002036	0.00559	0.005487	0.007336	0.002036
-0.5	-0.00308	-0.01233	-0.00179	0.002036	0.00559	0.005121	0.007018	0.002036
0	-0.00308	-0.00804	0.007273	0.002036	0.004865	0.004404	0.006749	0.002036
0.5	0.12	0.063111	0.038739	0.002036	0.014067	0.015981	0.012053	0.002036
1	0.150769	0.087967	0.041921	0.002036	0.020801	0.024918	0.011484	0.002036
1.5	0.163077	0.093548	0.046087	0.002036	0.023694	0.027993	0.009397	0.002036
2	0.193846	0.1088	0.041558	0.002036	0.022209	0.0297	0.011384	0.002036
2.5	0.212308	0.118898	0.050435	0.002036	0.025392	0.033251	0.009812	0.002036
3	0.230769	0.11751	0.04569	0.004071	0.023854	0.030361	0.012529	0.002665
3.5	0.249231	0.113619	0.045887	0.004071	0.026558	0.036255	0.013385	0.002665
4	0.249231	0.121875	0.063203	0.004071	0.024788	0.039805	0.014662	0.002665
4.5	0.243077	0.14031	0.045106	0.004071	0.026558	0.039476	0.014468	0.002665
5	0.261538	0.13384	0.054545	0.004071	0.025981	0.035464	0.016556	0.002665
5.5	0.273846	0.134351	0.049785	0.004071	0.032809	0.039644	0.018423	0.002665
6	0.273846	0.130534	0.04569	0.004071	0.030163	0.042699	0.013327	0.002665
6.5	0.286154	0.134866	0.067532	0.006107	0.030661	0.040648	0.015876	0.004284
7	0.286154	0.138168	0.05339	0.006107	0.030661	0.039287	0.01681	0.004284
7.5	0.310769	0.130038	0.054077	0.008142	0.026271	0.045669	0.017026	0.003078
8	0.329231	0.14636	0.075536	0.004071	0.026982	0.041986	0.013469	0.002665
8.5	0.323077	0.144151	0.057143	0.006107	0.033832	0.043113	0.017905	0.004284
9	0.341538	0.155472	0.062393	0.010178	0.030907	0.040848	0.016809	0.004284
9.5	0.329231	0.142537	0.045106	0.006107	0.026982	0.044686	0.016422	0.004284
10	0.353846	0.147925	0.058874	0.012214	0.034055	0.041668	0.016032	0.005104
10.5	0.341538	0.151128	0.07094	0.012214	0.033154	0.042012	0.013121	0.005104
11	0.353846	0.158052	0.078481	0.008142	0.033039	0.044124	0.01569	0.005331
11.5	0.353846	0.156877	0.069456	0.008142	0.028617	0.04316	0.019064	0.005331
12	0.347692	0.160595	0.065823	0.012214	0.03372	0.042562	0.018069	0.005104
12.5	0.36	0.16	0.061864		0.033268	0.044475	0.021478	
13	0.36	0.178519	0.070638		0.031273	0.040209	0.015463	
13.5	0.36	0.171636	0.065823		0.036316	0.038372	0.019338	
14	0.36	0.172263	0.066102		0.037445	0.041114	0.01541	
14.5	0.372308	0.183212	0.087288		0.026982	0.041754	0.020856	
15	0.372308	0.166787	0.081328		0.037344	0.043381	0.021438	
15.5	0.372308	0.169231	0.073333		0.034387	0.045021	0.020909	
16	0.366154	0.176557	0.061345		0.036936	0.04084	0.022724	
16.5	0.384615	0.175273	0.074894		0.033381	0.046926	0.025948	
17	0.378462	0.171636	0.082353		0.031394	0.046539	0.021978	
17.5	0.390769	0.172263	0.073333		0.030289	0.043832	0.020537	
18	0.378462	0.190511	0.082353		0.033495	0.044619	0.019419	
18.5	0.390769	0.179928	0.085833		0.031394	0.044543	0.020789	
19	0.390769	0.184838	0.06473		0.031394	0.046553	0.023187	
19.5	0.384615	0.176978	0.078814		0.033495	0.045237	0.023569	
20	0.403077	0.185507	0.082008		0.036001	0.042982	0.028386	
#ECs	10	10	10	8				

Green cells are the time point of laser ablation

Table 17 Medial cortical area change analysis

Time	average normalized area			SEM normalized area		
	Stage 6 NCC	Stage 9 NCC	Stage 9 OCC	Stage 6 NCC	Stage 9 NCC	Stage 9 OCC
-4	-0.00155	-0.00151	0.000436	0.002289	0.001171	0.001697
-3.5	0.001588	-0.00053	0.000981	0.001952	0.001624	0.001428
-3	-0.00029	0.000698	-0.00065	0.002023	0.001484	0.002445
-2.5	-0.00076	0.002167	0.004116	0.004773	0.00292	0.001149
-2	-0.00092	0.00278	-0.00311	0.003487	0.002038	0.002227
-1.5	0.000543	-0.00089	-0.00352	0.002595	0.002549	0.002356
-1	0.00305	-0.00077	0.002753	0.002459	0.001806	0.003669
-0.5	0.002632	0.00131	-0.00147	0.003173	0.003716	0.002627
0	0.005138	-0.00224	-0.00311	0.002283	0.001614	0.002668
0.5	0.074487	0.066823	0.031785	0.020281	0.017097	0.00901
1	0.092033	0.072824	0.033012	0.02121	0.019484	0.009435
1.5	0.098509	0.088375	0.035738	0.022344	0.021617	0.009793
2	0.100597	0.089967	0.043916	0.024841	0.023442	0.009042
2.5	0.119397	0.096825	0.032466	0.02867	0.025577	0.015916
3	0.11877	0.099519	0.047732	0.029473	0.02672	0.011846
3.5	0.128588	0.108458	0.050731	0.031919	0.025761	0.014006
4	0.135063	0.107968	0.056319	0.033146	0.027912	0.013673
4.5	0.140912	0.114091	0.05482	0.032723	0.027694	0.014738
5	0.14112	0.117642	0.068449	0.034742	0.029399	0.020901
5.5	0.148431	0.120214	0.064497	0.035467	0.029249	0.016037
6	0.150938	0.127928	0.049095	0.037421	0.030197	0.028413
6.5	0.157831	0.126459	0.078944	0.036609	0.03109	0.019455
7	0.157831	0.131969	0.070903	0.037208	0.032116	0.016064
7.5	0.165768	0.129887	0.068041	0.040949	0.031106	0.019361
8	0.165977	0.131234	0.068858	0.040679	0.032519	0.019514
8.5	0.173497	0.134296	0.068313	0.042094	0.032515	0.02279
9	0.173706	0.13601	0.079899	0.043521	0.034251	0.018757
9.5	0.17475	0.138459	0.090257	0.042179	0.033242	0.017492
10	0.184986	0.141766	0.067632	0.043297	0.033421	0.019278
10.5	0.185612	0.145807	0.080307	0.043577	0.034484	0.021472
11	0.181017	0.147398	0.092574	0.045318	0.033881	0.019331
11.5	0.177466	0.146051	0.075128	0.041912	0.035151	0.020014
12	0.193759	0.151684	0.08058	0.043765	0.03798	0.021683
12.5	0.201278	0.150827	0.093392	0.045369	0.035591	0.019541
13	0.202741	0.152174	0.091075	0.045195	0.03697	0.021486
13.5	0.19731	0.149725	0.093256	0.045572	0.037313	0.022842
14	0.207127	0.156827	0.092302	0.047759	0.03771	0.022082
14.5	0.209425	0.157317	0.096527	0.045502	0.037414	0.024015
15	0.209425	0.163195	0.099662	0.046472	0.036983	0.024653
15.5	0.215691	0.161113	0.084124	0.048458	0.039353	0.026857
16	0.213811	0.168338	0.103887	0.047612	0.039878	0.024548
16.5	0.216736	0.165399	0.102933	0.050349	0.039073	0.024864
17	0.215482	0.167848	0.099798	0.050293	0.040817	0.024563
17.5	0.217571	0.167359	0.107567	0.048437	0.040408	0.025418
18	0.218407	0.173481	0.104569	0.052187	0.039182	0.028795
18.5	0.218824	0.1714	0.107567	0.051634	0.039559	0.027441
19	0.225509	0.171155	0.102661	0.050554	0.041495	0.026948
19.5	0.228015	0.176665	0.109339	0.054351	0.041944	0.029317
20	0.221122	0.175441	0.117653	0.054033	0.041947	0.026142
20.5	0.231984	0.173849	0.116836	0.053836	0.042327	0.027345
21	0.235117	0.183155	0.104569	0.054323	0.042602	0.031574
21.5	0.234073	0.178869	0.117517	0.054822	0.042619	0.030384
22	0.235535	0.179604	0.122833	0.054215	0.042315	0.028603
22.5	0.241175	0.181441	0.111656	0.057174	0.045556	0.0292
23	0.241593	0.188298	0.127876	0.054901	0.045781	0.030205
23.5	0.231775	0.183155	0.123242	0.056876	0.04458	0.032035
24	0.240548	0.188053	0.124468	0.054866	0.043879	0.026625
24.5	0.248277	0.185727	0.128694	0.055743	0.046531	0.033994
25	0.244099	0.192952	0.128285	0.056922	0.044595	0.029129
25.5	0.245352	0.188666	0.128285	0.055444	0.045564	0.033284
26	0.252037	0.190747	0.133192	0.057364	0.047158	0.031316
26.5	0.24953	0.188298	0.13251	0.057411	0.045817	0.029992
27	0.250783	0.199564	0.11629	0.059191	0.048274	0.025336
27.5	0.251619	0.19136	0.11261	0.059807	0.04563	0.048322
28	0.249948	0.195646	0.145867	0.061205	0.04778	0.033358
28.5	0.250366	0.201156	0.173945	0.060582	0.049342	0.061379
29	0.256214	0.199687	0.145322	0.060113	0.047181	0.030954
29.5	0.261645	0.190625	0.131692	0.060147	0.048929	0.030537
30	0.254334	0.206177	0.1336	0.060703	0.046701	0.036068
30.5	0.259347	0.192829	0.107158	0.059263	0.048767	0.056433
31	0.26081	0.201034	0.113973	0.060601	0.049819	0.053413
31.5	0.262898	0.196993	0.14137	0.060713	0.050374	0.034284
32	0.267285	0.202381	0.139325	0.060312	0.049241	0.036129
32.5	0.272298	0.196993	0.152273	0.060974	0.049789	0.037051
33	0.272507	0.202136	0.137826	0.062032	0.050756	0.038053
33.5	0.273343	0.20287	0.149275	0.062536	0.051225	0.03781

## APPENDIX

#ECs	10	10	10
------	----	----	----

Green cells are the time point of laser ablation

**Table 18 Calculated junctional recoil velocities upon laser ablation**

	st6 NCC	st9 NCC	st9OCC
	0.369231	0.088183	0.090744
	0.123077	0.088183	0.090744
	0.246154	0.088183	0.090744
	0.246154	0.352734	0
	0.123077	0.088183	0
	0.246154	0.176367	0
	0.369231	0.26455	0
	0.369231	0.088183	0.181488
	0.246154	0.088183	0
	0.123077	0.088183	0.181488
<b>Mean</b>	<b>0.246154</b>	<b>0.141093</b>	<b>0.063521</b>
<b>SEM</b>	0.031778	0.029977	0.023624
<b>#ECs</b>	10	10	10

**Table 19 Calculated medial cortical area recoil velocities upon laser ablation**

	st6 NCC	st9 NCC	st9 OCC
	0.104441	0.182947	0.012267
	-0.01253	0.110209	0.120216
	0.225592	0.077146	0.134936
	0.254836	0.105801	0.019627
	0.058487	0.061717	0.071148
	0.233947	0.383527	-0.02208
	0.392697	0.085963	0.061335
	-0.00418	0.039675	0.061335
	0.125329	0.196172	0.169284
	0.008355		
<b>Mean</b>	<b>0.138697</b>	<b>0.138129</b>	<b>0.069785</b>
<b>SEM</b>	0.042516	0.033428	0.19715
<b>#ECs</b>	10	9	9

### 7.2.4 FLIM analysis

**Table 20 Fluorescence life times of junctions in NCCs and OCCs at stage 9 in DE-Cad TS egg chamber**

	Lifetime (ns)	
	stage 9 NCCs	stage 9 OCCs
	2.2378	2.208
	2.273	2.385
	2.339	2.172
	2.355	2.202
	2.346	2.383
	2.224	2.473
	2.435	2.339
	2.289	2.316
	2.267	2.328
	2.272	2.254
	2.21	2.291
<b>Mean</b>	<b>2.295254545</b>	<b>2.304636364</b>
<b>SEM</b>	0.0671	0.0274
<b>#ECs</b>	11	11

Table 21 Fluorescence life times of the front and rear of a migrating border cell cluster in DE-Cad TS egg chambers

TS	Lifetime (ns)	
	Border cells front	Border cells rear
	2.174	2.257
	2.168	2.386
	2.402	2.246
	2.299	2.271
	2.136	2.191
	2.197	1.814
	1.94	1.863
<b>Mean</b>	<b>2.188</b>	<b>2.147</b>
<b>SEM</b>	0.0541	0.0828
<b>#ECs</b>	7	7

Table 22 Fluorescence life times of the front and rear of a migrating border cell cluster in DE-Cad TS control egg chambers

TS-control	Lifetime (ns)	
	Border cells front	Border cells rear
	2.152	2.204
	2.298	2.13
	2.131	2.361
	2.091	2.073
	2.246	2.012
<b>Mean</b>	<b>2.184</b>	<b>2.156</b>
<b>SEM</b>	0.0383	0.0603
<b>#ECs</b>	5	5

## 7.2.5 Nurse cell aspect ratio and area measurements

Table 23 Total germline area measurements for different genotypes

	wt	<i>cnoOE</i>	<i>Rac1DN</i>	<i>rok</i>	<i>sqh</i>	wt <i>st10</i>
	20980.8	23312.4	26590	20941.2	15813	24447.43
	17429.8	27016.6	18987.9	22686.4	17579.7	26076.19
	16765.3	24724.5	27419.3	21935.8	17528	26783.46
	18122.3	29763.7	21566.7	23349.5	16162.7	27409.67
	19780.2	29805.7	34231	32824.1	22123.6	27671.3
	19261.6	33573.9	37868.7	28143.7	19108.2	28039.75
	17002.9	34675.5	38674.7	18079.7	14262.9	32038.76
	19934.9	35216.7	41706.2	18784.7	18756.1	32738.44
	24091.1	35273.9		22569.6	14786.4	38677.81
	24554.4	37256.1		21754.7	23923.6	43497.79
		39095.8		26366.6	26851.9	
		40006.4		29242.2		
		40062.1		29914.5		
		41408.9		33384.7		
<b>Mean</b>	<b>19792.33</b>	<b>33656.59</b>	<b>30880.56</b>	<b>24998.39</b>	<b>18808.74</b>	<b>30738.06</b>
<b>SEM</b>	870.4132	1574.074	2977.82	1330.781	1198.126	1932.907
<b>#ECs</b>	10	14	8	14	11	10

APPENDIX

Table 24 NC to OO area ratio measurements for different genotypes

	<i>wt</i>	<i>cnoOE</i>	<i>Rac1DN</i>	<i>rok</i>	<i>sqh</i>	<i>wt st10</i>
	4.8	5.7	4.7	4.2	4.1	3.105374
	4.2	3.5	5.9	3.5	2.5	3.828724
	4.4	4.2	4.3	3.9	2.7	2.655812
	4.4	2.8	5.9	3.6	3.7	2.70723
	4.8	2.8	2.1	2.9	2.9	2.945101
	3.6	2.2	2	2.6	3.1	2.987131
	5.8	1.9	2.1	3.6	4.8	2.034875
	4.1	2.8	1.3	4	2.7	2.877018
	3.5	1.8		3.5	4.2	2.271155
	3.7	1.6		2.8	1.5	2.466375
		1.8		3.1	3.5	
		2.6		2.3		
		1.3		2.4		
		2.7		1.9		
<b>Mean</b>	<b>19792.33</b>	<b>33656.59</b>	<b>30880.56</b>	<b>24998.39</b>	<b>18808.74</b>	<b>30738.06</b>
<b>SEM</b>	870.4132	1574.074	2977.82	1330.781	1198.126	1932.907
<b>#ECs</b>	<b>10</b>	<b>14</b>	<b>8</b>	<b>14</b>	<b>11</b>	<b>10</b>

Table 25 Nurse cell compartment, oocyte and total germline AP length for wildtype and FCE expression of *crb* RNAi

	<i>wt</i>			<i>crb RNAi</i>		
	Oocyte length	Nurse cells length	Germline length	Oocyte length	Nurse cells length	Germline length
	0.22636	0.815929	4.439392	0.184071	0.815929	6.490221
	0.183666	0.420552	7.165568	0.158896	0.841104	6.024528
	0.192488	0.254378	3.922746	0.236866	0.763134	7.056327
	0.240375	0.197284	10.09805	0.210863	0.789137	9.578152
	0.185741	0.168765	7.900597	0.156173	0.843827	4.475256
	0.215303	0.141757	10.54529	0.149459	0.850541	3.91584
	0.223608	0.109899	10.27151	0.23071	0.76929	11.07553
	0.17868	0.104504	4.981262	0.163966	0.836034	5.686226
	0.167922	0.091173	5.930186	0.179442	0.820558	6.68
	0.190141	0.083859	7.632816	0.161414	0.838586	3.694084
	0.257709	0.073564	12.12696	0.190791	0.809209	3.965577
	0.19882	0.068578	3.604551	0.177069	0.822931	9.306117
	0.182697	0.061718	2.761484	0.197666	0.802334	5.206104
				0.175513	0.824487	3.878156
				0.214689	0.785311	9.988489
				0.162378	0.837622	6.559828
				0.223047	0.776953	11.36751
				0.154202	0.845798	10.3981
				0.244774	0.755226	11.46625
				0.16246	0.83754	6.589889
				0.176973	0.823027	4.698071
				0.180063	0.819937	4.336219
				0.206304	0.793696	4.076952
<b>Mean</b>	<b>0.203347</b>	<b>0.199382</b>	<b>7.029264</b>	<b>0.184414</b>	<b>0.815586</b>	<b>6.891888</b>
<b>SEM</b>	0.007472	0.058303	0.843997	0.006231	0.006231	0.594161
<b>#ECs</b>	<b>13</b>	<b>13</b>	<b>13</b>	<b>21</b>	<b>21</b>	<b>21</b>

Table 26 Nurse cell compartment bulging measurements for different genotypes at stage 9

	<i>wt</i>	<i>cnoOE</i>	<i>Rac1DN</i>	<i>rok</i>	<i>sqh</i>
	1.417	1.095	1.235	1.343	1.521
	1.323	1.251	1.345	1.767	1.429
	1.31	1.413	1.316	1.056	1.2
	1.213	0.984	1.39	1.175	1.086
	1.262	1.264	1.163	1.461	1.233
	1.502	1.111	1.058	1.411	1.429
	1.619	0.98	1.273	1.411	1.603

1.396	1.114	1.279	1.471	1.163	
1.414	1.176	1.205	1.366	1.206	
1.397	1.199		1.466	1.368	
	1.116		1.446	1.093	
	0.847		1.117		
	1.297				
	1.31				
	1.195				
<b>Mean</b>	<b>1.3853</b>	<b>1.1568</b>	<b>1.251556</b>	<b>1.374167</b>	<b>1.302818</b>
<b>SEM</b>	0.037231	0.037749	0.33544	0.054745	0.053019
<b>#ECs</b>	<b>10</b>	<b>15</b>	<b>9</b>	<b>12</b>	<b>11</b>

Table 27 Nurse cell compartment aspect ratio measurements upon Collagenase treatment

	Untreated			Collagenase treated		
	width	length	l/w	width	length	l/w
180.637	196.665	1.08873	206.32	184.659	0.895013	
204.082	200.563	0.982757	281.876	251.962	0.893875	
169.768	204.783	1.206252	266.614	257.829	0.96705	
151.209	186.563	1.233809	140.395	148.102	1.054895	
178.094	232.577	1.305923	202.544	155.998	0.770193	
137.284	148.552	1.082078	272.417	274.858	1.008961	
160.006	163.425	1.021368	258.666	212.831	0.822802	
<b>Mean</b>		<b>1.16176</b>			<b>0.916113</b>	
<b>SEM</b>		0.044988			0.03824	
<b>#ECs</b>		<b>7</b>			<b>7</b>	

### 7.3 Statistics and analysis for recoil curves

Table 28 Fitting parameters for recoil curves in Figure 20

		$d_2 \pm \text{std. error}$	$T_1(s) \pm \text{std. error}$	$T_2(s) \pm \text{std. error}$
<b>Junctional cuts</b>	stage 6 NCC	0.121±0.008	7.063±0.523	0.304± 0.083
	stage 9 NCC	0.108±0.008	23.481±10.84	0.677± 0.125
	stage 9 OCC	0.041±0.005	26.569±30.878	0.201± 0.231
<b>Medial cortical cuts</b>	stage 6 NCC	0.090±0.003	17.741±1.001	0.392±0.055
	stage 9 NCC	0.08±0.002	18.227±1.176	0.396±0.049
	stage 9 OCC	0.030±0.005	27.075±7.159	0.191±0.354

Table 29 t- and P-values for the fitting parameters in Table 28

		$d_1$	$d_2$	$T_1(s)$	$T_2(s)$	$d_1$	$d_2$	$T_1(s)$	$T_2(s)$
<b>Junctional cuts</b>	st6 NCC	67.888	14.105	13.512	3.671	***	***	***	***
	st9 NCC	5.254	13.822	2.166	5.395	***	***	*	***
	st9 OCC	1.848	7.409	0.860	0.871	.	***	ns	ns
<b>Medial cortical cuts</b>	st6 NCC	61.253	33.714	17.715	7.071	***	***	***	***
	st9 NCC	56.692	38.556	15.495	8.112	***	***	**	**
	st9 OCC	8.150	6.329	3.782	0.539	***	***	***	ns

. indicates  $P < 0.1$ , \* indicates  $P < 10^{-2}$ , \*\*\* indicates  $P < 10^{-5}$

## Curriculum Vitae

Ramya Balaji

Born 26 July 1990, Dombivli, India

### Current

2013 – Present **PhD student in Biology**  
Graduate student of International Max Planck Research School of Life Science affiliated with Ludwig-Maximilians University  
Doctoral research being conducted in the lab of Dr. Anne-Kathrin Classen

### Education

2008 – 2013 **Masters and bachelor's degree in science**  
BS-MS dual degree from Indian Institute of Science Education and Research, Pune, India  
CGPA-9.5/10

### Publications

**Balaji R** \*, Bielmeier C\*, Harz H, Bates J, Stadler C, Hildebrand A, Classen AK  
*Calcium spikes, waves and oscillations in a large, patterned epithelial tissue*  
Scientific Reports. (2017).7:42786, \*shared authorship

### Manuscripts in preparation

**Balaji R**, Weichselberger V, Rodriguez M, Classen AK

Compliance and resistance to external forces coordinate cell shape transitions with organ growth and elongation in vivo

Dey B, Das T, Sherlekar A, **Balaji R** and Richa Rikhy

Lateral plasma membrane length supports polygonal epithelial-like geometry in syncytial *Drosophila* embryos

*Truth in science can be defined as the working hypothesis best suited to open the way to the next better one.*

*-Konrad Lorenz*